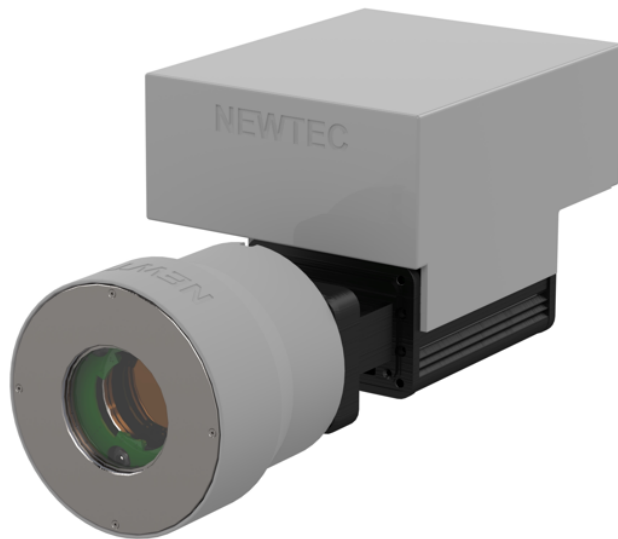# Methodologies for Hyperspectral Thermal Imaging

PhD-Thesis by:
Anders Christian Løchte Jørgensen
Newtec Engineering A/S and The University of Southern Denmark
October 31st 2021

Supervisors:
Bjarke Jørgensen
Head of Research and Development, Newtec Engineering A/S

Jakob Kjelstrup Hansen
Associate Professor
The Mads Clausen Institute, The University of Southern Denmark

This thesis is submitted to the Faculty of Engineering at the University of Southern Denmark in order to fulfil the requirements for obtaining a PhD-degree.

Abstract

This PhD project focuses on the development and characterisation of a hyperspectral thermal imaging system. The imaging system is based on a commercial microbolometer sensor, with a sensitivity in the long wave infrared (LWIR) range between 8 and 14 µm, followed by a scanning Fabry-Pérot interferometer (FPI) in front of the collecting optics. The hyperspectral datacube is therefore plane scanned, which allows the camera to build the hyperspectral datacube while being statically mounted.

The scanning FPI, acting as a wavelength filter, operates in the first order. The most essential components in the FPI are the thermal mirrors which constitute the focus of the first part of this thesis. Initial physical vapour deposition (PVD) experiments provided thermal mirrors that lead to hyperspectral thermal images which documented the concept of the imager. A mirror was produced by using a recipe which consisted of three-layer-structure including an absentee layer at the design wavelength of 10.5 µm. The thermal mirror recipe comprised of an antireflective coated ZnSe substrate upon which a $Ge/BaF_2/Ge$-coating was deposited. The two mirrors used in the FPI showed average absorption values of 10.5 % and 6.8 % measured by standard Fourier transform infrared spectroscopy (FTIR) measurements combined with a reflection-configured FTIR measurement. The mirrors were incorporated into an FPI and used to acquire hyperspectral thermal images. It was shown that the difference in the emission spectrum of five samples of polyimide tape, a carbon nanotube coated aluminium surface, borosilicate glass, black painted aluminium, and bare aluminium was measurable at 100 °C as opposed to the measurements of the emitted thermal radiation at room temperature (RT). The RT measurements were very inefficient using the high absorption homegrown mirrors, and at the final part of this project, commercially coated thermal mirrors were purchased and incorporated into the FPI. These mirrors consist of an antireflective coated ZnSe substrate coated with a $Ge/ThF_4/Ge$ coating with absorption values of <2 % within the sensor sensitivity range measured by a combination of FTIR and FTIRR measurements. These mirrors were incorporated into the FPI and used to acquire hyperspectral thermal images. A logistic regression model was used to differentiate between polyimide tape, Al_2O_3,

borosilicate glass, fused silica, and Al_2O_3 ceramic at temperatures as low as 34 °C. Each material was recognised with true positive rates above 94 %, calculated from the individual pixel spectrum. The surface temperature of the samples was subsequently predicted using pre-fitted partial least squares (PLS) models, which predicted all surface temperature values with a common root mean square error (RMSE) of 1.10 °C whereby it outperformed conventional thermography.

The last chapter concerns applications of the hyperspectral thermal imaging system developed in this thesis. Two separate images are analysed and documents a strong segregation of organic gasses based on transmission spectra, and a promising segregation of polymers based on emission spectra at 100 °C compound temperature.

In summary, it is concluded that an FPI based hyperspectral thermal imager is a viable instrument for hyperspectral acquisition of light emitted within the LWIR range.

Dansk Resumé

Dette PhD projekt omhandler designet, karakteriseringen og udviklingen af et hyper-spektralt termografisk kamera. Desuden omhandler projektet analysen af de løbende tredimensionelle hyperspekrale billeder, som er indfanget i løbed af forskellige stadier af fornævnte udvikling. Det hyperspektrale termografiske kamera bygger på et Fabry-Pérot interferometer (FPI) som fungerer som bølgelængde filter af det termiske lys der optages med kameraet.

En stor del kameraudviklingen drejede sig om produktionen af partielt transmitterende spejle til inkorporering i Fabry-Pérot interferometeret, som er blandt de mest essentielle komponenter i kameraet. Denne udvikling vedrørede pådampning af tyndfilm på zinkselenid substrater i form af halv- og kvartbølgelængde lag af skiftende materialer med henholdsvis højt og lavt refraktivt index. En succesfuld tyndfilmsstruktur bestående af tre lag af henholdsvis germanium/bariumfluorid/germanium blev deponeret på zinkselenid. Spejle af denne type blev inkorporeret it et FPI og det lykkedes at optage hyperspektrale termografiske billeder. På baggrund af disse billeder blev det vist at prøver bestående af en høj-emissivitets carbon-nanotube belagt overflade, aluminium, borosilikatglas, polyimid tape og sortmalet aluminum kunne skilles ad enkeltvist, baseret på deres termiske udstrålingsspektrum. Dette eksperiment viser at funktionaliteten i kameraet of understreget at termiske udstrålingsspektre kan opsamles med et hyperspektralt termografisk kamera, baseret på et FPI.

Senere i projektet blev lav-absorptions spejle anskaffet bestående af en tre-lags struktur af henholdsvis germanium/thoriumfluorid/germanium fra selskabet II-VI Incorporated. Disse spejle blev brugt til at optage hyperspektrale termografiske billeder med en nøjagtig materialegenkendelse ned til 34 °C af fem prøver bestående af polyimid tape, Al_2O_3, borosilikatglas, kvartsglas og keramisk Al_2O_3. Materialegenkendelsen kunne udføres ved 34 °C med korrekt bestemmelse over 94 % af tilfældende. Over 34 °C kunne materialerne bestemmes med 100 % nøjagtighed. Desuden kunne overfladetemperaturen af fornævnte prøver bestemmes indenfor en usikkerhed på 1.1 °C baseret på det termiske udstrålingsspektrum og materialespecifikke temperatur-

modeller.

I slutningen af dette projekt forsøges det hyperspektrale kamera anvendt til genkendelse af polymerer opvarmet til 100 °C og separering af transmissions spektret for specifikke gas-atmosfærer. Begge disse eksperimenter viste lovende resultater. Det kan dermed konkluderes at det hyperspektrale termografiske kamera udviklet i dette projekt kan anvendes til nyttefuld avanceret termografisk analyse.

Preface

This project is a 3-year Industrial PhD initiated as a collaboration between Newtec Engineering A/S and the Mads Clausen Institute at the University of Southern Denmark (SDU). The project was funded by the Innovation Fund Denmark and Newtec Engineering A/S. Several people have been involved in the project and although everyone has contributed, a few people must be pointed out individually.

First and foremost I want to send a huge thank you to Bjarke Jørgensen. Bjarke has been a great leader and taught me not only to deal with physics and research within industry, but also that life is pain, and how to get used to it. I am grateful for the never ending encouragement from Bjarke relating to all sorts of adventures, be it long hours in the cleanroom in Sønderborg or bungyjumping in Copenhagen.

My main supervisor at SDU, Jakob Kjelstrup-Hansen, must also be thanked for always being supportive and taking the time to answer calls and e-mails. While most of this PhD was carried out in Odense, a significant part of the development was carried out in the cleanroom facilities at SDU in Sønderborg. During these experiments, Jakob has always taken the time to help and tolerated every frustration along the way.

I have to thank Bjarke Jensen for being a technical mentor and moral support from the beginning until the end of this project. Several long ours was spent in the cleanroom wiping BaF_2 off chamber walls, and I'm thankful for all the Philosophical discussions along the way. Also a huge thanks for proofreading this thesis!

Also, a huge thanks to Victor Petrunin for being a walking Physics Encyclopaedia and for being cheerful no matter how many bad ideas I had along the way. Thanks for letting me try anyway.

A special thanks goes to the remaining guys in the laboratory at Newtec, and specifically Elmedina Dervisevic, Søren Stærke, Sune Fuglsang, Mads, and Mads for having the patience to listening to my bullshit for three full years. You all contribute to a great working environment, and I am grateful for the time spent with you. Mads (the reader may guess which) should be pointed out for being a stellar masters student!

Henrik Andersen has to be mentioned for always finding time to help on software related problems. And for being cheerful and teaching me everything I wanted to

Contents

Contents

List of Publications

Material classification via long range thermal emission spectroscopy using a first order scanning Fabry Pérot interferometer [1]
In the peer review process in the journal Optics Express in the year 2021

Acquisition and Analysis of Hyperspectral Thermal Images for Sample Segregation [2]
Published in the journal Applied Spectroscopy in the year 2020

Other publications not relevant to this thesis:

Growth and electronic properties of bi-and trilayer graphene on Ir (111) [3]
Published in the journal Nanoscope in the year 2020

Chemically-resolved determination of hydrogenated graphene-substrate interaction [4]
Published in the journal Physical Chemistry Chemical Physics in the year 2019

Abbreviations

AM   Additive Manufacturing

BMS   Battery Management System

EDX   Energy-dispersive X-ray spectroscopy

ETV   Edge Thickness Variation

FFT   Fast Fourier Transform

FPA   Focal Plane Array

FPI   Fabry-Perot Interferometer

FTIRR   Fourier Transform Infrared Spectroscopy (Reflection)

FTIR   Fourier Transform Infrared Spectroscopy

FWHM   Full Width at Half Maximum

GUI   Graphical User Interface

HSI   Hyperspectral Imaging

HSTC   Hyperspectral Thermal Camera

HSTI   Hyperspectral Thermal Image

IR   Infrared

LWIR   Long Wave Infrared

Contents

MCT   Mercury Cadmium Telluride

MLR   Multinomial Logistic Regression

OPD   Optical Path Difference

OT   Optical Thickness

PCA   Principal Component Analysis

PC   Principal Component

PI   Polyimide Tape

PLS   Partial Least Squares

PVD   Physical Vapor Deposition

QWIP Quantum Well Infrared Photodetector

QWOT Quarter Wave Optical Thickness

RT   Room Temperature

SEM   Scanning Electron Microscope

SNR   Signal to Noise Ratio

UHV   Ultra High Vacuum

UV   Ultra Violet

1

An Introduction to Hyperspectral Thermal Imaging

Rise above, focus on science.

1.1 Motivation

The aim of this PhD project is to understand the field of hyperspectral thermal imaging. A hyperspectral imaging system functions much like any other imaging system, however, the produced image is a three-dimensional image containing a continuous spectrum of all the "colours" present in the image frame. The Finnish company Specim and the Canadian company Telops are among the very few companies that build and sell hyperspectral thermal imaging systems. The specific design, benefits and limitations of each system is discussed later in this introduction. The main focus of this thesis is the characterisation and development of a Fabry-Pérot based hyperspectral thermal imaging system with specifications and price-point outside the range of the previously mentioned commercially available systems. The motivations for building this system are many, but the main incentive come from the key limitations of thermography related to the often unknown emissivity of the imaged object. The emissivity is essential for a correct temperature determination which will be presented later in this introduction. A hyperspectral thermal imaging system measures the emissivity indirectly, and it is therefore believed that such system is an important step in the right direction toward more accurate temperature determination and thermographic analysis in general.

As we shall see, the development of a hyperspectral thermal imaging system filtering light using a Fabry-Pérot interferometer (FPI) is indeed a viable solution. While the laws of physics do not prevent an FPI based hyperspectral imaging system to be built, only few attempts have been reported in the literature. As any experimentalist would know, the path between theory and practice is filled with obstacles, and therefore, starting out this project a list of success criteria was formulated. These criteria were:

- Design of a variable filter with a narrow transmission peak in the 8-14 μm range.

- Design of dielectric mirrors for a FPI with a high reflection in the 8-14 μm wavelength range using mathematical modelling. The FPI should have an effective bandpass with at least 60 % transmission and less than 1 μm full width half maximum (FWHM).

- Fabrication of optical components with a mid-infrared sensor in a camera; recording hyperspectral images with at least 30 distinguishable bands.

- Material and temperature recognition able to determine the material and temperature within 5 %.

1.2 Outline

Chapter 1 the remaining part of this chapter gives an introduction to the basic areas of physics which are relevant for understanding the working principle of hyperspectral imaging in general and thermal imaging specifically. The final part of the chapter deals with hyperspectral thermal imaging and serves an overview of our imaging system which is the main part of this thesis.

Chapter 2 provides a description of the working principle behind the main experimental techniques used during the project. The experimental techniques relate primarily to the FPI mirror development which took place in the cleanroom facilities at the Mads Clausen Institute at SDU in Sønderborg.

Chapter 3 provides experimental results and discussions regarding the development of FPI mirrors that can be integrated into a hyperspectral thermal imaging system. Additionally, the chapter includes the characterisation of the commercially available FPI mirror options acquired from the companies Giai Photonics and II-VI Incorporated. All results presented in this chapter are at the time of submitting this thesis unpublished.

Chapter 4 concerns the hyperspectral thermal imaging system developed at NEWTEC. The chapter provides a general description of the working principle of the imaging system as well as the key concepts regarding the physics behind the camera. Several iterations and developments were made during the three-year period and a selection of these are included in this chapter. Additionally, the development of a FPI mirror alignment station is described in detail, which is a key improvement and help during the assembly of the hyperspectral thermal camera.

Chapter 5 provides a theoretical background of the main algorithms used for the data analysis of the images obtained. The analysis includes data preprocessing techniques as well as the post processing algorithms such as principal component analysis (PCA), K-Means, partial least squares regression (PLS) and the multinomial logistic regression (MLR) classifier.

Chapter 6 concerns the initial results obtained using the FPI based hyperspectral thermal imaging system. The data presented in this chapter is based on the FPI mirrors produced in the cleanroom facilities at SDU and an early version of the

hyperspectral imaging system capable of acquiring 70 spectral bands. The chapter presents published results from [2].

Chapter 7 presents a study where the ability to determine the surface temperature of a selection of samples was investigated. The surface temperature of the samples was found by initially using an MLR classifier to predict the material measured for each pixel in the image frame and subsequently predicting the surface temperature using a material specific PLS model. The chapter presents results due to be published [1].

Chapter 8 presents results obtained in the search for industrial applications for a hyperspectral thermal imaging system. Two different experiments are presented where the hyperspectral thermal imaging system is used for measuring the transmission spectrum through an organic gas atmosphere and the emission spectrum from a selection of heated polymers. The results presented in this chapter are unpublished.

Chapter 9 provides a general summary of the key results presented throughout this thesis. Additionally, an outlook is included which discusses further development of the hyperspectral thermal imaging system, as well as some of the remaining barriers which need to be overcome in order to have a fully functioning and reliable system.

And here we go. Enjoy!

1.3   Introduction

Starting out in elementary school, the first principles taught in the physics classroom revolve around the periodic table of the elements and that atoms constitute the main building blocks of our universe. Moving on in life, the principles and laws of physics become increasingly complex and move from classical mechanics to quantum mechanics mixing up the relationship between mathematics and physics. That development does not, however, change the facts taught in elementary school, i.e. that the world consists of atoms interacting with the surrounding world. The possible interactions between atoms are limited and controlled by the four natural forces. The electromagnetic force, the strong nuclear force, the weak nuclear force, and the gravitational force. This thesis will primarily revolve around the electromagnetic force dealing with light matter interactions.

The increased complexity in our modern world calls for new methods for all different kinds of remote sensing spanning from the surveillance of crops and fields to medical diagnostics, and quality assurance within industrial processes. Thus, light sensors and cameras play important parts in the society at present day and continues to find new use cases within research and development and the industry.

This thesis specifically revolves around the characterisation and development of a hyperspectral thermal imaging system. The camera is based on a first order scanning Fabry-Pérot interferometer capable of filtering the light in the thermal range from 8-14 µm.

While this may sound complex to some at this point, the meaning and purpose of the following thesis is to ease the task of understanding the above paragraph for anyone.

1.4   The Electromagnetic Spectrum

Images of objects can be acquired through a wide variety of instruments and techniques, some of which will be introduced in Chapter 2, the most common way of constructing an image is through the collection of light. Our eyes collect light all the time and an image of the surrounding world is created as a complex biological process in the brain when we are awake. A complex digital and physical process which is very similar to the one in the human eye and brain, happens when we use our smartphones to grab an everlasting image as a memory of our surroundings. Both processes involve the collection of photons within the visible part of the electromagnetic spectrum. Thus, the visible region of the electromagnetic spectrum equals the range of different photons that we as human beings can perceive.
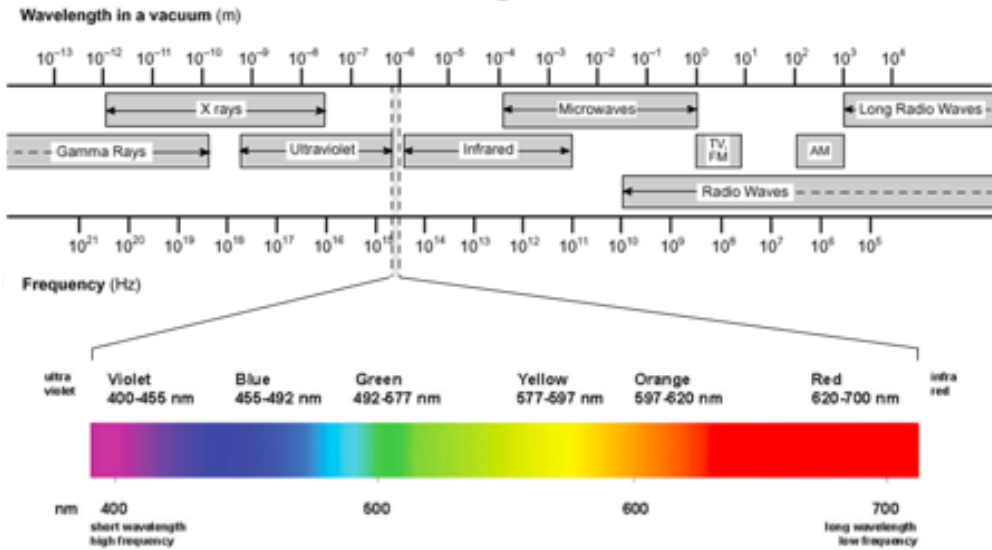
Figure 1.1: The electromagnetic spectrum with the high frequency, short wavelength (high energy) range to the left and low frequency, long wavelengths (low energy) to the right. The high energy region include gamma-rays, X-rays and ultraviolet light and the low energy region include thermal infrared, microwaves and radio waves. In between these regions lie the visible range of light. [5]

Having a visible part of the electromagnetic spectrum implies that there is also an invisible part. While the invisible part of the electromagnetic spectrum sounds thrilling, the invisible part of the electromagnetic spectrum has been divided into subgroups describing their uses and applications in our modern world. Figure 1.1 show a sketch of the electromagnetic spectrum and its subgroups outside of the visible light range. The sketch is sorted by both the wavelength and frequency of the light which follows the relations

$$f = \frac{c}{\lambda}, \text{ or } f = \frac{E}{h}, \text{ or } E = \frac{hc}{\lambda},$$

where f, is the light frequency, $c = 299\,792\,458 \text{ m s}^{-1}$ is the speed of light in vacuum, λ is the wavelength, E is the light energy, and $h = 6.626 \times 10^{-34} \text{ m}^2 \text{ kg s}^{-1}$ is Planck's constant. Looking at these equations it is immediately clear that the frequency and energy are inversely proportional to the wavelength. Since this project focuses on

the long wave infrared light and more specifically the 8-14 µm range, it should be noted that this light has low energy compared to the light visible to the human eye. The low energy of infrared photons is a significant drawback since it complicates the development of electron-hole excitation band gap detectors for this energy region. Bandgap detectors are desired due to their high sensitivity and efficiency.

1.5 Multispectral and Hyperspectral Imaging

Hyperspectral imaging was formally invented by Alexander Goetz as part of his work during the 1970's [6]. The working principle of hyperspectral imaging is illustrated in Figure 1.2. While a conventional image contains information in two dimensions, a hyperspectral image adds a third spectral dimension, and thereby the data structure gathered using a hyperspectral imager typically consists of a three-dimensional image cube. Most people never think about three-dimensional images, but almost everybody uses such images in their daily lives. Specifically, a standard image grabbed with a modern smartphone can be interpreted as a three-dimensional image, namely three two-dimensional images stacked on top of each other to form a single colour image. These images are commonly called RGB, where RGB is short for the three colours detectable by the human eye, namely red, green and blue. As with the smartphone, the human eye only detects red, green, and blue light and all other colours are perceived by the brain. A hyperspectral image does not differ much from an RGB image since the hyperspectral image consists of multiple images of different colours stacked on top of each other. A hyperspectral image cube can be constructed through several pathways. The three most common hyperspectral imaging types are the spatial scanning cameras, the spectral scanning cameras, and the non-scanning cameras. The spatial scanning cameras are often called line-scan or push broom cameras, and they function through the use of a diffracting element which scatters the incoming light onto the sensor focal plane array (FPA). Since most sensors have two dimensions, it is only possible to image one line at a time, which explains the name *line-scan camera*. A typical example of a spatial scanning setup is shown in Figures 1.2 A and B, where A shows a point scanning camera, and B shows a line-scanning camera. Both methods can construct a hyperspectral datacube by either moving the object imaged or moving the imager itself. Next in line is the plane-scanning hyperspectral imager and the working principle of this type is sketched in Figure 1.2 C. In this specific example, a filter on a rotating wheel is used to filter out most of the incoming light letting only a selected band or portion through. The hyperspectral datacube is constructed following the turning of the rotating wheel and the subsequent acquisition of an
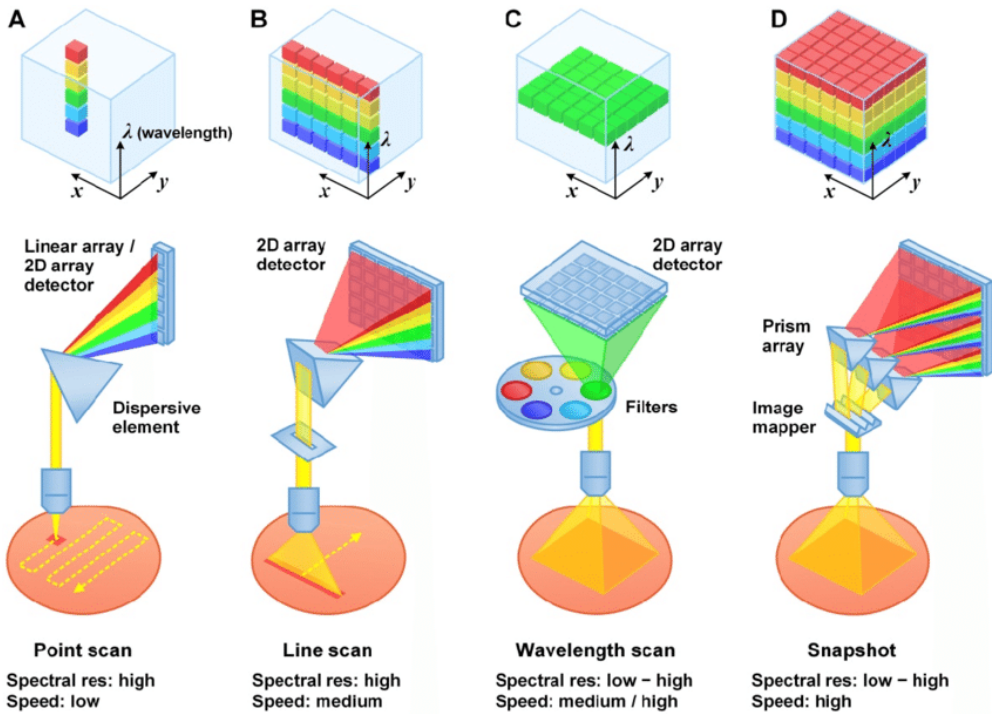
Figure 1.2: Graphical representation of the working principle of four hyperspectral imaging systems. (A) The working principle of a point scanning imager where the light spectrum of a single point is diffracted onto a linear sensor array. Noting the physical point of measurement, an entire array can be raster scanned, building a hyperspectral image. (B) The working principle of a line scanning setup where the spectrum of a single line is diffracted onto a two dimensional sensor. A hyperspectral imaging cube can be built by continously acquiring images while the imaged line is scanned a physical distance. (C) The working principle of a spectral scanning hyperspectral imager. The field of view of the imaging setup is altered by bandpass filters on the rotating wheel. Grabbing an image at multiple bandpass filters allows the hyperspectral image cube to be built up along the spectral axis whereas the object imaged is static. (D) The working principle of the snapshot imaging system where the entire hyperspectral image cube is built within a single snapshot with multiple difracting elements and a large two-dimensional sensor array. The three-dimensional datacube is typically constructed post-acquisition through computational imaging.[7]

image for every filter available. Figure 1.2 D shows the principle of a snapshot hyperspectral imager where the entire datacube is constructed in a single imaging event. A snapshot hyperspectral camera can be highly beneficial since the entire hyperspectral datacube is collected in a single image frame. This dramatically increase the speed of acquisition, however, the complexity of the optical system is increased along with the datacube construction and requirements for the sensor size which are the main reason why few snapshot hyperspectral cameras are available.

1.6 Thermal Imaging

Thermal imaging utilises Planck's law which dictates that all objects emit light, if the object temperature is above absolute zero. Planck's law, which can be derived from statistical thermodynamics, states that radiation is emitted continuously by matter and has a smooth continuous spectrum at all possible energy levels. Planck's law is given by

$$B(\lambda, T) = \frac{2\pi h c^2}{\lambda^5} \frac{1}{\exp\left(\frac{hc}{\lambda k T}\right) - 1} \tag{1.1}$$

B is the spectral radiance at wavelength λ and Temperature T. $c = 299\,792\,458\,\mathrm{m\,s^{-1}}$ is the speed of light, $h = 6.626 \times 10^{-34}\,\mathrm{m^2\,kg\,s^{-1}}$ is the Planck's constant, and $k = 1.381 \times 10^{-23}\,\mathrm{m\,kg^2\,s^{-2}\,K^{-1}}$ is the Boltzmann constant. Figure 1.3 (A) shows the spectral radiance of a perfect black body at elevated temperatures. Remembering from Figure 1.1 that visible light has a wavelength in the range 0.4-0.7 µm it is concluded that most of this light is not visible to the human eye until the object at hand reaches a temperature of several hundred degrees celsius. The radiance is concentrated around longer wavelengths (and lower energy) than the visible light and the as shown in Figure 1.1 this region is labelled the infrared (IR). The IR-range is often divided into sub-groups, such as the Near IR (NIR), short wave IR (SWIR), mid IR (MIR), and long wave IR (LWIR). The main focus of this thesis is the LWIR, which often is labelled the 8-25 µm region. This region is considered the thermal region of the electromagnetic spectrum, as most objects naturally emit light at temperatures near room temperature. The mean temperature of the earth is $\sim 14\,°\mathrm{C}$ [8], and plotting the spectral radiance at temperatures -20-$100\,°\mathrm{C}$ results in Figure 1.3 (B). This Figure shows the Planck distribution of a perfect black body near room temperature, which emulates the most likely theoretical distributions from objects in nature. Here it is seen that the peak position of the Planck distribution moves out of the plotting range set to 8-14 µm for the two most extreme temperatures.
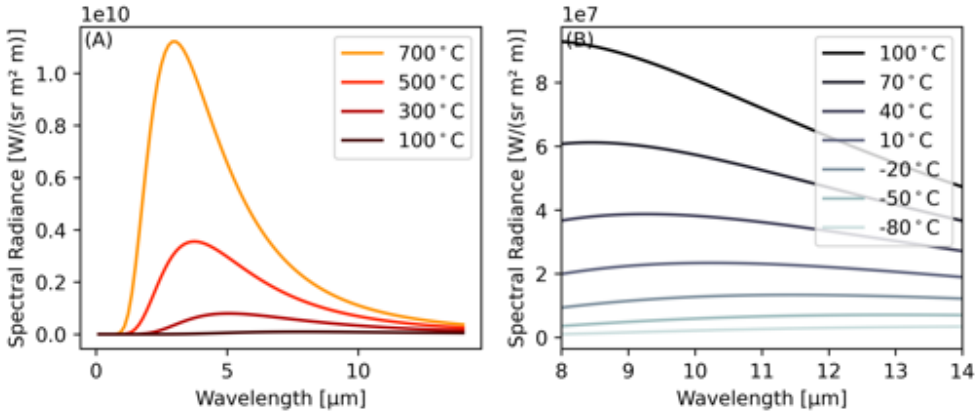
Figure 1.3: (A) A plot of the spectral radiance of a perfect emitter versus the wavelength of the emitted light is shown. The spectral radiance is plotted for emitter temperatures of 100, 300, 500, and 700 °C. The spectral radiance has the shape of the Planck distribution. (B) The spectral radiance is plotted versus wavelength for emitter temperatures between −80-100 °C in increments of 30 °C.

Theoretically, we can use Planck's law to derive the temperature of a given material by finding $\frac{dB_\lambda}{d\lambda} = 0$, the theoretically derived result is

$$\lambda_{max} = \frac{2898 \, \mu m \, K^{-1}}{T} \quad \Leftrightarrow \quad T = \frac{2898 \, \mu m \, K^{-1}}{\lambda_{max}} \tag{1.2}$$

and is commonly known as Wien's displacement law. This is a very useful law, since it gives a very simple pathway to finding the exact temperature of an object emitting light according to Planck's law. Constructing an instrument which measures the Planck distribution, finds the peak wavelength, and returns the temperature should therefore in theory be relatively straight forward. Unfortunately, the world is not that simple and most objects and materials in nature do not follow the Planck distribution of a perfect black body. The radiance of materials and objects in nature is modified by a physical quantity known as the emissivity. The emissivity is a factor describing a material or objects deviation from the ideal black body distribution. Since no material can naturally emit more light than the black body distribution dictates, the emissivity is a quantity less than unity which in the following will be termed $0 \leq \epsilon \leq 1$.

The emissivity is a wavelength-dependent parameter with values dependent on physical phenomena such as the intrinsic band gap, vibrational and rotational energies

10

of gas molecules, and the physical structure of the surface. Therefore, taking the emissivity of an object into account, the actual radiance from such object can be reduced to the following:

$$\text{Radiance from any object at any given } \lambda : \ B(\lambda, T) \cdot \epsilon(\lambda) \qquad (1.3)$$

i.e. it is clear that Wien's displacement law is no longer a viable option for determining the temperature by measuring the peak radiance of the black body emission. The emissivity could be significantly lower around the peak emission wavelength thereby creating a false peak position.

Within thermography in general, the emissivity is the main contributing factor to temperature misreadings, besides human errors. Thermal imaging cameras usually measure the thermal light radiated within a given wavelength range limited by the sensor sensitivity. The sensors are typically designed with sensitivities within two atmospheric windows. The first atmospheric window lies spectrally around $4\,\mu\mathrm{m}$ $\pm 1\,\mu\mathrm{m}$, and it is limited by the light absorbed by a combination of water vapour and CO_2 in the atmosphere. The second window lies within the range 8-14 $\mu\mathrm{m}$, and it is limited first by the absorption of water in the atmosphere (at $\lambda < 8\,\mu\mathrm{m}$) and, secondly, by the absorption of CO_2 in the atmosphere (at $\lambda > 14\,\mu\mathrm{m}$). This thesis focuses on the LWIR and these sensor types therefore measure the spectral radiance in this range, denoted B_{LWIR}, given by

$$B_{LWIR} = \int_{8\,\mu\mathrm{m}}^{14\,\mu\mathrm{m}} B(\lambda, T) d\lambda \qquad (1.4)$$

Equation 1.4 shows that thermal imaging cameras measure the temperature through the total amount of light emitted in the LWIR. Now moving one step closer to reality it is again seen that if adding emissivity to the equation, when dealing with everyday objects and materials, the exact temperature of the object under investigation becomes unpredictable, if the emissivity of the object is unknown since an underdetermined equation system is created

$$B_{LWIR} = \int_{8\,\mu\mathrm{m}}^{14\,\mu\mathrm{m}} B(\lambda, T) \epsilon(\lambda) d\lambda \qquad (1.5)$$

Using a conventional thermal imager, the intensity measured can then be calibrated to reveal the temperature of the object under investigation. However, this calibration

fails given that the emissivity across the wavelength range changes for two different objects. Typically, the mean emissivity of materials can be found as a table value, however, the surface structure of the material under investigation can alter this value and alleviate the temperature prediction error, within conventional thermography. Building a handheld camera capable of measuring the spectral radiance, $B(\lambda, T)$, at discrete wavelengths within the LWIR region would provide a method for estimating the emissivity at those exact wavelengths. Being able to measure the emissivity would bring us one step closer to an accurate temperature determination, since $B(\lambda, T)$ is well described by theory. That is the exact purpose of our hyperspectral thermal imaging camera.

The following sections will cover the three most common sensor types available for thermal imaging. These are the quantum well infrared photodetector (QWIP), the mercury cadmium telluride detector (MCT), and the microbolometer detector. Lastly, a brief summary of the current state of hyperspectral thermal imaging is summarised before reaching the core of this project.

The Mercury Cadmium Telluride Detector

Mercury Cadmium Telluride (MCT) sensors are electronic interband transition detector and therefore, they rely on the excitement of electrons from the valence band to the conduction band. In the thermal range, these band gaps are extremely small. With an energy value equivalent to 0.1550-0.0886 eV for 8-14 µm light the band gap of the detector would need to be lower than this value, to detect the photon. This energy level is comparable to the thermal energy at room temperature (0.0259 eV at 300 K), and thus, in order to minimise the spontaneous measurement of signals from thermally excited electrons, the MCT sensors must be cooled. Typically, these sensor types are cryogenically cooled to 77 K using either liquid nitrogen or advanced Stirling cycle coolers. Since MCT sensors are electronic interband transition sensors, the sensitivity of the sensors is very high. These devices are typically low resolution and high priced.

The Quantum Well Infrared Photodetector

The QWIP detector is typically made of the semiconductors gallium and arsenide which, mixed in the right ratio, produce quantum wells between the band gap which most commonly is much wider than the energy of the infrared light. The ground states in the quantum wells of the conduction band are typically filled by n-doping, and the infrared light can be detected as photocurrent, as the electron is excited to its

first excited state. Typically, this energy is designed to match the energy of the infrared light.[9, 10, 11, 12] This kind of energy transition is typically named an intersubband transition, and it is also highly affected by spontaneous thermal excitation, du to the low energy required for exciting the ground state quantum well electron. Thus, the QWIP requires cooling at cryogenic temperatures as well, which make both the MCT and the QWIP detector ill suited for low cost mobile applications.

The Microbolometer Detector

The relatively cheap and reliable alternative to MCT detectors is microbolometer sensors which commonly is operated at room temperature. The microbolometer utilises the principles of the second law of thermodynamics which states that:

"The spontaneous flow of energy stops when a system is at, or very near, its most likely macrostate, that is, the macrostate with the greatest multiplicity." [13]

Now without diving too deeply into thermodynamics and the concept of entropy, the meaning is that when two objects are in thermal equilibrium, the system has reached its steady state. This concept is utilised in a microbolometer sensor where the heat exchange between the two systems happen in the form of the interaction of light. As explained in section 1.6, any object with a temperature above absolute zero emits light which ultimately reduces the temperature of the object. The microbolometer sensor absorbs the light, which, however, leads to the microbolometer heating up itself. The laws of physics apply to the bolometer pixel as well, and therefore, at temperatures above absolute zero, the bolometer pixel emits radiation. Given enough time, this system reaches a thermal equilibrium where the light emitted by the bolometer pixel equals the light absorbed by the bolometer pixel. At this point the pixel is read out. The signal measured in the bolometer pixel is altered by the bolometric effect, which is defined as the resistivity change within a material caused by the material heating. As mentioned the pixels heat up from incoming long wave radiation and the electric signal, measured as the current running through each pixel, is therefore directly related to the amount of radiation absorbed by the individual pixel. A sketch of a typical microbolometer design is shown in Figure 1.4. The pixel design consists of a highly reflecting layer on the back-plane of the bolometer. The bolometric absorber is placed in suspension above this reflecting layer and is connected to the read out circuit through vertical wires. A design like this allows the thermal radiation to reflect multiple times between the absorber and the reflector.
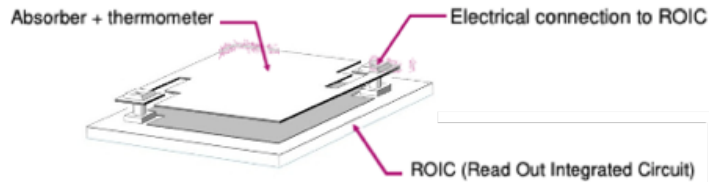
Figure 1.4: A sketch of a typical microbolometer. The absorber and thermometer is suspended above a reflecting back plate which allow the thermal light to heat up the thermometer. As the temperature of the thermometer changes, the current running through the bolometer changes as well. This change in current is measured by the ROIC through the electrical connections as a measure for the radiance.

1.7 Hyperspectral Thermal Imaging

All of the above mentioned types of infrared detectors have been used in various hyperspectral thermal imaging applications, and a few of these will be summarised here. The most complex hyperspectral thermal imaging systems are developed by NASA and these are either mounted in satellites such as the HyspIRI [14, 15] or an airplane as the HyTES [16]. Both of these instruments rely on cryogenically cooled QWIP sensors, and are high cost and high resolution instruments. Having left the atmosphere of the earth it should be mentioned that the mars rovers spirit and opportunity both were equipped with thermal emission spectrometers. Both of these were used to characterise and investigate the mineral and rock formations on Mars [17, 18, 19].

Besides space and airborne applications the field of hyperspectral thermal imaging is limited. A reason for this could be the limited commercial options. The Finnish company Specim provides two variants namely the Spectral Camera LWIR HS and the Spectral Camera OWL [20]. Both cameras are made from thermal spectrographs which refract the long wavelength light directly onto the sensor. The two cameras differ in that one is equipped with a cooled MCT sensor and the other with an uncooled bolometer sensor. Due to the choice of optical system, both cameras are line-scan cameras which require movement to function properly as mentioned in section 1.5.

The HyperCam-LW is available from the Canadian company Telops and this system is based on a Michelson interferometer and an MCT detector functioning in the 7.7-11.8 µm. The HyperCam-LW has a very high spectral resolution but a much lower imaging resolution of 320x256 pixels compared to. The system has been shown to have

14

applications within defence and strategy[21], where detection of thermal radiance from camouflaged targets is beneficial[22, 23]. Furthermore, a wide range of reports show the possibility of detecting minerals using the HyperCam-LW based on the spectral features of these materials within the sensitivity range [24, 25, 26, 27]. Aside from commercial solution a few custom solutions has been built and used within medicine quality assurance[28] and pathogen detection[29].

1.8   Overview of our Hyperspectral Thermal Imaging System

At this point it should be clear that the applications for a hyperspectral thermal imaging system spans a wide variety of fields. The price point of the Telops HyperCam-LW is reflected by the use of a cryogenically cooled MCT detector and a complex Michelson optical system. As mentioned the goal of this thesis is the development of a Fabry-Pérot based hyperspectral imaging system and the sensor of choice is the microbolometer. A demonstration of a Fabry-Pérot based hyperspectral imager has been reported previously [30] based on an MCT detector. Additionally, recent studies have reported the applicability of microbolometer sensors in hyperspectral thermal imaging systems. With that being said, no previous study has been found that combines the much cheaper bolometer sensor with the Fabry-Pérot interferometer which is reported in this thesis. For now, it is important to remember that the camera system in this project is a plane-wave hyperspectral imaging system building on four main components. These are the following:

- A scanning Fabry-Perot Interferometer acting as the image plane wavelength filter necessary for building the hyperspectral datacube.

- A focusing optical system

- A microbolometer sensor with sensitivity in the range 8-14 µm

- A QTechnology camera body capable of building and processing the hyperspectral datacube

The Hyperspectral Thermal Imaging Data Structure

It is of highest priority to define the data structure which is the typical result of a hyperspectral thermal imaging (HSTI) acquisition event. By now it should be clear that our hyperspectral thermal imaging camera is a plane-wave scanning device,

which constructs three-dimensional datacubes. Throughout this thesis a matrix is denoted as a capital letter in bold, and thus the datacubes are defined as

$$\text{Full datacube: } \mathbf{\Lambda}_{x_i, y_j, \lambda_k} \tag{1.6}$$

In the following sections the size of $\mathbf{\Lambda}$ is thus given by $x \times y \times \lambda$, individual entries are denoted x_i, y_j, and λ_k and the full length of an axis in any of the three dimensions is given by an asterix, $*$. Most often the analysis revolves around an individual spectrum measured from the radiance of a single object in a single pixel of the microbolometer sensor, and this spectrum will therefore be selected as:

$$\text{Single spectrum: } \mathbf{\Lambda}_{x_i, y_j, *} \tag{1.7}$$

The following chapters, 2 and 3 deal with the experimental techniques necessary for the FPI mirror development and the actual development of the mirrors, respectively. An elaboration of the camera components and working principle follows in Chapter 4.

2

Experimental Methods for Dielectric Mirror Deposition and Characterisation

The first section of the following chapter is devoted to a description of the working principle of the FPI itself, which is one of the four key components in the imaging system. The section elaborates the theory behind the FPI as a wavelength filter and underline the importance of the properties of the FPI mirrors. The remaining part of the chapter focuses on the working principle and physics behind the experimental techniques used during this project. The techniques have been employed in the FPI mirror development which is the main topic of Chapter 3. The description focuses primarily on the aspects of the techniques that are relevant to the experimental work of this project.
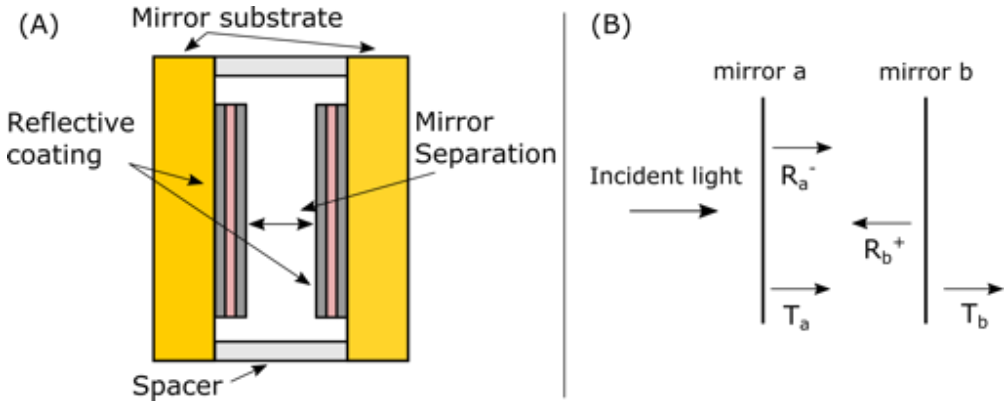
Figure 2.1: (A) Sketch of a typical Fabry-Pérot interferometer with two mirror substrates coated with reflective coatings. The two mirrors are arranged such that the reflective coatings are parallel and spacers are inserted which keep a certain mirror separation. (B) In the description and calculation of the theory of the Fabry-Pérot interferometer each mirror can be treated as a single interface (mirror **a** and mirror **b**). A fraction of the incident light is let into the cavity (T_a) and the light reaching mirror **b** is divided in two fractions given by the reflectivity, R_b^+, and transmittivity, T_b. The back reflected light from mirror **b** is reflected again by mirror **a**, R_a^-.

2.1 The Fabry Pérot Interferometer (FPI)

The FPI is one of the four main components of our hyperspectral thermal camera and it is therefore of highest importance to understand the basic physics behind. It is used as a tunable bandpass filter which sort the incoming LWIR radiation into discrete wavelengths. It is placed in the optical path of the incoming thermal light in order to create the individual image planes in the hyperspectral datacube.

The FPI was first described in 1899 by Charles Fabry and Alfred Pérot [31]. It consists of two ideally flat and parallel partially transmitting and reflecting mirrors separated by a distance which throughout this thesis will be referred to as the mirror separation (MS). In real life the FPI often looks like the sketch shown in Figure 2.1 (A) which show two transparent substrates with reflecting coatings separated by spacers. A sketch of the theoretical setup is shown in Figure 2.1 (B) where the solid vertical lines indicate each mirror. A theoretical description of the collective transmission of two partially reflecting, parallel mirrors including multiple reflections can be described as[32]

$$T = \frac{T_a T_b}{[1 - (R_a^- R_b^+)^{1/2}]^2} \left[1 + \frac{4(R_a^- R_b^+)^{1/2}}{[1 - (R_a^- R_b^+)^{1/2}]^2} \sin^2\left(\frac{\phi_a + \phi_b}{2} - \delta\right)\right]^{-1} \quad , \quad (2.1)$$

with T being the total transmitted light, T_a the fraction transmitted from mirror **a**, T_b the fraction transmitted from mirror **b**, R_a^- the reflected fraction from mirror **a**, and R_b^+ the reflected fraction from mirror **b**. ϕ_a equals the phase shift at mirror **a** and ϕ_b equals the phase shift at mirror **b** while $\delta = (2\pi n_s MS \cos(\theta)/\lambda$, with n_s and MS being the refractive index of the spacer layer and MS being the mirror separation distance. θ_s equals the angle of incidence for the plane wave. This equation allows the system as a whole to be described based on its effective performance. Thus a multilayer coating can be described based on a single effective layer. Additionally, the equation takes multiple reflections into account, and it is therefore ideal for the description of the theory of an FPI.

Often the two mirrors within a FPI have identical properties, and continuing with this assumption the above equation can be simplified by:

$$T = \frac{T_s^2}{(1 - R_s)^2} \frac{1}{1 + [4R_s/(1 - R_s)^2]\sin^2 \delta} \tag{2.2}$$

This equation is simplified by defining

$$F = \frac{4R_s}{(1 - R_s)^2} \quad . \tag{2.3}$$

This expression is sometimes abbreviated the coefficient of 'finesse', where the finesse is defined as the the ratio of the separation of two adjacent fringes to their full with at half maximum (FWHM). The effect of F becomes clear in a few steps, but first equation 2.2 is shortened to

$$T = \frac{T_s^2}{(1 - R_s)^2} \frac{1}{1 + F \sin^2 \delta} \quad . \tag{2.4}$$

Now, if we assume that the absorption in the FPI mirrors is non-existing, which is a quality highly wanted for FPI mirrors, the following is true for the reflection and
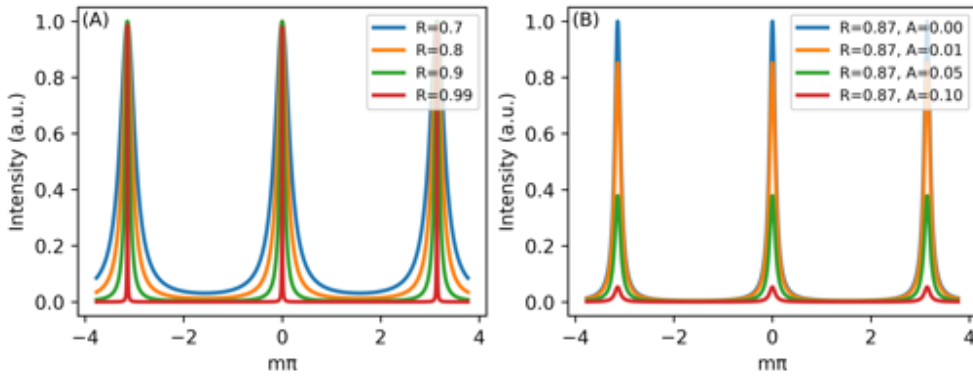
Figure 2.2: (A) Theoretical transmission of a Fabry-Pérot interferometer with mirrors having a reflectivity of 70%, 80%, 90% and 99%. (B) Theoretical transmission of a Fabry-Pérot interferometer with mirrors having 87% reflectivity and absorption values of 0.00%, 0.01%, 0.05%, and 0.10%.

transmission:

$$1 - R_s = T_s \qquad (2.5)$$

Substituting 2.5 into equation 2.4 results in

$$T = \frac{1}{1 + F \sin^2 \delta} \qquad , \qquad (2.6)$$

and it is possible to conclude that as F increases the width of T decreases, and thus the higher the reflectivity the higher the finesse of the FPI.

Equation 2.6 describes the transmission of the perfect Fabry-Pérot with non-absorbing mirrors. The equation is plotted in Figure 2.2 (A) as a function of the reflectivity of the mirrors as well as the value of δ plotted as $m\pi$ where $m = \frac{\lambda}{\lambda_0}$. The key points to remember related to this project is the fact that the full width at half maximum (FWHM) of the transmitted light is directly dependent on the reflectivity of the mirrors.

$$1 - R_s - A_s = T_s \qquad (2.7)$$

Solving for R_s and substituting into equation 2.4 the following expression for the transmission through the FPI is obtained.

$$T = \frac{1}{(1 + A_s/T_s)^2} \frac{1}{1 + F \sin^2 \delta} \tag{2.8}$$

Here, it is observed that the ratio of the absorption versus the transmission of the mirror substrates is the determining factor for the actual transmission through the FPI. It is furthermore noted that setting $A_s = 0$ we return to equation 2.6 once again. Figure 2.2 (B) shows the behaviour of equation 2.8 as the absorption is changed of a theoretical mirror substrate with a reflectivity of 87 %. This graph shows that the transmission percentage drops heavily with increasing absorption of the mirror substrate. This fact is quite important during the development of dielectric mirror substrates which is the main topic of the following Chapter 3. Before reaching the actual development of the semi-reflecting mirrors it is important to understand how the reflective coating can be made and characterised which is described next.

2.2 Physical Vapour Deposition (PVD)

Physical vapour deposition (PVD) is a common name for the process in which a solid material is typically vaporised within a vacuum chamber and deposited onto another material in order to alter the properties of the object as a whole. The properties in question may be everything from the hardness of the surface to its colour and appearance, and therefore PVD is highly relevant and can be found in every sector dealing with physical materials. In fact, chances are high that any reader of this thesis has a physical object within reach where PVD is a crucial part of the fabrication process. Relevant objects include gold coatings on jewellery, and colour coatings on metal parts, including watches and smartphones. While both of these applications concern aesthetics, PVD is used for critical functionality as well. Examples include the fabrication of custom sensors, transistors and microchips in general. Furthermore, sub-nanometer thin and even layers can be deposited to form anti-reflective, reflective, band-pass, short pass, and long pass coatings for everyday glasses, and filters and optics in research labs.

In this project PVD is used to make the thin film coating needed for the dielectric optical filters in the Fabry-Pérot interferometer. The specific design and experiments involved are discussed in Chapter 3.

All types of depositions are carried out in a specially designed vacuum chamber. The chamber is equipped with turbo pumps, roughing pumps, pressure gauges, and gas inlets for sputtering gasses. Typically the vacuum chamber is pumped to a pressure in the 10×10^{-5} mbar range before the evaporation begins. Pumping vacuum inside the

chamber ensures that the partial pressure of the deposition material is dominant once a sufficient temperature and vapour pressure from the material is reached. The atoms and clusters which undergo a phase transition and escape into vacuum will have kinetic energy roughly equivalent to the temperature of the liquid or solid phase of the deposition material. Removing most other molecules inside the vacuum chamber ensures that the kinetic energy is conserved and not lost in collision events. This means that the speed and direction of the deposition atoms are conserved, and that the evaporant essentially moves in straight lines between the source and the substrate.

2.2.1 Thermal Evaporation

The simplest type of physical vapour deposition is thermal evaporation. Here a tantalum boat is typically used to carry the material to be deposited. The tantalum boat is heated until the material starts to vaporise. Once a vaporising temperature is reached material starts to flow from the tantalum boat and into the chamber with a direction and kinetic energy matching the temperature of the boat. The material clusters with sufficient energy to escape into the gas phase and a direction towards the substrate will reach the substrate surface and cool down. The material has now been deposited onto the substrate surface, and given enough time a fully cohesive thin film will be created.

Thermal evaporation is a technique that can be applied in almost any vacuum chamber with wire inlets for power supply. The most prominent drawback is that some materials need to be heated to several hundreds or thousands degrees celsius in order to reach their vaporising temperature. In these cases e-beam evaporation is used, which is described in the following section.

2.2.2 E-beam Evaporation

E-beam evaporation is a technique to deposit a material by melting the substrate and thereby create a gas phase inside the ultra high vacuum (UHV) chamber. Unlike thermal evaporation where the direct heat from a filament is used to heat the deposition material during e-beam evaporation, a filament is used to create a beam of electrons which is directed to collide with the deposition material. The heat dissipated in the deposition material during the slow-down and collisions of the electrons functions as the primary heating source of the deposition material. A sketch of the typical e-beam system is shown in Figure 2.3 (A).

Once again the transfer of material takes place as small material clusters escape from the e-beam crucible and move into the gas phase and reach the substrate surface.
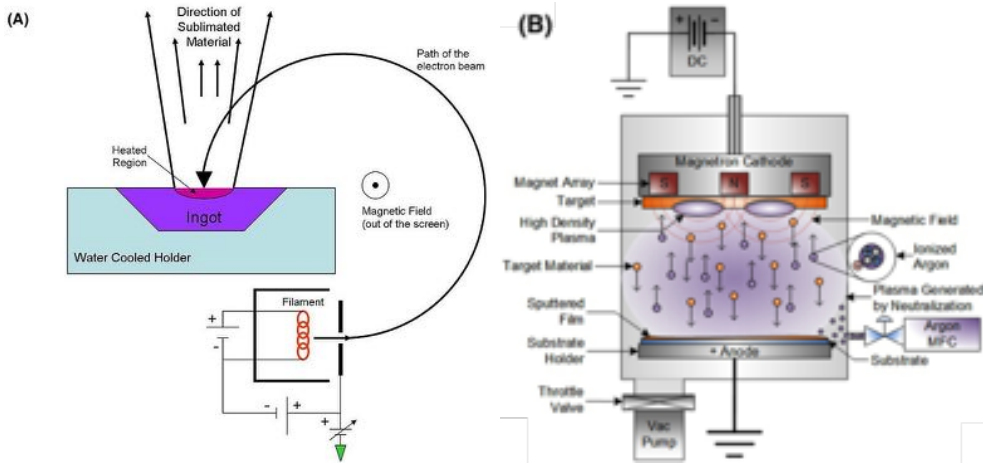
Figure 2.3: (A) Sketch of the working principle of a typical e-beam evaporation source. The electrons are generated by a heated filament and are subsequently directed into the crucible holding the solid evaporant. (B) Sketch of the working principle of a DC-sputtering setup. A plasma is generated by a strong electric field in combination with a permanent magnetic field. The ions generated are then bombarded into the sputtering target upon which atoms and clusters escape with a kinetic energy which is much higher than during standard vaporisation. The figures have been reprinted from [33, 34].

2.2.3 Sputtering

During sputtering the evaporated material is released from the solid phase by a bombardment of ions generated from a sputtering gas. The sputtering gas is introduced to the chamber through a gas inlet. The pressure during deposition is typically higher than during thermal or e-beam deposition. The sputtering gas is typically an inert gas such as argon or nitrogen in order to avoid that the gas chemically reacts with the sputtering target.

Sputtering is a deposition technique where the thin film is grown by substrate adsorption of clusters with a significant kinetic energy. The clusters are created by ion-bombardment of the target material. Typically a UHV chamber is filled with an inert ionisation gas, usually argon. See Figure 2.3.

2.2.4   RF-Sputtering

RF-sputtering was not used directly as a part of this PhD-project, but is mentioned here for the sake of covering the most important areas within PVD. RF-sputtering is typically used on non-conducting materials where charges might accumulate and prohibit the ion bombardment. The plasma is made using a radio frequency power supply which ensure that charges do not build up on the sputtering target.

2.2.5   Thin Film Thickness Monitoring

During PVD it is normally essential to monitor the thickness of the film deposited, since the thickness often is a crucial parameter for the property of the thin film. Two different monitoring systems are commonly used in PVD chambers where the use of a quartz crystal microbalance is the most common. The other monitoring system is an optical system, which is much more complex.

The quartz crystal microbalance (QCM) is a technique for monitoring the film thickness. The QCM consists of a piezo crystal upon which a metal surface with a high sticking coefficient is mounted. The piezo crystal is driven to its resonant frequency, which is monitored by a frequency controller. The QCM is mounted inside the vacuum chamber at a fixed position within the path of flight of the evaporants. The evaporant will adhere to the QCM during the deposition process and the weight added alters the resonant frequency of the QCM crystal. By monitoring the resonant frequency and taking geometric tooling factors into account, direct measure of the evaporated weight on the substrate can be found.

An optical monitoring system determines the thickness of the thin film by measuring the interference of light transmitted through the thin film and substrate undergoing deposition. A system like this can be more precise since it measures the substrate under deposition directly in real time.

2.3   Scanning Electron Microscopy (SEM)

Scanning Electron Microscopy (SEM) is an imaging technique where electrons are used as the primary source of information as opposed to more common optical microscopes where light serves the purpose.

A heated filament or a field emission cathode is used as the electron source. The electrons, being charged particles, are focused and accelerated using a series of electrostatic lenses into a spot size of a few nanometers. The electron beam is focused onto a sample substrate and the interaction of the high energy electrons and atoms within the

sample generates a wide variety of effects. The two processes that are most relevant for imaging are the production of secondary electrons and backscattered electrons. Secondary electrons are generated from the inelastic scattering process between the incident electrons and the core electrons within the sample. The secondary electrons are therefore lower energy compared to the impinging electrons. This in turn means that the surface sensitivity of measuring secondary electrons is increased due to lower inelastic mean free path of low energy electrons. The SEM image is created by focusing the electron beam onto a spot on the surface and raster scanning this beam across the substrate sample while collecting the generated secondary electrons. The amount of secondary electrons generated correlates with the Z-number of the substrate as well as the surface structure. These two factors are the primary contributors to the contrast in an SEM image.

The secondary electrons are primarily used for for SEM imaging, but the backscattered electrons can be collected as well. These backscattered electrons are the product of elastic scattering between the impinging electrons and the sample. Therefore, the kinetic energy of the electrons is maintained which means that this measuring technique is less surface sensitive. The main reason for measuring backscattered electrons anyway is a stronger correlation with the Z-number of the sample. This allows for valuable information on the sample composition.

2.4 Energy Dispersive X-ray Spectroscopy (EDX)

Energy dispersive X-ray spectroscopy (EDX) is a technique for measuring the constituents of a sample. The EDX analyser typically consist of a silicon drift detector capable of measuring the energy dispersion of incident ionising X-rays. This analyser is typically placed within an SEM chamber and utilises the X-rays produced as a consequence of the impinging high energy electrons. As mentioned, the high energy electrons that inelastically scatter with the sample, produces secondary electrons. Some of these electrons are the result of core electrons that are excited and released from their respective nucleus. This process leaves a hole behind in the inner core shell which can be occupied by an outer shell electron more loosely bound. The resulting excess of energy is released as emitted X-rays. The energy distribution of the generated X-rays is dependent on the element which allow for the constituents of the sample to be found through a database lookup.

2.5   Fourier Transform Infrared Spectroscopy (FTIR)

Fourier Transform Infrared Spectroscopy (FTIR) is a widely and common technique for performing spectroscopy in the infrared region. For this thesis it has been a vital technique for the characterisation and analysis of the optical components functioning in the LWIR. Therefore, FTIR has frequently been used for characterising the FPI mirrors used in the hyperspectral imaging system during these studies. An FTIR uses a Michelson interferometer[35] to measure the intensity of wavelengths in the range of 4-25 µm. The light of a broadband source is let through a Michelson interferometer which allow multiple selected wavelengths through the sample compartment. As the mirror distance within the Michelson interferometer is scanned the combination of wavelengths let through the interferometer will cover the entire range of the spectrometer. A fourier-transform based algorithm is then used to calculate and construct the full spectrum based on single wavelengths.
In its basic configuration the FTIR measures the transmission of any substrate by relating the intensity of an incoming light beam to the intensity of the same light beam following a passthrough of the substrate under investigation. This configuration is sketched in Figure 2.4 (A). The FTIR spectrometer is always calibrated to take the absorption in the atmosphere of the light beam into account, and thus the spectrum gathered represent the light transmitted through the sample. Thus, based on the law of energy conservation the following statement is true for our sample in the FTIR spectrometer.

$$|E_{total}| = 1 = T_s + A_s + R_s + S_s \tag{2.9}$$

Here, $|E_{total}|$ represent the total intensity of the light and T_s, A_s, R_s, and S_s represent the transmitted, absorbed, reflected and scattered fractions of the incident light respectively. These four contributions are the only pathways for the light, and normally, dealing with flat and non-corrugated optics the scattered fraction of the light is assumed to be negligible. Thus, according to Figure 2.4 (A) the measured spectrum in this configuration reveals information about the transmission of our sample, T_s, as mentioned. Normally, the transmission spectrum would be enough to reveal information about e.g. chemical species, since it would be assumed that the reflectivity is wavelength independent which leaves an implicit measurement of the absorption within the sample due to vibrational and rotational modes. During these studies a detailed analysis of the reflectivity of the measured samples was
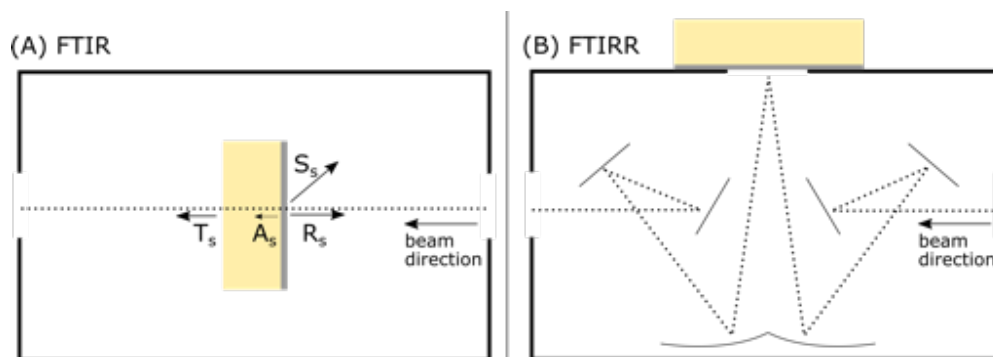
Figure 2.4: Graphical representation of two different configurations for measuring spectroscopy in the infrared region. (A) Conventional transmission FTIR where the light beam path of the infrared light travels directly through the sample compartment to the analyser. (B) reflection configured FTIRR where the light beam path is reflected through a set of mirrors onto the sample surface and thereafter reflected towards the analyser at the other end of the sample compartment.

needed, and therefore the transmission measurements were supported by reflection measurements as elaborated in the following section.

2.5.1 Reflectance Fourier Transform Infrared Spectroscopy (FTIRR)

In order to do reflection based infrared spectroscopy of the optical substrates used in this study an SRM-8000A reflection accessory was bought from Shimadzu. In the following sections, these measurements will be referred to as FTIRR measurements. The optical path of the light let into the FTIR sample compartment is directed perpendicular to the incident light through a set of mirrors as sketched in Figure 2.4 (B). Placing the sample on top of the accessory compartment the reflected light from the sample surface is once again directed towards the analyser to be measured. Taking the longer beam path into account during calibration a full spectrum of the reflectivity of the sample surface is now found. This reduces equation 2.9 to two unknowns which are the absorption and scattered fractions of light. Once again, assuming that the scattered fraction of the light is negligible, the absorption of the sample under investigation can be found based on an FTIR and the FTIRR measurement. The assumption that the scattered fraction of the light is negligible is not necessarily good and cannot be applied as a general rule for all surfaces. In our application the scattered and absorbed light are both pathways to the loss of light and therefore the

27

distinction between the two is of little importance.

3

A First Order Scanning Fabry-Pérot Interferometer

This chapter focuses on the physical vapour deposition experiments related to the production of mirrors capable of being incorporated in a low order thermal FPI. The results presented in this chapter stretches over several years of the project and describes the pursuit for low absorption dielectric partially reflecting mirrors.

3.1 The Development of a Partially Reflective Coating for the LWIR

A multilayer structure of high and low refractive indices is needed in order to produce a highly reflecting coating. For this project, high reflectivity is needed in the range 8-14 µm in order to utilise the entire sensitive region of the microbolometer sensor. Since the mirrors must be partially transmitting, it is essential to consider only transparent materials in the infrared region. These materials are typically insulators or semiconductors since the band gap in such materials ensures that the range of light with an energy lower than the band gap energy passes through the material. Typical semiconductors transparent in the infrared region include silicon and germanium which have band gap energies of 1.13 eV and 0.75 eV corresponding to light with wavelengths of 1.1 µm and 1.65 µm, respectively [36]. The relatively high refractive index of silicon and germanium of 3.5 and 4.0, makes both materials ideal candidates for the high index material in a coating design with interchanging high and low index materials. Other possibilities for the high index material include tellurium with a refractive index of 4.8 at 10 µm [37, 38, 39] and lead telluride with a refractive index of 5.6 at 10 µm[40, 41, 42, 43, 44]. Tellurium and lead telluride both have optical transmission up to 14 µm and low absorption [45]. For this project, germanium was chosen as the high index material since the deposition parameters is widely accessible. Additionally, germanium has a relatively flat transmission at wavelengths up to 14 µm in contrast to pure silicon.

Fluoride compounds are typically used for the low index material in an infrared optical coating. Fluorides are chemically extremely stable, which means that they do not decompose over time [46]. Provided that the stoichiometry of the fluoride is kept, the chemical stability reduces absorption, which is essential for the application in a Fabry-Pérot or experiments including high energy lasers where low absorption is critical. One of the most common materials to use for the low index layer in a multilayer coating is ThF_4. Though ThF_4 is the most commonly used material within the industry, it was not allowed to conduct experiments in the facilities at hand with this material because it is radioactive. Deposited layers of ThF_4 are dense, stable and can have low absorption, however the radioactive nature of thorium also makes it a non-ideal material for consumer products. Although the radioactivity can be controlled by depositing a thick top layer, which inhibits the alpha particles from penetrating [47], a development started in the 1980s towards finding a non-radioactive replacement[48, 49, 50]. These studies resulted in the use of a wider variety of fluorides such as MgF_2, CeF_3 and fluoride mixtures. This will be elaborated later in
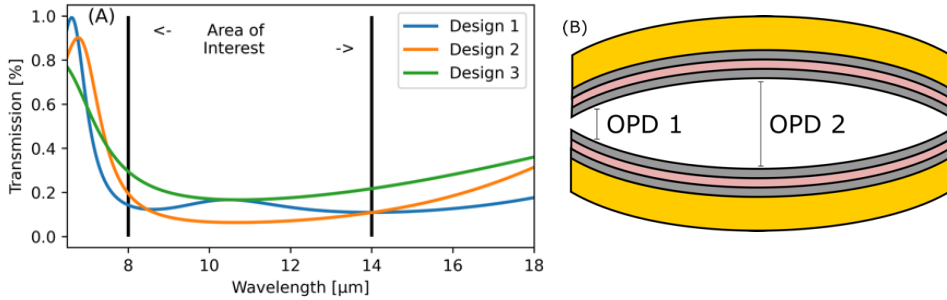
Figure 3.1: (A) Theoretical simulations of mirror coatings based on the three coating designs shown in Table 3.1. (B) Sketch of the result of too much tensile stress in the coated thin film. The bending substrates change the optical path difference between two mirrors, which is crucial for the FPI application.

this chapter, but first the structural design and thicknesses of the coating layers must be determined.

3.1.1 Thin Film Coating Design

An earlier attempt at designing a first order FPI have been made using a mirror recipe of alternating layers of sinc sulfide and germanium [51]. This mirror recipe consist of a four layer structure of quarter wave optical thicknesses (QWOT). The optical thickness (OT) is given by

$$OT = n(\lambda) \cdot T_m \tag{3.1}$$

with $n(\lambda)$ being the refractive index assumed to be constant throughout the thickness of the film, and T_m being the physical thickness of the film. Ideally the transmission curve for a single mirror in our application should be flat in the range from 8-14 µm. This coating can be achieved by using a number of QWOT layers, where the amount of layers increases to achieve a very high reflecting coating [52]. In our application it is preferable to keep the number of layers at a minimum. The first reason is that we do not aim for a very high reflecting coating, cf. the theory of the FPI introduced in section 2.1 and more specifically equation 2.3. The equation shows that the reflectivity of the FPI mirrors increases the finesse of the transmission profile which lowers the intensity that is let through the FPI. While the increased finesse essentially improves the spectral resolution it also significantly decreases the signal measured due to the lower FWHM. The second reason is that it is important to minimise the number of

thin film layers since the thin films typically have an intrinsic tensile stress which is strong enough to bend the substrate at a microscopical level. This phenomenon is sketched in Figure 3.1 (B) where two identical FPI mirrors with a three-layer-coating have been stacked. Due to the physical bending of the substrates, the optical path difference (OPD) of the light multiple reflected in the center of the FPI assembly differs from the light in the edge, and thus

$$OPD_1 \neq OPD_2 \tag{3.2}$$

The non-equal OPD has a broadening effect on the light transmitted by the FPI due to the distribution of mirror separations caused by the substrate bending. The shape of the band transmitted is therefore a function of the curve of the individual mirror substrates. It is therefore vital to keep the ZnSe substrates flat, and the best way of doing so is keeping the number of layers in the optical coating at a minimum.

At the beginning of this project two substrates were produced based on a three-layer-coating consisting of germanium and barium fluoride. The dielectric layer stack was made from a design of an initial half wavelength layer and two quarter wavelength layers. The physical thicknesses of the mirror design are listed in Table 3.1 as Design 1.

| | Design 1 | | Design 2 | | | Design 3 | |
Material	OT	Physical thickness	OT	physical thickness	Material	OT	physical thickness
Ge	1/4 wave	0.656 µm	1/4 wave	0.656 µm	-	-	-
BaF$_2$	1/4 wave	1.836 µm	1/4 wave	1.836 µm	Ge	1/4 wave	0.656
Ge	1/2 wave	1.315 µm	1/4 wave	0.656 µm	BaF$_2$	1/4 wave	1.836
ZnSe	Inf	5 mm	Inf	5 mm		Inf	5 mm

Table 3.1: Table summarising the three different FPI mirror design recipes considered for the thermal hyperspectral imaging project. BaF$_2$ has in this case been used as the second layer consisting of a low refractive index material, and germanium has been used for the high refractive index material as specific examples. It is important to note, however, that the optical thickness is the important physical quantity.

It was chosen to design the optical coating based on a wavelength of 10.5 µm and at this wavelength the initial 1/2 wave germanium layer has no effect. A half wavelength layer is sometimes abbreviated an absentee layer, and although it has no effect at the design wavelength, it broadens the reflective region around the design wavelength [36]. Therefore, while a thick layer of germanium is added to the substrate, the average reflectivity of the coating remains relatively high at a theoretical average value of 13.6 %, and the total number of layers are kept relatively low. The optical properties of a layer stack can be calculated using the transfer matrix method (TMM).

For this project the TMM calculations have been performed in a Python environment using the readily available TMM library made by Steven Byrnes [53]. The reader is referred to the documentation for a detailed description of the theory behind the TMM. The theoretical transmission curve of a coating equal to Design 1 in Table 3.1 is shown in Figure 3.1 (A) as the blue graph.

An alternative design was proposed which is named Design 2 in Table 3.1. The theoretical transmission curve belonging to this design is shown in Figure 3.1 (A) as an orange line. The figure shows that the transmission of the design is generally lower than for Design 1 which also means that the reflectivity is higher. As mentioned earlier, increased reflectivity also means increased finesse of the FPI. Therefore, this design would be ideal for detecting the fingerprint spectral features of materials in the LWIR due to the increased spectral resolution. The average transmission of a single mirror based on Design 2 within the sensor sensitivity range is 8.5 %.

As a last alternative, a mirror coating consisting of only two layers could be considered. This design is named Design 3 in Table 3.1, and the simulation based on the TMM calculation is shown in Figure 3.1 (A) as a solid green line. The average transmission within the sensor sensitivity range is 19.1 %, and therefore this design would have the broadest average transmission peak. It is important to notice the option for this two-layer, design since having a recipe with only two layers could mean that completely flat mirrors are obtained. The flatness of the mirrors would compensate for the broadened transmission peak, and therefore the mirror system constitutes a standard cost-benefit system.

3.1.2 FTIR Measurements of Homemade Mirrors

A prestudy was carried out prior to this project, where two FPI mirrors were produced based on Design 1 in Table 3.1. These mirrors were characterised using a combination of FTIR and FTIRR measurements as presented in chapter 2. Figure 3.2 shows the FTIR transmission and reflection profiles. Figure 3.2 (A) shows both measurements for the first mirror with an acceptable transmission profile which is mostly flat, between 8 and 14 μm, and has a mean value of 23.8 %. The transmission of the second mirror, shown in Figure 3.2, matched the first within a few percent with a mean value of 24.5 %. Even though these values are notably higher than the theoretical transmission calculated using TMM, both mirrors were accepted as first versions. The most critical drawback of these homegrown mirrors are the absorption, which is found from the law of energy conservation as stated in equation 2.9.

Figures 3.2 (A) and (B) both show that from 6 to 10 μm the percentage of total light
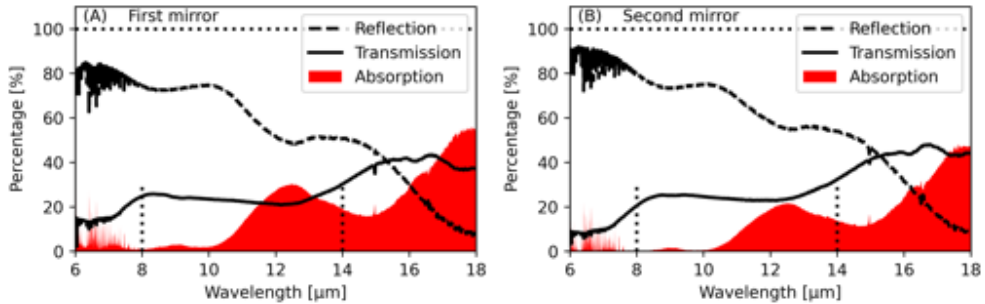
Figure 3.2: (A) and (B) Transmission and reflection measurements of the first home-grown (A) FPI mirror and second homegrown (B) FPI mirror, respectively. The absorption has been calculated as $Absorption = 100\,\% - (T\% + R\%)$. The two vertical lines in each figure represent the sensor sensitivity range.

is close to 100 %. In both figures the percentage of total light means the sum of transmitted and reflected light. Above 10 µm a huge dip is seen in the total percentage of light which is ascribed purely to absorption, since it is assumed that the scattered light is negligible. The average percentage of reflected light between 8 and 14 µm is 65.7 % and 68.7 %, which gives in mean absorption values of 10.5 % and 6.8 % and maximum absorption values of 30.4 % and 21.96 % for the first and second mirror, respectively.

While the mirrors seem to have good transmission profiles for a hyperspectral thermal imaging application, the mirrors suffer from a large amount of absorption, which impacts the data acquisition negatively due to low transmission intensity through the FPI. This was measured as well, by placing the two mirrors parallel to each other at close distance. This configuration constitutes an FPI and the transmission through both mirrors was measured by FTIR. The results from these measurements are graphically plotted in Figure A.4 (A). The effective bandpass of the FPI based on homegrown mirrors was measured to a maximum of 55 % with a FWHM transmission peak of 440 nm at wavelengths below 11 µm. At 11 µm the transmission was below 40 %, which is much below the success criteria. Still, the mirrors were used in the first version of the hyperspectral thermal camera (HSTC) to demonstrate the principle of the HSTC, and the results are presented in Chapter 6.

A series of experiments were conducted in order to improve the mirrors by lowering the absorption, and the results and considerations are presented in the following sections.

3.2 Experimental Methods

After having concluded that the first generation homegrown mirrors were not ideal for our hyperspectral thermal imaging application, an attempt was made to improve the coating. Consequently, the primary purpose of the mirror experiments was to reduce absorption, reach a high reproducibility, and lastly to mass produce mirrors if the first two aims proved successful. The depositions were carried out using a Cryofox 600 manufactured by the Danish company Polyteknik A/S. The deposition chamber is capable of performing RF and DC sputtering and contains a carousel fitting four crucible liners for e-beam deposition. All of these deposition techniques are described in Chapter 2. The sputtering target used during the depositions was a 2" and 3 mm thick germanium target of 99.999 % purity. All depositions were carried out using argon as the main sputtering gas (99.998 % purity). The sputtering distance was 18.5 cm, and therefore is a significant geometric deposition factor which needs to be accounted for, to ensure a homogeneous deposition with the right thickness.[54]. The chamber is equipped with a Huber Unichiller water cooling system capable of keeping the sample holder at temperatures within -20-$90\,°C$. Additionally, the system rotates the sample holder during deposition around the central axis of the substrate.

The scanning electron microscope used for analysis was a Hitachi S-4800 and the SEM chamber is fitted with a Bruker Quantax 200 EDX system. Both of these techniques are described in Chapter 2 as well.

3.2.1 Experimental Depositions of BaF$_2$

A test deposition was carried out in order to replicate the FPI mirror used in the early version of the HSTC. Thus, a Ø2" and 5 mm thick ZnSe window was used as primary mirror substrate and a smaller Ø20 mm and 1 mm thick window was placed in the vicinity of the primary substrate for post-deposition tests. The smaller substrates were used in order to examine the coating through a cross sectional analysis in the SEM. The measurements were performed by cracking the substrates through the middle and imaging the coating from the side. Note here that the geometric dependency of this specific deposition chamber has been studied previously by Hausladen and Kjelstrup-Hansen[54], and the geometric dependency of any system in general have been described by Thornton[55]. When taking the geometric dependency into account it is clear that the different position of the test ZnSe substrate change the film thickness relative to the mirror substrate, and, therefore, a cross-sectional image analysis of these do not perfectly reflect the film thicknesses of the mirror substrate itself. The
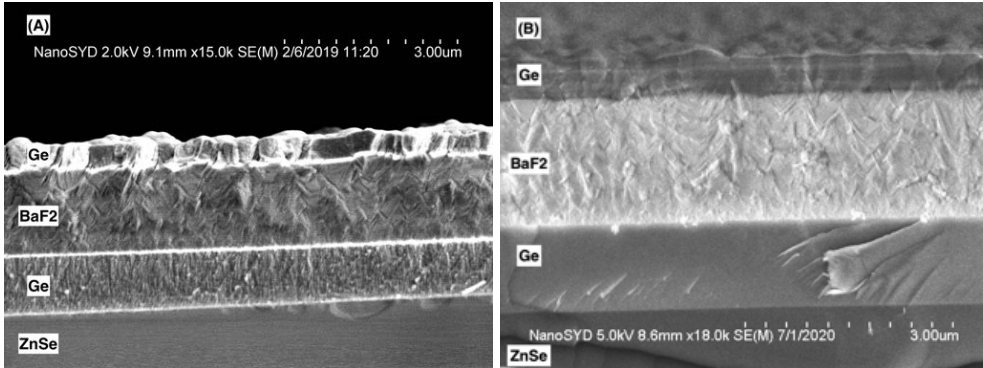
Figure 3.3: (A) SEM image of the test deposition of a full FPI mirror recipe. The columnar growth in the BaF$_2$ layer have a negative impact on the flatness and homogeneity of the third, germanium, layer. (B) SEM image of a ZnSe Ge/BaF$_2$/Ge mirror coating using a argon inlet flow of 15 SCCM during germanium sputtering.

test substrate can, however, be used to examine the overall structure of the film and give an overview of the film thickness which was the main objective of the substrates testing during these experiments.

An attempt was made to produce a full mirror recipe which matched Design 1 in Table 3.1. The germanium layers were sputtered with an argon gas flow of 45 Standard cubic centimetres per minute (SCCM) resulting in pressures in the 4.7×10^{-5} mbar range, and the BaF$_2$ layer was deposited at a pressure in the 2×10^{-5} mbar range. The base pressure of the system was in the 3×10^{-7} mbar range. The deposition was successful, and the coating was examined by a cross sectional analysis in the SEM. An image of the coating is shown in Figure 3.3 (A). After investigating this image, a few hypotheses was made relating to the growth of the BaF$_2$ film. The triangular pattern visible in the BaF$_2$ layer indicates that the film grows in a crystalline and column-like structure. A generalised model for the growth and structure of thin films has been described in the literature, known as the Thornton zone model[56]. According to this model, the crystalline and columnar growth of the BaF$_2$ film is caused by the film growing in the first growth zone where the substrate temperature is much lower than the melting temperature. The columnar growth is described as a result of the low diffusion and mobility of the impinging atoms. This theory is backed by the high melting point of BaF$_2$ of 1368 °C and that BaF$_2$ sublimates upon deposition. A few growth models have been formulated and reported in the literature many of which cite the pioneer work within thin film zone models conducted by the

Russians Movchan and Demichishin in 1962. Since their work is written in Russian (and therefore not understood by the author), the work by Thornton will be cited in the following sections. Films growing in the first growth zone have a rough surface structure, and since the growth in the first BaF$_2$ layer and second overall is comparably more column-like than the germanium seen in the first layer, the third germanium layer also has high surface roughness, which is also clearly seen in Figure 3.3 (A).

Recipe [substrate | coating]	Ar flow [SCCM]	Sample holder T	2nd layer conclusion	Figure
ZnSe | $\frac{1}{2}\lambda$ Ge/ $\frac{1}{4}\lambda$BaF$_2$/ $\frac{1}{4}\lambda$Ge	45	$-20\,°C$	columnar/crystalline	-
ZnSe | $\frac{1}{2}\lambda$ Ge/ $\frac{1}{4}\lambda$BaF$_2$/ $\frac{1}{4}\lambda$Ge	45	$20\,°C$	columnar/crystalline	3.3 (A)
ZnSe | $\frac{1}{2}\lambda$ Ge/ $\frac{1}{4}\lambda$BaF$_2$/ $\frac{1}{4}\lambda$Ge	45	$90\,°C$	columnar/crystalline	-
ZnSe | $\frac{1}{2}\lambda$ Ge/ $\frac{1}{4}\lambda$BaF$_2$/ $\frac{1}{4}\lambda$Ge	15	$20\,°C$	columnar/crystalline	3.3 (B) and 3.4 (A)

Table 3.2: Overview of the deposition parameters tested using BaF$_2$ as the low refractive index layer.

Two additional test depositions were made using the same mirror recipe but covering the temperature span of the water cooling system which is connected to the sample holder. This means that a ZnSe/Ge/BaF$_2$/Ge coating was deposited on two mirror substrates held at $-20\,°C$ and $90\,°C$, respectively. While the $-20\,°C$ substrate temperature was not expected to provide a positive result on the columnar growth, the $90\,°C$ did not solve the problem either. Several sources state that the film growth is improved with rising temperatures, and therefore, a too low substrate temperature is the most likely reason why the second layer did not show any improvement [57, 58, 36]. Because it was not possible to increase the substrate temperature further the attempts on improving the BaF$_2$ layer was terminated, and focus was shifted to improving the third layer of germanium. This was done by growing the germanium film with a reduced argon gas flow during the film growth process. By reducing the argon gas flow into the chamber during deposition, the mean free path is increased of both the germanium clusters released from the substrate and the bombarding Ar ions. The overall effect is an increased kinetic energy of the germanium clusters released from the substrate. A deposition was carried out with the argon gas flow rate reduced from 45 SCCM to 15 SCCM. BaF$_2$ was used again as the low refractive index layer and the resulting coating is shown in Figure 3.3 (B). The SEM image shows a less corrugated transition between the second BaF$_2$ layer and the third Ge layer. It is noticeable that the third germanium layer is not homogeneous and contain horizontal lines which may indicate that the germanium has been mixed/fused into the top layer of the BaF$_2$ coating due to the increased energy during deposition. It should further be noted
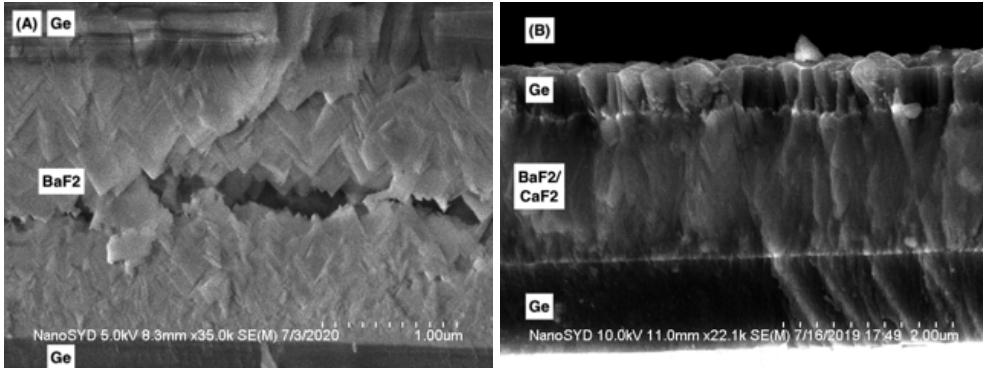
Figure 3.4: (A) SEM image of a ZnSe Ge/BaF$_2$/Ge mirror coating using a lowered argon inlet flow of 15 SCCM during germanium sputtering. The image shows a faulty BaF$_2$ and thereby underline the importance of finding a suitable candidate to substitute BaF$_2$. (B) SEM image of a test deposition of a full mirror recipe where the low refractive index layer was a 9:1 mix of BaF$_2$ and CaF$_2$.

that the columnar structure of the BaF$_2$ layer is still observed. The columnar structure was continually a problem and an attempt to reproduce this coating showed failing BaF$_2$ layers as shown in Figure 3.4 (A).

FTIR measurements were made of the film shown in Figure 3.3 (B) in both transmission and reflection configurations. The results of these measurements are shown in Figure 3.5 (A). Note that prominent absorption appears at transmitted wavelengths above 10 μm. In order to locate the source of the absorption peak, two different reference depositions were made along with a measurement of a clean mirror substrate. The measurement of the clean ZnSe substrate is shown in Figure 3.5 (B), where it is seen that the absorption is low at wavelengths below 15 μm. The fall in transmission and increase in absorption at wavelengths above 15 μm can be ascribed to the inherent material properties of the ZnSe substrate. A BaF$_2$ layer was deposited onto a fresh substrate, and the transmission and reflection spectra were measured. The spectra are plotted in Figure 3.5 (C) along with the sum of the two measurements. The graph shows a very limited absorption in the BaF$_2$ layer compared to the graph seen in (A) which illustrates the full mirror stack. A single germanium layer was deposited onto a ZnSe substrate, and the transmission and reflection spectra were measured, as seen in Figure 3.5 (D). Here, the absorption dip in the germanium layer is clearly seen which could be due to oxygen contamination and the formation of GeOx [59]. Oxygen contamination could arise from either the deposition chamber

or the introduction of the sample to the ambient atmosphere [60, 61]. This problem could possibly be circumvented by adding a protective coating of BaF_2 on top of the mirror substrate, but was not attempted at the time of deposition. Such a procedure is a possible pathway to preventing oxidization of aluminum mirror coatings using MgF_2 as the protecting material [62, 63]. Additionally, previous studies have shown that dielectric reflective coatings consisting of alternating ThF_4/ZnS or $ThF_4/ZnSe$ both show an increased hardness and resistance to water vapour when protected by a CeF_3 overcoating [57].

Recipe [substrate | coating]	Ar flow [SCCM]	Plasma cleaning	Sample holder T	Absorption
ZnSe | $\frac{1}{2}\lambda$ Ge/ $\frac{1}{4}\lambda BaF_2$/ $\frac{1}{4}\lambda$Ge	15	yes	20 °C	yes
ZnSe | $\frac{1}{2}\lambda$ Ge/ $\frac{1}{4}\lambda BaF_2$/ $\frac{1}{4}\lambda$Ge	45	yes	20 °C	yes
ZnSe | $\frac{1}{2}\lambda$ Ge	15	yes	20 °C	yes
ZnSe | $\frac{1}{2}\lambda$ Ge	45	yes	20 °C	yes
ZnSe | $\frac{1}{2}\lambda$ Ge	45	no	20 °C	yes
ZnSe | $\frac{1}{2}\lambda$ Ge	45	yes	90 °C	yes
ZnSe | $\frac{1}{2}\lambda$ Ge	45	yes	90 °C + annealing to 300 °C	yes

Table 3.3: Overview of the deposition parameters checked for germanium absorption.

3.2.2 Experimental Depositions of CeF_3

A series of experiments were made in order to improve the low refractive index layer of the three-layer mirror coating. Having tested the extremes of the deposition parameters available for the Cryofox 600, the following tests revolved around the deposition of alternative materials in order to improve the second layer. As mentioned in the introduction to this Chapter, a wide variety of materials may be used, where some may be better than others. Su et al.[64] showed that CeF_3 films can be grown with decent structural parameters to an optical thickness of 3.6 µm. In this study, the CeF_3 films were deposited at substrate temperatures in the range 100-250 °C, which again is outside the range of the PVD chamber used in these experiments. Therefore, two depositions were made with substrate temperatures held at 90 °C and deposition rates of 5 and 100 Å s^{-1}. The 100 Å s^{-1} deposition rate was used in order to check whether a faster rate could compensate for the lower substrate temperature. None of these depositions resulted in stable films, and the CeF_3 seemed to crystallise in microscopic crystals which could be scraped off the surface using a tissue. An image of the film using optical microscopy is included in the Appendix in Figure A.3. This figure shows the interference and diffraction of light from macroscopic crystals on the surface. Earlier studies have shown that CeF_3 grows in a crystalline structure
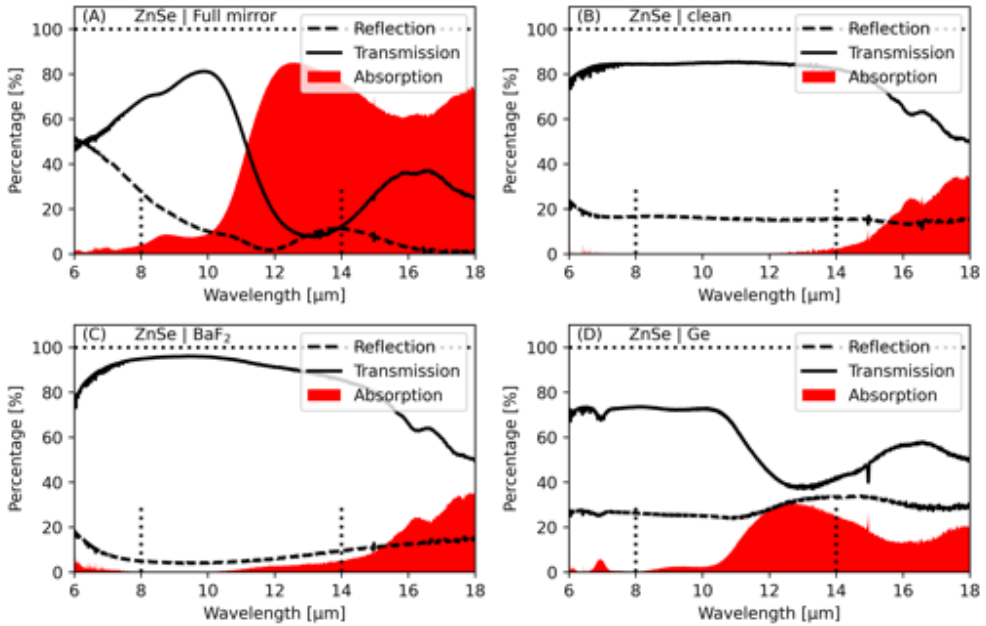
Figure 3.5: (A) Transmission and reflection FTIR measurements of the ZnSe | Ge/BaF$_2$/Ge stack shown in Figure 3.4 (A). (B) Transmission and reflection FTIR measurements of a clean ZnSe substrate with a pre-coated broad band antireflective coating. (C) Transmission and reflection FTIR measurements of a ZnSe | BaF$_2$ coating. The measurements show that the barium fluoride is not responsible for the high absorption in the mirror coating. (D) Transmission and reflection measurements of a ZnSe | Ge coating. The measurements show that the barium fluoride is not responsible for the high absorption in the mirror coating. The absorption has been calculated as *Absorption* $= 100\,\% - (T\% + R\%)$. The two vertical lines in each figure represent the sensor sensitivity range.

with a packing density of 0.8 [58]. Other studies, however, note that the intrinsic tensile stress in a 100 nm film of CeF_3 increases by 53 % as the substrate temperature is lowered from 230 °C to 20 °C [65, 48].

Recipe [substrate ǀ coating]	Sample holder T [°C]	Deposition rate	2nd layer conclusion
ZnSe ǀ 50 nm Ge/ $\frac{1}{2}\lambda$ CeF$_3$	90 °C	5 Å/s	Macroscopic crystalline
ZnSe ǀ 50 nm Ge/ $\frac{1}{2}\lambda$ CeF$_3$	90 °C	100 Å/s	Macroscopic crystalline

Table 3.4: Summary of the deposition including CeF_3 as the low refractive index layer.

3.2.3 Experimental Depositions of a CaF$_2$/BaF$_2$ Mixture

After concluding that pure cerium fluoride resulted in worse films than BaF_2, a deposition series was performed with a mixture of BaF_2 and CaF_2 in a weight ratio of 9:1. Each matter, consisting of 3-6 mm pieces, was weighted in the correct ratio and was subsequently added to the e-beam crucible for mixing. Since both the materials sublimate upon deposition, the material mixing is non-ideal and could therefore be a major source of error. Previous studies, however, indicate that mixing these materials provide fluoride films of higher density [66]. An attempt was made to do a full mirror recipe, and an SEM image of the resulting coating is shown in Figure 3.4 (B). The substrate temperature was kept at 90 °C, and the germanium layers were deposited at a pressure of 4.7×10^{-3} mbar, and the BaF_2/CaF_2 layer was deposited at a pressure of 9.5×10^{-5} mbar. The columnar and crystalline growth can be seen in the low refractive index layer, which strongly affects the third germanium layer.

Recipe [substrate ǀ coating]	Sample holder T [°C]	Deposition rate	2nd layer conclusion
ZnSe ǀ $\frac{1}{2}\lambda$ Ge/ $\frac{1}{4}\lambda$CaF$_2$/BaF$_2$/ $\frac{1}{4}\lambda$Ge	90 °C	5 Å/s	Macroscopic crystalline

Table 3.5: Summary of the depositions including CaF_2/BaF_2 as the low refractive index layer.

3.2.4 Experimental Depositions of IRX, a CeF$_3$/BaF$_2$ Mixture

A final material was used in order to grow a durable film which was the commercial material CIROM-IRX (IRX). IRX was acquired from the American company Materion, and according to the material safety data sheet[67] it consist of a mixture of CeF_3 and BaF_2 at a weight percentage ratio of about 9:1. The exact ratio is a trade secret. IRX is sold as a non-radioactive replacement of ThF_4, which is widely used in high intensity CO_2 laser coatings due to low absorption [50]. The effect of mixing CeF_3 and BaF_2 have been studied and reported by Pellicori[48], who conclude that it

is possible to grow quarter wave films of a design wavelength of $10\,\mu m$. Pellicori and Colton[68] claim that IRX can be grown to thicknesses of 1800 nm which is higher than the thickness needed for our recipe. Materion recommends a substrate temperature between 225-250 °C and state that the substrate temperature should not be less than 150 °C [69]. The initial deposition of IRX was carried out with high hopes Even though these temperatures could not be reached in the facilities at hand. The recipe used was a thin 50 nm germanium layer followed by $\frac{1}{4}\lambda$IRX. The substrate temperature was kept at 90 °C and the main pressure during germanium deposition was 4.78×10^{-3} mbar. The main pressure during IRX deposition was 7.6×10^{-5} mbar. An image was grabbed using the optical microscope, since most of the coating peeled off the surface. Part of the coating remained intact at the edge of the substrate, which may be due to shadowing effects from the sample holder which give rise to thinner coating layers. An image of the edge of the coating is shown in Figure 3.6 (A), where it is seen that the coating peels off to a lesser extent. It is furthermore noticed that the germanium is peeled off the ZnSe substrate by the IRX layer which can be concluded since germanium is opaque to visible light. In Figure 3.6 (A) the germanium only remains in the center of the IRX grain boundaries. The deposition rate was increased to $20\,\text{Å s}^{-1}$ since increasing the deposition rate has improved adhesion in previous studies [70]. This coating was unsuccessful and it was therefore decided to increase the thickness of the germanium layer and decrease the thickness of the IRX layer. Two depositions followed where 300 nm Ge / 875 nm IRX was deposited as summarised in Table 3.6. Both structures were stable coming out of the PVD chamber, however, during imaging in the SEM the coating curled off the substrate as is shown in Figure A.1 (A) in the Appendix. The curling of the coating may be reasoned by a charge buildup from the electron beam in the SEM. An out of focus image was acquired of the structure as shown in Figure A.1 (B), and this showed a very flat second layer of IRX, which motivated further experiments. An IRX deposition of a full mirror recipe was deposited, and the substrate temperature was maintained at 90 °C. The main pressure during IRX deposition was 9.57×10^{-5} mbar. The main pressure during germanium deposition was 4.68×10^{-3} mbar. The resulting coating peeled off the ZnSe substrate and SEM images could only be acquired of fractions of the coating. One of these images is shown in Figure 3.6 where it is also noticed that the coating bend upwards which indicate tensile stress in the structure. During analysis it was further noticed that in some region the initial germanium layer stuck to the ZnSe substrate, while the IRX layer with the quarter wave germanium layer on top was peeling off.
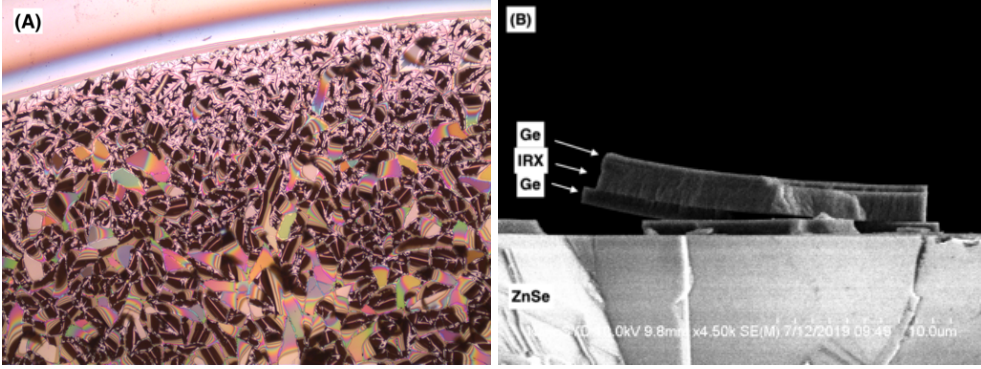
Figure 3.6: (A) Optical microscopy image using a 5x objective lens. Tensile stress is seen in the IRX layer. (B) SEM image of a piece of a Ge/IRX/Ge coating. This image shows that the IRX coating bends upwards, which indicates tensile stress in the coating. It is, furthermore, observed that the initial germanium layer is released from the surface, which indicates that the ZnSe/Ge adhesion is the main weakness of the coating.

Recipe [substrate | coating]	Ar flow [SCCM]	Sample holder T	IRX deposition rate
ZnSe | 50 nm Ge/ $\frac{1}{4}\lambda$IRX	45	90 °C	5 Å/s
ZnSe | 50 nm Ge/ $\frac{1}{4}\lambda$IRX	45	90 °C	20 Å/S
ZnSe | 300 nm Ge/ 875 nm IRX	45	90 °C	5 Å/s
ZnSe | 300 nm Ge/ 875 nm IRX	45	90 °C	20 Å/S
ZnSe | $\frac{1}{2}\lambda$ Ge/ $\frac{1}{4}\lambda$IRX/ $\frac{1}{4}\lambda$Ge	45	90 °C	20 Å/S

Table 3.6: Overview of the deposition parameters used during IRX depositions.

Following the initial depositions of IRX, it was realised that the adhesion of germanium to the ZnSe substrate significantly affect the quality of the coatings. It was further concluded that the adhesion between the germanium layers and the IRX could be improved, and therefore during the following depositions a thin binder layer of Y_2O_3 was added to the recipe. Previous studies have conducted adhesions tests of ZnS films on germanium substrates and conclude that the adhesion is increased dramatically using a substrate temperature of 150 °C following a post deposition annealing to 225-250 °C [70]. Therefore, four ZnSe substrates were coated with a 400 nm germanium layer of which two were annealed post deposition in an oven to 170 °C. These four samples were split in two sets containing one germanium sample with and without a post deposition annealing treatment. Hereafter, a 500 nm IRX layer and a 1000 nm IRX layer was deposited to the first and second sample set, respectively. A

summary of the depositions is shown in Table 3.7. Only sample #4 in Table 3.7 survived being introduced to the SEM chamber. This sample received a post deposition annealing to 170 °C and it was therefore concluded that the method worked to some extent. The IRX layer deposited onto sample #4 peeled of during imaging, and it was therefore concluded to be an effective improvement of the substrate adhesion.

Sample #	Ge [nm]	Ar SCCM	post anneal	Y$_2$O$_3$ [nm]	IRX [nm]	Film after deposition	SEM
1	400 nm	45	no	2	1000	cracked Ge - IRX liftoff	-
2	400 nm	45	170	2	1000	cracked Ge - IRX liftoff	-
3	400 nm	45	no	2	500	intact	cracked
4	400 nm	45	170	2	500	intact	cracked

Table 3.7: Experimental details and recipes used to investigate germanium films deposited onto ZnSe substrates using DC sputtering. IRX was subsequently deposited onto the initial germanium layer in order to test the IRX adhesion.

As mentioned earlier in section 3.2.1, the density and crystallinity of the germanium layer increases as the argon pressure during deposition is lowered. It was also mentioned that the energy of the sputtered clusters was increased with a lower argon pressure. Therefore, it was attempted to grow the initial germanium layer using an argon inlet flow of 10 SCCM in order to improve the adhesion to the substrate. Four samples were introduced to the PVD chamber and a complete $\frac{1}{2}\lambda$ germanium layer was deposited on all substrates. Following this deposition one sample was annealed by placing the sample on a hotplate heated to 250 °C. The remaining three samples were annealed to 170 °C in an oven.

The importance of the thin binder layer of Y$_2$O$_3$ was investigated and therefore 1000 nm of IRX was deposited onto three samples where only one of the samples had an adhesion binder layer included in the recipe. The last sample was saved for a deposition of a full $\frac{1}{2}\lambda$ IRX layer. Table 3.8 summarises these depositions and as can be seen, the effect of the Y$_2$O$_3$ adhesion layer is substantial.

Sample #	Ge [nm]	Ar SCCM	post anneal	Y$_2$O$_3$ [nm]	IRX [nm]	Film after deposition	SEM
1	1350 nm	10	250C	0	1000	intact Ge - rough IRX	-
2	1350 nm	10	170	0	1000	intact Ge - rough IRX	-
3	1350 nm	10	170	2	1000	intact	Large flakes
4	1350 nm	10	170	2	1750	intact	Intact Ge - cracked

Table 3.8: Experimental details and recipes used to investigate germanium films deposited onto ZnSe substrates using DC sputtering. IRX was subsequently deposited onto the initial germanium layer in order to test the IRX adhesion.

Optical microscopy images of the initial three samples are shown in Figure 3.7. Image
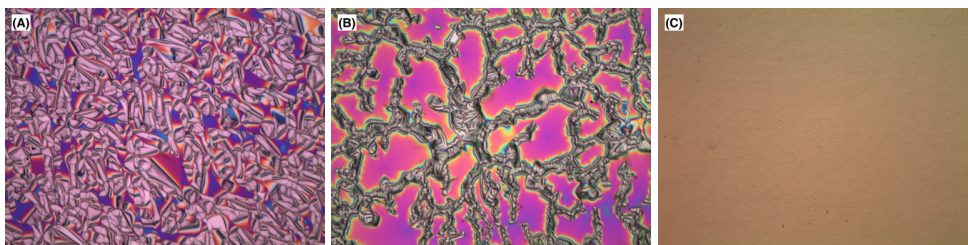
Figure 3.7: (A) Optical microscopy image of the coating following IRX deposition on sample 1 in Table 3.8. (B) Optical microscopy image of the coating following IRX deposition on sample 2 in Table 3.8. (C) Optical microscopy image of the coating following IRX deposition on sample 4 in Table 3.8.

(A) in Figure 3.7 shows an optical microscopy image following the IRX test deposition number 1 in Table 3.8. This image shows a semi-cracked film, however, it is not possible to locate the main source of error based on this image. Figure 3.7 (B) shows an optical microscopy image of deposition number 2 in Table 3.8 and comparing this to Figure 3.7 it was concluded that the annealing to 170 °C provided the best results. IRX was deposited onto the remaining two samples and this time an adhesion layer was included in the recipe. An IRX layer of thickness 1000 nm and 1750 nm was deposited onto sample number 3 and sample number 4 in Table 3.8, respectively. Both depositions were successful and an optical microscopy image of sample number 4 is shown in Figure 3.7 (C). This image shows a coating which stuck to the surface, however, a pattern of small cracks is seen covering the sample.

Sample number 3 in Table 3.8 was broken in two and a cross sectional image was acquired in the SEM. Two images have been included here and are shown in Figures 3.8 (A) and (B). Both images show that the thin film coating releases from the surface as the sample is introduced to the SEM. However, the quality of the IRX film is remarkably better than the previously grown BaF$_2$ films shown in section 3.2.1. Figure 3.8 shows a non-corrugated second layer of IRX which looks homogeneous and less crystalline than BaF$_2$.

The remaining sample number 4 in Table 3.7 was introduced to the PVD system once again, and a third layer consisting of germanium was deposited onto the IRX layer, even though cracks appeared on the surface. SEM images following this deposition is included in the Appendix Figure A.2. Since the cracks dominated the surface, the resulting three-layer mirror coating was not uniform, and FTIR measurements was not performed.
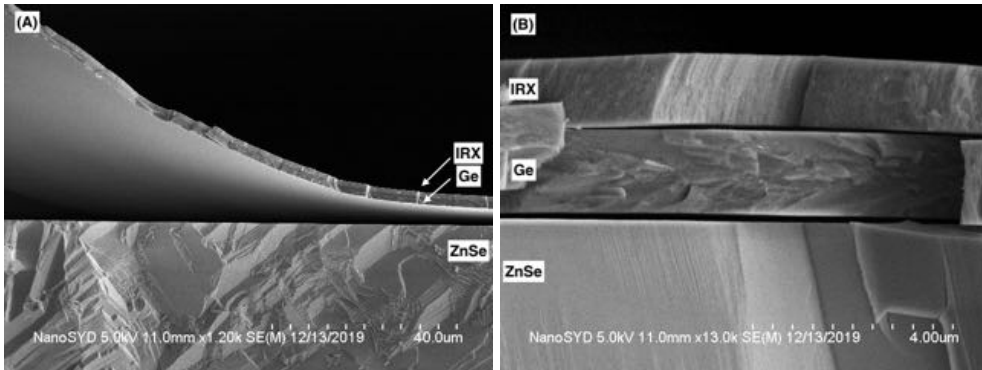
Figure 3.8: (A) SEM image of a ZnSe Ge/IRX. (B) SEM image of the Ge/IRX coating showing the smooth thin film layers, and the weak bonding between all three layers.

3.3 Characterisation of Giai Photonics Mirrors

During the development of our home grown FPI mirrors we attempted to outsource the production of the mirrors. This involved the Chinese company Giai Photonics which made early promises of mirrors that satisfied the specifications needed in the first order scanning Fabry-Pérot interferometer. Following several failed attempts to produce a mirror coating which satisfied the requirements we received a set of mirrors that showed promising transmission profiles.

The transmission profile is shown in Figure 3.10 below, where the transmission and reflection profiles are measured using a Shimadzu IRAFFINITY-1S FTIR spectrometer. As can be seen in Figure 3.10, the transmission percentage within the sensor sensitivity range of 8-14 µm has a mean value of 16.3 %. The average reflectivity of the mirror in the range 8-14 µm is 81.3 %. Subtracting both the average transmission and average reflectivity from 100 % results in an average absorption of 2.4 % assuming that no light is scattered. As is seen in Figure 3.10 (A) the absorption gradually rises with the increased wavelength and has a value of 15 % at 14 µm. The absorption values are lower than those observed for the homegrown mirrors. The absorption of 15 % at 14 µm is still too high, and too much light is lost at these wavelengths. Since the mirror recipe was unknown when we received the substrates, a cross sectional analysis of the mirrors using a Hitachi S-4800 SEM was performed. The mirror substrate was broken in half and the coating was imaged from the side. The image acquired is shown in Figure 3.9 (A), which reveals that a multilayered structure is deposited counting nine layers excluding the thin top coating. The total coating thickness was
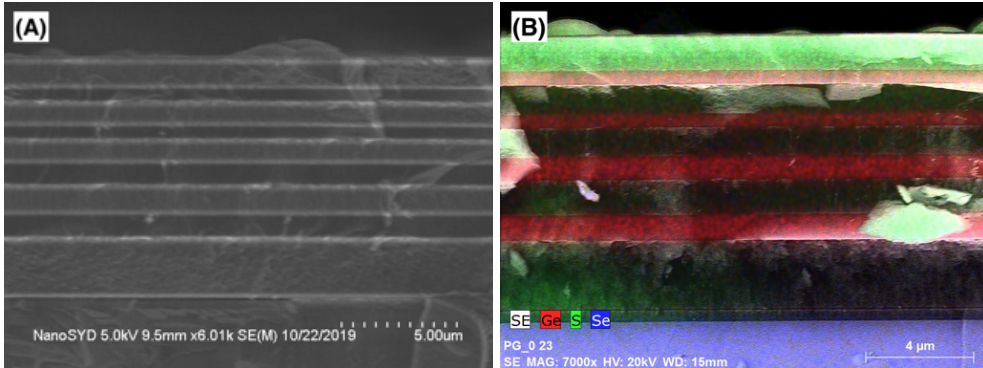
Figure 3.9: (A) shows an SEM image of the FPI mirrors from Giai Photonics. (B) shows an EDX analysis of the FPI mirrors from Giai Photonics. The overlays of colour red, green and blue indicate the presence of Germanium, Sulphur and Selenium, respectively.

measured to $10.5\,\mu m$ using the analysis software provided by the instrument. An EDX analysis was performed in order to determine the coating materials used. A graphical summary of the results is shown in Figure 3.9 (B). Here the emission energy of the x-rays produced in every region of the image is compared to database values during the image scanning. Here it is seen that four germanium layers are present in the coating, and that the five additional layers supposedly consist of ZnS. During the scan we also checked for fluoride compounds and the fluoride compound check was negative.

The most important reason why the Chinese mirrors cannot be used in our hyperspectral imaging application is that the mirror substrates bend significantly. A generalisation of this problem was introduced in Section 3.1.1 and shown in Figure 3.1 (B). The extent of the bending is shown in Figure 3.11 (B) where the interference fringes arising from the cavity between the mirror top surface and the reference substrate are clearly seen. Drawing a straight line across the center of the mirror substrate, it is seen that four fringes cross the center line. The physical bending of the substrate can be calculated by using the equation:

Figure 3.10: (A) and (B) Transmission and reflection FTIR measurements of the Giai Photonics (A) and II-VI Incorporated (B) FPI mirrors, respectively. The absorption has been calculated as $Absorption = 100\% - (T\% + R\%)$. The two vertical lines in each figure represent the sensor sensitivity range.

$$m\lambda = 2nd\cos(\theta)$$
$$\Updownarrow$$
$$d = \frac{m\lambda}{2n\cos(\theta)}$$

Using $n = 1$ and $\theta = 0$ we see that the difference in thickness between fringes are half integer values of λ. Counting ≈ 4 fringes and using a mean value of $500\,\text{nm}$ for visible light the resulting mirror bending is $1\,\mu\text{m}$. This is way too much for the FPI since placing two bending mirrors on top of each other result in MS differences of $2\,\mu\text{m}$.

3.4 Characterisation of II-VI Incorporated Mirrors

Following several failed attempts to buy and develop mirrors for the Fabry-Pérot, we contacted the company II-VI Incorporated. II-VI accepted making our mirror coating suggesting a low refractive index layer consisting of either ytterbium fluoride or thorium fluoride. Owing to the thickness of our middle layer, II-VI chose to deposit thorium fluoride, since the thicknesses needed for a $10.5\,\mu\text{m}$ design is close to the maximum thickness possible for ytterbium fluoride.

Our mirrors still consist of two-inch substrates of a thickness of 5 mm. The flatness of the substrates is crucial for the performance of the mirrors, and thus the flatness
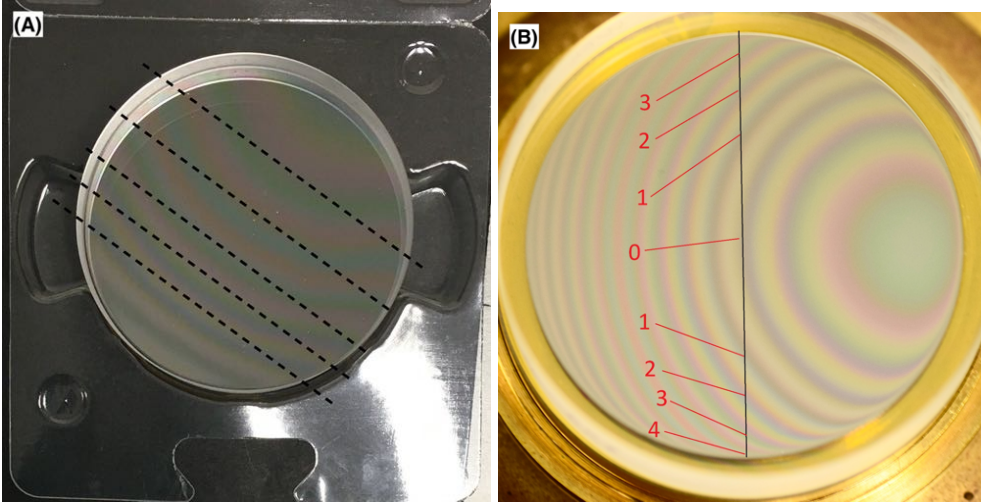
Figure 3.11: (A) Image of the II-VI mirror stack with a $\lambda/50$ substrate on top. The bending of the interference fringes reveals that the mirror is not ideally flat. (B) RGB image of the interference pattern when placing a $\frac{\lambda}{50}$ substrate on top of the Giai photonics FPI mirrors.

specification is set to a quarter fringe peak to valley (PV) at a He-Ne wavelength of 632.8 nm. The homogeneity of the surface is also an important factor, which influences the smoothness of the fringes observed. We, therefore, asked for the highest surface finish available in the industry, which is specified as an S/D 20/10. This number indicates the scratch and dig size in micrometers, which are common defects on the mirror surface.

The edge thickness variation (ETV) is specified to be less than three arc minutes corresponding to $\frac{3}{60}°$. Across a two inch substrate the maximum ETV in physical distance is

$$ETV = \sin\left(\frac{3}{60}\frac{2\pi}{360} \cdot 50.8 \cdot 10^{-3}\text{m}\right) = 4.43 \cdot 10^{-5}\text{m} = 44.3\,\mu\text{m} \tag{3.3}$$

The mirror recipe deposited by II-VI is summarised in Table 3.9. All substrates were additionally coated with a broadband antireflective coating consisting of ThF$_4$ and ZnSe on the backside. Both coatings had an aperture of 43 mm.

	II-VI Design	
Material	OPL	Physical thickness
Ge	1/4 wave	0.656 µm
ZnS	-	100 Å
ThF$_4$	1/4 wave	1.836 µm
ZnS	-	100 Å
Ge	1/2 wave	1.315 µm
ZnSe	Inf	5 mm

Table 3.9: Overview of the deposition parameters for the II-VI Incorporated mirrors.

The transmission profile of the II-VI mirrors is shown in Figure 3.10 (B) along with the reflection profile. The average transmission within the sensitivity range of the bolometer sensor is 13.94 %, and the average reflectivity within this range is 84.34 %. This results in an average absorption of 1.72 % with values of 3.43 % and 1.85 % at the 14 µm and 8 µm ends respectively. A minimum in absorption of 1 % is measured at the design wavelength of 10.5 µm. The values are close to perfect and lie within the measurement errors of the FTIR instrument used in this setup. The effective bandpass of an FPI assembly was measured using the II-VI mirrors and the results have been graphically shown in Figure A.4 (B). The transmission percentage using the II-VI mirrors was measured to be ∼80 % at the design wavelength. At wavelengths just above and below the design wavelength the transmission drops in percentage to ∼75 % due to the small absorption. The transmission percentages agrees with the theoretically calculated values based on equation 2.8.

Figure 3.11 shows the substrates with a $\lambda/50$ substrate placed on top which results in interference fringes from the fluorescent lamps in the laboratory. The broken lines on the figure are placed as tangents to the interference fringe (the red lines). The bending of the substrates can be calculated accordingly and was determined to be ≈ 250 nm. This bending is acceptable but not ideal.

An FPI mirror recipe matching the II-VI mirrors has been used in a transfer matrix method simulation. The thin adhesion layers of ZnS were omitted from the simulation.Figure 3.12 (A) and (B) show the theoretical transmission profile of the FPI using the II-VI mirrors. The transmission profile was found based on an unpolarised light source, and the wavelength range was chosen according to the sensitivity range of the microbolometer sensor. Several useful facts can be derived from Figure 3.12, which eases the understanding of the hyperspectral thermal imaging datacubes gathered when using an FPI as a wavelength filter. First of all, the FWHM of the first and second order transmission peaks are directly comparable. In Figure 3.12 (A) it is
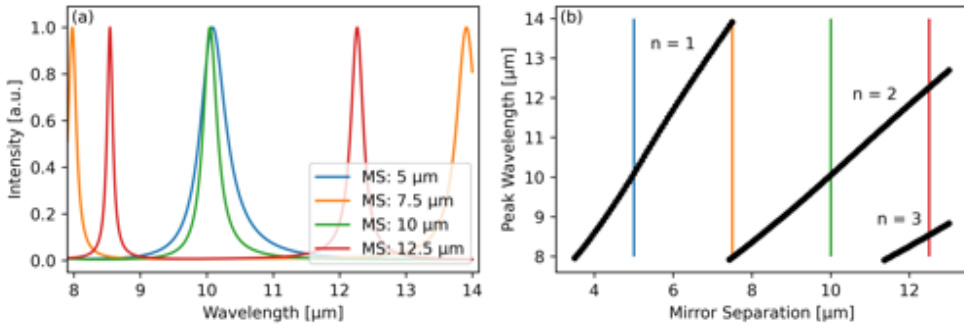
Figure 3.12: (A) Simulations of the Fabry-Pérot interferometer with mirror separations of 5, 7.5, 10 and 12.5 µm in the range from 8 to 14 µm. (B) The peak positions of the transmitted band as a function of the mirror separation. The orders transmitted are marked with their order. It should be noted that several orders lie within the sensitivity gap of the sensor at mirror separations above 11.3 µm.

clearly seen that the FWHM is reduced in the second order transmission, which is most noticeable for the two mirror configurations with mirror separations (MS) of 5 µm and 10 µm in Figure 3.12 (A). Additionally, note that the peak wavelength as a function of the mirror separation has different slopes for each of the transmission orders. Therefore, we can conclude that:

$$\left.\frac{d\lambda_{Trans}}{dMS}\right|_{n=1} \neq \left.\frac{d\lambda_{Trans}}{dMS}\right|_{n=2} \neq \left.\frac{d\lambda_{Trans}}{dMS}\right|_{n=3} \tag{3.4}$$

The information above becomes relevant in Chapter 6.

3.5   Summary and Conclusion

While the experiments did not provide perfect FPI mirrors, they did provide a lot of insight into the important factors for the process of developing optical thin film coatings. Most notably, a sufficient substrate temperature is needed in order to produce high quality dielectric thin films. The three layer mirror recipe was successfully reproduced. However, the strong absorption centered around LWIR wavelengths of 13 µm has a significant impact on the light transmitted by the FPI. This will be evident in Chapter 6, which presents the data analysis of images grabbed using these mirrors. Following the experiments it has been concluded that in order to obtain the highest

grade coatings with good structural parameters and low absorption, several deposition parameters must be tuned in order to reach the specifications desired. The ability to heat the substrate is the most important parameter to ensure, provided that future experiments should be carried out. This is mentioned widely in the literature, and the post deposition annealing experiments of the initial germanium layer slightly supports this fact.

Several additional experiments could be carried out in order to improve the mirror substrates having the ability to heat the substrates during deposition. Especially, the experiment involving alternative mirror designs presented in Figure 3.1 and Table 3.1 where the two-layer coating is the most interesting, since it may benefit the substrate bending. Even though the two layer coating would broaden the transmission peak of the FPI, the effect of a broadened peak is reduced by the flat substrate.

Future experiments could also include a protective coating on top of the top germanium layer in order to prevent oxidation of the surface layer.

As a final note, an increased uniformity of the coating could be achieved by using a planetary rotation system, the ability to monitor the coating thickness in situ using optical transmission monitoring, and to perform ion assisted deposition.

Several optical coating companies were contacted during this project, where II-VI Incorporated and GIAI photonics agreed to produce our FPI mirrors. GIAI photonics chose to deposit a multilayered structure which ended up as a failure due to too high tensile stresses causing the substrate to critically bend. II-VI Incorporated deposited a three layer structure of $Ge/ThF_4/Ge$ with low absorption. The bending of the substrate as a consequence of the coating was within tolerances and the II-VI mirrors were therefore used for imaging during the final part of this project.

4

Development and Functionality of a Hyperspectral Thermal Imaging Prototype

The following chapter will describe the technical details and physical assembly of the hyperspectral thermal imaging system in detail. The chapter describes the actual components used in our imager and the most important details about the working principle of the camera.
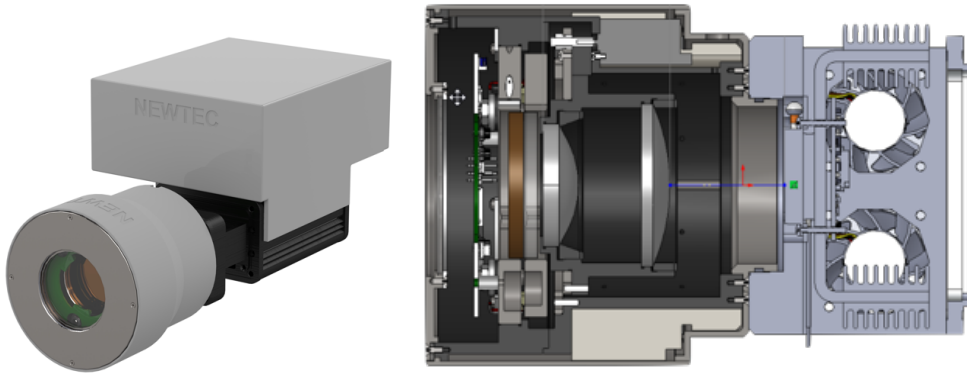
Figure 4.1: 3D design of the hyperspectral thermal lens connected to the QTechnology camera body.

4.1 Physical assembly of the Hyperspectral Thermal Camera

During the course of this PhD project a functional and mobile prototype of the hyperspectral thermal camera has been assembled. A 3D-render of the camera setup is shown in Figure 4.1 (A). This prototype can be divided into three main components consisting of the lens housing in front, the camera body in the middle, and the battery package enclosure on top. A short description of the battery package is included in Appendix A.2.2 and for information on the camera body the reader is referred to he most critical functionality is located within the lens housing and a detailed cut-through of this is shown in Figure 4.1 (B). Starting from the left the lens housing consist of a protective window, the scanning FPI, the collecting optics, and lastly the microbolometer sensor attached to the camera body. An individual description of each component follows in the coming sections, although we do skip the description of the protective window.

4.1.1 The Scanning FPI

A sideview of the scanning FPI is shown in Figure 4.2 (A). The FPI mirrors are placed inside two circular steel flanges which fit inside the lens housing shown in Figure 4.1. During assembly, three piezoelectric crystal stacks are placed as separators between the steel flanges. The piezoelectric elements are placed at an equal angular distribution of 120° around the edge of the flanges. During this project, two different piezoelectric stacks have been used. The first stack is the Thorlabs PK2JA2P2 with a maximum expansion of 8.0 μm provided that a bias of 75 V is applied along with a

load of 144 N. This piezo stack was later upgraded to the Thorlabs PK2FMP2 piezo stack with a maximum expansion of 11.2 μm at a bias of 75 V and a load of 400 N. The load is provided by a nut, fastened to the back flange, which tightens onto disc springs on the front flange. This is illustrated in Figure 4.2. The disc springs[1] used for the PK2FMP2 piezo has a maximum force of 673 N and a maximum travel of 0.22 mm. Using four of these, a total travel of 0.88 mm is available to reach a force of 400 N. The tightening of the M5 bolt needed for the recommended load can then be calculated by

$$\frac{400\,\text{N}}{673\,\text{N}} \cdot 0.88\,\text{mm} = 0.52\,\text{mm}$$

this equals:

$$\frac{0.523\,\text{mm}}{0.8\,\text{mm}\,\text{turn}^{-1}} = 0.65\,\text{turn}$$

The FPI mirrors are typically inserted into the center of the flanges following assembly and tightening of the nuts. The steel flanges are designed such that the ZnSe mirror substrates have three contact points with the flange. Two of these contact points are static and the last consist of a bendable plate which is tightened to the mirror by two screws. This design is necessary in order to prevent physical bending of the mirror substrate as a result of fixing the mirror in place. Following the placement of the mirrors inside the steel flanges the mirrors must be aligned before imaging, which is described in the following section.

Control and Scanning of the FPI

The FPI can be scanned following the assembly of the mirrors. This is carried out by the Qtechnology print circuit board (PCB) QT5062, which is mounted on the outside of the steel flanges. The main components of the QT5062 PCB for the control and scanning of the FPI are three laser diodes and three photo diodes mounted at positions around the uncoated mirror edge matching the piezoelectric stacks. The photo diodes are single pixel CMOS detectors and the laser diodes have a wavelength of 655 nm. The wavelength of the laser diodes is important since the transmission of the ZnSe substrates starts at ∼550 nm.

A voltage is swept in the range 0-75 V and back on all three piezoelectric stacks during the acquisition of a hyperspectral thermal image (HSTI). As all three piezos expand, the steel flanges are separated and the mirror separation is increased which change the bandpass wavelength of the FPI. As the voltage is lowered from 75 V the
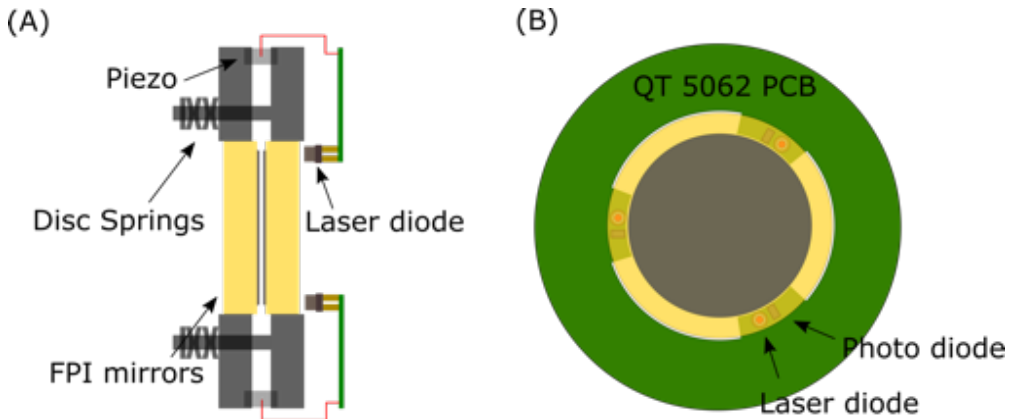
---

[1]https://www.fjedre.dk/01202700

Figure 4.2: (A) Sketch of the FPI assembly which is used in this project. The yellow ZnSe substrates are placed at ~ 3 μm separation and each is held in place by a steel flange. The steel flanges are separated by three piezoelectric stacks which extend as a voltage is applied by the QT5062 PCB. The expansion of the piezoelectric elements separate the steel flanges, and thereby also separates the mirrors. Once the bias is lowered the disc springs push the mirrors back to their original separation. (B) The QT5062 PCB sets the voltages which is applied across each piezo element separately. Three laser diodes and three photo diodes are mounted on the PCB. The laser diodes illuminates 655 nm light into the uncoated cavity created by the bare ZnSe substrate, and the photo diodes measure the interference caused by the cavity.

force from the disc springs brings the mirror separation back to its original value. A HSTI is thus generated by continuously acquiring images during the forward voltage sweep of 0-75 V. The images are acquired during the forward sweep since the piezoelectric elements have a nonlinear behaviour in relation to the applied voltage. During expansion the piezo crystals exert creep and thus maintaining the piezo at a set expansion is not possible, since the piezo will continue moving in the same direction. Another important characteristic is hysteresis which can be checked by monitoring the interference fringe pattern which is measured from each photo diode on the QT5062 when the FPI is scanned. The hysteresis was measured by scanning the FPI linearly across the voltage range with steps of 0.1 V. Between each step a waiting period of 3 ms was added and the three photo diodes were read out and saved. In order to get a hysteresis curve the voltage is cycled from 0 V to 75 V and back again. The resulting interference fringe pattern is shown in Figure 4.3 (A) for a single photo diode. The blue graph shows the interference pattern for the forward scan and the orange graph shows the interference pattern for the backwards scan
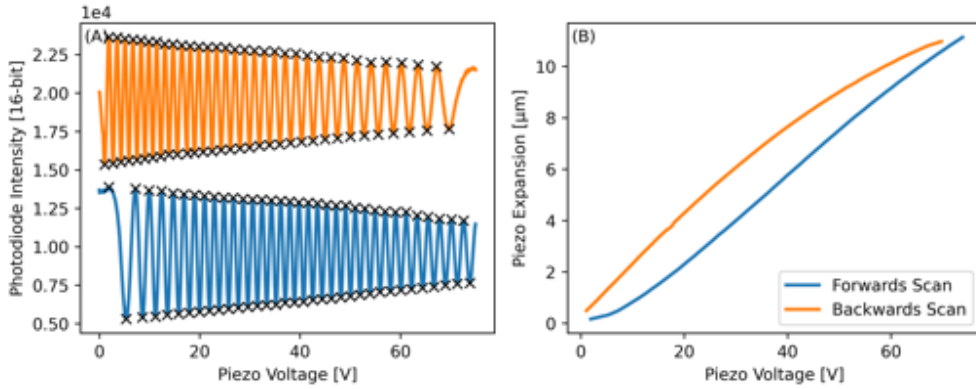
Figure 4.3: (A) Interference fringes from the specular reflected 655 nm laser diode light source. The black crosses mark the maxima and minima positions of the individual fringes during the scan. The blue graph shows the interference measured during forward scanning, and the orange graph shows the backwards scanning. The orange graph has been offset for visualisation purposes. (B) The hysteresis curve associated with the scan shown in (A). The hysteresis arise from the expansion and contraction of the piezoelectric crystal.

which has been offset for visualisation purposes. Once again, we know that positive interference happens at integer values of the wavelength and thus

$$m\lambda = 2nd\cos(\theta) \tag{4.1}$$

using $n = 1$ and approximating $\theta = 0$ we find that the separation of the substrates between two interference maxima changes by half the wavelength of the laser diode. The same procedure is applicable for the interference minima substituting m by $(m + \frac{1}{2})$ and thus the relative expansion and contraction of the substrates can be found by measuring the interference extremes. These are shown as black crosses in Figure 4.3 (A) and the expansion and contraction of the substrate separation has been calculated and shown in Figure 4.3 (B). The substrate separation is crucial during image acquisition, since it has to be equal for all three piezoelectric elements in order to keep the mirrors aligned and parallel while the HSTI is acquired. The control software for the image acquisition checks the position of the interference fringes shown in Figure 4.3 (B) and adjusts the voltage steps individually on the three piezoelectric elements. The control happens through an open loop system that checks the fringe positions following a full hysteresis cycle. As the FPI reaches 0 V the voltage steps between fringes are recalculated for each piezo until a sufficient accuracy is

reached. In the first part of this project the voltage was swept using steps of 0.1 V and an image was grabbed every tenth step. Some of the range is lost during consecutive full hysteresis sweeps and thus the datacube contained ~ 70 spectral bands. Later the algorithm was improved and the voltage steps were reduced to 0.05 V resulting in datacubes of approximately ~ 140 spectral bands and thus

$$\mathbf{\Lambda}_{x,y,\lambda \approx 70} \xrightarrow{\text{smaller V-steps}} \mathbf{\Lambda}_{x,y,\lambda \approx 140} \tag{4.2}$$

The specific length of λ will be stated in each individual section regarding image analysis. The subject of the following section continues to focus on the alignment of the mirrors because it is not only important during the image acquisition but also as a part of the FPI assembly.

FPI mirror alignment

Until now we have briefly touched upon the importance of the bending of the substrates which broadens the transmission peak of the FPI. A visualisation of this effect is shown in Figures 4.4 (A) and (B) where 133 images have been acquired while continuously scanning the piezo voltages from 0-75 V. The FPI have been placed in front of the camera at the nearest focal plane. Additionally a 10 µm bandpass filter with a FWHM of 356 nm was placed in front of the FPI. The band pass filter only allows light at wavelengths centered around 10 µm to reach the FPI.

The mean spectrum of each coloured square box shown in Figure 4.4 (B) have been calculated and plotted in Figure 4.4 (A). The graph shows that a maximum transmission is let through the FPI at step 50. It is additionally observed that the peak transmitted by the FPI at the edge of the mirror substrate and at the center of the mirror substrate is let through the FPI at different band numbers. This is due to the substrate bending mentioned in Chapter 3.

A similar analysis can be made where the mean spectrum along the edge of the FPI mirrors is calculated. This is done to check that the mirrors are aligned, since the 10 µm peak would be transmitted at the same step number given that the mirrors are aligned. An example of such situation is shown in Figures 4.4 (C) and (D) where (C) shows the transmission of the squares along the edge of the mirror substrates shown in (D).

During assembly, the FPI mirrors are placed on top of each other and the distance between the mirrors is therefore difficult to control. This can result in a misaligned FPI which is shown in Figures 4.4 (E) and (F). The graph shown in Figure 4.4 (E) show that the transmission peak of the 10 µm light begins at step 60 and that the

transmission peak is distributed across ~ 30 steps starting at the black and yellow square in Figure 4.4 (F) and ending with the red squares. The first transmission of the 10 µm light is moved to higher step counts compared to Figure 4.4 (C) since the mirrors have a lower MS, and the skewering of the peaks is due to misalignment which means that the MSs for the black and red square are different during the entire sweep. Such an alignment was frequently the best obtainable during the first part of this project, since the alignment of the FPI was checked by visual inspection of the fringes in the edge of the ZnSe substrates. While the starting MS of 3 µm could be controlled to some extent the method seldomly provided perfectly aligned mirrors. The more precise alignment of the FPI for HSTI acquisition was found by ofsetting each piezo element in the FPI flange by a certain voltage before initiating a HSTI scan. While this has a positive effect on the alignment of the FPI mirrors during image acquisition, the piezo offset has a negative effect on the scanning range of the FPI. The offset parameters were found by keeping the voltage of one of the three piezoelectric elements at 0 V while offsetting the two remaining channels by a certain amount. These offset were iteratively scanned while the transmission through the FPI was monitored. The perfect alignment was then chosen as the offset voltage combination giving the highest intensity through the FPI. Later, an experimental setup meant for FPI alignment was created, which is the main topic of Section 4.2. Before we reach this section the description of the camera setup will continue along the direction of the light, which following the interference within the FPI reaches the collecting optics.
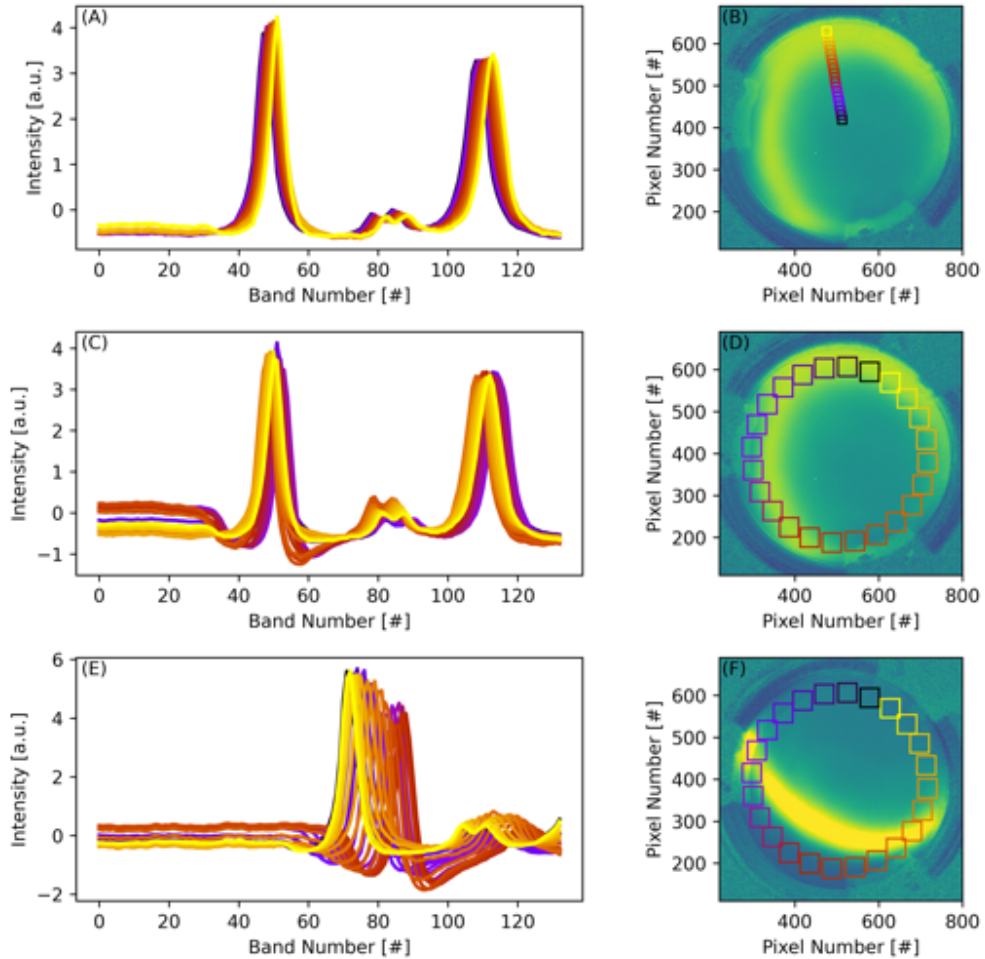
Figure 4.4: (A) Mean transmission of all pixels within the squares shown in (B) for all spectral bands. The colour or each spectrum matches the corresponding square in (B). (B) Image of the FPI placed in the far field optical path of the thermal camera. The squares used for analysis have been placed from the edge of the FPI to the center of the FPI. The colour of the squares correspond to the mean spectrum within the square plotted in (A). (C) Mean transmission profile of the squares shown in with colours matching the squares in (D). The graphs show a well aligned FPI since the 10 µm light is transmitted at the same band number for all squares along the edge of the FPI. (D) Image of the FPI placed in the far field optical path of the thermal camera. The squares used for analysis have been placed along the edge of the FPI mirrors. (E) Mean transmission profile of the squares shown in (F) with matching colour. The graphs show a misaligned FPI since the 10 µm light is transmitted across a range of band numbers. (F) Image of the FPI placed in the far field optical path of the thermal camera. The squares used for analysis are placed along the edge of the FPI mirrors.

Lens	Surface 1	Surface 2
Front aspherical	High durability AR for LWIR 8-12 µm <0.5 % >96 %	High Efficiancy AR for LWIR 8-12 µm <0.3 % >98 %
Back spherical	High Efficiancy AR for LWIR 8-12 µm <0.3 % >98 %	High Efficiancy AR for LWIR 8-12 µm <0.3 % >98 %

Table 4.1: Overview of the antireflective coatings applied to the germanium lenses in the collecting optics of the camera system.

4.1.2 The Collecting Optics

The collecting optics consist of two lenses bought of the Israeli company Ophir Optronics. The front lens of the collecting optics is a Ø43 mm germanium lens consisting of one concave aspherical and one convex aspherical surface. The second lens is a Ø56.8 mm germanium lens consisting of a one spherical concave and one spherical convex surface.

A high durability broad band antireflective coating is deposited onto the outwards facing surface of the front lens, since the collecting optics is designed by the manufacturer to be the only lenses in the imaging system. This coating protects the lens against repetitive cleaning, dust, and general wear and tear. However, the transmission of the antireflective coating is lowered as summarised in Table 4.1. The narrow band of the antireflective coating of 8-12 µm is a considerable drawback of the imaging system, and suppliers capable of producing antireflective coated optics in the 8-14 µm should be found. All surfaces have S/D values rated to 80-50. The collecting optics make up a system with an f-number of 1 and a focal length of 35 mm. The resulting angular field of view is approximately 26.5 °C and the focusing range is $\sim 30 - \infty$ cm. Each lens was bought individually and integrated into the camera lens system which is shown in Figure 4.1. Both lenses are mounted in a steel cylinder which is capable of sliding within the lens housing. The steel cylinder is fastened to a piezo inchworm driven linear actuator bought from the company PiezoMotor. The focus of the lens is then controlled through USB-serial commands sent by the QT5022 body. As the light is focused it reaches the microbolometer sensor which capture the light in order to produce a HSTI.

4.1.3 Spectral Bending

The nature of the collecting optics in combination with the FPI creates an artefacts which is caused by the angle of incidence of the incoming light. Since the Fabry-Pérot interferometer is placed in front of the Germanium lens system the light reaching the sensor for imaging will travel at an angle within the FPI as well. This will effectively change the optical path within the FPI of this light by a factor of $\sin(\theta)$, which results

in an altered transmitted band wavelength depending on the angle of the incoming light and thus the effect is named spectral bending. Since the field of view is constant for our lens system, the angle of the light incident on each pixel in the FPA is constant. This angle can be calculated through trigonometric from the physical size of the sensor FPA. Since the light reaching every pixel is a sum of the contributions from every possible angle from the lens system the angle of the light is found relative to the center optical axis. In order to calculate this effect it is needed to shift the coordinate system of the sensor pixels to the physical distance from the optical center, and therefore the pixel coordinates are shifted to [px,py]. Reminding once again that the resolution of the Pico 1024 Gen2 sensor is 1024x768 pixels it is true for p_x and p_y that

$$p_x = \{n \mid n \text{ is an integer, and } n \in [-512, -1] \cup [1, 512]\} \tag{4.3}$$

$$p_y = \{n \mid n \text{ is an integer, and } n \in [-384, -1] \cup [1, 384]\} \tag{4.4}$$

Thus the center of the image plane is located at $px = 0$, $py = 0$, however, no pixel is located at this coordinate. This requires a perfect assembly of the sensor relative to the optical axis, however, it is true in theory. The spectral bending correction factor $\lambda_{corr}[px, py]$ can be found from the relation

$$\lambda_{corr}[px, py] = \cos\left(\tan^{-1}\left(\frac{\sqrt{\left(p_x^2 + p_y^2\right) p_{pitch}^2}}{f_{lens}}\right)\right) \tag{4.5}$$

where, $f_{lens} = 1$ and $p_{pitch} = 17\,\mu\text{m}$. This gives a spectral bending factor which alter the wavelength in the image plane. The spectral bending factor is naturally a continuous distribution, however it must be quantised when measuring due to the individual pixels and their physical size. Still, the spectral bending factor lies within the interval:

$$(\lambda_{corr}[512, 384], \lambda_{corr}[1, 1]) = \{\lambda_{corr} \in \mathbb{R} \mid 0.955 \leq \lambda_{corr} \leq 1.0\} \tag{4.6}$$

The spectral bending effect has been tested experimentally by imaging a uniform hotplate and investigating the transmitted band from three different bandpass filter with center wavelengths of 8.2 µm, 10.04 µm and 11.3 µm. The uniform hotplate was constructed by machining pyramid shaped structures on the surface with a height twice as large as their width resulting in faces pointing at 63.4° relative to the surface.
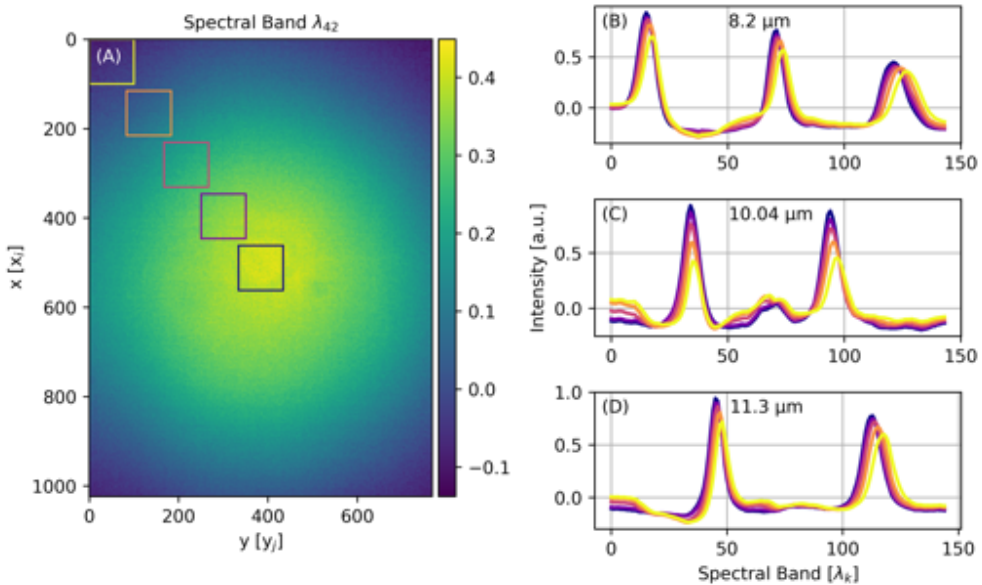
Figure 4.5: (a) Hyperspectral thermal image of an antireflective uniform hotplate with a 11.322 μm bandpass filter in front of the camera lens where the band number 68 has been shown. The spectral bending effect is seen as an intensity shift in the image plane. (B) The mean spectrum of the squares in (A) is plotted for the 8.2 μm bandpass filter. (C) The mean spectrum of the squares in (A) is plotted for the 10.04 μm bandpass filter. (D) The mean spectrum of the squares in (A) is plotted for the 11.2 μm bandpass filter.

Having these structures ensure that reflections in the image of the camera itself are minimised. The entire lens was covered with a bandpass filter and the bending of HSTI was investigated by investigating the mean transmitted spectrum through the bandpass filter. Such measurement is shown in Figures 4.5 (A), (B), (C), and (D). Figures (B), (C), and (D) shows the mean transmitted spectrum found in the square regions marked in (A) for the 8.2 μm, 10.04 μm and 11.3 μm bandpass filter respectively. Is is seen that the shift of the transmitted peak in HSTI data structure is increased for the second and third order which is due to the different rate of change for the transmitted band relative to the MS as explained in equation 3.4.

A potential circumvention of the spectral bending caused by the angular distribution of the light is a mathematical correction of the wavelength of the transmitted light. This results in a transformation of the hyperspectral datacube which can be found
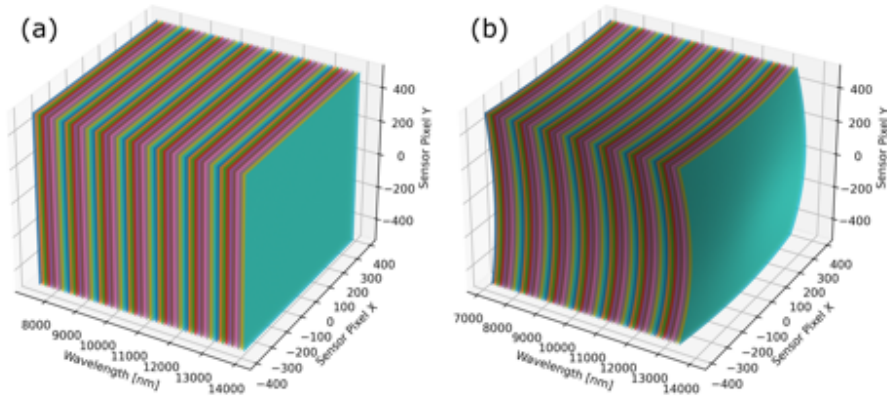
Figure 4.6: (a) A graphical illustration of a hyperspectral thermal datacube with a spectral axis ranging between 8-14 µm and with an image plane size of 1024x768 pixels. (b) A graphical illustration of the same image cube as presented in (a) which has been transformed by the image bending factor on the spectral axis. Each plane in the transformed datacube represent an image grabbed by our hyperspectral thermal imager. The spectral axis shows the corresponding wavelength, and it is thereby clear that the images contain systematically different wavelengths.

straight forwardly by multiplying the spectral axis in each pixel of the image plane by the wavelength correction factor. Such experiments have been carried out, without success, and the spectral bending is therefore still a task to be solved. An example of a transformed datacube is shown in Figure 4.6 below where (a) shows the standard datacube and (b) shows the wavelength transformed datacube.

4.1.4 The Microbolometer Sensor

The specific sensor used in the thermal camera setup is the Pico1024 Gen2 produced by the company Lynred. The sensor consists of a focal plane array (FPA) of 1024x768 individual pixels with a pixel pitch of 17 µm. The size of the datacubes is defined by the pixel resolution of the Pico 1024 Gen2 microbolometer, and the length of the spectral axis is defined by the number of images acquired during the voltage sweep of the piezoelectric crystals in the FPI. The resulting three dimensional matrix is then defined as

$$\mathbf{\Lambda}_{x,y,\lambda} \xrightarrow{\text{Pico1024}} \mathbf{\Lambda}_{x=1024,y=768,\lambda} \qquad (4.7)$$

with $\mathbf{\Lambda}$ being an $x \times y \times \lambda$ matrix with $x = 1024$ and $y = 768$ using the Pico1024 Gen2 microbolometer sensor. These axes could be expanded having a sensor of higher pixel resolution, however, throughout the rest of this thesis the x and y axes are kept at constant values. It should be noted that image cropping is always a possibility, and therefore the $\mathbf{\Lambda}$ matrix can always be reduced in size at the consequence of removing information.

Each pixel in the sensor is a microbolometer in itself which, as mentioned in the introduction, measures the incident thermal radiation by absorbing the thermal light. As the pixel absorbs the light it heats up, and the resistivity is changed, which can be measured as a change in current. An image grabbing event requires 33 ms, which gives a framerate of 30 Hz with an integration time of the analog pixel output of 42 µs. All images in this thesis were handled and stored as 16-bit. The sensor spectral sensitivity has been supplied by Lynred and is shown in Figure 4.7 (A). The Figure shows that the sensor has a uniform sensitivity in the range 8-14 µm and that the sensitivity rapidly drops at wavelengths above 14 µm.

The FPA is enclosed in a vacuum sealed compartment with a broadband antireflective coated germanium window in front. The vacuum sealing protects the FPA and enhances thermal insulation. The transmission profile of the germanium window in front of the sensor has been supplied by Lynred as well and is shown in Figure 4.7 (B). Here it is observed that the transmission profile is relatively flat within the sensor sensitivy region as well.

The responsivity to thermal radiation of the Pico1024 Gen2 is configurable through three different sensor settings. The first sensor setting is the the signal gain which has four discrete values of 1.00, 1.25, 2.30, and 4.10. The two remaining settings is configured by applying a voltage on two different pins on the sensor itself. These voltages are referred to as the GFID voltage and the GSK voltage. Both of these voltages lie within the range 1.0-3.2 V. As the GFID voltage is increased the dynamic temperature range of the sensor becomes shallower. This effectively increases the microbolometer responsivity. The GSK voltage functions as an offset which changes the range of emitted radiation needed for under and over saturating the output values. A small experiment was designed for measuring the influence of the GFID voltage primarily, which is elaborated in the following section.
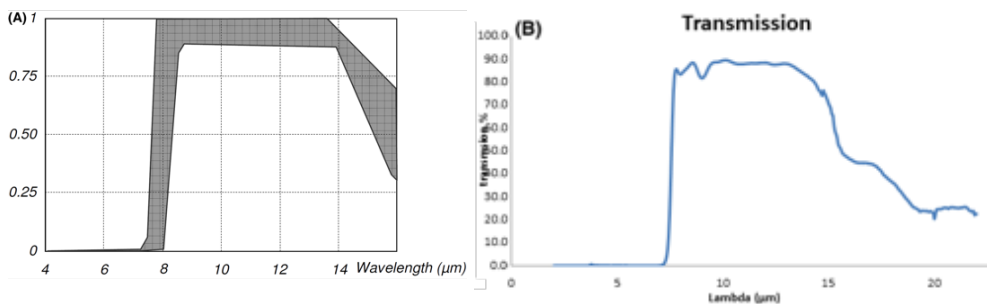
Figure 4.7: (A) Graph showing the sensor sensitivity as provided by the manufacturer. The graph shows a uniform sensitivity between 8-14 µm. Above 14 µm the sensitivity rapidly drops to 0. (B) Graph showing the transmission profile of the germanium window on the sensor enclusore.

A Study of the Sensor Responsivity

An experiment was designed for mapping the influence of tuning the responsivity of the Pico1024 bolometer. The bolometer responsivity can be increased by setting the GFID voltage on the sensor chip itself. This effectively reduces the temperature range of the bolometer chip and thereby increases the responsivity to small temperature fluctuations. While this limits the temperature range visible by the sensor, the sensor voltage GSK can be used to shift this range.

In order to find the width of the temperature range of the bolometer sensor an experimental setup was made where the pixel output response to a temperature perturbation was measured. The following explanation and results rely on a sensor gain of 4.1x. A similar measurement series is presented in Appendix A.2.1 using a sensor gain of 1.25x. A PID controlled print circuit board (PCB) hotplate was used for measuring the pixel response at four different temperatures of 40, 50, 60 and 70 °C. The PCB was covered in high emissivity polyimide tape and the GSK voltage was chosen such that both the 40 °C and the 70 °C measurement were within the dynamic range. A linear fit of the sensor response was used to find the temperature range, by extrapolating the temperature value to the extremes of the measurement range of the bolometer sensor. The sensor output was set to 16-bit and therefore the output responses of 0 and 2^{16} was used. The mean output intensity of all pixels that did not either over or under saturate was used. Figure 4.8 (A) shows the mean intensity development measured for the 40, 50, 60, and 70 °C hotplate measurements for 7 different GFID voltage settings. The slopes derived from the linear fit has been plotted
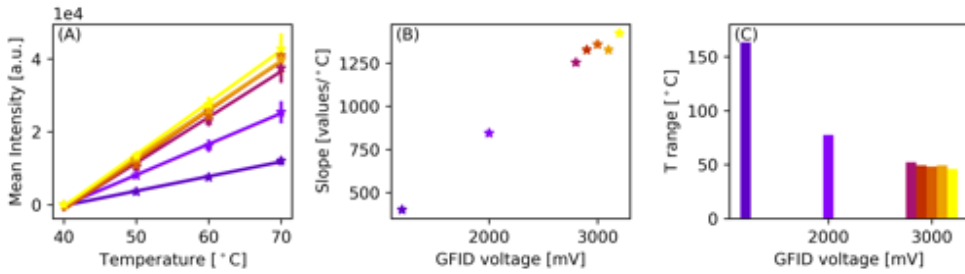
Figure 4.8: Measurements of the influence of altering the GFID voltage on the thermal camera using a 4x gain. (A) The mean intensity of the active area of a standard thermal image of a hotplate at temperatures of 40, 50, 60, and 70 °C. (B) The slopes of the linearly regressed lines in (A). (C) The corresponding temperature range provided that 16-bit images are acquired. The temperature range can be moved freely by setting the GSK voltage on the sensor.

versus the GFID voltage in Figure 4.8 (B). The seven different GFID voltages used were 1200, 2000, 2800, 2900, 3000, 3100, and 3200 mV. The corresponding temperature range that the sensor is capable of measuring can be calculated by dividing 2^{16} by the slope values in (B). The resulting temperature ranges and their related GFID voltage has been shown in Figure 4.8 (C). Setting a maximised temperature responsivity is crucial for our hyperspectral thermal imaging application since the spectral emissivity differences are measured as radiant power changes which in this regard is comparable to the temperature range. Thus, the higher GFID voltage should result in better exploitation of the sensor 16-bit output range.

4.2 Mirror Alignment Station

During the first part of this PhD project, the mirror alignment was carried out by placing the two FPI mirrors on top of each other, and checking the interference of the visible light in the uncoated region of the FPI using visible inspection. While the method works, it was tedious and often resulted in slightly misaligned mirrors. As mentioned earlier in section assembly, it is desired to assemble the FPI mirrors as parallel as possible from the beginning. This reduces the need for offset calibration during image acquisition, which reduces the total range available for hyperspectral imaging. Therefore, an effort was made to improve this procedure and reduce the time needed for aligning the FPI mirrors.
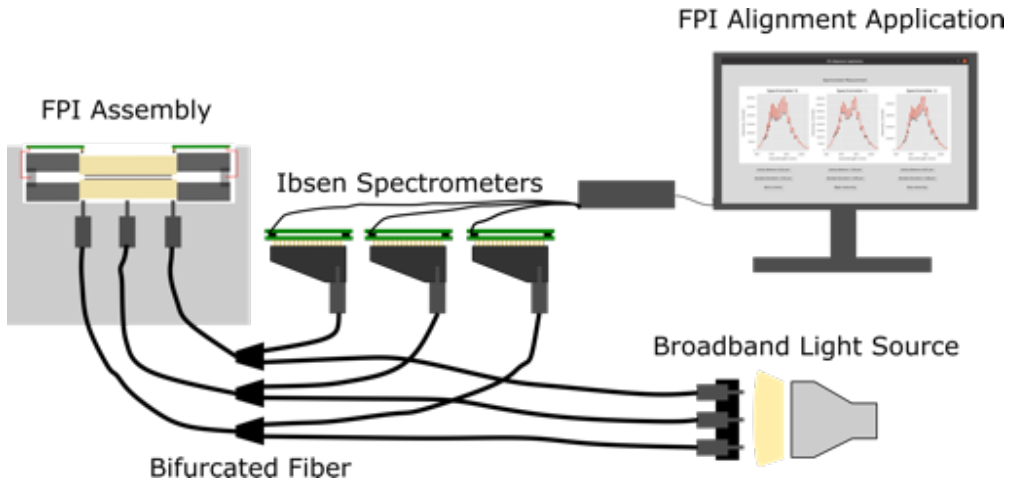
Figure 4.9: Graphical representation of the experimental setup built for fastening and aligning the mirrors in the FPI. Three small Ibsen spectrometers functioning in the range 600-1000 nm measure the interference pattern arising in the cavity of uncoated region of the ZnSe mirror substrates. Three bifurcated fiber optics are used to direct the light from a broadband light source into the cavity and back to be measured in the spectrometer. Each spectrometer is connected through USB to a PC showing the interference pattern in a Python application.

The resulting experimental setup is sketched in Figure 4.9. The figure shows an FPI alignment station, where it was possible to mount and fix the mirror substrates. This setup is made from three spectrometers of the model FREEDOM VISNIR FST-101 from the danish company Ibsen Photonics. The spectrometers measure light in the range 600-1000 nm and their main purpose is to measure light interference between the FPI mirror edge, where the substrates are uncoated. The spectrometers are bought with a USB-SPI interface which functions by the use of a FTDI FT4222H chip.[2] Demo software was provided by IBSEN where communication with the spectrometers is established through a C compatible Python script. This script is slightly modified but otherwise included as is in Appendix A. A python application was made which use the communication script provided by IBSEN to communicate physically with the spectrometers. The collected spectra are read and plotted in a graphical user interface based on the TKinter package. The custom application is shown in Appendix A Along with an image of the GUI, and sketched in Figure B.1.

---

[2]The libft4222 driver is downloaded from the FTDI homepage at https://www.ftdichip.com/Support/SoftwareExamples/libft4222-linux-1.4.4.44.tgz

Following assembly the mirrors are fixed at specific minimum mirror separations which may vary a lot from leg to leg. This distance can be measured exactly when the uncoated mirror cavity is illuminated by a broadband light source which in our case is a halogen lamp. Three bifurcated fiber optic waveguide cables (Thorlabs BFY105LS02) were used to direct light from the halogen lamp to the mirror cavity and back to the spectrometers for analysis.As seen before, the interference between the substrates is given by the relation

$$2nd\cos(\theta) = \lambda m \tag{4.8}$$

This time, the substrate separation d is kept constant while the range of lambda spans several orders. As the interferogram is measured across the visible to the near infrared range, the measured interferogram will be unique for the given mirror separation. In Figure 4.9 the three spectrometers measure the absolute distance at each point along the circumference of the mirrors where a piezoelectric element resides. Thus, by comparing the three measured distances, a good estimate of the alignment is obtained. A fine tuning of the mirror alignment can be carried out by fastening or loosening the nuts applying force on the disc springs in the steel flange assembly. This is utilised, along with the live measurements of the mirror separation at each "leg", to obtain well aligned FPI mirrors prior to image acquisition. A variety of options for calculating the absolute distance between the mirror substrates is included in the following section.

Absolute Position Calculation

Several methods can be applied to calculate the distance between the mirror cavities. In the following section, two approaches will be shown. Theoretically, the mirror separation can be determined based on the top position of two maxima or minima. The relation for calculating the absolute distance can be deduced from the equation introduced earlier and taking two extremes separated by one order into account. This gives us the exact distance between the substrates based on the wavelength measured for two extremes by

$$d = \frac{1}{2n\cos(\theta)} \frac{\lambda_m \lambda_{m+1}}{\lambda_{m+1} - \lambda_m} \quad . \tag{4.9}$$

where d is the absolute distance between mirror substrates and λ_{m+1}, λ_m are the wavelengths measured for two adjacent extremes. The derivation for this equation
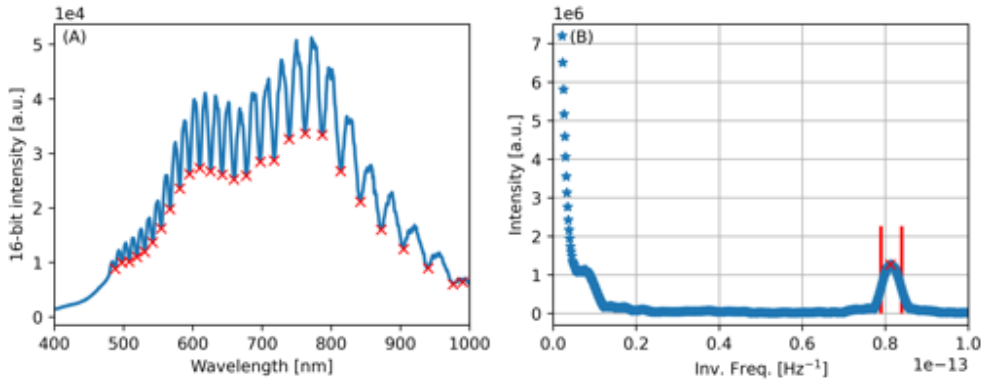
Figure 4.10: (A) Calibrated raw data from the FST-101 spectrometer. The interference pattern arise from the mirror cavity at the point measured by the bifurcated Thorlabs cable. The red crosses indicates minima positions which can be used to calculate the absolute distance between the ZnSe substrates. (B) An FFT analysis of the frequency transformed spectrum shown in (A). The frequency of the equidistant interference fringes arise and the maximum position has been marked by a red cross and the FWHM by two vertical red lines.

is shown in Equation (A.1). Several factors affect the quality of the result from such a measurement. First, the resolution on the spectrometer is limited by the sensor size and distance between the grating and the sensor. Using the FREEDOM VISNIR FST-101 spectrometer a maximum resolution of 1.7 nm is obtained with a 2048 pixel Hamamatsu S11639 linear CMOS detector. This results in uncertainty of a single measurement, and therefore, in the alignment application the result is calculated for all the measured interference minima. Figure 4.10 (A) shows a typical measurement for a single spectrometer, where the minima are located and plotted as red crosses. Inserting all possible values into equation A.1 and calculating the mean distance results in a measurement of $d = 12.19\,\mu m$ with a standard deviation of $\sim 307\,nm$. An alternative way of calculating the absolute substrate distance is to calculate the Fourier transform of the measured spectrum. For this analysis the fast Fourier transform is used and calculated by

$$X_k = \sum_{n=0}^{N-1} x_n e^{-i2\pi kn/N} \quad k = 0, 1, ..., N-1$$

with N being the total number of sampling points, and x_n being individual data

points in the frequency domain. Since the data is gathered from the spectrometers in the wavelength domain the data has to be transformed to the frequency domain where the interference fringes are equidistant. In this domain the data points are not equally spaced which is a necessity for calculating the FFT. Two transformations has to be calculated for performing an FFT analysis of the data in order to extract the dominating interference distance on the mirrors. First, the data is converted to the frequency domain since the interference peaks will be equidistant in this domain. This transformation is given by the simple equations regarding the energy, wavelength, and frequency relation of light introduced in Chapter 1. Second, the data is interpolated in order to create a dataset where the data points are equidistant and thereby creating an artificial constant sampling rate. This is done by calculating the spline of the frequency transformed data set and picking equally spaced data points. Now, the FFT can be calculated and the resulting graph is shown in Figure 4.10 (B) where the dominating inverse frequency of the interference measurement is observed to lie at $1/f = 8.13 \times 10^{-14}\,\mathrm{Hz}^{-1}$. The related substrate distance can be calculated straight forwardly by inserting into equation 4.8 using $n = 1$, and $\theta = 0$. Additionally we calculate our common value of λm by transforming the inverse frequency found by the FFT back to the wavelength-equivalent using the relations introduced in Chapter 1.

$$d = \frac{\lambda m}{2} \;\Rightarrow\; \lambda m = \frac{c}{f}$$

The resulting value for the substrate thickness is 12.19 µm and the positions of the FWHM lines lie at $\pm 349\,\mathrm{nm}$. While the accuracies of the measurements are very comparable, the FFT analysis is more robust. One drawback of the FFT method is the frequency resolution which is given by the relation

$$resolution = \frac{F_s}{N}$$

where F_s is the sampling frequency and N is the number of sampling points. In our case the sampling frequency is calculated by dividing the spectral range by the number of sampling points given by pixels on the sensor. Hence, the only pathway to increasing the resolution is by measuring the interference on a broader spectrum. The resulting FFT resolution from the Ibsen spectrometers is 25 nm.

The spectrometer measurements from the IBSEN FST-101 spectrometers prove that the concept of the spectrometers work as intended, and is a helpful setup in the

alignment of the mirrors. It has been considered to test the setup for the control of the FPI mirrors during image acquisition and the following section summarises the results.

Inclusion of Spectrometers on the QT5062 PCB

The possibility of adding small spectrometers to the QT5062 PCB has been investigated, and the initial experiments for the proof of concept has been made. A compact spectrometer was bought from Hamamatsu which fit within the camera housing. The specific spectrometer bought was the Hamamatsu C14384MA-01 Mini-spectrometer which has 256 pixels and measures 11.5 x 4.0 x 3.1 mm. A testing setup was made where a light source illuminates the uncoated rim on the FPI and the reflected light is directed into the slit of the spectrometer. In essence the setup is identical to the FPI mirror alignment setup presented in Chapter 4. The interference pattern caused by the cavity in the FPI is measured by the mini-spectrometer and the absolute distance can be found through the same equations as presented earlier. The big difference between these two setups is the physical size of the sensor in each spectrometer. Since the Ibsen spectrometer is equipped with a 2048 pixel linear sensor and the Hamamatsu spectrometer is equipped with a 256 pixel linear sensor, the resolution on the Hamamatsu spectrometer is extremely limited. While this is no problem at small mirror separations, the problem becomes significant as the piezo elements are fully extended and the mirror separation is at its maximum value. This is due to the fact that the number of interference fringes rises as the mirror separation is increased, and at some point the diffraction limit is reached. Figure 4.11 (A) shows the spectrum of the interference pattern arising from the cavity between the thermal mirrors using a broad band LED as a light source. The LED used is the Osram Oslon P1616 with a spectral radiance in the 600-1050 nm range.

The Hamamatsu spectrometer was set to acquire spectra with an integration time of 1000 µs and 1000 spectra were continously sampled while the FPI scanned forwards and backwards between 0 and 75 V. The spectrum in Figure 4.11 (A) is acquired at the beginning of an FPI scan and therefore the interference fringes are easily visible. The spectrum is plotted in the frequency domain which once again means that the interference fringes are equidistant. An FFT was performed on the spectrum and the result is shown in Figure 4.11 (B). Knowing the typical mirror distance from our FPI the peak associated with the interference pattern can easily be distinguished from the noise in the FFT spectrum. Figure 4.11 (B) shows the result of the FFT analysis and

the peak position is marked with a red 'x' and the FWHM of the peak is marked with red vertical lines. In this particular experiment the mirrors were relatively separated and the peak intensity observed in (B) corresponds to a separation of 8.5 μm. As mentioned the interference fringes are smoothed out once the mirror separation becomes too large which results in a less prominent peak following an FFT. Figure 4.11 (D) shows the measured spectrum with fully extended piezoelectric elements and the resulting FFT is shown in (E). While the peak is much less pronounced at full elongation the peak position can still be determined with a satisfactory accuracy. Measuring a full spectrum and finding the peak position during an FPI scan, the hysteresis curve of the piezoelectric elements is found once again. Note that the absolute distance travelled is calculated by this method, in contrast to measuring the interference fringes of the single wavelength laser diode. Thus, including the mini-spectrometers on the QT5062 PCB would allow for an exact calibration of the mirror separation for each HSTI acquired. The resulting mirror separation axis in this experiment is shown in Figure 4.11 (C) where the distance is actuated in the range 8.5-17.4 μm, and both the forward and backward scan is included.

The frequency resolution of the FFT is limited by the number of samples which in the case of the mini-spectrometers is low. Thus, the FFT peak position can be determined with an accuracy of ± 120 nm which is non-ideal for the mirror control algorithm and band wavelength determination.

A pathway to achieving a high resolution mirror control is to illuminate the FPI with light of two different wavelengths. Doing so makes up a beat plot due to the interference of the light waves inside the cavity. This beat plot can be constructed by hand picking different wavelengths using the Hamamatsu spectrometer. Figure 4.11 (F) shows the interference pattern arising from the multiplication of the signal measured in pixel number 105 and 145 with corresponding wavelengths of 681 nm and 828 nm. The resulting graph shows the beat plot with declining intensity due to the decreasing difference between the peak intensity minima and maxima. These results are promising and show that the incorporation of the mini-Hamamatsu spectrometers is a viable improvement of the mirror control and calibration.
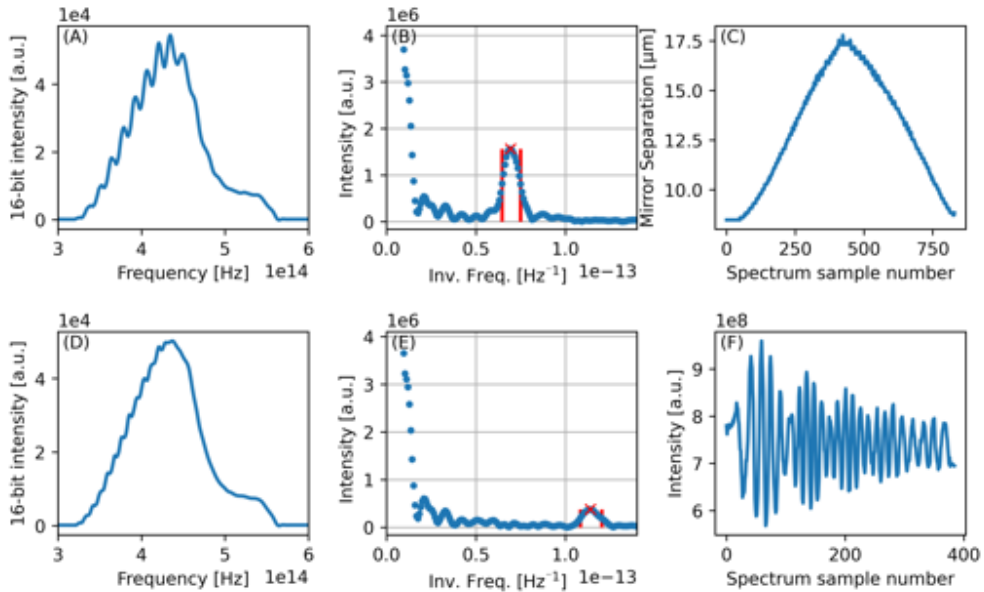
Figure 4.11: (A) shows the raw spectrum acquired using the Hamamatsu mini-spectrometer. (B) shows the result from an FFT analysis of the spectrum shown in (A). The red cross and the two red lines accompanying marks the full width at half maximum lines in the FFT analysis. (C) shows the resulting mirror seperation from logging the peak position found using the FFT analysis in (B). (D) (E) (F) The raw output of the spectrometer during an FPI scan forward and backwards where 1000 spectrometer measurements were grabbed simultaneously. The figure shows the direct product of the pixel readout of pixel 105 and 145 marked by broken lines in (A) and (B). The black and red line in (C) mark the data points belonging to the spectra shown in (A) and (B).

4.3 Summary and Conclusion

The experimental setup and working principle of the hyperspectral thermal camera has been described. The setup can be divided into four separate parts which are the FPI assembly, the collecting optics, the microbolometer sensor and the battery package. The development of the hyperspectral thermal camera has been a continuous process throughout the last three years and therefore HSTIs were acquired using several different combinations of the improvements presented above. For the final chapters of this thesis the main focus will be HSTI analysis and the state of the hyperspectral thermal camera can be divided into two major prototype categories.

The prototype categories are named 'HSTC V0.1' and 'HSTC V0.2' below, and their main characteristics are summarised. The 'HSTC V0.1' reflect the early version of the camera and 'HSTC V0.2' reflect the state of the camera at the time of writing.

Chapter 6
'HSTC V0.1':

- 8.2 µm range piezo elements

- Homegrown PVD mirrors

- ∼ 70 band image acquisition algorithm

- Visual check of mirror fringes and maximisation of FPI transmission following piezo offset sweeping

- Two point wavelength calibration

- 1.25x gain, and GFID = 2800

Initially hyperspectral thermal images were grabbed in a single thread, and every command was thus done serially. The sensor was uncooled, since the camera was placed in laboratory conditions where the temperature is highly controlled.

Chapter 7 & 8
'HSTC V0.2':

- 11.2 µm range piezo elements

- Mirrors produced by II-VI Incorporated

- ∼ 140 band image acquisition algorithm

- Near perfect mirror alignment measured optically and no piezo offset

- Multipoint wavelength calibration.

- 4.0x gain, and GFID = 2800

5

Methods for Data Analysis of Hyperspectral Thermal Images

In order to fully comprehend the conclusions and analyses of the coming section, the chapter is introduced with a description and detailed review of the methods used for data-analysis and preprocessing of the hyperspectral thermal images.

5.1 Imaging Data Preprocessing

In the following section a number of different techniques for data analysis will be presented, all of which are essential for the analysis of hyperspectral thermal images.

5.1.1 Non-Uniformity Correction

The bolometer sensor is produced by micro machining a silicon slab, which naturally induces a lot of production variations in each separate pixel, such as size, shape, and defect density. These effects alter the performance of each individual pixel, which again affects how the resistivity correlates with temperature. These effects create an FPA pattern, which affect the readout values of the individual pixels in the form of a constant offset as well as well as the correlation to incoming radiance. Thus, each pixel has a linear relationship with the incoming radiance, which must be calibrated for given that the goal is temperature prediction using a thermal imaging camera. Such calibration is most often named a non-uniformity correction (NUC), and can be carried out by imaging a uniform background at several different temperatures [71, 72, 73]. The offset and responsivity to radiance changes are then found for each individual pixel, and serves as a one time calibration of the entire sensor FPA. These values are found for each pixel by the relationship

$$\mathbf{\Lambda}_{x_i, y_j} = R_{x_i, y_j} \cdot B_{LWIR}(T) + O_{x_i, y_j} \quad , \tag{5.1}$$

with $\mathbf{\Lambda}_{x_i, y_j}$ following the notation introduced in section 1.8 and thereby denoting a single thermal image frame acquired without an FPI. B_{LWIR} thus again denote the spectral radiance measured by the sensor in the entire sensitivity range 8-14 µm. R_{x_i, y_j}, and O_{x_i, y_j} denote the responsivity and offset measured in the pixel at position x_i, y_j. The non-uniformity correction can be applied by

$$\mathbf{\Lambda}_{x_i, y_j} = a_{x_i, y_j} \cdot R_{x_i, y_j} + O_{x_i, y_j} + b_{x_i, y_j} \quad , \tag{5.2}$$

with a_{x_i, y_j} and b_{x_i, y_j} being correction parameters for the responsivity and offset in order to get a uniform image.

5.1.2 Spectral Preprocessing

Mean Centering

The spectra in the HSTI can be mean centered in order to do a simple clustering of the samples containing identical spectra. As the HSTI is mean centered it is modified by

$$\bar{\Lambda}_{x_i, y_j, *} = \Lambda_{x_i, y_j, *} - \frac{1}{\lambda} \sum_{k=0}^{\lambda} \Lambda_{x_i, y_j, \lambda_k} \qquad . \tag{5.3}$$

This preprocessing technique can be highly beneficial, since it completely removes the non-uniformity of the bolometer sensor. Thus, as we measure the spectrum of a given sample within the LWIR and calculate the spectral mean, we get a set of values that are only distinguished by the offset in the given pixel. As we subtract the mean the resulting datacube will contain clean images in most of the spectral bands. The datacube does, however, still suffer from the differences in responsivity in each individual pixel.

Standardisation

Another highly useful preprocessing technique is standardisation calculated by

$$\Lambda'_{x_i, y_j, *} = \left(\Lambda_{x_i, y_j, *} - \frac{1}{\lambda} \sum_{k=0}^{\lambda} \Lambda_{x_i, y_j, \lambda_k} \right) \frac{1}{\sigma(\Lambda_{x_i, y_j, *})} \qquad , \tag{5.4}$$

where

$$\sigma(\Lambda_{\mathbf{x_i, y_j}, *}) = \sqrt{\frac{1}{\lambda} \sum_{k=0}^{\lambda} \left(\Lambda_{x_i, y_j, \lambda_k} - \frac{1}{\lambda} \sum_{k=0}^{\lambda} \Lambda_{x_i, y_j, \lambda_k} \right)^2} \qquad . \tag{5.5}$$

While this method produces images free from the fixed pattern it also removes most of the intensity information in a HSTC. However, the shape of the underlying Planck distribution is kept. Unless stated otherwise, this method is used for the principal component analyses (PCA) carried out in this thesis. The PCA processing technique is explained below.

Normalisation

In some cases it is preferred to keep the intensity variation along the spectral axis, and here the spectra have been normalised by

$$\hat{\mathbf{\Lambda}}_{x_i,y_j,*} = \frac{\mathbf{\Lambda}_{x_i,y_j,*}}{\sum_{k=0}^{\lambda} \mathbf{\Lambda}_{x_i,y_j,\lambda_k}} \qquad . \tag{5.6}$$

Baselining

A special preprocessing technique is possible to perform when dealing with our hyperspectral thermal imaging system. The technique will be named baselining and it utilises the fact that at mirror separations lower than 3.8 µm the FPI acts as a perfect mirror for the 8-14 µm thermal radiation. With mirror separations below this distance the FPI will reflect all radiation emitted from the sensor itself. These images can then be used as a baseline. The baselining is carried out by subtracting the spectral band equal to zero from the spectra

$$\mathbf{\Lambda}_{x_i,y_j,*} = \mathbf{\Lambda}_{x_i,y_j,*} - \mathbf{\Lambda}_{x_i,y_j,\lambda_{k=0}} \qquad . \tag{5.7}$$

5.2   Imaging Data Processing

In the following section the methods used for the data processing of hyperspectral thermal images will be presented. Throughout this project the free to use sci-kit learn library has been used for the implementation of machine learning algorithms and data decomposition [74]. The methods have been implemented in a Python 3.7 environment. A selected number of methods has been used for this project, however, the entire module counts several other methods that may be applicable.

5.2.1   Principal Component Analysis

Principal Component Analysis (PCA) [75, 76] is a highly useful tool within the analysis of hyperspectral imaging data. Hyperspectral imaging data structures are multivariate by nature, and often the important spectral components do not fill the entire spectral axis and are strongly correlated. This results in datacubes that contain much more information than necessary to explain the important features within the datacube. The PCA is a multivariate statistical tool which enable data reduction

and serves the purpose of simplifying the original data structure by transforming it into a new structure. This new data structure consists of principal components which are representation of the directions of most variance within the original data structure. Thus, a PCA first identifies the hyperplane of highest variance in the data, and then project the datapoint onto this plane. The second component describes the hyperplane orthogonal to the first, which has the highest remaining variance. A data reduction can then be carried out by selecting the number of planes required to describe the data sufficiently, and ignoring the rest. Typically a dataset is noise and information abundant, and in these cases a PCA is capable of selecting the relevant and noise-less data from the rest of the dataset which can be highly useful for the analysis of hyperspectral data. Additionally, the PCA is used for finding variance in datasets that are too complex for human interpretation. In our case the PCA is used to find the emissivity and radiance differences in individual spectra that are hard to find manually. Presuming that we measure pure emission spectra of two objects with differing emissivities but equal temperature, the principal components following a PCA of these two spectra would at some point describe the measured variance in emissivity. In the case of the HSTC the individual datapoints are highly correlated to system specific variances, such as the bandwidth of the FPI. As we shall see, it is therefore not guaranteed that the emissivity variance lies in the first component. A two dimensional dataset of mixed variance in the 1st and 2nd variables have been shown in Figure 5.1 (A). A PCA have been performed and the transformed data is plotted in Figure 5.1 (B) with the two resulting principal components on each axis. In Figure 5.1 (B) the dataset has been flattened along the directions of highest variance, of which PC1 contain most of the total variance. Thus, a PCA is highly relevant for the HSTC as well since the data acquired is influenced by a multitude of effects, such as reflected, transmitted and absorbed light, temperature variance and emissivity variance.

The mathematical starting point of the PCA is an NxM data matrix denoted **X** with N measurements of a multivariate sample of M variables. In our case the hyperspectral thermal three dimensional datacube measures the multivariate thermal spectrum consisting of λ bands and each datacube contains a number of measurements equal to the set of pixels in the focal plane array (FPA) which is $x \cdot y = 786.432$ measurements. Formally, the PCA requires a standardised datacube where the mean subtraction removes the offset correction and the division of the standard deviation eliminates intensity variations for each pixel. This procedure leaves spectral variance for the PCA to find. The principal components found by solving the equation system
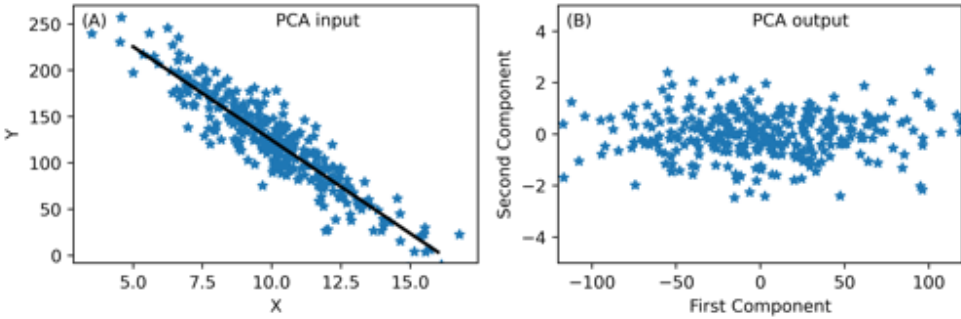
Figure 5.1: (A) Two dimensional dataset described by the cartesian coordinates x and y. The solid black line indicates the plane closest to all datapoints, which in the two-dimensional case is a linear fit. (B) A PCA have been made of the data presented in (A) and is here plotted as the first two principal components.

$$\mathbf{\Lambda}'_{x \times y, \lambda} = \mathbf{T}\mathbf{P}^\mathbf{T} + \mathbf{E} \qquad , \tag{5.8}$$

where P is the $\lambda \times K$ loading matrix and T is the $(x \cdot y)) \times K$ score matrix. K lies in the range from 1 to λ and determines the number of principal components. Thus, the number of principal components can be chosen freely, and K would have to equal λ in order to explain all the variance in the original datacube. The reader is referred to the original work of Wold et al. for a full description of the mathematical decomposition. In the following sections PCA is used as a tool for the initial analysis of hyperspectral thermal images, in order to locate variance within a datacube. In some cases the PCA is used in combination with a K-means analysis, which is the subject of the following section, in order to locate the regions within an image frame where the distance to the hyperplane of highest variance in each principal component is the same. These regions are then assumed to have equal spectral features.

5.2.2 K-means Analysis

The K-means algorithm is one of the most simple machine learning algorithms, which can be extremely powerful in combination with the PCA clustering. The aim of k-means clustering is to partition the dataset into a predefined number of clusters. Each of these clusters are calculated by minimising the distance between each datapoint

and the center of the cluster. In this regard it is immediately clear why the k-means algorithm and PCA are powerful, since the PCA creates clusters, while the K-means algorithm searches for and find the individual datapoints within these clusters. The k-means algorithm will then calculate

$$\sum_{i=0}^{n} \arg\min_{\mu_j \in C}(||x_i - \mu_j||^2) \qquad , \tag{5.9}$$

and the minimisation of such problem can be carried out through various algorithms. The important fact to remember is that given a set of individual data points x_i of n points the k-means algorithm will place the centroid, μ_j, of the cluster C in the point that minimises equation 5.9. Equation 5.9 then returns the sum of all distances between the centroid and the individual data points. The number of clusters chosen for a given dataset may vary, and typically the algorithm is iterated over a range of total amount of clusters. The total sum of squared errors (SSE) can then be plotted as a function of the number of clusters, which typically will drop rapidly due to the square in equation 5.9. Having individual collections of data points separated in groups will result in an 'elbow' in this plot, which may be used to reveal the optimal amount of cluster centroids. These plots will be presented during the analysis of HSTIs as the SSE plotted as a function of the number of clusters.

5.2.3 Multinomial Logistic Regression

The post-processing techniques presented until now has been examples of unsupervised models which may be used to analyse and process data without previous fitting or training. During this project a Multinomial Logistic Regression (MLR) has been used to sort new and unknown data into a specified set of classes. These classes are created during the model creation phase and therefore, the logistic regression classifier is a supervised learning model. The purpose of using the MLR model was to verify that spectral differences in the thermal range could be measured and recognised on an individual pixel level based on the pre-processed data obtained from the HSTC. The MLR model works by calculating the probability that an instance of input data belongs to one of the pre-specified classes. Given two possible classes the Logistic Regression model will calculate the probability of the input data belonging to either one of the two. The class having the highest probability, which in this case is $> 50\%$, is chosen by the model and the output is converted to a binary result. Thus, the positive class is labelled "1" and the negative class is labelled "0". The logistic regression

model calculates a weighted sum and outputs the logistic of this result, based on the equation,

$$\hat{p} = h_\theta(\mathbf{\Lambda}_{x_i,y_j,*}) = \sigma(\text{`}^T \cdot \mathbf{\Lambda}_{x_i,y_j,*}) \qquad , \tag{5.10}$$

where $\hat{p}$ is the probability that the input spectrum $\mathbf{\Lambda}_{x_i,y_j,*}$ belongs to the class supervised class h_θ. The probability is calculated based by the $\sigma(t)$ function which takes the measured spectrum as input weighted by θ^T. The $\sigma(t)$ function is defined as

$$\sigma(t) = \frac{1}{1 + exp(-t)} \qquad . \tag{5.11}$$

Having calculated the probability of the input features belonging to the the class h_θ, the result can be binary formulated as

$$\hat{y} = \begin{cases} 0, & \text{if } \hat{p} < 0.5, \\ 1, & \text{if } \hat{p} \geq 0.5. \end{cases} \qquad , \tag{5.12}$$

where the input spectrum is assigned to the class h_θ given that the probability is higher than 0.5. As mentioned the logistic regression model can be expanded to support multiple classes directly and in the following sections the MLR model is trained based on a set of known classes fitted from previously measured spectra. The fitted model is subsequently used to predict the probability of an unknown spectrum belonging to each class. Additional information on the MLR model, and a wide variety of other classification models can be found in Abraham et al..

5.2.4 Partial Least Squares Regression

The partial least squares regression (PLS) was invented in 1975 by Herman Wold, and is further development of the multiple linear regression where a number of properties or output values $\mathbf{Y}$ is described by a number of input variables $\mathbf{X}$. The multiple linear regression method is typically used for systems of few uncorrelated variables, whereas the PLS model is capable of predicting the $\mathbf{Y}$ properties based on a large amount of mutually correlated variables. In the case of the HSTC the input variables are hyperspectral datacubes and thus represented by $\mathbf{\Lambda}_{x \times y, \lambda}$ and the

predicted output values $\mathbf{Y}$ is dimensioned by $(x \times y) \times M$ where M can have any value. In this project the output values becomes univariate since the PLS models will be used to predict the temperature of a given input spectrum. In principle, a PLS model can be trained consisting of $M = T_{object} + \epsilon_\lambda$ values, in order to predict the temperature and emissivity from a given input spectrum. Experiments involving such models was not carried out in this project. The PLS model bears resemblances with the PCA, however the PLS searches for the covariance for the planes of maximum covariance between the input block, $\mathbf{\Lambda}_{x \times y, \lambda}$, and the output block, $\mathbf{Y}$, through the relations

$$\mathbf{\Lambda}'_{x \times y, \lambda} = \mathbf{T}\mathbf{P}^{\mathbf{T}} + \mathbf{E}$$
$$\mathbf{Y}_{x_i \times y_j, *} = \mathbf{U}\mathbf{Q}^{\mathbf{T}} + \mathbf{F} \qquad , \tag{5.13}$$

with $(\mathbf{T}, \mathbf{P})$ and $((\mathbf{U}, \mathbf{Q}))$ are the scores and loadings for the input and output, respectively. During PLS fitting the number of components used for the scores and loadings matrices alter the prediction error of the fitted model, and an optimum is typically found between under fitting, where relevant data of the $\mathbf{\Lambda}_{x \times y, \lambda}$ is left out of the equation, and over fitting where irrelevant noise disturbs the prediction accuracy. During model training the PLS model will be fitted perfectly by including all components in the decomposition, and therefore the optimum number of components is either chosen arbitrarily or by testing multiple PLS models of different number of components on a dataset kept for evaluating the model performance. The underlying mathematics of the PLS regression can be found in the original reports, and later reviews describing the applications for chemical and physical systems [78, 79].

5.3 Summary and Conclusion

This chapter has provided a summary of the post processing techniques used for the analysis of hyperspectral thermal imaging data in this project. Several pre-processing techniques have been described as well, where each pre-processing technique have different effects on the acquired spectra. These effects have a high relevance for the analysis of hyperspectral data, since they lay the basis for the choice of post-processing and most of the derived conclusions in each experiment.

6

Hyperspectral Thermal Imaging Using Homemade Mirrors

In the following chapter a selected number of hyperspectral thermal images will be presented to the reader. The images presented are among the earliest captures using the HSTC and therefore lay the basis for understanding the progress made during the three years of this PhD-project, as well as showing a variety of the use-cases within the field of hyperspectral thermal imaging.

6.1 Hyperspectral Thermal Imaging at Room Temperature

The following section presents an experiment with a goal of performing hyperspectral thermal imaging at room temperature in mind. While image acquisition at room temperature was not an official success criterion at the start of this project it changed into an important milestone if the camera is to be used outside of the laboratory. The application of a microbolometer chip in a mobile hyperspectral thermal imaging system has been demonstrated to be feasible in the studies of SO_2 plumes from active volcanos based on a Sagnac interferometer [80, 81]. Thus, the goal of room temperature imaging should be within reach using the microbolometer chip and the following sections present a short analysis based on the earliest attempts on room temperature imaging using homemade mirrors for the FPI.

6.1.1 Experimental Methods

An aluminium block measuring $160\,mm \times 160\,mm$ was covered in several strips of polyimide tape (PI) to increase the emissivity of the surface. PI is widely known to have a high emissivity and good temperature resistance, which will be relevant later. The increased emissivity of the aluminium block was expected to improve the signal-to-noise ratio in this experiment. Five samples were used in total consisting of a circular borosilicate glass petri dish, a 10 mm thick square piece of plywood, a Vantablack[82] sample, a bare section of the aluminium block surface, and the PI region of the aluminium block. The Vantablack sample is dimensioned 40x40x3 mm and is used as a black body reference. This sample was produced by Surrey Nanosystems and consists of an aluminium plate onto which a covering layer of carbon nanotubes is grown.

At this point in time the hyperspectral thermal camera corresponded to version 'V0.1' as introduced, and thus it was equipped with a the high loss homegrown FPI mirror set. The transmission and reflection profile of both thermal mirrors are shown in Figure 3.2 (A) and (B). The piezo elements used during these experiments were capable of expanding $\sim 8.0\,\mu m$, covering the first order transmission and approximately half of the second order transmission, as can be seen in Figure 3.12. A single hyperspectral thermal image (HSTI) containing 70 spectral bands was acquired and the raw data was standardised in order to perform a PCA of the entire cube and thus

$$\Lambda_{1024,768,70} \xrightarrow{\text{Preprocessing}} \Lambda'_{1024,768,70} \quad .$$

The HSTI was acquired using a sensor gain of 1.25x and a GFID voltage of $2800\,mV$. The wavelength axis of the HSTI was calculated by scanning the FPI and determining

the two points with maximum intensity transmitted through the FPI with a 10 µm bandpass filter in front. These two points correspond to the first and second order transmission of light with the bandpass filter wavelength. The correlation between these points and the interference fringes measured from the photodiodes were used to calculate the wavelength of each individual band in the HSTI. This method was later revised, which is elaborated in Chapter 7.

6.1.2   Results and Discussion

Having the FPI directly in the optical path of the collecting optics attenuates the total transmission within the range 8-14 µm by $\sim 95\%$. The attenuation was measured by numerical integration of the FTIR measurement of the transmitted peak shown in Figure A.4 (A). Measuring the radiance from objects at RT leaves a very small amount of light to be detected by the microbolometer. Thus, in order to separate the signal from the noise a PCA was carried out of the datacube.

The results of a PCA of the HSTI is shown in Figure 6.1. These figures show the ordered reconstructed images from the principal component analysis. As explained, the PCA finds the hyperplanes in a multidimensional dataset with the highest variance, and transforms the data into the orthogonal planes of highest variance. The resulting images are thus representations of the features in the HSTI with highest variance ordered from highest to lowest. PC1 in Figure 6.1 (A) shows an image dominated by the a radial intensity gradient. This intensity gradient is a result of the spectral bending and will be visible in most images presented to the reader. The radial gradient is observed in PC2 as well but hardly visible in PC3 in Figure 6.1 (C). The experimental setup is hardly visible in any of the PCs in Figure 6.1, and Figure 6.1 (D) shows PC4 where no features is seen. This PC is representable for the higher order PCs in the 70 component analysis. The sample positions had been found prior to this experiment, and selected regions of each are marked by 100x100 pixel bounding boxes in Figure 6.1 (A). The abbreviations BG, AL, VB, PI and W are short for borosilicate glass, aluminium, Vantablack, polyimide tape and wood. Figure 6.1 (F) shows two kinds of spectra of the standardised HSTI for each sample. The solid line represent a single pixel spectrum, and the dashed line represent the mean spectrum of the 100x100 pixels within the bounding box

$$\textbf{100px box:}\quad \frac{1}{100^2} \sum_{x_i,y_j}^{+100} \bar{\mathbf{\Lambda}}_{\mathbf{x_i},\mathbf{y_j},*} \quad .$$

The spectra are noise dominated and the mean spectra within the bounding boxes show no apparent spectral differences between the samples. This conclusion is backed
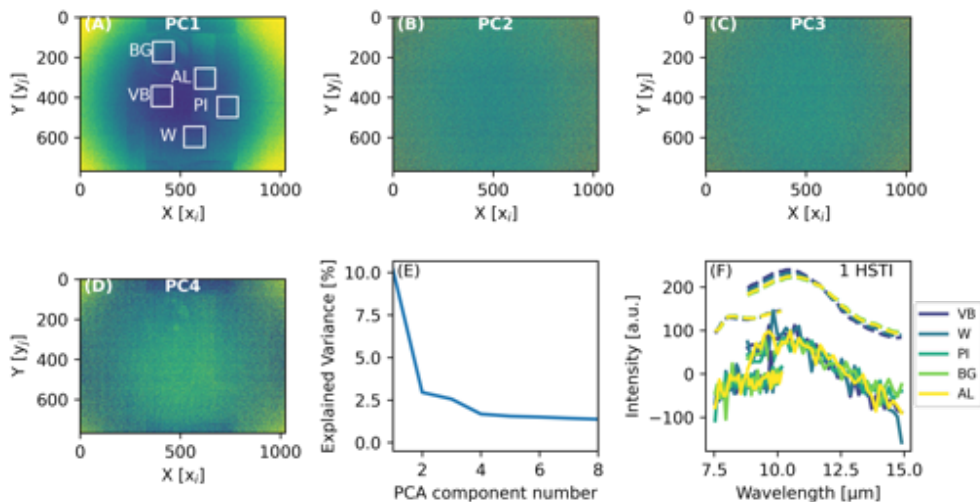
Figure 6.1: (A)-(D) reconstructed images of the PCA components 1-4 following a 70 component analysis. (E) The normalised explained variance of each individual principal component. (F) Measured spectra of the samples marked in (A). The dashed lines represent individual pixel spectra and the solid lines represent meaned spectra within the bounding boxes in (A) calculated by $\frac{1}{100^2} \sum_{x_i,y_j}^{+100} \bar{\Lambda}_{\mathbf{x_i,y_j},*}$

by the PCA not highlighting sample features in any PCs. Figure 6.1 (E) show the normalised explained variance of the PCs and here it is seen that PC1 only contribute to $\sim 10\,\%$ of the measured variance in the original HSTI. This too backs the conclusion that mostly noise is measured, since a common hyperplane for random noise is hard to find in a multidimensional space. Note that an overall shape of the measured spectra is observed, indicating higher intensity centered around a wavelength equal to $10.5\,\mu\text{m}$. At this wavelength, the homemade mirrors had the lowest reflectivity and a relatively low loss, leading to low attenuation and thus a higher intensity measured by the bolometer. To summarise, this datacube was noise dominated and an attempt to solve this problem was carried out. A common circumvention of low signal to noise is to summarize several datapoints and exploit that white noise is random in contrast to the measured signal. Summming several datapoints therefore increase the contribution of the signal compared to the noise and the signal may then be more easily extracted by a PCA. This is possible with our hyperspectral camera as well, and therefore a data series was acquired consisting of 50 images of the same sample scene. One issue arises in the summation of HSTI from the fact that the number of bands in

the HSTI datacube differs due to the alignment procedure during imaging. Thus a summed datacube can only be constructed with a size equaling the smallest. In this experiment the resulting datacube has 69 spectral bands

$$\mathbf{\Lambda}_{1024,768,\lambda} \xrightarrow{\text{50xHSTI sum}} \mathbf{\Lambda}'_{1024,768,69} \qquad .$$

Figure 6.2 shows the eight first principal components of the summed datacube from the 50 individual HSTI acquired at room temperature. While the two first principal components PC1 and PC2 shown in (A) and (B) in Figure 6.2, both are dominated by the spectral bending mentioned earlier, PC3 shown in (C) in Figure 6.2 reveals a more clear image than PC3 in Figure 6.1 (C). The contours of the samples are slightly visible which is most clearly seen by the circular BG sample and the apparent variance difference between the low emissivity strip of AL and high emissivity strip of PI. The remaining principal components are once again dominated by noise, however, the graph of normalised explained variance shown in 6.2 (E) tells that much more variance is contained in the first principal component compared to Figure 6.1. Additionally, the spectra shown in 6.2 (F) reveals that the summation of datacubes is a viable option for decreasing the single pixel spectrum noise.

Based on these measurements it was concluded that the most dominating noise contributor in the HSTIs is the spectral bending, since it was located in the first two principal components for both RT experiments. The spectral intensities related to the samples comes second to this effect, and it is concluded that the signal-to-noise ratio at RT for the homegrown was too low for additional quantitative analysis. It was then decided to increase the signal-to-noise ratio by other means. Here, the most obvious experiment was to increase the temperature in order to increase the radiance from the samples.

6.2 Separation of materials using logistic regression at 100 °C

The remaining part of this chapter is dedicated to an experiment carried out where the signal signal-to-noise ratio was increased by imaging heated objects. The images and analysis is presented in the paper *Acquisition and Analysis of Hyperspectral Thermal Images for Sample Segregation* published in the journal Applied Spectroscopy. A summary of the findings is added below including most of the results and analysis section. The section has been edited to fit with the notation used in this thesis. The entire article in its published version has been included in Appendix C.1.
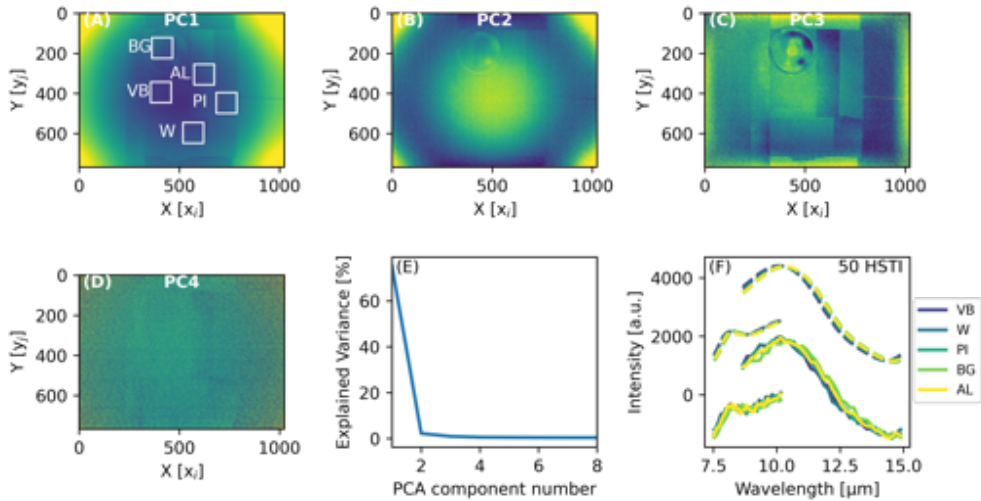
Figure 6.2: (A)-(D) reconstructed images of the PCA components 1-4 following a 69 component analysis. The PCA was carried out on a summed over 50 individual HSTI. (E) The normalised explained variance of each individual principal component. (F) Measured spectra of the samples marked in (A). The dashed lines represent individual pixel spectra and the solid lines represent meaned spectra within the bounding boxes in (A) calculated by $\frac{1}{100^2} \sum_{x_i,y_j}^{+100} \bar{\Lambda}_{\mathbf{x_i},\mathbf{y_j},*}$

6.2.1 Experimental Methods

The imaged object consisted of an aluminium block of 5 cm thickness and 16 cm height x 16 cm width onto which various samples were attached. The surface was covered with several strips of standard 25 μm thick PI in order to increase the emissivity. The aluminium block was heated to 103 °C by a constant current heatplate placed a short distance behind the block itself. After a waiting period of several hours, the temperature of the entire block stabilised to a precision of < 0.1 °C checked by a digital thermometer measuring inside a hole drilled into the aluminium block. Heating the block ensures sufficient thermal radiance from the samples in each band of the HSTI. Additionally, the waiting period ensures that all samples remain at a constant temperature throughout image grabbing, even though the surface temperature of the individual samples might vary. Three samples were attached to the front side of the PI using silicone heatpaste in order to get a high thermal conductance as well as good attachment. Each corner of the Vantablack sample is free from carbon nanotubes, and therefore consists of bare aluminium as can be seen in Figure 6.3 (B). A 64x54x1
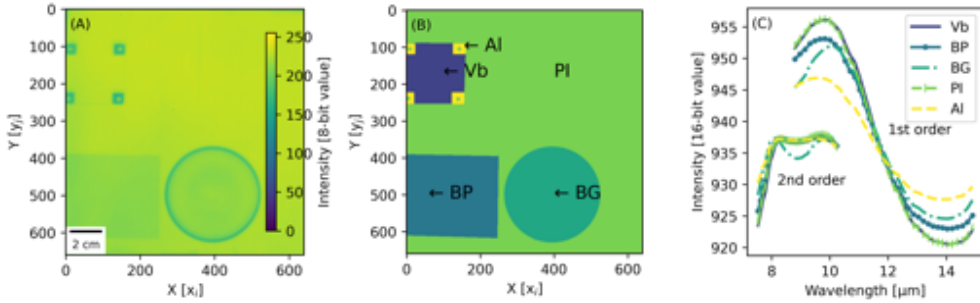
Figure 6.3: (A) A raw standard thermal image of the imaged scene with no FPI in front of the camera lens. (B) A masked image of the materials present in the image. The background consists of a aluminum plate where the surface is covered by PI. (C) The mean spectrum observed from each individual material in the image [2].

mm aluminium plate painted with regular black paint and a Ø 60 mm petri dish made from borosilicate glass were also attached to the polyimide tape as shown in Figure 6.3. The aluminium block with the samples was placed at a distance of 45 cm from the front of the camera. The short distance to the heated aluminium block has a small effect on the temperature of the bolometer chip itself; when the scene is changed, a new equilibrium temperature is reached within seconds and therefore had no influence on the measurement.

The HSTI contains 70 spectral bands within the wavelength interval covering the bolometer sensitivity as can be seen in Figure 6.3 (C). The spectrum in each pixel was normalised to a sum of 2^{16} in order to eliminate the most extreme intensity variations caused by temperature differences leaving mostly spectral differences and thus

$$\mathbf{\Lambda}_{1024,768,*} \xrightarrow{\text{Preprocessing}} 2^{16}\hat{\mathbf{\Lambda}}_{1024,768,*} \qquad . \qquad (6.1)$$

The FPI is continuously scanned from a physical separation of 4 μm to 7.5 μm, so the first order transmission of the filter is shifted from 8 μm to 15 μm, which corresponds to the spectra indicated with "1st order" in Figure 6.3 (C). As the FPIs mirrors are scanned beyond 7.5 μm, the first order transmission moves out of the sensitivity range of the bolometer sensor, however, the second order transmission starts moving into the sensitivity range. Further scanning of the mirrors up to 10 μm separation distance was then used to acquire the spectrum in the wavelength range from 7.5 μm up to 10

µm as indicated by "2nd order" in Figure 6.3 (C).

A NUC is calculated for each pixel in order to eliminate these sensor artefacts. In our calibration, an aluminium block covered with PI functions as the graybody. The calibration was performed by letting the aluminium block fill the image plane whereafter 23 images were sequentially captured at temperatures ranging from 19.3 °C to 95.6 °C. These images are used to find the correction parameters for the sensitivity and offset for each pixel as explained in Section 5.1.1. The correction parameters were subsequently used on all raw images from the hyperspectral datacube.

The specific HSTI analysed in this study was originally 1024x768 pixels with 70 spectral bands. In order to simplify the analysis, the background located outside of the aluminium block is cropped out of the image plane leaving a HSTI of 660 x 640 pixels with 70 spectral bands and thus

$$\mathbf{\Lambda}_{1024,768,70} \xrightarrow{\text{Spatial Crop}} \mathbf{\Lambda}_{660,640,70} \qquad .$$

6.2.2 Results and Discussion

A standard thermal image, shown in Figure 6.3 (A), was taken alongside the HSTI in order to compare the two methods. Comparison of the thermal image presented in Figure 6.3 (A) and the sketch of where the samples are positioned in Figure 6.3 (B) shows that the contours of the different samples are relatively easily distinguished. The least noticeable difference lies between the Vantablack surface and the PI background. Table 6.1 presents the mean and standard deviation of the intensity values of all five samples. It can be observed that Vantablack and PI are indistinguishable having essentially the same mean and standard deviations. Black paint and glass show the same behaviour with almost equal mean intensities but slightly different standard deviation. However, both have intensities within a standard deviation of the other, making them indistinguishable by standard thermography. With our hyperspectral thermal imaging system, however, we are capable of distinguishing between the samples, which initially can be seen by observing Figure 6.3 (C). From the figure it is immediately seen that the glass sample has a significant dip in 2nd order emission intensity around 9 µm, which is attributed to the Si-O-Si bond[83]. The remaining samples have more similar spectra and therefore statistical regression models were used to distinguish between these.

A PCA of the hyperspectral datacube revealed the six principal components (PCs) with the highest variance, shown in Figure 6.4. Figure 6.4 (G) shows the relative variance

Sample Material	Mean Intensity	σ
Vantablack	227.3	5.5
Polyimide Tape	227.7	5.6
Black Paint	210.4	2.5
Borosilicate Glass	208.2	9.6
Aluminum	186.2	13.7

Table 6.1: Mean grayscale intensities and standard deviations, σ, for each individual sample based on the thermal image presented in Figure 6.3

explained by each of the six principal components. The first three components (see Figure 6.4 (A)-(C)) explain 91.4 % of the total variance. Each successive component contains less than 0.3 % of the total variance. The distribution of the variance in the remaining components is seen in Figure 6.4 (H). Based on the data in Figure 6.4 (G)-(H) it can be concluded that the variance continues to gradually descent at components below 8.

PC1 and PC3 clearly distinguish the borosilicate petri dish from the rest of the image. It can be noted that the edge of the petri dish has a different intensity from the rest of the dish. This is due to the fact that the edge walls of the petri dish protrude from the surface of the heated aluminium block giving a noticeable temperature difference relative to the remaining part of the glass. The clear radial gradient across the image in Figure 6.4 (B) suggests that this component contains information related to temperature variations across the aluminium block or the spectral bending. This leaves PC1 and PC3 through PC6 with the information related to material characteristics. PC3 and PC5 contains a noticeable dark line between the Vantablack and the black paint marked by red bounding boxes. This is a region on the heated aluminium block where the PI is overlapping and thus two layers are present. This region is not visible on the pure thermal image shown in Figure 6.3 (A), which again underlines the fact that the PCA of the hyperspectral datacube is capable of distinguishing between the aluminium/PI region and the PI/PI region. This may be described by the transparency of the 25 µm PI at selected wavelengths within the HSTI. A reference FTIR measurement of a single layer of PI is shown in Figure A.7 revealing transmission regions located at wavelengths of 10-11 µm and 13-14 µm.

The ability to distinguish the samples from the hyperspectral images was tested using the Multinomial Logistic Regression model. The model was given five classes, which corresponds to one class per material present in the image. Initially the full hyperspectral datacube was used as input features to fit a prediction model. The fitted model was given a balanced weight of the classes, which ensures that the cost function
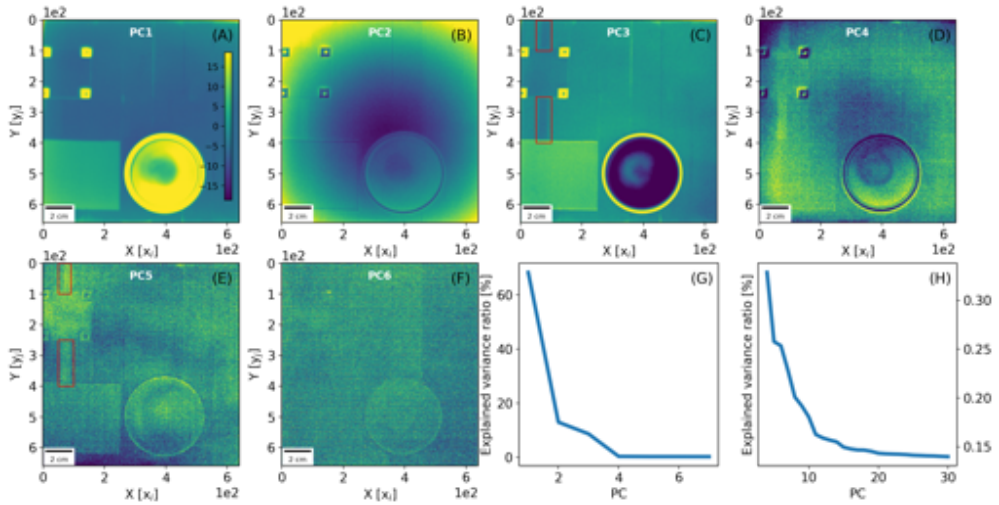
Figure 6.4: The figure shows six reconstructed images from the six first principal components following a principal component analysis of the hyperspectral image stack shown in Figure 6.3. Additionally inset G and H shows the relative explained ratio for the principal components following the PCA. Figure G shows the relative variance for the initial seven principal components and Figure H shows the relative variance for the last 26 principal components [2].

is equally biased for all classes. Additionally, the Liblinear[84] solver was used to find the global minimum of the cost function. A slightly less accurate model can be fitted where the first five principal components are used as input features, which increases the speed of the process. This again underlines the promising applicability of the technique since accuracy might be sacrificed for speed in a handheld camera.

Since computation time was no issue in this case, the results obtained from the full hyperspectral datacube are presented. The model was fitted to a selected region of the hyperspectral image shown in Figure 6.5 (A). Hereafter the full hyperspectral datacube was fed to the model to predict and find the samples present in the image. The results from this prediction are shown in Figure 6.5 (B) and the performance of the model is summarised in the confusion matrix shown in Figure 6.5 (C). The confusion matrix presented in Figure 6.5 (C) has been normalised for each row, and thus the main diagonal shows the true positive rate (TPR) for each sample, which is the ratio of true positives to the sum of true positives and false negatives. During this analysis, focus is put on the TPR since this makes the most sense for our application. The
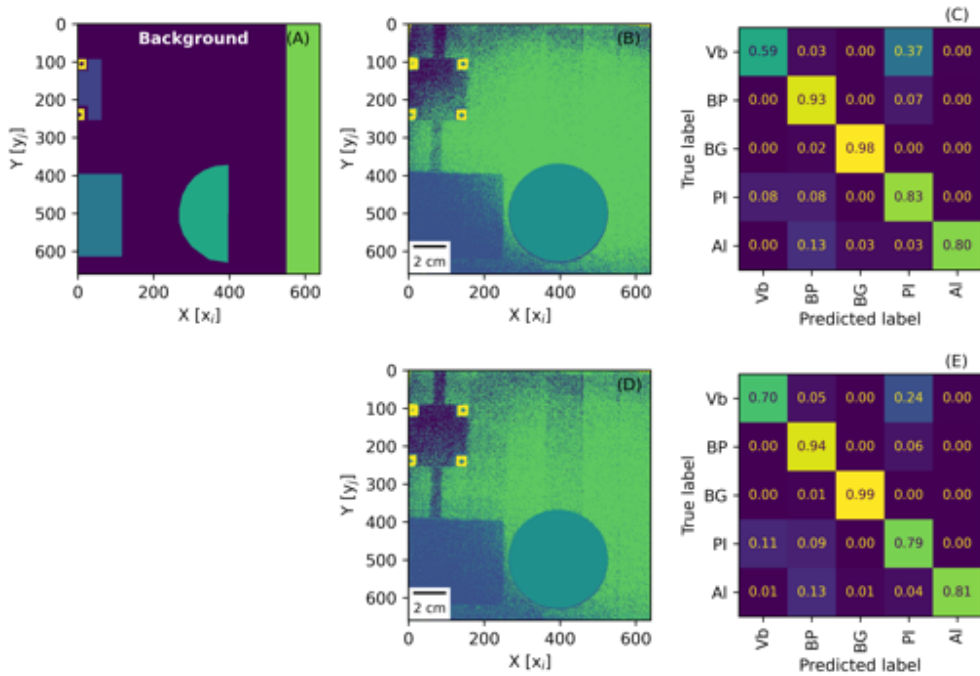
Figure 6.5: Figure A shows the mask used to fit the Logistic regression model. The dark blue region marked "Background" is unused and therefore left out of the fit. Figure B shows the results following a prediction of the materials using the fitted model and the full hyperspectral image stack. Figure C shows the confusion matrix of the predictions versus the true pixel values determined by image B in Figure 6.3. Figure D shows the results following a prediction of the materials using 69 principal components. Figure E shows the confusion matrix of these predictions versus the true pixel values determined by image B in Figure 6.3. For both confusion matrices the abbreviations; Vb, BP, BG, KT, and Al have been used for Vantablack, black paint, borosilicate glass, PI, and aluminium respectively [2].

highest TPR is obtained for borosilicate glass with a value of 98 %. This is followed by black painted aluminium with a TPR of 92 %, PI with 83 %, bare aluminium with 75 % and Vantablack with 59 %. It is important to note the fact that five classes are defined. Therefore, a completely random guess would on average result in a 20 % TPR of each class no matter its relative occupation of the image. Within the area covered by PI (see Figure 6.3 (B)), the prediction of PI in Figure 6.5 (B) shows a slight gradient from the corners to the center region of the image, with the most correctly predicted pixels concentrated in the center. Similarly, part of the Vantablack sample is mistakenly predicted to be PI where most errors appear near the center of the image. This pattern is very similar to the one observed in PC2 shown in Figure 6.4 (B), which was ascribed to the spectral bending. Therefore, in an attempt to improve the prediction, another model was fitted using 69 out of 70 available principal components with PC2 excluded. Excluding the principal component which primarily contain the spectral bending contributions is an attempt to flatten out the bending datacube, and thus performing the transformation between the cubes shown in Figure 4.6 (A) and (B). The performance of the resulting model is shown in Figure 6.5 (D) and (E) showing the predicted pixels and the summarising confusion matrix, respectively. As can be seen in the confusion matrix in Figure 6.5 (E) this model performs slightly better than the previous one having all samples predicted with a TPR of at least 70 %. More importantly the gradient observed in Figure 6.5 (B) is much less pronounced underlining the fact that true material characteristics are present in the spectra. Furthermore, it should be noted that the overlapping PI 'line' is much more apparent in Figure 6.5 (D) than (B) underlining that even slight spectral features is measured and can be distinguished from an image. The most surprising result is the capability of distinguishing between Vantablack and PI which, as seen in Figure 6.3 (C), have very similar spectra. Figure 6.6 (A) and (B) show the 2nd and 1st order mean spectra of each individual sample, respectively. The raw mean spectra of each sample have been ratioed against the PI spectrum, which exhibits the highest intensity across the entire measurement range, and thus the following calculation is performed:

$$\textbf{Relative sample spectrum:} \ \frac{\hat{\mathbf{\Lambda}}_{\mathbf{x_i=PI,y_j=PI,*}}}{\hat{\mathbf{\Lambda}}_{x_i=PI,y_j=PI,*}} \ .$$

It is immediately noticed that small variations are measured between the two samples. These variations most likely originate from the PI, since the Vantablack sample is expected to perform essentially as a blackbody source of radiation. Another important
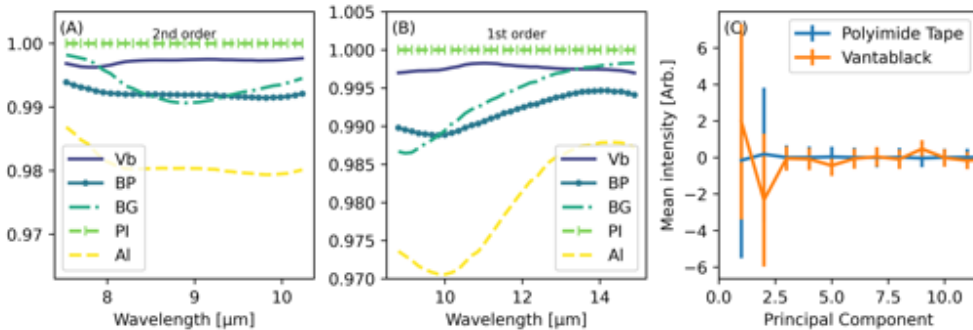
Figure 6.6: (A) The 2nd order spectrum of each sample ratioed against the mean PI spectrum. (B) The 1st order spectrum of each sample ratioed against the PI spectrum. (C) The mean value of the principal components for PI and Vantablack plotted for components 1-11. The standard deviation is used as error bars [2].

feature is the fact that the differences can be measured in each individual pixel. A visualisation of this is shown in Figure 6.6 (C) where the mean principal component value of components 1-11 is plotted. The standard deviation of each component is plotted as error bars for the related sample. As can be seen the components 1,2,5, and 9 show variations between the two samples where the standard deviations of the two samples overlap to a less extent than the remaining principal components. It is believed that these principal components are the main contributors to the 70 % correctly predicted Vantablack pixels.

The reproducibility and validity of the sample segregation and recognition was checked by acquiring three separate HSTI of the same scene followed by an analysis similar to that in the main manuscript. Each hyperspectral data cube consists of 70 images acquired at wavelengths covering the sensor sensitivity range from 8.0-14.0 μm. However, since the FPI moves dynamically, the images are not grabbed at the exact same image wavelengths as mentioned in the previous section. The difference in band wavelength is generally low, however, it becomes significant in some cases. Figure 6.7 (A)-(C) show 3 sequential measurements of the mean spectrum of each sample present in the related image. All sample positions are identical and the HSTIs were grabbed subsequently following each other. It is seen that small deviations occur for some of the samples. This is particularly noticeable in the short wavelength region which might be explained by small differences in the FPI mirror alignment.

The Logistic Regression model was fitted using 69 principal components of a 70

component PCA performed on the original images. In all cases the second component was sorted out and ascribed to spectral bending which is nonuniform on the image plane. The model was fitted to selected representable regions of all samples from all three images. This model was then used to predict all pixels based on the 69 remaining components. The results from this prediction is shown in Figure 6.7 (D)-(F). Figure 6.7 (G)-(I) show the confusion matrices of the predictions made in Figure 6.7 (D)-(F). It can be noticed that the TPR of Vantablack pixels is reduced from 0.7 obtained by fitting the prediction model on the same image as the prediction test, where the TPR across three HSTIs lies at 0.3. The lower TPR can be ascribed to the difference in wavelength for the individual bands which the prediction model is unable to take into account. The effects related to the instability of the image acquisition thus dominates the spectral differences observed between Vantablack and PI in a single image.
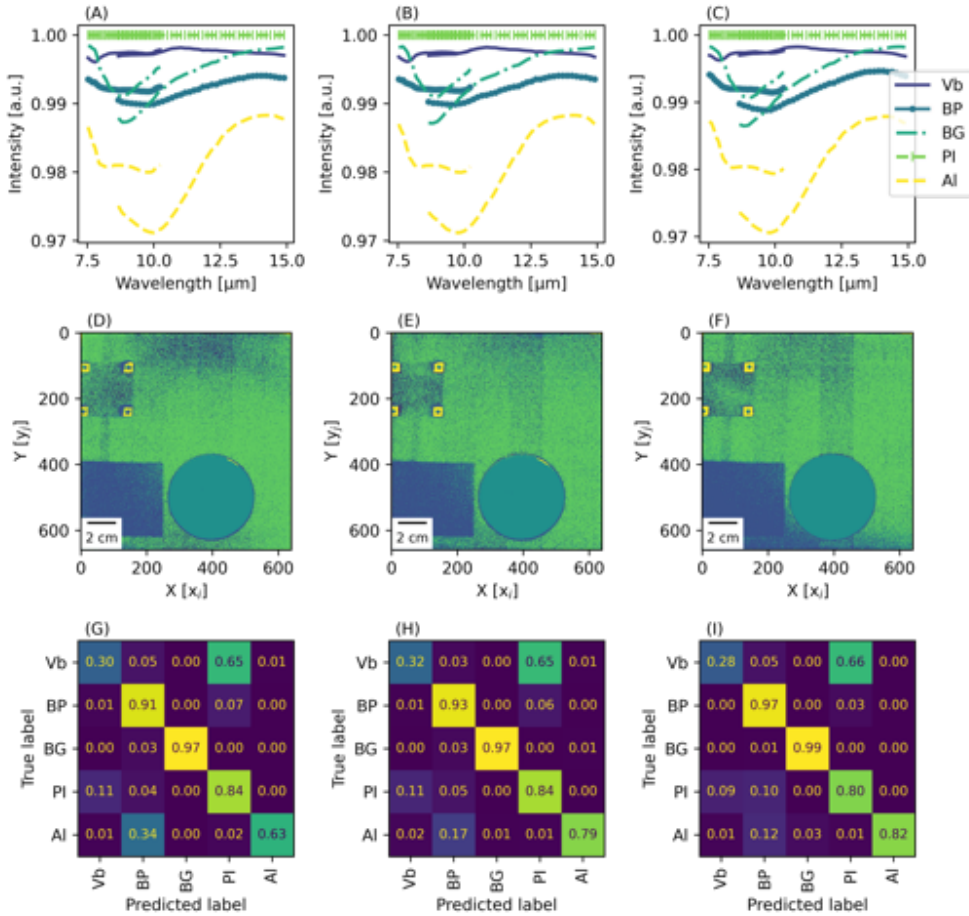
Figure 6.7: (A)-(C) The relative mean spectra have been shown for all five samples in the HSTI. Each sample spectrum have been divided by the mean PI spectrum. (B) The predictions following the application of the MLR model is shown for each HSTI in the reproducibility test. A single MLR model have been calculated based on all three HSTIs, and this model was then applied on each individual HSTI. (G)-(I) The confusion matrices belonging to the predictions shown in (D)-(F).[2]

6.3 Summary and Conclusion

Two experiments have been included in this chapter showing the results of a hyperspectral thermal imaging experiment carried out using samples at RT and at an elevated temperature of 100 °C. Both experiments were carried out using an early version of the HSTC equipped with short range piezoelectric elements in the FPI and homegrown mirrors with a relatively large amount of absorption. The results of the room temperature imaging were inconclusive in the regard of measuring spectral differences between materials of various emissivities. An attempt of improving the signal-to noise ratio was carried out through the summation of 50 separate HSTIs without luck. This led to an experiment where the radiance of the imaged samples was increased by heating the samples to ~ 100 °C. The HSTI acquired following this procedure was used to successfully segregate five individual samples based on spectral differences. The sample segregation was possible using a single HSTI, however, testing a classification model across three independent HSTIs revealed weak segregation of the Vantablack and polyimide tape samples. The main contributor to the weak reproducibility is ascribed to system specific variances during acquisition. Such variances include the microscopic mirror alignment during acquisition and the variance in the exact mirror separation during acquisition.

The results presented in this chapter proofs the principle of the hyperspectral imaging system and demonstrates that even slight variances sample emissivities is detectable. The results are among the earliest obtained using the HSTC and a significant amount of time was spent improving the system, throughout this project. As we have seen, the experiments involving the perfection of the FPI mirrors was a major part of the development and the remaining chapters are based on results obtained following inclusion of low absorption mirrors in the FPI.

7

Hyperspectral Thermal Imaging Using II-VI Mirrors

This chapter is based on an investigation of the surface temperature prediction of samples requiring differentiated emissivity settings for a true temperature prediction. The study covers the possibility of recognising sample spectra automatically, using the HSTC, which allow for application of a correct temperature prediction model based on previous calibrations.

7.1 Surface Temperature Determination of Glass Types Using Hyperspectral Thermal Imaging

In the previous chapter it was argued that the signal-to-noise ratio of our camera
system was too low to acquire hyperspectral thermal images at room temperature
with sufficient information to conclude anything quantitatively. As mentioned in
Chapter 3, elimination of absorption in the FPI mirrors is the most important factor for
improving the signal to noise ratio without the need for heating the imaged samples,
and the following images were acquired using the second version of the hyperspectral
camera abbreviated 'V0.2'. In the following experiment the reproducibility test carried
out as a final part of the previous chapter was included by segregating the datasets
used for model training and model evaluation. Additionally, the samples chosen for
this study are inspired by the previous studies using the HyperCam-LW for mineral
emission spectra [24, 25, 26, 27].

The following images and analysis are presented in the paper *Surface temperature
determination using long range thermal emission spectroscopy based on a first order scanning
Fabry-Pérot interferometer* which is currently under peer review in the journal Optics
Express. A description of the experimental setup and a summary of the results follow
in the sections below. The work was made in collaboration with former master student
Mads Nibe Larsen.

7.1.1 Experimental Methods

The experiment was carried out using Thorlabs PK2FMP2 piezo stacks in the me-
chanical assembly of the FPI. The piezo stack is operated by applying a voltage
in the range 0-75 V and has an expansion of 11.2 µm at optimal conditions. With
this expansion range the FPI is scanned through the entire first and second order
transmission peaks along with parts of the third order transmission shown in Figure
3.12 in Chapter 3. Additionally, the FPI is assembled using an identical set of II-VI
Incorporated mirrors with a mirror coating matching that introduced in Chapter 3.
The images were acquired using a GFID voltage of 2800 mV and 4x analog gain on
the microbolometer sensor in order to optimise the temperature range and sensitivity
of the sensor. The images were acquired using the latest version of the operating
software, which allows the hyperspectral thermal camera to acquire 140 spectral bands
while scanning the FPI. The sensor itself, collecting optics and camera hardware, is
identical to that specified in Chapter 4. Additionally, all images were standardised

and cropped during preprocessing and thus the datastructure is

$$\mathbf{\Lambda}_{1024,768,\lambda} \xrightarrow{\text{Preprocessing}} \mathbf{\Lambda}'_{800,768,140}$$

In the experiment, an aluminium block was used with samples of glass types at-
tached on the front surface. The aluminium block is placed against a heating element,
which is used to control the temperature of the entire setup. In order to monitor the
temperature, a digital thermometer is placed in a hole drilled into the aluminium
block. Two alumina (AlO_2) samples were used, one alumina ceramic bar, and the
other pure sapphire wafer. The two remaining glass types are the two silicon dioxide
(SiO_2) variants of fused silica and borosilicate glass. While fused silica is an ordered
crystal, the borosilicate glass resembles an amorphous structure with boron trioxide
incorporated into the matrix.

The calibration of the FPI was modified for this experiment, in order to find an
accurate measure for the mirror separation during image acquisition. The calibration
was carried out using three bandpass filters from the company Andover Corporation.
The bandpass filters had center wavelengths of 8.226 µm, 10.224 µm, and 11.322 µm,
respectively, which covers most of the sensitivity range of the sensor. The peak trans-
mission and full width half maximum of each filter is 461 nm & 96 %, 356 nm & 77 %,
and 498 nm & 92 %, respectively. The transmission profile of each filter measured
by FTIR is shown in Figure 7.1 (B) for each bandpass filter in the wavelength range
of 8-16 µm. In this figure it is seen that each filter has a single transmitted band
within the main sensor sensitivity range of 8-14 µm. It is, however, also observed
that each filter transmits light at wavelengths above 14 µm, which can be measured
with the bolometer chip owing to the sensitivty tail of the sensor in this range. The
sensitivity of the sensor is sketched as a part of Figure 7.1 (B). A simulation of the
theoretically observed transmission spectrum through each bandpass filter is shown
in Figure 7.1 (A). Here, the FTIR transmission measured through each bandpass filter
has been multiplied with the theoretical sensitivity of the bolometer sensor. The
resulting spectrum is further multiplied with the theoretical transmission of the FPI
calculated using the TMM at the mirror separations shown in Figure 7.1 (A). Figure
7.1 (C) shows the spectrum measured through the bandpass filters imaged by the
hyperspectral thermal camera. The spectra are acquired from three HSTIs where
the field of view was covered by the bandpass filter. The figure shows the mean
spectrum from each HSTI calculated from a 100x100 pixel square in the center of
the image. This part of the image was used in order to circumvent any wavelength
correction caused by the spectral bending, which arise from the angular incidence
of the thermal light. Comparing Figures 7.1 (A) with Figure 7.1 (C) it is seen that
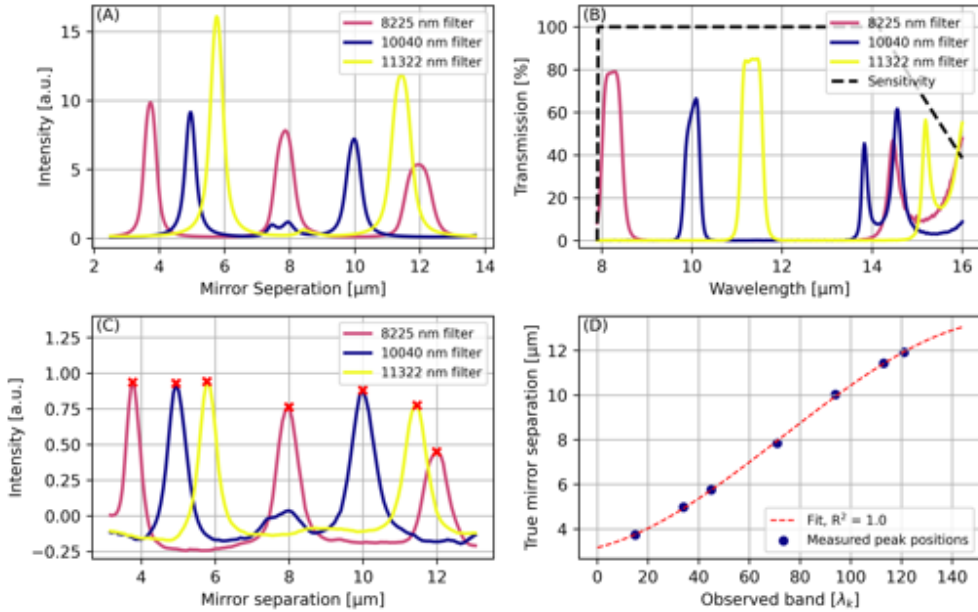
Figure 7.1: (A) Raw FTIR spectra of the bandpass filters multiplied by the simulated
transmission of the FPI at the mirror separation indicated at the x-axis. (B) Raw FTIR
measurements of the three bandpass filters used as part of the FPI calibration. (C)
Mean spectra of the measured transmission through the three bandpass filters. The
blue dots indicate the band number of the transmission peaks in (A). (D) A calibration
curve obtained using the peak positions of the transmission through the bandpass
filters.

the theoretically calculated spectra are comparable to those measured experimentally.
Additionally, note that the transmission peaks observed for the 10 μm bandpass filter
around 14 μm in Figure 7.1 (B) are measured by our hyperspectral imaging system at
a mirror separation distance of 8 μm.

The mirror separation axis has been calibrated using the position of the transmission
peaks measured through each bandpass filter. The band number (λ_k) of each transmis-
sion peak is found for each HSTI grabbed in this data series. This band number (λ_k) is
plotted against the true mirror separation of each transmission peak, which is found
theoretically as explained earlier, and the corresponding measurements are shown in
Figure 7.1 (C). The red crosses mark the maximum transmission measured through
each filter. The band numbers matching the maximum transmission datapoints are

plotted as a function of their theoretical mirror separation and the resulting graph is shown in Figure 7.1 (D). A third order polynomium is used to determine the relation between the observed band number and the true mirror separation which is added as a dashed red line in the graph. A third order polynomium is used since it follows the expected displacement profile of an open loop forward scanned piezo element.

Using the calibrated mirror separation axis, the wavelength axis of the hyperspectral datacube can be found by cross comparing to the simulated results from the transfer matrix method. This will, however, not be done in the following sections, since the second half of the second order peak transmission is contaminated by the transmission of the third order peak as mentioned earlier. It is, therefore, not possible to label the bands with a single transmitted wavelength in this region.

Two datasets were acquired, and they cover the temperature range of 27.1-97.0 °C. Both dataset consist of HSTI acquired at temperatures covering most of the temperature range, and the specific HSTI grabbing temperatures, c.f. Table 7.1. The first dataset, named the training set, is used for fitting a Multinomial Logistic Regression Classifier and a Partial Least Squares model, which is used in order to predict the surface temperature of the samples in the HSTI. The other dataset, named the evaluation set, is used for evaluating the performance of both statistical models. An image of the scene is shown in Figure 7.2 (A), where the position of each sample can be deduced from the mask used for data analysis shown in Figure 7.2 (B). The material mask shows regions marked by dashed red squares. These regions indicate double layers of PI used for fixating the samples. The double layer PI was excluded from the classification analysis in this experiment, but was used for tempereature calibration, which is described later.

A 50x50 pixel bounding box is placed inside every sample c.f. Figure 7.2 (A). The spectra within these boxes have initially been collectively mean centered and thus

$$\textbf{50px box:} \quad \frac{1}{50^2} \sum_{x_i, y_j}^{+50} \bar{\Lambda}_{\mathbf{x_i, y_j}, *} \quad ,$$

where x_i and y_j equals the corner coordinate of the bounding box of size $n = 50$. The spectra are plotted and shown in Figure 7.2 (C). For visualisation purposes, the AC, FS, BSG, and S spectra have been offset from the main axis by 1.2, 2.4, 3.6, and 4.8. As seen in Figure 7.2 (C) the sample spectra differ distinctively and the following results will show that the spectra are recognisable on an individual pixel level in the various samples.
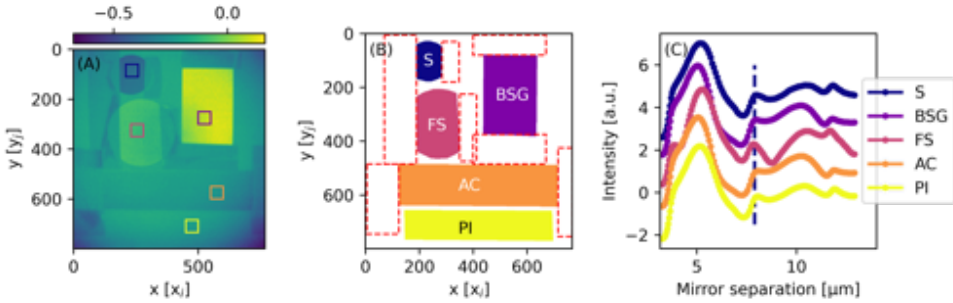
Figure 7.2: (A) Image of the substrates mounted on an aluminium heating block using
polyimide tape. The image is recorded at 96°C with a mirror separation of 7.9 μm.
(B) The material mask which is used to fit the logistic regression model for material
recognition. The dashed red boxes mark areas where double layers of polyimide tape
have been used to tape the samples to the block. These regions are not included in
the material recognition data analysis. (C) A selection of each material is indicated by
the coloured squares in (A) and their average spectra are plotted. The spectra have
been offset on the y-axis for visualization purposes. [1].

Training set T [°C]	27.1	32.0	36.5	43.3	49.9	59.0	67.2	74.8	83.7	92.3
Evaluation set T[°C]	30.2	34.0	40.0	46.7	54.5	63.0	70.4	79.6	88.3	97.0

Table 7.1: Temperatures in the center of the aluminum block during image acquisition
of the training data set and the evaluation data set. The two rows seperate the dataset
used for fitting the MLR and PLS models and for testing their performance.

7.1.2 Results and Discussion

The overall goal of these experiments was to predict the surface temperature of ma-
terials of unknown and differing emissivity within the same thermal image frame.
Our approach is to first recognise the imaged material on the individual pixel level
using the material specific thermal emission spectrum. Following the correct material
classification, the PLS regression model associated to the classified material is used to
predict the surface temperature based on the measured spectrum.

Figure 7.3 shows the prediction results following the application of the Multinomial
Logistic Regression function on the evaluation set fitted. The MLR function was
fitted on the training dataset. Figures 7.3 (A), (B) and (C) show the predictions from
HSTIs collected at temperatures of 30, 34, and 97 °C, respectively, and the images are
reconstructions with color codes matching the predicted material by the MLR model.
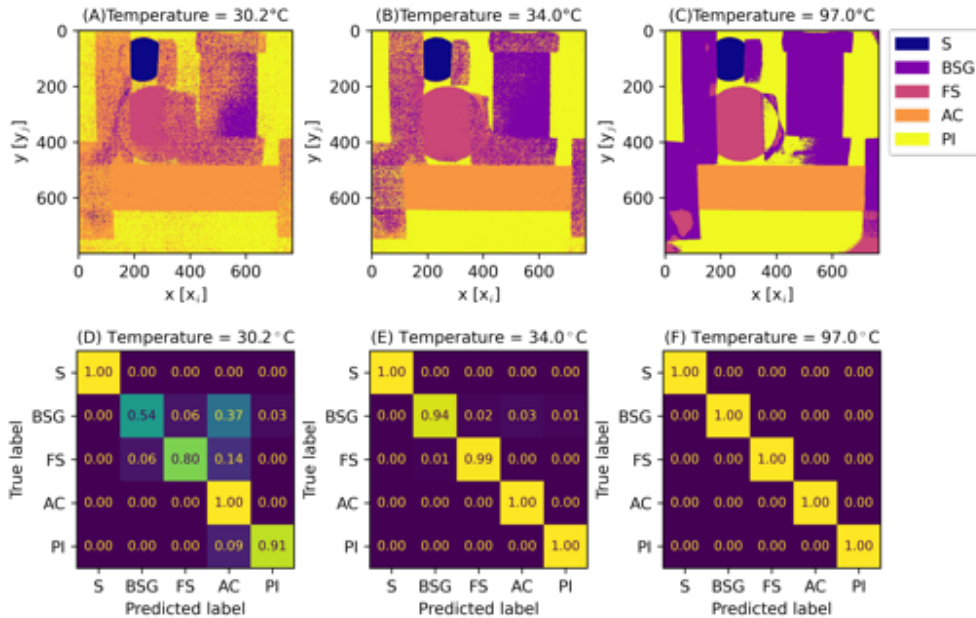
Figure 7.3: (A), (B), and (C) Predicted classes for HSTIs acquired at temperatures of 30.2ºC, 34.0ºC and 97.0ºC using the testing set and applying the fitted logistic regression classification model. The colour-coded materials follow that of Figure 7.2 (A). (D), (E), and (F) Normalised confusion matrices describing the relationship between the true pixel material seen in the material mask in Figure 7.2 (B) and the predictions of the MLR model. Each row is normalised to a sum of 1 such that the diagonal represents the true positive predictions divided by the sum of true positives and false negatives. S, BSG, FS, AC, and PI are abbreviations for the five materials: sapphire, borosilicate glass, fused silica, alumina ceramic and polyimide tape. [1].

The predictions shown in Figure 7.3 (A) are clearly affected by the low signal accompanying the aluminium block temperature, which impacts the signal to noise ratio. The results are significantly improved by increasing the temperature to 34 °C as seen in Figure 7.3 (B) which show a near perfect prediction of all five materials excluding the double layered PI. The near perfect predictions are observed for all temperatures up to 97 °C which is the highest temperature used in this experiment. The prediction for this HSTI is shown in Figure 7.3 (C). In the corners of the image in this figure, the effect of the spectral bending can be seen in the form of misclassification of the PI. The predictions of the intermediate temperatures used in this experiment are included in Appendix Figure A.9 and show near perfect predictions as well.

The prediction results are summarised in the confusion matrices, which have been presented in Figure 7.3 where the dataset of (D), (E), and (F) match the predictions in (A), (B), and (C). Confusion matrix (A) further shows that the main source of error in the predictions of the 30 °C dataset is the misclassification of borosilicate glass with alumina ceramic. This makes little sense given that the two materials are different, however, the spectra measured in these two samples are very similar as seen in Figure 7.2 (C). For the 34 °C dataset it is seen that the predictions all have a true predictability rate above 94 %, and for the 97 °C dataset all predictions are perfect. Note here that the predictions of the PI only include the region marked PI in the image mask shown in Figure 7.2 (B). Therefore, the misclassification due to the spectral bending in the corners of the image are not represented in the confusion matrix. The overall conclusion of the material predictions remains that near perfect predictions can be obtained at temperatures above 34 °C and therefore it is possible to proceed with the overall goal of surface temperature predictions based on material specific PLS temperature models. First, however, it is important to elaborate on the measurements of the true surface temperature of each sample.

The thickness and materials of the samples differed, and the surface temperature of each sample did not equal the reference temperature measured inside the aluminium block. Consequently, a method for determining the true surface temperature of the samples was needed. As stated, the samples were taped to the aluminium block using PI, and therefore the PI was in direct contact with all sample surfaces. Since the tape has a thickness of only 25 μm it is assumed that the temperature of the PI is comparable and close to equal to the surface temperature of the samples. Thus, the regions with PI taped directly to the sample surfaces were used to estimate the sample surface temperature based on thermal imaging and a reference temperature model for the PI itself. Such method is commonly used within thermography to

improve temperature predictions of very low emissivity surfaces [73].

For this experiment a temperature model was constructed by conventional thermography without the FPI in the optical path. An additional temperature dataseries was made of the experimental setup consisting of single images from the camera at eight different aluminium block temperatures. A linear fit was constructed of the intensity measured of the PI directly taped to the aluminium block as a function of the measured temperature in the center. The resulting linear fit was applied on the PI taped directly on each sample to find their true surface temperature. Each linear fit is shown in Figure A.8. The temperature model for the PI can be applied on the entire image frame in order to check the resulting error of a measurement of the sample surfaces without such calibration. These errors are presented in Table 7.2 and serve the purpose of demonstrating the measuring error using non-calibrated conventional thermography with a fixed emissivity. As can be seen the resulting errors can be of substantial magnitude, and the biggest error is found for sapphire at 15 °C difference. The just mentioned dataseries show the magnitude of the expected surface temperature deviances of the sample set, however, it cannot be applied to the acquired full HSTI dataseries, since the measured intensities are heavily altered by the addition of the FPI in the optical path. Thus, in order to validate the PLS predictions, a calibration of the samples surfaces is needed for our main dataset as well, and a similar method as the one presented above can be made. Thus a new PI temperature model must be constructed, which can be carried out in various ways. Dealing with hyperspectral images it is important to remember that PI with a thickness of 25 µm transmits in the LWIR. The transmitting regions are located around 10-11 µm and 13-14 µm (measurement using FTIR is shown in Figure A.7), and therefore it is important to choose a spectral band with 0 % transmission for the PI temperature model. A spectral band without transmission prevents that the radiance of the underlying sample influence the model. Spectral band $\lambda_k = 48$ was chosen which corresponds to an MS of 6.01 µm and a transmission center wavelength of 11.72 µm. A linear fit was then created of the intensities measured in each individual HSTI in spectral band $\lambda_k = 48$. Note that neither standardised nor mean centered spectra can be used for this purpose. The standardised spectra cannot be used since they primarily contain material-specific information and intensity variations are eliminated. The mean centered spectra cannot be used due to several node points at the points where the spectra crosses the center line equal to zero. An example of the mean centered spectra is shown in Figure 7.4 (A). The dashed line represents $\lambda_k = 48$ which lies close to a node of the spectra. Therefore, baselined spectra were used where the intensity measured in every band correlates with the temperature. The baselined spectra are shown in Figure 7.4 (B).

Sample	Polyimide Tape	Alumina Ceramic	Fused Silica	Borosilicate	Sapphire
Measurement [°C]	73.2	75.1	82.6	79.2	88.2
Error [°C]	0	1.9	9.4	6.0	15.0

Table 7.2: Measurement error of the sample surfaces of alumina ceramic, fused silica, borosilicate and sapphire when using conventional thermography and an emissivity setting that matches the polyimide tape. The measurement errors are found at a polyimide temperature of 73.2 °C.
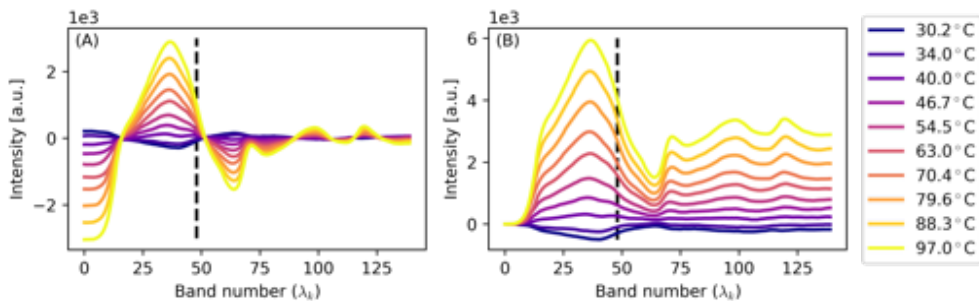

Figure 7.4: (A) A plot of the mean centered spectra. Several node points appear along the spectral axis, and a linear fit in a single spectral band cannot be performed. (B) A plot of the baselined spectra. The intensity in every band is correlated with the temperature and thus the radiance transmitted through the FPI.

This procedure ensures a direct linear correlation between the temperature and the spectral band intensity. The linear fit of the PI band intensity in $\lambda_k = 48$ was then used in all images to determine the true surface temperature of the samples. The resulting true surface sample temperature was used as an input to fit the PLS models of the training set. Additionally, the true sample surface temperatures were used to calculate the root mean square error (RMSE) of the PLS temperature predictions of the evaluation set. During the PLS analysis all spectra were low-pass filtered, to minimise readout noise.

Figure 7.5 shows the temperature predictions of the PLS models. Ten different PLS models were fitted with 1-10 components. Each fitted model was used on the evaluation dataset, and both the RMSE for each surface temperature material and the combined RMSE for the entire dataset were found, c.f. Figure 7.5 (F). The overall tendency for all five materials is a lower RMSE as the number of components increase.

As is seen in Figure 7.5 (F) the local minimum of the RMSE is different for the five different materials. For this reason, the RMSE of the combined dataset is used to determine the number of components for the model used in the surface temperature predictions. Assessing the RMSE for the combined dataset, it can be concluded that if using six components the RMSE flattens, and if using ten components the RMSE slightly increases due to overfitting. Therefore, the six component solution was chosen for the surface temperature predictions in this experiment.

The six-component-PLS-model was fitted for each material using the training dataset. Hereafter, the material-specific PLS model was used to predict the surface temperature of the sample, based on the sample prediction from the previous logistic regression function. The surface temperature predictions for each sample is shown in Figures 7.5 (A)-(E). In these figures, the green datapoints shown illustrate temperature predictions of individual pixels in each image frame in the evaluation dataset. The individual pixels have been sorted such that the temperature is ascending. The first pixel of each sample is thus abbreviated sample # 0. The remaining pixels in each sample are plotted as samples # 1,2,3... etc.. For each HSTI the cycle is repeated at the elevated temperature which in the end makes up the stair case graph seen in Figures 7.5 (A)-(E). The orange line shows the temperature measured for each sample which is assumed to be the true temperature. The root mean square error is thus calculated as the error difference between the predicted temperatures and the true temperature. As seen in Figure 7.5, all PLS models perform well with sapphire showing the best temperature predictability with an RMSE of 0.77 °C and PI showing the worst RMSE of 1.39 °C. Note that the temperature predictions of the borosilicate glass seem to show a slope which increases with the rising temperature. This behaviour could be the result of either reflections in the borosilicate glass from the camera itself or weak adhesion to the PI covered aluminum block resulting in non-homogeneous heating. A gradient in the material predictions of the borosilicate glass is observed in Figure 7.3 (A) as well which supports this hypothesis.
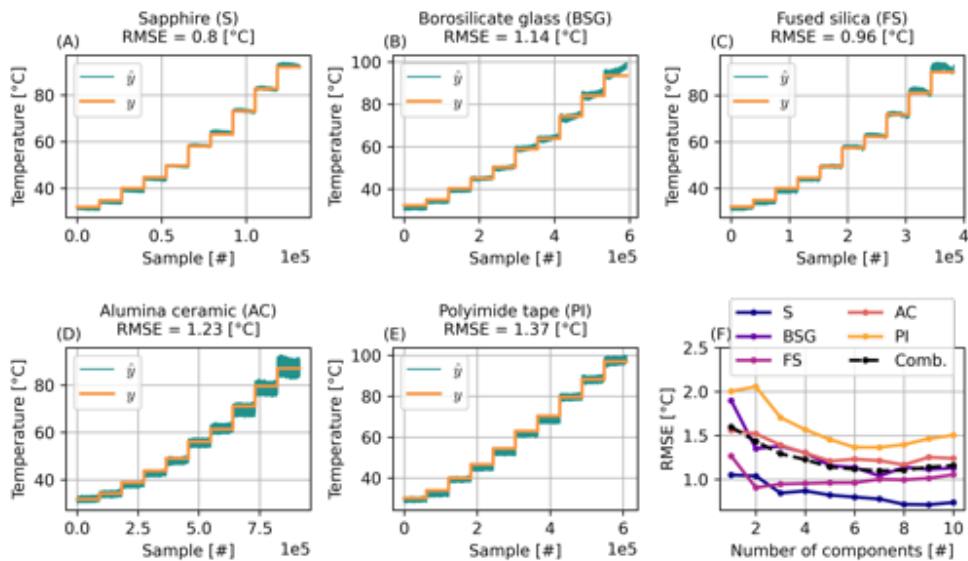
Figure 7.5: Surface temperature predictions based on PLS models fitted on all the HSTIs in the training set. The PLS models have been fitted to the spectrum of each individual material marked by the mask in Figure 7.2 (B). Each individual figure shows the pixelwise surface temperature predictions of every material present in the image. The predictions have been sorted in order to match a stepwise increase in temperature. The solid orange line, y, indicates the temperature measured, which is considered the true temperature. The solid green line, $\hat{y}$, indicates the temperatures predicted. (F) The root mean squared error (RMSE) of the entire set is shown in every plot title and lastly the RMSE is plotted as a function of the PLS number of components [1].

7.2 Summary and Conclusion

To summarize the hyperspectral thermal imaging system was used to acquire HSTIs at temperature covering the range 27.1-97.0 °C. The dataset was split in order to create a training dataset and validation dataset for a MLR material classification model and a PLS temperature prediction model. The MLR model was used to predict the materials present in the evaluation dataset. The results showed TPR values above 94 % for all samples at temperatures of 34 °C and above. This shows that the emission spectra of materials can be measured by a Fabry-Pérot-based hyperspectral camera and that the spectra contain significant information at temperatures as low as 34 °C. The hyperspectral imaging system was used to predict the surface temperature of the samples present in the experimental setup based on sample specific PLS models.

The results shown in this chapter are extremely important in that they show that the HSTC work as intended. The temperature calibration carried out using conventional thermography reveals that a emissivity setting matching that of PI would lead to misreadings of the temperature in the range 1.9-15 °C for the samples used in this experiment. Using the HSTC the material specific temperature models predicted the surface temperature with a common RMSE of 1.10 °C. The results demonstrate the benefits of an advanced thermographic imaging system capable of determining the surface temperature based on differentiable emissivity settings within an image frame. Being able to use such imaging system for thermographic inspection could potentially improve the analysis significantly. Reaching accurate material classifications and temperature predictions of temperatures below 34.0 °C is the next step and the thoughts and considerations for reaching this goal is presented in the outlook in Chapter 9.

8

Alternative Applications of Hyperspectral Thermal Imaging

A few direct applications of the HSTC have been investigated throughout this project. These include the detection of organic gasses and the segregation and sorting of polymers based on hyperspectral imaging in the LWIR. Potential use-cases could therefore be oil and gas facilities for the task of leak detection, and sorting facilities specialising in polymer sorting which has become a major area within the last couple of years.

8.1 Detection of Organic Gasses Using Hyperspectral Thermal Imaging

The following section presents results obtained from the HSTC where the absorption spectra of the gas phase of a selection of chemical species was measured. Many organic gasses have characteristic absorption lines in the thermal range detectable by the HSTI camera[85, 73]. These absorption lines are primarily due to vibrational secondly rotational modes of the specific gas molecule under investigation. Typically, the rotational modes of molecules are lower energy and longer wavelength than imaged by the HSTC.

The Telops Hyper-Cam LW has been used previously for the measurement of SO_2,CH_4, H_2S, and N_2O gas plumes [86, 87]. Matching studies have shown that modified K-means algorithms can be used to detect likewise gas plumes of O_3 and CO_2 based on hyperspectral images acquired by an airborne imager [88]. Additionally the emission of ammonia from land surfaces has been measured by the NASA developed HyTES [89], and therefore measuring the transmission spectra of gas-phases is a natural application for the FPI based HSTC as well.

This work was done in close collaboration with former master student Mads Nibe Larsen and the final section in this experiment would not have made this thesis without him.

8.1.1 Experimental Methods

The experimental setup used during these experiments is sketched in Figure 8.1. The hyperspectral thermal imager was placed in front of a commercial blackbody source (Newport CS1050-100) with a cavity diameter of 1 inch. The blackbody temperature is controlled using a PID controller and the temperature accuracy is $\pm 0.25\,°C$ and $\epsilon(\lambda) = 0.97 - 0.99$. During this experiment the blackbody source was set to a temperature of $100\,°C$ and thereby acting as a illumination source. As the light is emitted from the cavity it travels through the gas cell and is ultimately collected by the camera. The gas cell consist of a cylindrical stainless steel container fitted with two uncoated zinc selenide windows at each end of the steel cylinder. The zinc selenide windows are used in order to allow thermal light from the blackbody through to the camera. This constitutes a closed container in which gasses of different chemical composition can be maintained.

Before acquiring each image the gas cell was evacuated using a vacuum pump followed by letting a continuous flow of gas through the cell for some time before closing the valve. This procedure was done in order to ensure that the entire volume of
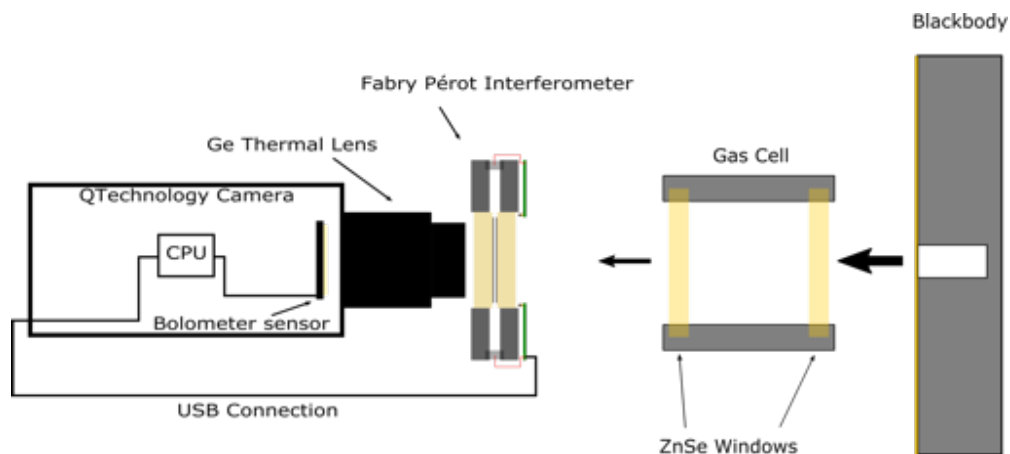
Figure 8.1: Experimental setup used during the test of a separation and clustering of organic gasses based on their transmission spectrum. The hyperspectral thermal camera was placed in front of a gas-cell containing different organic gasses. The gas-cell is equipped with ZnSe windows in order to transmit thermal light and a commercial blackbody was used as light source.

the gas cell was filled with the inlet gas. Four different organic gasses were examined in this experiment in combination with a reference measurement where the gas cell contained atmospheric air. The gasses used in this experiment are tetrafluoropropene, ethylene, and NO. As the light travels through the gas cell the chemical species present within the volume are vibrationally, and to some extent rotationally, excited by the light at a specific energy. This energies is absorbed and will be imaged by the camera as an absorption line. Additionally, an FTIR spectrum of each gas was measured in a transmission configuration through the gas cell.

A hyperspectral thermal image was acquired for each individual gas resulting in five images in total.

8.1.2 Results and Discussion

Each individual HSTI was cropped to fit a size equal to the 1 inch cavity of the blackbody source and the spectral axis was cropped to the length of the shortest one. This results in five datacubes (4 compounds and one reference) of sizes 300x300 pixels x 135 spectral bands. All five datacubes were used to construct a single datacube by fusing the five cubes into a new datacube of size 1500x300 pixels x 135 spectral bands,

resulting in the preprocessing

$$\Lambda_{1024,768,\lambda} \times 5 \xrightarrow{\text{Preprocessing}} \Lambda_{1500,300,135} \qquad .$$

This datacube was used for data analysis which is presented in the following section. The mean spectra of each gas cell is found for the circular aperture in which the emitted light from the blackbody source can transmit. These spectra have been extracted for all five gasses and plotted in Figures 8.2. Figure 8.2 (A) shows the measured spectra following a mean centering and Figure 8.2 (B) shows the spectra following standardisation. Figure 8.2 (C) shows transmission FTIR measurements through the gas cell. The FTIR measurements in (C) show that few to none absorption lines are present in the Methane, NO and air filled gas cell. The transmission percentage of each gas is, however, different where the methane show transmission above 60 %. The air filled gas cell show transmission directly below 40 % and the NO filled gas cell show a transmission percentage around 40 %. Both the ethylene filled gas cell and tetrafluoropropene gas cell show characteristic absorption lines.

It has previously been argued that the standardisation removes intensity variations in the hyperspectral datacube leaving pure material specific features within the measured spectrum. This can be beneficial in the recognition of material spectra, however, at times the intensity variation are needed. That becomes clear in this experiment where the transmission percentage of the compounds are different while the spectral features are not. The NO, methane, and air measurements are only distinguished by their transmission percentage through the gas cell, which leaves only the transmission variations to be measured by the HSTC in the form of intensity. These variations are seen most clearly in Figure 8.2 (A) where the spectra have been mean centered. The methane measurement has much higher variance in the spectral axis compared to NO and air. Standardising the spectra as shown in Figure 8.2 (B) eliminates these differences and the measurements of all three spectra merge into a single indistinguishable graph.

Comparing the FTIR measurements in Figure 8.2 (C) with the measured spectra in (A) and (B) it is seen that the strong absorption line in the 9.8-11.8 µm observed for ethylene is measured at mirror separations of 5.2 µm and around 10.5 µm using the HSTC. The same thing is observed for the tetrafluoropropene where large absorption dips are observed in the ranges 8-9.5 µm, 10.8-12.1 µm, and 14-15.5 µm. The segregation of the individual spectra can be performed by the combination of a PCA and K-means analysis. Figure 8.3 shows the results from a PCA of the fused image
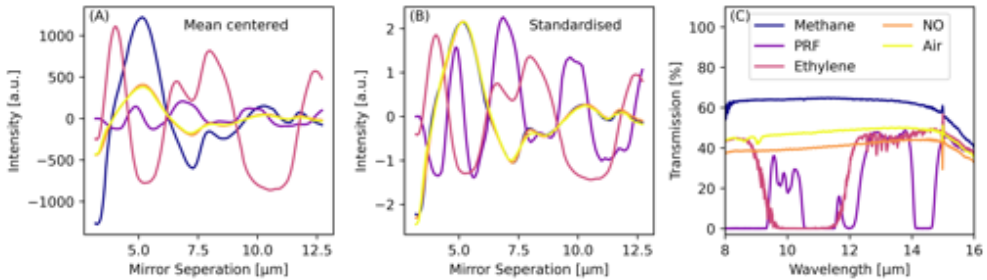
Figure 8.2: (A) Mean centered spectra of the five gas cells used in this experiment. The spectra have been measured using the HSTC. (B) Standardised spectra of the five gas cells used in this experiment. The spectra have been measured using the HSTC. (C) FTIR spectra measured through the five gas cells used in this experiment. The spectra have been measured using a Shimadzu FTIR-8400S.

following both preprocessing procedures. Looking at the first principal component it is immediately clear that tetrafluoropropene and ethylene are easily distinguishable from NO, methane, and the air cell with no absorption. Furthermore tetrafluoropropene and ethylene are mutually distinguishable. As expected the methane cell is only distinguishable using the mean centering for preprocessing which is clear observing PC1, PC2 and PC6 in Figures 8.3 (D), (E), and (F). The intensity variations in the PCs are equal, and therefore hardly distinguishable. A K-means analysis can be performed in order to segregate the gas cells based on the variations seen in the PCA. Figures 8.4 (A) and (B) show the results of a K-means analysis of four and five clusters, respectively. The amount of clusters has been chosen based on the sum of squared error (SSE) analysis performed and shown in Figures 8.4 (C) and (D) where the vertical black line indicate the chosen amount of clusters based on the flattening of the error curve. As expected the mean centering preprocessing allow methane to be distinguished from NO and air, while all three gasses are contained within the same cluster in Figure 8.4 (B).

This experiment demonstrates the ease of segregating gasses based on measured absorption spectra. This underline one use-case for the hyperspectral imaging system in the form of leak detection. A wide variety of organic gasses is known to have absorption lines in the long wave infrared region. A selection of compounds with absorption lines in the range from 8-16 μm are chloroform, methanol, ethylene, freon, SF_6, carbon tetrachloride, ammonia, sulfur oxides, nitrogen dioxide, ozone and carbon oxides [73]. Being able to recreate the FTIR spectra, shown in Figure 8.4 (C), from
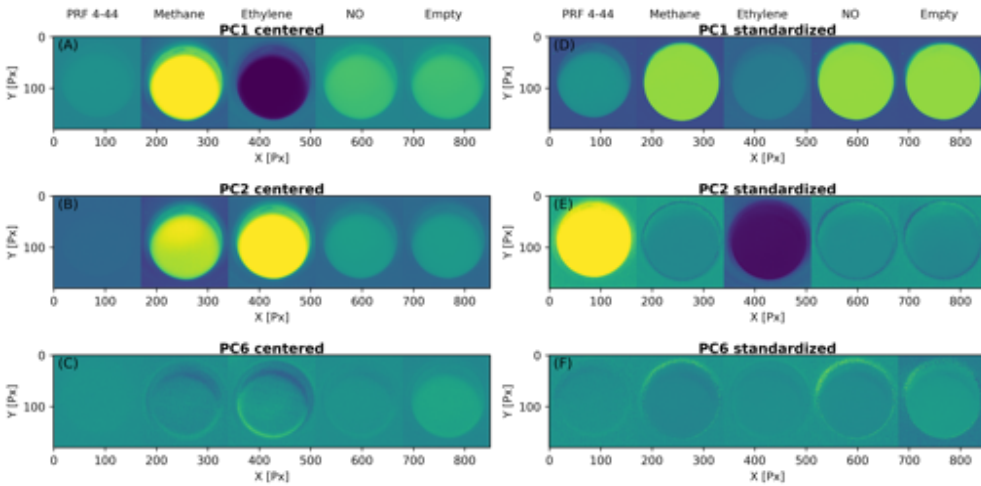
Figure 8.3: (A) first principal component of the mean centered fused image. (B) second principal component of the mean centered fused image. (C) sixth principal component of the mean centered fused image. (D) first principal component of the standardised fused image. (E) second principal component of the standardised fused image. (F) sixth principal component of the standardised fused image.

the measured HSTC spectra is work in progress and the following section elaborates on the initial task of simulating the spectrum measured by the HSTC. The spectrum measured can be constructed from what is known at this point based on the design of the mirror coating, the resulting theoretical transmission of the FPI, the spectral bending and the extent of absorption of light in its path between being emitted from the object surface and absorbed in the microbolometer pixel.

A Note on the Camera System Transfer Function

It is of high relevance to establish the transfer function of the camera system, which allows us to theoretically model the measured spectra of the HSTC based on any given input. As briefly discussed in the introduction to chapter 1, the emitted spectrum of any object is given by the blackbody distribution multiplied by the object emissivity $\int B(\lambda, T)\epsilon(\lambda)d\lambda$. Thus, if we measure a spectral band, λ_k, based on pure emission the transfer function multiplied by the radiance equals a single datapoint in the hyperspectral thermal imaging datacube
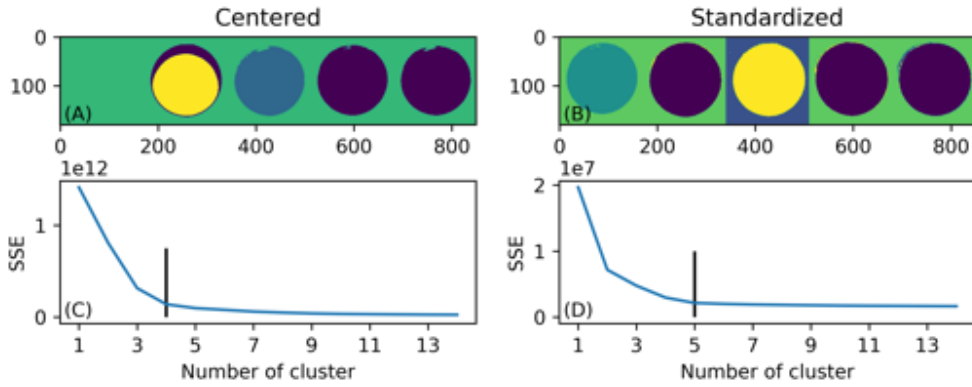
Figure 8.4: (A) The result of a four cluster K-means analysis of the mean centered datacube. (B) The result of a five cluster K-means analysis of the standardised datacube. (C) A K-means sum of squared errors plot of the mean centered datacube. (D) A K-means sum of squared errors plot of the standardised datacube.

$$\Lambda_{px,py,\lambda_k} = T_{HSTC}(\lambda, MS, \theta(px, py)) \int B(\lambda, T)\epsilon(\lambda)d\lambda \qquad ,$$

where λ is the wavelength of the light, MS is the FPI mirror separation and θ is the angle related to the spectral bending, and x_i, y_i, λ_k are entries in the HSTI datacube, Λ. While the exact transfer function remains unknown at this point, it is possible to decompose the transfer function into a set of separate contributions based on the working principle of the camera. For example, it is known that each image frame only captures the light within the sensor sensitivity, and that the light reaching the sensor is limited by the FPI. It is also known that the light passes through the collecting lens, and that the spectral bending modifies the measurement, and thus

$$T_{HSTC} = T_{FPI}(MS, \lambda)S_{sensor}(\lambda)T_{lens}(\lambda)C_{\lambda_{corr}}(\theta(px, py))C_{unknown}(s) \qquad , \qquad (8.1)$$

where T_{FPI} is the transmission of the FPI, S_{sensor} is the sensor sensitivity, T_{lens} is the transmission of the lens, $C_{\lambda_{corr}}$ is a correction factor for the spectral bending, and $C_{unknown}$ contains the remaining factors of s variables that still can be discovered. Finding these parameters is work in progress, however, a simplified equation system
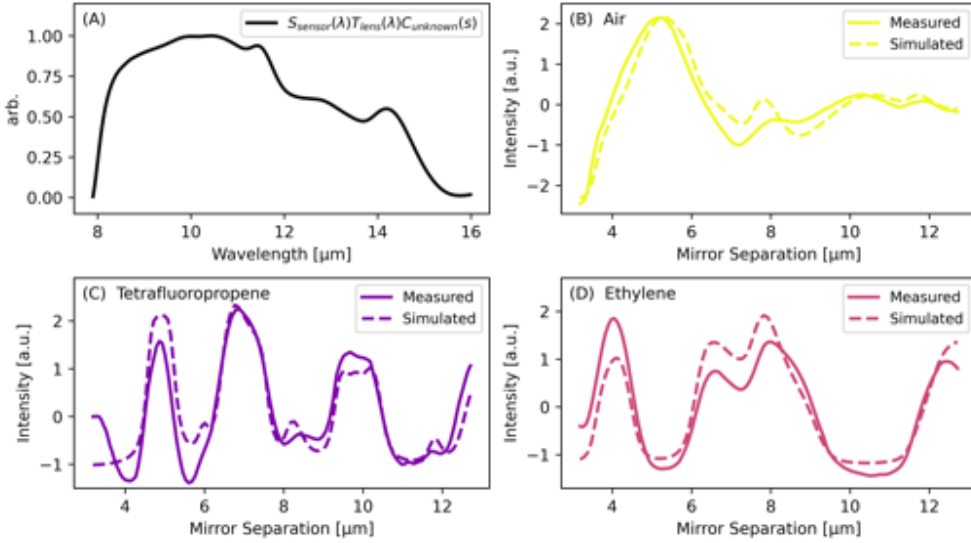
Figure 8.5: (A) Combined transfer function variables found by minimising equation 8.3, resulting in the marked variables shown in equation 8.3. (B)-(D) Simulated and measured spectrum of the gas cell filled with air, tetrafluoropropene, and ethylene, respectively. The dashed line shows the simulated spectrum, and the solid line shows the spectrum measured by the HSTC.

can be constructed based on the facts known at the time of writing. Focusing on a single spectrum in the full hyperspectral datacube the equation system can be described as

$$\mathbf{T_{HSTC}} \cdot \mathbf{B}_\epsilon = \mathbf{\Lambda_{x_i,y_j,*}} \quad , \tag{8.2}$$

with $\mathbf{T_{HSTC}}$ being the matrix representation of the collective transfer function for the hyperspectral camera. $\mathbf{B}_\epsilon$ is the column vector representing the input of the camera given by the spectral radiance and $\mathbf{\Lambda_{x_i,y_j,*}}$ is the column vector representing the measured output spectrum of the camera. Using the HSTI acquired in the gas cell transmission experiment as an example $\mathbf{\Lambda_{x_i,y_j,*}}$ would be an 135x1 vector, and therefore $\mathbf{T_{HSTC}}$ would be limited to a size of 135xn. The 135 rows are given by the transmission spectra calculated at the MSs at the time of image acquisition multiplied by the n remaining transfer function variables. $\mathbf{B}_\epsilon$ is an nx1 matrix consisting of the n individual wavelength dependent inputs. Setting $n = 135$ would create a system of equations that could potentially be solved analytically, however, doing so reduces the

rank of the $\mathbf{T_{HSTC}}$ leaving the square matrix with linearly dependent rows. Setting $n > 135$ creates an underdetermined system from the beginning, but such a system can be numerically solved. The numerical solutions to this problem can be many, but given the right constrains a physically meaningful solution can be found. A minimisation problem can be constructed where the variables of the $\mathbf{T_{HSTC}}$ matrix are found based on a known set of $\mathbf{B}_\epsilon$ inputs. In this experiment the input is well described by the measured FTIR spectra and the blackbody emission. Simplifying equation 8.1 by choosing the center of the image frame it is reduced to

$$T_{HSTC} = T_{FPI}(MS, \lambda) \overbrace{S_{sensor}(\lambda) T_{lens}(\lambda) C_{unknown}(s)}^{\text{Figure 8.5 (A)}} \qquad . \qquad (8.3)$$

Such minimisation has been carried out by former master student Mads Nibe Larsen resulting in the graph shown in Figure 8.5 (A). This graph resembles the sensor sensitivity curve shown in Chapter 4 and the fall in intensity above 12 µm is most likely caused by the antireflective coating on the collecting optics which is designed for the range 8-12 µm. Having a reasonable matrix representation for the transfer function it is possible to calculate simulated spectra, given that the input is known. In this section, the input is approximated by the radiance multiplied by the FTIR spectrum measured through the gas cell. The tetrafluoropropene, ethylene and air spectra were chosen out due to their individual spectral differences and all three are plotted again in Figure 8.5 (B), (C), and (D) along with their theoretical HSTC spectrum. The simulated graph results from the calculation of $\mathbf{T_{HSTC}} \cdot \mathbf{B}_\epsilon$. Based on Figure 8.5 (B), (C), and (D) it is concluded that the measured spectra can be constructed to a high accuracy. Some deviations remain, and a refinement can be done by improving the minimisation of the unknown variables of the transfer function and including the substrate bending of the FPI mirrors, and the mirror absorption in the simulation of the FPI transmission.

8.1.3 Summary and Conclusion

To summarise, this chapter contains the results and analysis following the acquisition of HSTIs containing absorption transmission spectra from organic gas atmospheres. The absorption lines of organic gasses are measurable with high accuracy using the HSTC and a K-means analysis of the PCA containing several different gas atmospheres is sufficient for segregating the gasses with absorption lines within the measuring range. The transmission spectra were used in combination with measured FTIR

spectra to test our understanding of the system transfer function. The transfer function is used to calculate the theoretical spectrum measured by the HSTC based on the measured FTIR spectra with decent accuracy. These studies lay the foundation for a pathway to calculating an accurate wavelength spectrum. Having a perfect transfer function matrix, it would be possible to develop methods for reconstructing the camera input purely based on the measured output, which is of highest relevance for a temperature emissivity separation algorithm. Attempts on developing such algorithms has been carried out before through the analysis of hyperspectral thermal data acquired from satellites and airplanes [90, 91, 92].

The results presented in the section above are not only an important step towards a full understanding of the HSTC but also shows a direct application of the camera.

8.2 Detection of Polymers using Hyperspectral Thermal Imaging

Hyperspectral imaging in the visible region of the electromagnetic spectrum is an emerging technique, and one of the most promising application areas is the field of polymer sorting. Earlier studies have shown that a wide range of polymers can be sorted using hyperspectral imaging and that some of these polymers show spectral differences in the 8-12 µm range [93]. While hyperspectral imaging already plays a significant role in the sorting industry, it is expected to continue along this path the coming years [94].

Therefore, an experiment was set up in order to investigate the possibility of segregating polymers with a goal of polymer sorting based on hyperspectral thermal imaging.

8.2.1 Experimental Methods

The camera was placed in front of a 16 cm x 16 cm aluminium block of 5 cm thickness. The aluminium block was covered in polyimide tape in order to increase the emissivity of the surface. Another piece of polyimide tape was fixed onto the aluminium block with the adhesive side facing outwards. Polymer granules were flattened and stuck onto the surface. A sketch of the experimental setup is shown in Figure 8.6. Prior to image acquisition a laboratory hotplate was used as a heatsource and placed at a fixed distance behind the aluminium block acting as a heat reservoir. The temperature of the aluminium block was measured and kept at 100 °C.

Polypropylene (PP), Polyethylene (PE), Polyethylene terephthalate (PET), akrylonitril-butadien-styren (ABS), and polymethylmethacrylat (PMMA) were the five polymers investigated in this experiment. Samples of all five polymers in neutral colour were used while ABS and PMMA both were investigated in variants with colour pigments added. The PMMA samples were larger tiles with various pigments added, and the ABS samples consisted of smaller granule pieces of different colour LEGO-blocks. All polymer samples were arranged as shown in Figure 8.7 (A) which shows the imaging mask used for the spectral data analysis. The figure shows that each polymer type was arranged in smaller clusters containing five individual granules except for the five PMMA plates. The four center ABS clusters contain colour pigments marked by light green (LG), blue (B), orange (O), and dark green (G). The remaining four clusters to the right were all of neutral colour (n). Figure 8.7 (A) shows a region marked polyimide tape (PI), which is used for the spectral analysis, which we will get back to. Lastly, it should be noted that the background material, polyimide, is a
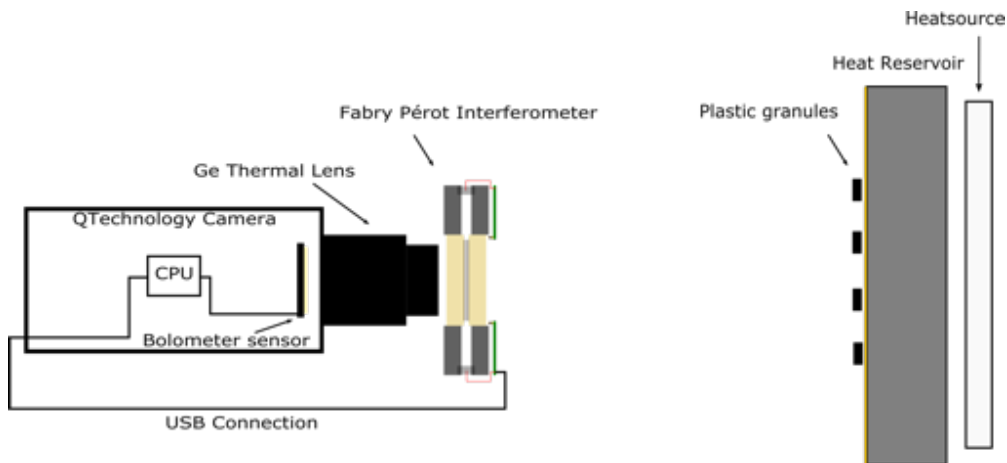
Figure 8.6: (A) Experimental setup used during image acquisition of polymer granules. The hyperspectral camera was placed in front of the experimental setup. polymer granules were stuck on the adhesive side of a 200x200 mm piece of polyimide tape. The polyimide tape was subsequently fastened to a 160x160 mm aluminium block, which was heated by a heatsource.

polymer as well.

The camera was configured to a gain of 4x and a GFID voltage on the sensor of 2800 mV. A single HSTI was acquired with 146 spectral bands. The HSTI was subsequently standardised and cropped to only fit the aluminium block within the image frame and remove most of the spectral bending. Thus the datastructure for this experiment was

$$\Lambda_{1024,768,146} \xrightarrow{\text{Preprocessing}} \Lambda'_{600,650,146} \qquad .$$

The polymer samples for this experiment were kindly provided by Mogens Hinge and Martin Lahn Henriksen from the plastic and polymer engineering group at Aarhus University.

8.2.2 Results and Discussion

The initial data analysis of the HSTI acquired in this experiment showed very few spectral features, and therefore an additional preprocessing step was employed. All

spectra were baselined followed by a division of the mean PI spectrum found in the region marked PI in Figure 8.7 (A) and thus the spectra shown in Figure 8.7 (B)-(D) are calculated as

$$\textbf{Relative sample spectrum: } \frac{\mathbf{\Lambda}'_{*,*,*} - \mathbf{\Lambda}'_{*,*,\lambda_{k=0}}}{\mathbf{\Lambda}'_{x_i=PI,y_j=PI,*} - \mathbf{\Lambda}'_{x_i=PI,y_j=PI,\lambda_{k=0}}} \quad .$$

The baselining prior to division is important due to the nodes around zero mentioned previously in Chapter 7. The additional preprocessing step enhances the spectral differences between the PI background and the polymers used in this experiment. The standardised mean spectra measured from the image position equal to each polymer type has been calculated based on the additional preprocessing step. The resulting spectra have been shown in Figures 8.7 (B), (C), and (D). The spectra have been divided into three different plot windows for visualisation purposes, and therefore the axis labels are common for all. Figure 8.7 (B) shows the pre-processed spectra of the four polymer clusters PP, ABS, PE, and PET. The PI background has been plotted as well to underline that the plotted spectra are relative differences to PI. The spectra shows small but clear differences in the spectra of PP, PET, and the remaining two polymers. The spectral differences between ABS (n) and PE are less clear however small bumps are observed at the MSs slightly above 6 µm and 8 µm. The bump at 6 µm is observed again above 12 µm.

Figure 8.7 (C) shows the pre-processed spectra of the four polymer clusters of ABS containing different colour pigments. Here, it is observed that the spectral signature and shape are very similar. Spectral differences are, however, observed at MSs around 7 µm. Note that these differences correlate to the distance to the center of the image, and thus may be caused by the spectral bending. The same trend is observed in Figure 8.7 (D) where the dip in intensity at MSs around 7 µm becomes deeper as the sample gets closer to the image center. Figure 8.7 (A) shows a red and white 'bulls eye' which mark the center of the original image and thereby the physical center of the sensor.

A PCA was performed on the original standardised datacube. Figure 8.8 shows the first twelve principal components sorted by the variance explained of the full datacube from highest to lowest with PC1 explaining most of the variance. All twelve principal components show distinct variations of intensity which indicate that a multitude of effects is present in the image. All of these effects are thus measurable by the hyperspectral thermal camera, ranging from material properties to differences in transmission and reflections of the thermal light. Based on the twelve principal
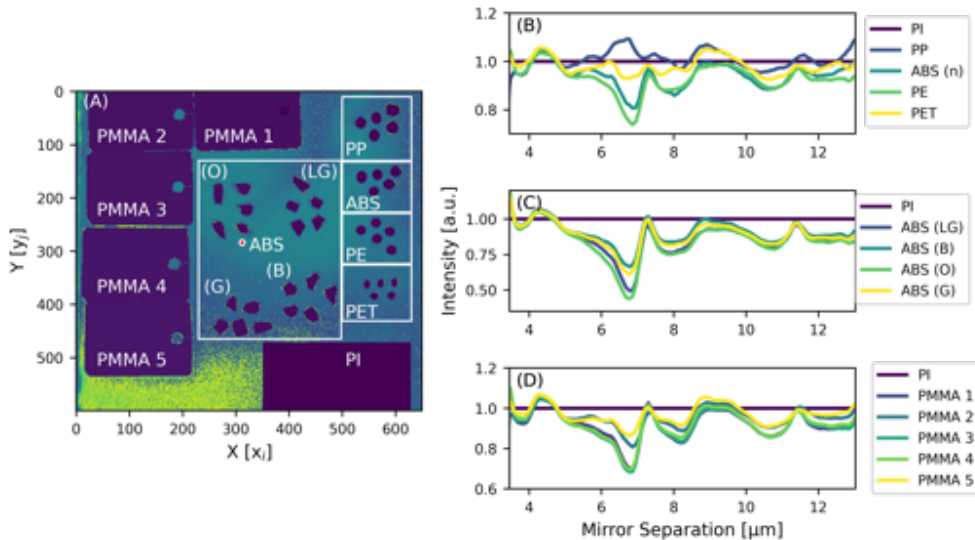
Figure 8.7: (A) Image showing the mask used for the polymer HSTI. (B) mean relative spectra of the polymers shown in (A) marked PI, PP, ABS, PE and PET. (C) mean relative spectra of the polymers shown in (A) marked PI and ABS LG, B, O, and G. (D) mean relative spectra of the polymers marked PMMA 1, PMMA 2, PMMA 3, PMMA 4, and PMMA 5.

components it can be difficult to point out the exact reason why a specific component stands out. However, it can be concluded that the component contributes specifically with systematic variance to the original datacube. For example, the effect of spectral bending, is most strongly observed in PC1 in image A as a radial shadowing effect which is darkest in the center of image A and becomes brighter along the edge and corners. This is the most dominating effect in PC1 which also reveals that the spectral bending is one of the main contributors to the variance in the hyperspectral datacube, which underline the observations from Figure 8.7. The polymer granules are all barely visible and effectively indistinguishable. The spectral bending effect is less prominent in PC2 and all polymers stand out of the image more clearly, although a slight radial effect is observed in the PMMA samples. The intensity variations between the polymers is observed at higher order PCs which indicate that the polymers may be sorted spectrally. In PC5 and PC10 the PET cluster stand out slightly from the remaining neutral colour polymers. In PC6 the ABS polymer granules stand out from the rest and appear darker than the remaining samples. In PC7, PC8 and PC9 the PP
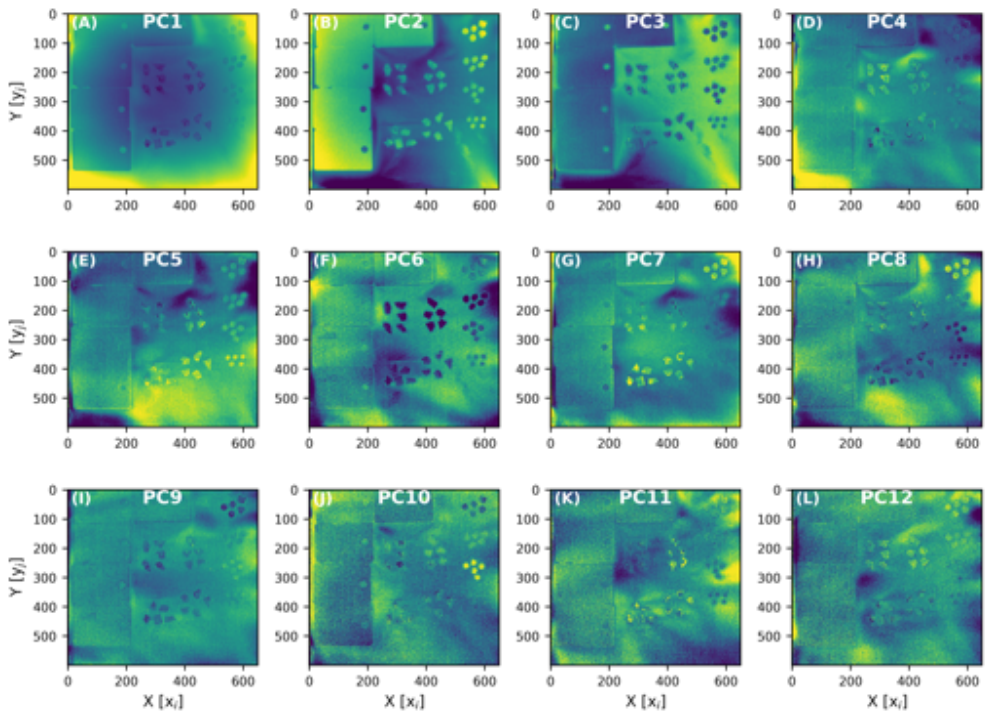
Figure 8.8: (A) through (L) shows the reconstructed images resulting from a PCA of the standardised HSTI in this experiment. The twelve images are sorted, and therefore PC1, which is the principal component with highest variance is shown first. The images show the spectral bending in PC1 as well as significant variance in the polyimide tape used for sample fixture. Aside from this, the images also show differentiable intensity variations in the polymers imaged, which is used for the analysis and classification.
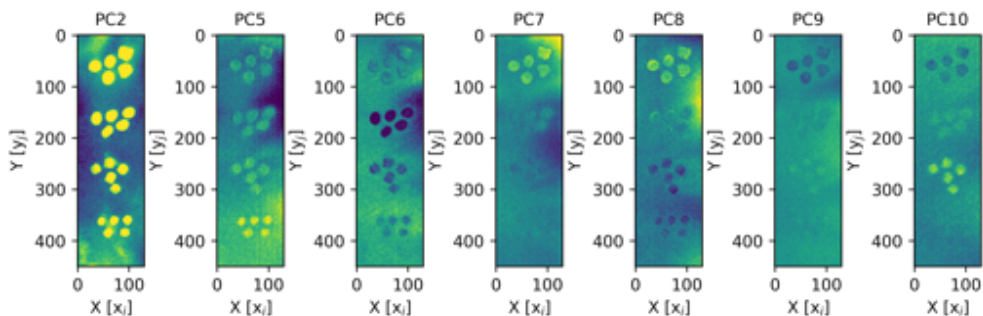
Figure 8.9: A selection of the principal components in Figure 8.8 has been shown. Additionally, the hand picked principal components showing differences between the groups of polymers have been selected. The principal components resulting from this selection are PC2, PC5, PC6, PC7, PC8, PC9, and PC10.

sample stand out slightly from the remaining neutral colour polymers, and in PC10 the PE cluster stand out clearly from all other samples. In all images the intensity of the PI tape background disturbs the image frame which may be due to reflections and temperature differences since the tape was loosely tightened to the aluminium block surface. As mentioned, PI is a polymer as well, and the spectra observed in Figure 8.7 (B), (C), and (D) indicate that the PI spectrum is different from all other polymers used in the experiment. These spectral differences may be those observed in PC2 and PC3 where the intensity of the background is close to homogeneous compared to the higher order PCs. Thus, to conclude on the PCA it is very likely that some of the intensity variances observed in the individual principal components arise from the spectral differences of the polymers and a more detailed analysis can be carried out based on this assumption.

A K-means analysis can be made based on the PCA components shown in Figure 8.8. For this analysis we focus on the four polymers PP, ABS, PE, and PET which appear to stand out individually in the PCs from the image acquired in this experiment as mentioned. The principal components selected for the following analysis are therefore PC2, PC5, PC6, PC7, PC8, PC9, and PC10 and a zoom in of these PCs in the region of interest is shown in Figure 8.9. Following this selection of principal components a K-means analysis was performed containing two clusters which effectively separates the four groups of polymers from the PI background. The effectiveness of this method is mainly assigned to PC2 which clearly separates the polymer granules from the polyimide tape background as seen in Figure 8.9. For the higher order PCs the background

is disturbing, and therefore the cluster containing the background was then used to remove all variance in the remaining PCs by assigning the background a value of zero. Following this a K-means analysis containing five clusters was performed on all PCs shown in Figure 8.9 which allow the clusters and background to be contained with one cluster each. The result of the analysis is shown in Figure 8.10 where the new clusters have been shown collectively and individually. This analysis shows a very decent separation of the polymers where only the PE, and to a lesser extent ABS, is clustered along with the edge of the remaining polymers. The polymer segregation carried out in this experiment shows promising early stage results, and these experiments could continue with the addition of polyvinyl chloride (PVC), polyoxymethylene (POM), polytetrafluoroethylene (PTFE) and polycarbonate. Previous studies report significant spectral features in the range 8-12 µm for these polymers as well [93]. The sorting of PVC is generally of high importance due to the byproducts from the process of PVC combustion [95]. The toxic byproducts from these processes are mainly HCl and benzene. The results presented above are early stage, and more images should be acquired to improve the statistical foundation. Furthermore, the multivariate case of the PLS model may be used to solve this problem based on a large dataset of different spectra with known solutions. The results show that the spectral bending is a persisting problem which highly affects the results obtained, and this factor may not be described by the PLS model. A few solutions to the spectral bending is discussed in the outlook in the following chapter.

8.2.3 Summary and Conclusion

It is concluded that the emission spectrum of the polymers PP, ABS, PE, and PET heated to 100 °C may contain sufficient spectral features in the thermal range, to be segregated individually. It is furthermore concluded that the spectral differences in ABS and PMMA polymer samples based on added colour pigments were too small to be measured in the thermal range.
Inclusion of hyperspectral thermal imaging for polymer sorting could be beneficial for the overall performance of such sorting facility. It should be mentioned that polymer sorting in the visible and near infrared range is very robust at room temperature but the illumination and reflections arising from light sources can be substantial which impacts the classification negatively. As we have seen, hyperspectral thermal imaging is not free from the disturbance of reflections but the reflections and artefacts seen in the thermal range are not necessarily correlated with those in the visible and near infrared. Therefore, the two techniques could be combined to support each other.
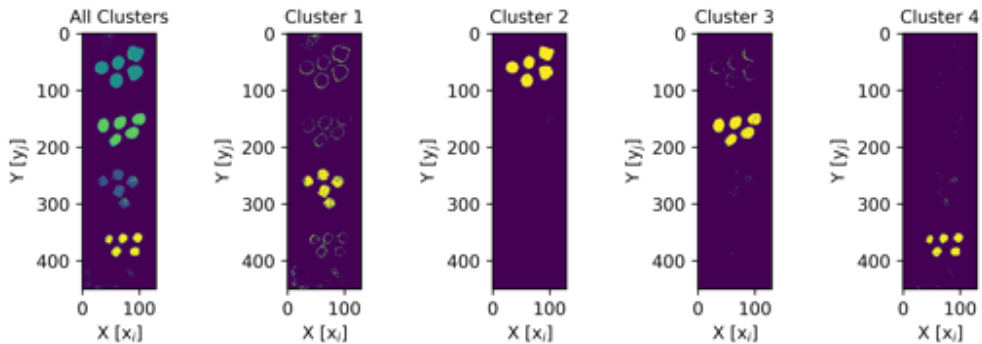
Figure 8.10: Results from a K-means analysis of a selected region of the HSTI containing four groups of polymers. Each group has five polymer granules, and the groups contain PP, ABS, PE, and PET sorted from top to bottom. The background has been set to zero and a K-means analysis with five clusters have been performed on PCA components 1, 5, 6, 7, 8, 9, and 10 shown in Figure 8.8. The initial image shows all five clusters colour coded, and the remaining images show the individual K-means clusters apart from the background containing cluster.

Although heating the polymers may be inefficient to reach the desired signal to noise in a sorting facility, the technique could be applied as a pre-check in combustion facilities where high temperatures are naturally occurring.

9

Summary and Outlook

This chapter present a summary of the main results presented in this thesis. The summary is finalised with a conclusion summarising the key findings of the thesis related to the original list of success criteria. Lastly, an outlook including ideas for further studies and developments is included.

9.1 Summary

Having written this thesis, and lived through most of it during the last three years, it is now time to sum up the current state of the project and the results and findings presented throughout this thesis. The main goal of the project was the development of a hyperspectral thermal camera capable of producing hyperspectral thermal images using a scanning first order FPI. Starting out the project a set of FPI mirrors were available which were grown using BaF_2 and Ge. These FPI mirrors were absorbing a significant part of the light travelling through the interferometer, which strongly affected the quality of the hyperspectral thermal datacube. Several images were produced using these FPI mirrors and a selected set of images was shown to demonstrate the state of the HSTC at this point in time. It was concluded that the signal to noise ratio at room temperature was too low for material identification and temperature determination using these mirrors. However, a HSTI was acquired and analysed at sample temperatures near $100\,°C$ showing that samples of different materials could be segregated and recognised using a PCA and a multinomial logistic regression classification model. The HSTC acquired contained 70 bands.

PVD experiments were conducted in order to improve the FPI mirror coating. Test depositions were carried out with the exchange of the low refractive index layer material and more specifically BaF_2, CeF_3, BaF_2/CaF_2, and IRX. The crystallinity and corrugation of the low refractive index layer was concluded to be lowest for the commercial material Cirom-IRX, however, the intrinsic tensile stress in the film made it impossible to grow thin films of the thicknesses required for the mirror coating. Therefore, to this day the most successful mirror coating is achieved using a three layer coating recipe of $Ge/BaF_2/Ge$.

Following several test depositions it was concluded that the high refractive index layer of Ge was the primary contributor of absorption in the mirror coating. This was measured using standard transmission FTIR in combination with reflection configured FTIR measurements. It was found that the absorption in the Ge layer was due to the amorphous structure of the layer and the fact that no protective coating was deposited onto the Ge.

Alongside the FPI mirror PVD experiments a search for commercially available FPI mirrors was made. The company II-VI Incorporated agreed to produce the FPI mirrors and chose to deposit a $Ge/ThF_4/Ge$ coating. These mirrors were measured to have a mean absorption of $< 1\,\%$ in the sensitivity range of the microbolometer sensor and were therefore used during the final part of this PhD project. These FPI mirrors ensures a much higher signal to noise ratio and allows for HSTIs to be acquired at

temperatures near room temperature.

Using the low absorption II-VI mirrors HSTIs were produced of an experimental setup containing Al_2O_3, Al_2O_3 ceramic, Fused Silica, and Borosilicate glass. All of these materials have fingerprint emission spectra in the LWIR range and are therefore suitable candidates for the goal of material recognition and temperature determination. These materials were recognised based on their specific standardised spectra using a multinomial logistic regression model at temperatures as low as 30.0 °C where the materials were recognised with an accuracy above 54 %. At 34 °C the material recognition was above 94 %. Using the recognised material specific fingerprint spectra the surface temperature was determined based on pre-fitted PLS models. These models were capable of predicting the surface temperature with a RMSE accuracy of 1.1 °C.

Two different alternative applications of HSTI were tested out during the PhD in a search for industrial use-cases of hyperspectral thermal imaging. The first was recognition of organic gasses using HSTI. Here NO, CH_4, tetrafluoroprone, and ethylene were imaged through a zinc selenide gas cell. A PCA was made to distinguish the different gasses with success, showing that the absorption spectra of gasses can be measured with high accuracy. Each individual gas was succeedingly clustered using the K-means algorithm. This study lays the foundation for a larger study searching for the applicability of gas leakage detection in oil and gas facilities.

The second application was recognition and separation of heated polymer granules using HSTI. This experiment shows a strong segregation of individual polymers, and subsequent studies should follow.

Taking time to reflect on the initial success criteria of this project it can be stated that a variable filter with a narrow peak in the range 8-14 µm was constructed. This filter was based on thermal mirrors resulting in an effective bandpass of up to 80 % and a full width at half maximum of 480-280 nm. The FPI mirrors were used in combination to acquire hyperspectral thermal images of 140 spectral bands of various co-dependence. Lastly, a pre-fitted material and temperature recognition model was used to recognise materials of up to 100 % accuracy and determine the temperature with a RMSE of 1.1 °C. This concludes that all success criteria have been met.

9.2 Outlook

Having reached this part of the thesis it is immediately clear that the most obvious point of attack, in order to improve the hyperspectral thermal camera, is the spectral

bending. Thus, the spectral bending will be the first of the following sections, which describes the planned future work regarding the camera. For the reader, reaching this part of the thesis it should be clear that the imaging system has a huge potential. Therefore, the following section serves as inspiration anyone who will work with this system.

9.2.1 Spectral Bending

The spectral bending measured in each individual pixel of the FPA is an important factor to take into account during the further development of the hyperspectral thermal imager. The most obvious workaround of the spectral bending feature is to take the wavelength of each individual pixel on the FPA into account during model fitting and prediction. It is possible to make a full calibration series where the logistic regression functions are fitted relative to the center of the FPA. While the process is tedious the radial dependency of the logistic regression models is a relatively simple programmable solution.

Another possibility is to transform the data according to the spectral bending and spline the datapoint in order to use the material recognition at the correct wavelength bands. This is a more complex solution at the results based on such approach have been inconclusive till this point. A major barrier for a pure mathematical transformation may be the overlapping of wavelengths transmitted through the FPI, which has been mentioned a few times throughout the thesis.

9.2.2 FPI Mirror Development

Several further studies could be carried out regarding the FPI mirrors in order to determine the perfect mirror recipe. The FPI mirrors available at present time show low absorption, however, the physical bending of the substrates, due to tensile film stresses, broaden the transmission peak which essentially lowers the resolution of the hyperspectral imaging system. Several creative solutions can be followed in order to improve the substrate bending such as depositing a two-layer mirror coating or conducting experiments with either pre-polished substrates which compensate the bending effect or the deposition of anti-bending coatings on the backside of the mirror substrate.

Additionally, it is of high importance to conduct experiments which investigate the effect of a protective coating on top of the topmost germanium layer, in order to prevent oxidation of the surface.

Lastly, in order to make the camera mobile, it is of high relevance to find a solution

to the fastening of mirror substrates within the FPI, without substrate bending. This will be a challenge, but it surely can be solved!

9.2.3 Integration of Spectrometers in the Mirror Control Software

The integration of mini-spectrometers on the QT5062 PCB would allow for an on-camera calibration of the mirror substrate separation, which does not require a bandpass filter. This would be a great addition to the HSTC. since the camera would be able to check its own state.

9.2.4 Room Temperature Imaging

A few ideas can be tested out in order to improve room temperature measurements. As seen in chapter 6 the addition of multiple hyperspectral thermal images is a possible pathway to improving the signal to noise ratio. Thus, acquiring several HSTI and meaning the intensity could be beneficial. The practical implementation of this can be done through several pathways. The most efficient, but difficult task would be to acquire images during the forward scan of the FPI as well as during the backwards scan resulting in the acquisition of two datacubes. While this may appear simple the implementation of such a functionality is more complex. This is primarily due to the hysteresis curve of the piezo elements which is shown earlier in Figure 4.3 in chapter 4. Having this hysteresis in the system means that the images grabbed during the backwards scan will have very different mirror separation distances compared to the forward scan. A circumvention of this problem is a complete control of the image acquisition points as mentioned related to the inclusion of spectrometers on the QT5062 PCB. The interferogram of the laser diodes should then be used to determine the transmitted band and the images could then be added. The most difficult part here is to acquire the images at the exact same wavelengths as during the forward scan. Having spectrometers on the QT5062 PCB along with a two wavelength light source would be highly beneficial along with the possibility of sending a triggering signal for the image acquisition.

9.2.5 FPI distinct band selection

Having full control of the Fabry-Pérot interferometer and the transformation between the measured mirror separation and the wavelength axis, it is possible to select one or more specific wavelength bands which belong to certain absorption bands in any gas or material. Keeping the FPI mirrors at these bands with a fixed mirror separation or

jumping between several mirror separations, the choice of materials can be scanned for at a faster rate than during a standard HSTI image acquisition event.

9.2.6 Temperature and Emissivity Separation Algorithms

Based on the results of transmission spectra of gas atmospheres presented in Chapter 8, it is believed that the possibility of developing a temperature and emissivity separation algorithm is within reach. The strong understanding of the camera transfer function at this point in times sets a clear goal for the further development of algorithms. Multivariate PLS models may be used to solve this problem, and this work is surely in progress.

9.2.7 Battery Package Development

In order to make a fully assembled and integrated system a battery management system is needed. This should be fully integrated in the camera, in order to bring the imager to the field with ease. A simple battery solution was made as part of this project, which allowed the camera to be tested in the field. A small description of the battery system is included in Appendix A.2.2. This is a clear step in the direction towards a true mobile camera.

9.2.8 RGB camera addition

The addition of an RGB camera on top of the thermal camera has been made already, and the analysis of HSTIs in combination with RGB images is on the checklist for future work. The addition of an RGB camera is done in order to test the ability of adding even more information to the hyperspectral thermal imaging datacube.

A few studies has appeared during the last decade which combine the spatial information of a conventional image with the spectral information of a hyperspectral image [96].

Now. This is the end of this PhD thesis, but as the reader may realise there is a lot of remaining work to be carried out.

Bibliography

[1] A. L. Jørgensen, M. N. Larsen, J. Kjelstrup-Hansen, B. Jensen, V. Petrunin, and B. Jørgensen, Unpublished - In peer review in Optics Express (2021).

[2] A. L. Jørgensen, J. Kjelstrup-Hansen, B. Jensen, V. Petrunin, S. F. Fink, and B. Jørgensen, Applied Spectroscopy **75**, 317 (2021), ISSN 0003-7028, URL `http://journals.sagepub.com/doi/10.1177/0003702820972382`.

[3] C. F. Kastorp, D. A. Duncan, M. Scheffler, J. D. Thrower, A. L. Jørgensen, H. Hussain, T. L. Lee, L. Hornekær, and R. Balog, Nanoscale **12**, 19776 (2020), ISSN 20403372.

[4] A. L. Jørgensen, D. A. Duncan, C. F. Kastorp, L. Kyhl, Z. Tang, A. Bruix, M. Andersen, B. Hammer, T. L. Lee, L. Hornekær, et al., Physical Chemistry Chemical Physics **21**, 13462 (2019), ISSN 14639076.

[5] *Introduction to Spectroscopy* (2020), URL `https://chem.libretexts.org/@go/page/189392`.

[6] J. S. MacDonald, S. L. Ustin, and M. E. Schaepman, Remote Sensing of Environment **113**, S2 (2009), ISSN 00344257, URL `http://dx.doi.org/10.1016/j.rse.2008.10.017https://linkinghub.elsevier.com/retrieve/pii/S0034425709000716`.

[7] Y. W. Wang, N. P. Reder, S. Kang, A. K. Glaser, and J. T. Liu, Nanotheranostics **1**, 369 (2017), ISSN 22067418.

[8] J. Hansen, R. Ruedy, M. Sato, and K. Lo, Reviews of Geophysics **48**, RG4004 (2010), ISSN 8755-1209, URL `http://doi.wiley.com/10.1029/2010RG000345`.

[9] S. D. Gunapala and S. V. Bandara, *Chapter 4 Quantum Well Infrared Photodetector (QWIP) Focal Plane Arrays*, vol. 62 (1999), ISBN 0127521712.

[10] S. D. Gunapala, S. V. Bandara, J. K. Liu, J. M. Mumolo, C. J. Hill, S. B. Rafol, D. Salazar, J. Woolaway, P. D. LeVan, and M. Z. Tidrow, Infrared Physics and Technology **50**, 217 (2007), ISSN 13504495.

[11] H. Sakaki, L. L. Chang, R. Ludeke, C. A. Chang, G. A. Sai-Halasz, and L. Esaki, Applied Physics Letters **31**, 211 (1977), ISSN 00036951.

[12] B. F. Levine, K. K. Choi, C. G. Bethea, J. Walker, and R. J. Malik, Applied Physics Letters **50**, 1092 (1987), ISSN 00036951.

[13] D. V. Schroeder, *An Introduction to Thermal Physics* (Oxford University Press, 2021), ISBN 9780192895547, URL `https://oxford.universitypressscholarship.com/view/10.1093/oso/9780192895547.001.0001/oso-9780192895547`.

[14] C. M. Lee, M. L. Cable, S. J. Hook, R. O. Green, S. L. Ustin, D. J. Mandl, and E. M. Middleton, Remote Sensing of Environment **167**, 6 (2015), ISSN 00344257, URL `http://dx.doi.org/10.1016/j.rse.2015.06.012`.

[15] M. J. Abrams and S. J. Hook, in *Thermal Infrared Remote Sensing, Sensors, Methods, Applications* (2013), pp. 117–130, URL `http://link.springer.com/10.1007/978-94-007-6639-6_6`.

[16] W. R. Johnson, S. J. Hook, P. Mouroulis, D. W. Wilson, S. D. Gunapala, V. Realmuto, A. Lamborn, C. Paine, J. M. Mumolo, and B. T. Eng, IEEE Aerospace Conference Proceedings **91109**, 1 (2011), ISSN 1095323X.

[17] P. R. Christensen, S. W. Ruff, R. L. Fergason, A. T. Knudson, S. Anwar, R. E. Arvidson, J. L. Bandfield, D. L. Blaney, C. Budney, W. M. Calvin, et al., Science **305**, 837 (2004), ISSN 00368075.

[18] S. Silverman, R. Peralta, P. Christensen, and G. Mehall, Acta Astronautica **59**, 990 (2006), ISSN 00945765.

[19] P. R. Christensen, M. B. Wyatt, T. D. Glotch, A. D. Rogers, S. Anwar, R. E. Arvidson, J. L. Bandfield, D. L. Blaney, C. Budney, W. M. Calvin, et al., Science **306**, 1733 (2004), ISSN 00368075.

[20] *Specim LWIR HS and OWL*, URL `https://www.specim.fi/hyperspectral-cameras/`.

[21] Y. Montembeault, P. Lagueux, V. Farley, A. Villemaire, and K. C. Gross, 2nd Workshop on Hyperspectral Image and Signal Processing: Evolution in Remote Sensing, WHISPERS 2010 - Workshop Program pp. 7–10 (2010).

142

[22] M. T. Eismann, J. N. Cederquist, and C. R. Schwartz (1994), vol. 2235, pp. 130–147, URL http://proceedings.spiedigitallibrary.org/proceeding.aspx?articleid=966385.

[23] M. T. Eismann, J. H. Seldin, C. R. Schwartz, J. R. Maxwell, K. K. Ellis, J. N. Cederquist, A. D. Stocker, A. Oshagan, R. O. Johnson, W. A. Shaffer, et al. (1995), vol. 2819, pp. 80–97, URL http://proceedings.spiedigitallibrary.org/proceeding.aspx?articleid=1007009.

[24] T. L. Myers, T. J. Johnson, N. B. Gallagher, B. E. Bernacki, T. N. Beiswenger, J. E. Szecsody, R. G. Tonkyn, A. M. Bradley, Y.-F. Su, and T. O. Danby, Journal of Applied Remote Sensing **13**, 1 (2019), ISSN 1931-3195.

[25] M. Schlerf, G. Rock, P. Lagueux, F. Ronellenfitsch, M. Gerhards, L. Hoffmann, and T. Udelhoven, Remote Sensing **4**, 3995 (2012), ISSN 20724292.

[26] S. Boubanga-Tombet, A. Huot, I. Vitins, S. Heuberger, C. Veuve, A. Eisele, R. Hewson, E. Guyot, F. Marcotte, and M. Chamberland, Remote Sensing **10**, 1 (2018), ISSN 20724292.

[27] B. Yousefi, S. Sojasi, C. Ibarra Castanedo, G. Beaudoin, F. Huot, X. P. V. Maldague, M. Chamberland, and E. Lalonde, Thermosense: Thermal Infrared Applications XXXVIII **9861**, 986118 (2016), ISSN 1996756X.

[28] Y. Roggo, A. Edmond, P. Chalus, and M. Ulmschneider, **535**, 79 (2005).

[29] P. Lasch, M. Stämmler, M. Zhang, M. Baranska, A. Bosch, and K. Majzner, Analytical Chemistry **90**, 8896 (2018), ISSN 0003-2700, URL https://pubs.acs.org/doi/10.1021/acs.analchem.8b01024.

[30] W. J. Marinelli, C. M. Gittins, A. H. Gelb, and B. D. Green, Applied Optics **38**, 2630 (1999), ISSN 15394522.

[31] C. Fabry and A. Pérot, Ann. Chim Phys. **16 115–44** (1899).

[32] S. D. Smith, Journal of the Optical Society of America **48**, 43 (1958), ISSN 0030-3941, URL https://www.osapublishing.org/abstract.cfm?URI=josa-48-1-43.

[33] Semicore, *DC-Sputtering Diagram*, URL http://www.semicore.com/images/photos/diagram-dc-magnatron.png.

[34] Wikipedia, *E-beam Diagram*, URL `https://upload.wikimedia.org/wikipedia/commons/f/ff/Electron_Beam_Deposition_001.jpg`.

[35] A. A. Michelson and E. W. Morley, American Journal of Science **s3-34**, 333 (1887), ISSN 0002-9599, URL `http://www.ajsonline.org/cgi/doi/10.2475/ajs.s3-34.203.333`.

[36] H. A. Macleod, Thin-Film Optical Filters, Fourth Edition pp. 1–782 (2010).

[37] R. S. Caldwell and H. Y. Fan, Physical Review **114**, 664 (1959), ISSN 0031-899X, URL `https://link.aps.org/doi/10.1103/PhysRev.114.664`.

[38] T. S. Moss, Proceedings of the Physical Society. Section B **65**, 62 (1952), ISSN 0370-1301, URL `https://iopscience.iop.org/article/10.1088/0370-1301/65/1/309`.

[39] R. G. Greenler, Journal of the Optical Society of America **45**, 788 (1955), ISSN 0030-3941, URL `https://www.osapublishing.org/abstract.cfm?URI=josa-45-10-788`.

[40] F. Weiting and Y. Yixun, Infrared Physics **30**, 371 (1990), ISSN 00200891, URL `https://linkinghub.elsevier.com/retrieve/pii/002008919090055Z`.

[41] C. Evans, R. Hunneman, and J. Seeley, Optica Acta: International Journal of Optics **23**, 297 (1976), ISSN 0030-3909, URL `https://www.tandfonline.com/doi/full/10.1080/713819255`.

[42] J. S. Seeley, R. Hunneman, and A. Whatley, Applied Optics **20**, 31 (1981), ISSN 0003-6935, URL `https://www.osapublishing.org/abstract.cfm?URI=ao-20-1-31`.

[43] Y.-h. Yen, L.-x. Zhu, W.-D. Zhang, F.-s. Zhang, and S.-y. Wang, Applied Optics **23**, 3597 (1984), ISSN 0003-6935, URL `https://www.osapublishing.org/abstract.cfm?URI=ao-23-20-3597`.

[44] K. Zhang, J. S. Seeley, R. Hunneman, and G. J. Hawkins (1990), p. 45, URL `http://proceedings.spiedigitallibrary.org/proceeding.aspx?doi=10.1117/12.961354`.

[45] N. Gupta, V. B. Voloshinov, G. A. Knyazev, and L. A. Kulakova, Journal of Optics **13**, 055702 (2011), ISSN 2040-8978, URL `https://iopscience.iop.org/article/10.1088/2040-8978/13/5/055702`.

[46] G. Hass, J. B. Ramsey, and R. Thun, Journal of the Optical Society of America **49**, 116 (1959), ISSN 0030-3941.

[47] James D. Rancourt, *Optical Thin Films: User Handbook* (SPIE - The International Society for Optical Engineering, 1996), ISBN 9780819465092.

[48] S. Pellicori, Thin Solid Films **113**, 287 (1984), ISSN 00406090, URL `https://linkinghub.elsevier.com/retrieve/pii/004060908490470X`.

[49] J. D. Targove and A. R. Murphy, Thin Solid Films **191**, 47 (1990), ISSN 00406090, URL `https://linkinghub.elsevier.com/retrieve/pii/004060909090273G`.

[50] A. Schnellbuegel, H. Hagedorn, and R. Anton (1994), vol. 2253, p. 839, URL `http://proceedings.spiedigitallibrary.org/proceeding.aspx?doi=10.1117/12.192160`.

[51] J. T. Knudtson, Optical Engineering **35**, 2313 (1996), ISSN 0091-3286, URL `http://opticalengineering.spiedigitallibrary.org/article.aspx?doi=10.1117/1.600806`.

[52] D. L. Perry, Applied Optics **4**, 987 (1965), ISSN 0003-6935.

[53] S. J. Byrnes, pp. 1–20 (2016), `1603.02720`, URL `http://arxiv.org/abs/1603.02720`.

[54] M. Hausladen and S. J. Kjelstrup-Hansen (2014).

[55] J. A. Thornton, J Vac Sci Technol **11**, 666 (1974), ISSN 0022-5355.

[56] J. A. Thornton, in *Journal of Chemical Information and Modeling*, edited by M. R. Jacobson (1988), vol. 53, p. 95, ISBN 9788578110796, ISSN 1098-6596, `arXiv:1011.1669v3`, URL `http://proceedings.spiedigitallibrary.org/proceeding.aspx?doi=10.1117/12.941846`.

[57] A. M. Ledger, Applied Optics **18**, 2979 (1979), ISSN 0003-6935.

[58] H. K. Pulker, Applied Optics **18**, 1969 (1979), ISSN 0003-6935, URL `https://www.osapublishing.org/abstract.cfm?URI=ao-18-12-1969`.

[59] O. De Gryse, P. Vanmeerbeek, J. Vanhellemont, and P. Clauws, Physica B: Condensed Matter **376-377**, 113 (2006), ISSN 09214526, URL `https://linkinghub.elsevier.com/retrieve/pii/S0921452605014195`.

[60] S. Rivillon, Y. J. Chabal, F. Amy, and A. Kahn, Applied Physics Letters **87**, 253101 (2005), ISSN 0003-6951, URL `http://aip.scitation.org/doi/10.1063/1.2142084`.

[61] Y. A. Bioud, E. Paradis, A. Boucherif, D. Drouin, and R. Arès, Electrochemistry Communications **122**, 106906 (2021), ISSN 13882481, URL `https://linkinghub.elsevier.com/retrieve/pii/S1388248120302575`.

[62] G. Hass and E. Ritter, Journal of Vacuum Science and Technology **4**, 71 (1967), ISSN 0022-5355.

[63] B. I. Johnson, T. G. Avval, R. S. Turley, M. R. Linford, and D. D. Allred, OSA Continuum **4**, 879 (2021), ISSN 2578-7519.

[64] W. T. Su, B. Li, D. Q. Liu, and F. S. Zhang, Infrared Physics and Technology **52**, 204 (2009), ISSN 13504495, URL `http://dx.doi.org/10.1016/j.infrared.2009.07.008`.

[65] A. E. Ennos, Applied Optics **5**, 51 (1966), ISSN 0003-6935.

[66] E. N. Kotlikov and Y. A. Novikova, Optics and Spectroscopy (English translation of Optika i Spektroskopiya) **117**, 381 (2014), ISSN 15626911.

[67] *MATERION SAFETY DATA SHEET LIBRARY*, URL `https://materion.com/resource-center/environmental-health-and-safety/safety-data-sheets`.

[68] S. F. Pellicori and E. Colton, Thin Solid Films **209**, 109 (1992), ISSN 00406090.

[69] Materion, *CIROM-IRX Overview*, URL `https://materion.com/resource-center/product-data-and-related-literature/inorganic-chemicals/fluorides/cirom-irx-a-non-radioactive-replacement-for-thf4`.

[70] S. A. Firoozifar, A. Behjat, E. Kadivar, S. M. Ghorashi, and M. B. Zarandi, Applied Surface Science **258**, 818 (2011), ISSN 01694332, URL `http://dx.doi.org/10.1016/j.apsusc.2011.08.105`.

[71] R. W. Helfrich (1979), pp. 110–123, URL `http://proceedings.spiedigitallibrary.org/proceeding.aspx?articleid=1228368`.

[72] O. Riou, S. Berrebi, and P. Bremond, Thermosense XXVI **5405**, 294 (2004), ISSN 0277786X.

[73] M. Vollmer and K.-P. Möllmann, *Infrared Thermal Imaging* (Wiley-VCH Verlag GmbH & Co. KGaA, Weinheim, Germany, 2017), ISBN 9783527693306, URL `http://doi.wiley.com/10.1002/9783527693306`.

[74] F. Pedregosa, G. Varoquaux, A. Gramfort, V. Michel, B. Thirion, O. Grisel, M. Blondel, A. Müller, J. Nothman, G. Louppe, et al., Journal of Machine Learning Research **127**, 2825 (2012), ISSN 15529924, 1201.0490, URL `http://arxiv.org/abs/1201.0490`.

[75] K. Pearson, The London, Edinburgh, and Dublin Philosophical Magazine and Journal of Science **2**, 559 (1901), ISSN 1941-1982.

[76] S. Wold, K. Esbensen, and P. Geladi, Chemometrics and Intelligent Laboratory Systems **2**, 37 (1987), ISSN 01697439, URL `https://linkinghub.elsevier.com/retrieve/pii/0169743987800849`.

[77] A. Abraham, F. Pedregosa, M. Eickenberg, P. Gervais, A. Muller, J. Kossaifi, A. Gramfort, B. Thirion, and G. Varoquaux, *Hands-On Machine Learning with Scikit-Learn and TensorFlow.pdf* (2014), 1412.3919, URL `http://arxiv.org/abs/1412.3919`.

[78] S. Wold, M. Sjöström, and L. Eriksson, Chemometrics and Intelligent Laboratory Systems **58**, 109 (2001), ISSN 01697439.

[79] I. S. . Helland, Scandinavian Journal of Statistics **17**, 97 (1990), URL `https://www.jstor.org/stable/4616159`.

[80] A. Gabrieli, R. Wright, P. G. Lucey, J. N. Porter, H. Garbeil, E. Pilger, and M. Wood, Bulletin of Volcanology **78** (2016), ISSN 14320819.

[81] R. Wright, P. Lucey, S. Crites, K. Horton, M. Wood, and H. Garbeil, Acta Astronautica **87**, 182 (2013), ISSN 00945765, URL `http://dx.doi.org/10.1016/j.actaastro.2013.01.001`.

[82] A. Adams, F. Nicol, S. McHugh, J. Moore, G. Matis, and G. A. Amparan, in *Infrared Imaging Systems: Design, Analysis, Modeling, and Testing XXX*, edited by K. A. Krapels and G. C. Holst (SPIE, 2019), p. 28, ISBN 9781510626676, URL `https://www.spiedigitallibrary.org/conference-proceedings-of-spie/11001/2518768/Vantablack-properties-in-commercial-thermal-infrared-imaging-systems/10.1117/12.2518768.full`.

[83] L. J. Bellamy, *The Infra-red Spectra of Complex Molecules* (Springer Netherlands, Dordrecht, 1975), ISBN 978-94-011-6019-3, URL `http://link.springer.com/10.1007/978-94-011-6017-9`.

[84] *LIBLINEAR – A Library for Large Linear Classification*, URL `https://www.csie.ntu.edu.tw/$\sim$cjlin/liblinear/`.

[85] G. Socrates, *Infrared and Raman characteristic group frequencies, third edition* (2001), ISBN 978-0-470-09307-8.

[86] A. Gabrieli, R. Wright, J. N. Porter, P. G. Lucey, and C. Honnibal, Bulletin of Volcanology **81** (2019), ISSN 14320819.

[87] G. C. Hulley, R. M. Duren, F. M. Hopkins, S. J. Hook, N. Vance, P. Guillevic, W. R. Johnson, B. T. Eng, J. M. Mihaly, V. M. Jovanovic, et al., Atmospheric Measurement Techniques **9**, 2393 (2016), ISSN 18678548.

[88] C. Funk, J. Theiler, D. Roberts, and C. Borel, IEEE Transactions on Geoscience and Remote Sensing **39**, 1410 (2001), ISSN 01962892, `arXiv:1011.1669v3`, URL `http://ieeexplore.ieee.org/document/934073/`.

[89] L. Kuai, O. V. Kalashnikova, F. M. Hopkins, G. C. Hulley, H. Lee, M. J. Garay, R. M. Duren, J. R. Worden, and S. J. Hook, IEEE Journal of Selected Topics in Applied Earth Observations and Remote Sensing **12**, 4798 (2019), ISSN 21511535.

[90] S. J. Hook, W. R. Johnson, and M. J. Abrams, *NASA's Hyperspectral Thermal Emission Spectrometer (HyTES)*, vol. 17 of *Remote Sensing and Digital Image Processing* (Springer Netherlands, Dordrecht, 2013), ISBN 978-94-007-6638-9, URL `http://link.springer.com/10.1007/978-94-007-6639-6`.

[91] A. Gillespie, S. Rokugawa, T. Matsunaga, J. Steven Cothern, S. Hook, and A. B. Kahle, IEEE Transactions on Geoscience and Remote Sensing **36**, 1113 (1998), ISSN 01962892.

[92] H. Haixia, Z. Bing, L. Bo, Z. Wenjuan, and L. Ru, 2009 Joint Urban Remote Sensing Event (2009).

[93] A. Vázquez-Guardado, M. Money, N. McKinney, and D. Chanda, Applied Optics **54**, 7396 (2015), ISSN 0003-6935.

[94] H. Wotruba, IMPC 2006 - Proceedings of 23rd International Mineral Processing Congress pp. 21–29 (2006).

[95] Z. Wang, R. Wei, X. Wang, J. He, and J. Wang, Materials **11** (2018), ISSN 19961944.

[96] Y. Liu, S. Zhou, W. Han, W. Liu, Z. Qiu, and C. Li, Analytica Chimica Acta **1086**, 46 (2019), ISSN 00032670, URL `https://linkinghub.elsevier.com/retrieve/pii/S0003267019309675`.

[97] M. N. Larsen, Master thesis, Southern University of Denmark (2021).

A

Appendix

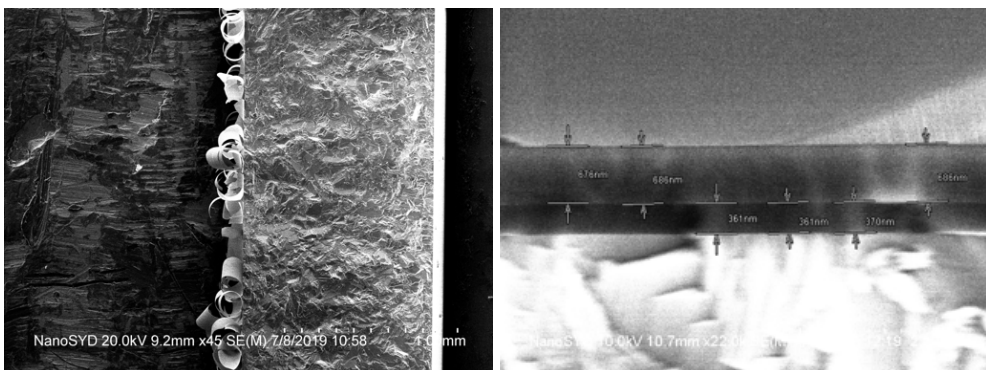## A.1 A First Order Scanning Fabry Pérot Interferometer

Figure A.1: (A) SEM image of a PVD deposition on ZnSe of 300 nm Ge / 875 nm IRX. (B) SEM image of a PVD deposition on ZnSe of 300 nm Ge / 875 nm IRX.
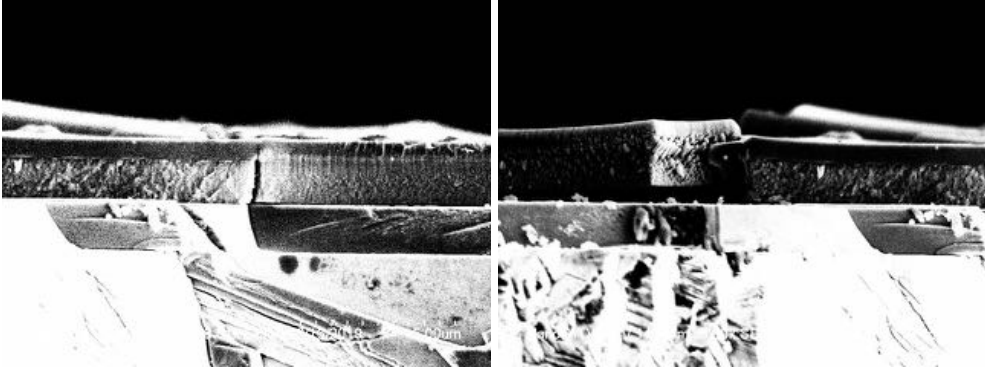
Figure A.2: (A) SEM image showing a cross-sectional analysis of the final ZnSe | Ge/IRX/Ge film deposition. The structure shows major individual craks throughout the IRX layer, affecting the final Ge layer as well. (B) SEM image showing a cross-sectional analysis of the final ZnSe | Ge/IRX/Ge film deposition. The structure shows major individual craks throughout the IRX layer, affecting the final Ge layer as well.
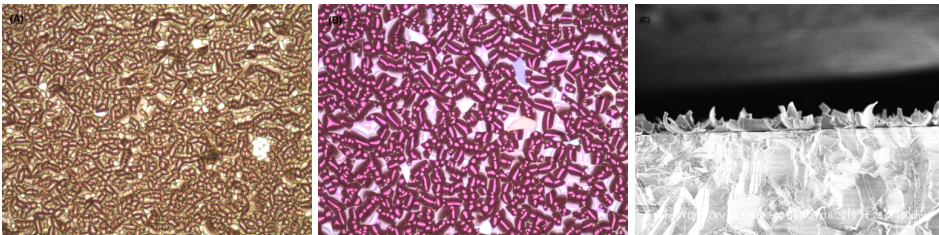

Figure A.3: (A) Optical microscopy image of a CeF$_3$ deposition at 90 °C using a 5 Å s^{-1} deposition rate. The image is acquired using a 20x objective. (B) Optical microscopy image of a CeF$_3$ deposition at 90 °C using a 100 Å s^{-1} deposition rate. The image is acquired using a 20x objective. (C) SEM image of the coating mentioned in (B).

A.1.1 FTIR Measurements of an FPI Assembly

The graph below show FTIR measurements through an FPI assembly. A constant mirror seperation is kept between the mirrors during a scan. While the alignment of the mirrors was unknown during measurment, the small spotsize of the FTIR ensures that any slight misalignment has little impact on the width of the transmitted peak.
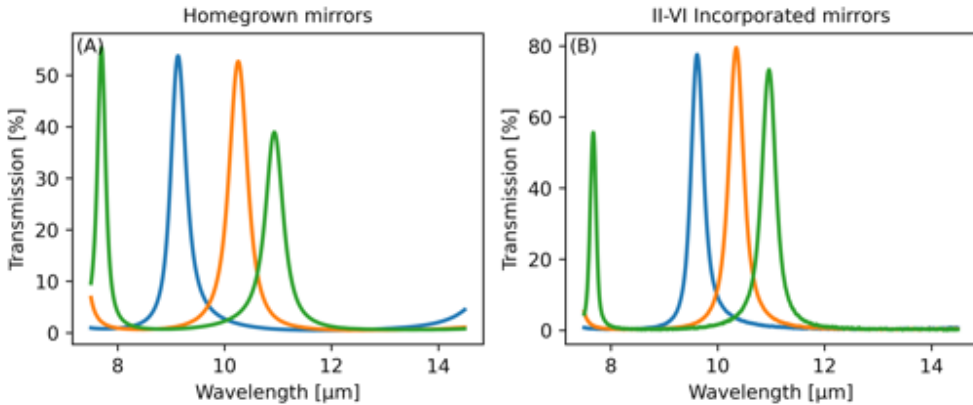
Figure A.4: (A) FTIR measurements of an FPI assembly containing two homegrown mirrors with a mirror recipe of ZnSe | Ge/BaF$_2$/Ge. The transmitted intensity is located around 50 % for wavelengths below 11 µm. At 11 µm the transmitted intensity is around 40 %. These values can be reproduced theoretically cf. equation 2.8 and the measured absorption found in Figure 3.2. (B) FTIR measurements of an FPI assembly containing two II-VI Incorporated mirrors. The transmission percentage lies slightly below 80 %. These values can be reproduced theoretically cf. equation 2.8 and the measured absorption found in Figure 3.10.

A.2 Development and Functionality of a Hyperspectral Thermal Imaging Prototype

A.2.1 Sensor Sensitivities at 1.25x Gain

A dataseries was made in order to quantify the temperature ranges observable by the bolometer sensor. The experimental setup is shown in Figure A.5 where (A) shows the raw output of the camera. Figure A.5 (B) show the background image of the sensor which was acquired while blocking the sensor with a shutter, and (C) shows the resulting image from a subtraction of (B) from (A). Figure A.5 (D) shows an RGB image of the setup.

The data used for analysis includes background subtracted images as shown in Figure A.5 (C). These images do not suffer from the permanent pixel offset characteristic of the bolometer chip, and therefore more pixels contribute to the actual data analysis. Note that a single point non-uniformity correction is used, which explain the rising standard deviation in Figure A.6 (A). Figures A.6 (B) and (C) are derived from the slopes of (A) and (C) show the resulting temperature span following the marked GFID settings and an 1.25x sensor gain.
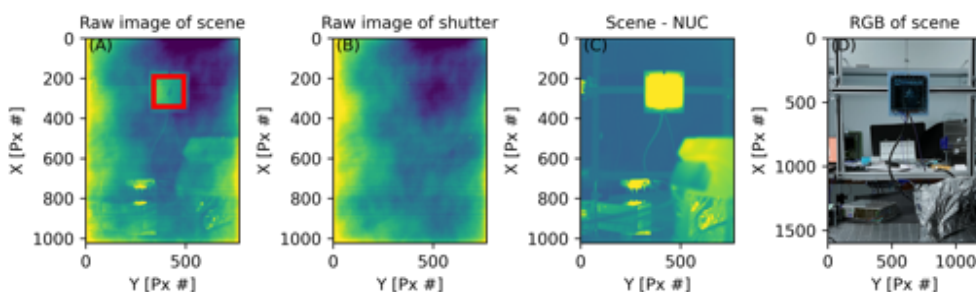

Figure A.5: (A) A raw image of the scene used for investigating the Pico 1024 GFID setting. (B) A raw image of the non uniformity of the sensor, which has been grabbed by inserting a shutter in front of the lens. (C) The resulting image when subtracting the image shown in (B) from the image shown in (A). (C) An RGB image of the setup.
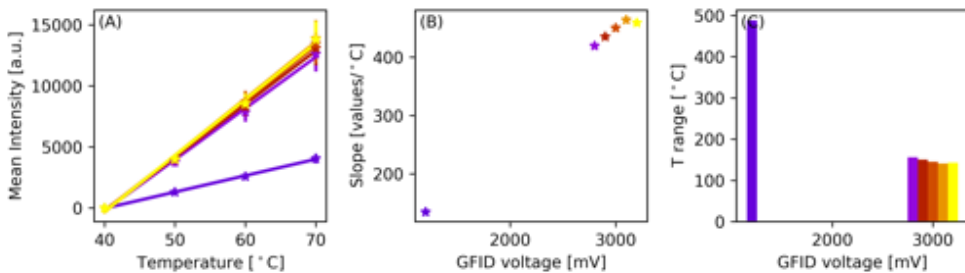
Figure A.6: Measurements of the sensor setting GFID with a gain of 1.25. (A) The mean intensity of the active area of a standard thermal image of a hotplate at temperatures of 40, 50, 60, and 70 °C. (B) The slopes of the linearly regressed lines in (A). The corresponding temperature range provided that 16-bit images are grabbed.

A.2.2 The Battery Package

In order to bring the hyperspectral thermal camera to the field, a lithium ion battery package was made which fitted the camera. The battery package has a 7S2P configuration and consists of 18650 lithium ion battery cells. The specific cell used is an ICR18650 Samsung cell with a charging voltage of 4.2 V and an energy capacity of 2600 mAh. Having 7 cells in series and two parallel rows the battery pack will hold 29.4 V at full charge with an energy capacity of 5.2 Ah. The charging voltage of 29.4 V lies within the tolerances of the QT5022 camera body and the battery package is therefore perfectly capable of running the hyperspectral thermal camera. The battery pacakage is made from a PCB assembly based on the design of Jehu Garcia[1]. Since the battery pack is equipped with rechargeable lithium ion cells a battery management system (BMS) is needed in order to protect the cells from both under voltage and over voltage during charging. The BMS used in this system is a single 20 A system which measures the voltage of each individual Li-ion cell. As the voltage drops the BMS will turn off the current supplied by the battery pack.

During the final part of this PhD project the hyperspectral thermal camera was brought out of the lab in order to acquire hyperspectral thermal images of the front facing wall of Sorø Abbey church running on battery power. The image analysis has been documented by Larsen[97].

---

[1] Available at: JAG35.com

A.2.3 Absolute Distance Derivation

The distance between two completely flat mirror substrates is calculated as

$$\lambda_m m = 2nd\cos(\theta) \qquad\qquad \lambda_{m+1}(m+1) = 2nd\cos(\theta)$$

$\Updownarrow$

$$m = \frac{2nd\cos(\theta)}{\lambda_m} \qquad\qquad m+1 = \frac{2nd\cos(\theta)}{\lambda_{m+1}}$$

$\Updownarrow$ substituting for m

$$1 = 2nd\cos(\theta)\left(\frac{1}{\lambda_m} - \frac{1}{\lambda_{m+1}}\right)$$

$\Updownarrow$

$$d = \frac{1}{2n\cos(\theta)}\frac{\lambda_m\lambda_{m+1}}{\lambda_{m+1} - \lambda_m} \qquad\qquad . \qquad\qquad (A.1)$$

A.2.4 Ibsen Calibration Parameters

All spectrometers are calibrated using the following relation:

$$\lambda = B_0 + B_1 pix + B_2 pix^2 + B_3 pix^3 + B_4 pix^4 + B_5 pix^5$$

This calibration is accounted for every spectrometer as shown in the alignment application in.[reference] The calibration parameters for each FST-101 is shown in Table A.1.

Serial number: 161393	Serial number: 161392	Serial number: 161391
Calibration:	Calibration:	Calibration:
B_0: $5.14536E + 01$	B_0: $4.86887E + 01$	B_0: $4.81564E + 01$
B_1: $6.13356E - 01$	B_1: $6.24021E - 01$	B_1: $6.19383E - 01$
B_2: $6.27419E - 05$	B_2: $4.98578E - 05$	B_2: $6.43391E - 05$
B_3: $1.56729E - 08$	B_3: $2.36372E - 08$	B_3: $1.07503E - 08$
B_4: $-2.10190E - 11$	B_4: $-2.28991E - 11$	B_4: $-1.87932E - 11$

Table A.1: Table summarising the calibration parameters needed for a truw wavelength reading on the three IBSEN VIS-NIR spectrometers used as part of the FPI mirror alignment application.

A.3 Hyperspectral Thermal Imaging using II-VI mirrors

A.3.1 Surface Temperature Determination of Glass Types Using Hyperspectral Thermal Imaging - Additional Results
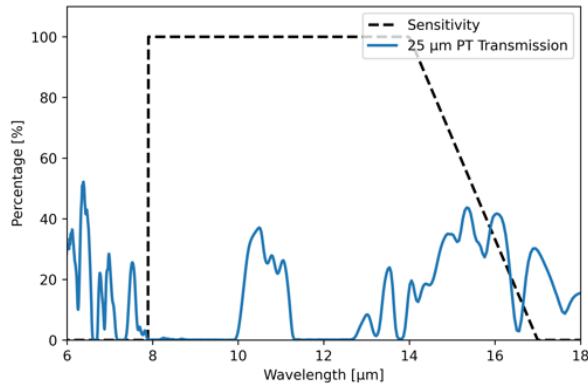
Figure A.7: Figure showing an FTIR measurement of the polyimide tape (PT) of 25 µm thickness used during this project. The figure shows that the PT is not completely opaque to the LWIR.
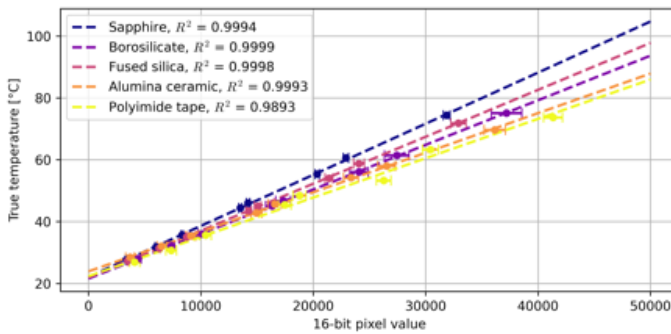
Figure A.8: A calibration dataseries is shown where the mean intensity of the area covering the surfaces of each sample is plotted against their true temperature. The true temperature was measured using polyimide tape as a reference. The graph shows the errors arising from various emissivity settings within this experiment.
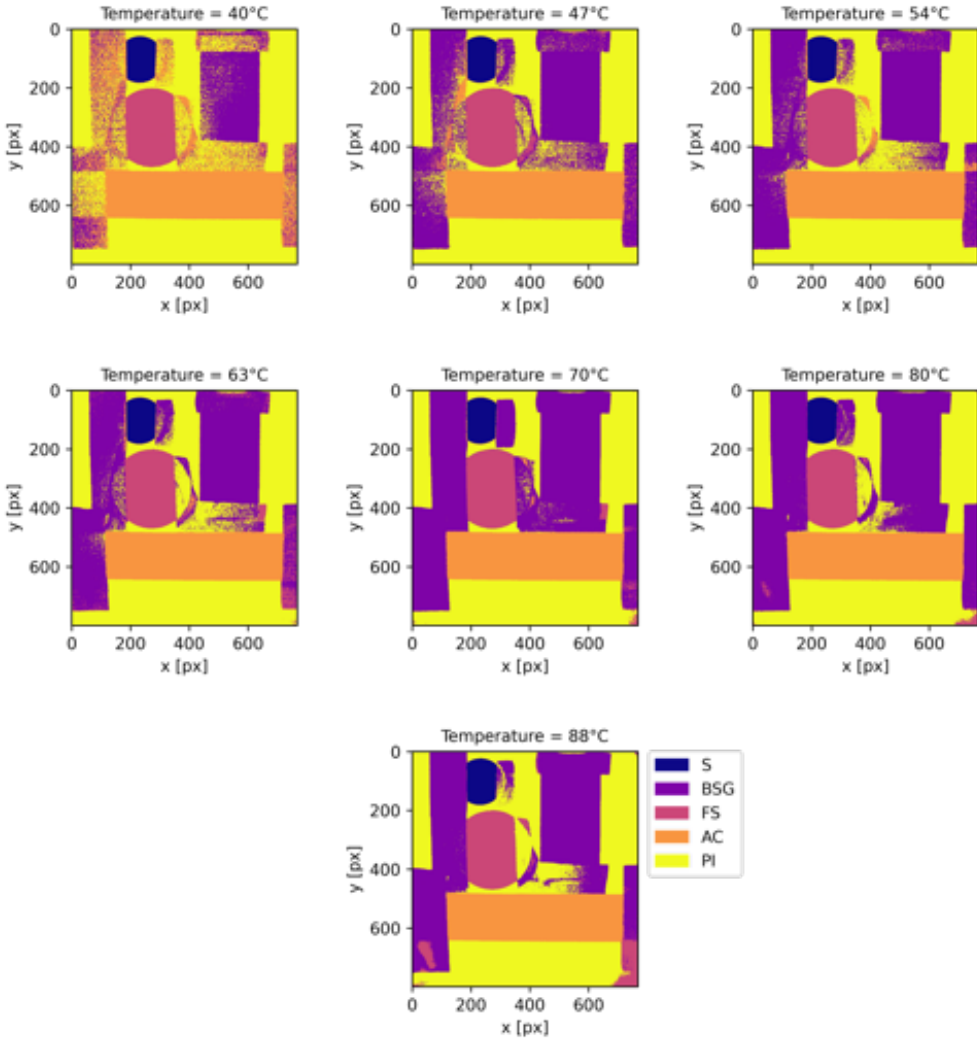
Figure A.9: Prediction results based on the MLR function used for classifiyng materials in Chapter 7. The images show the results of the 7 intermediate temperatures in the dataset.
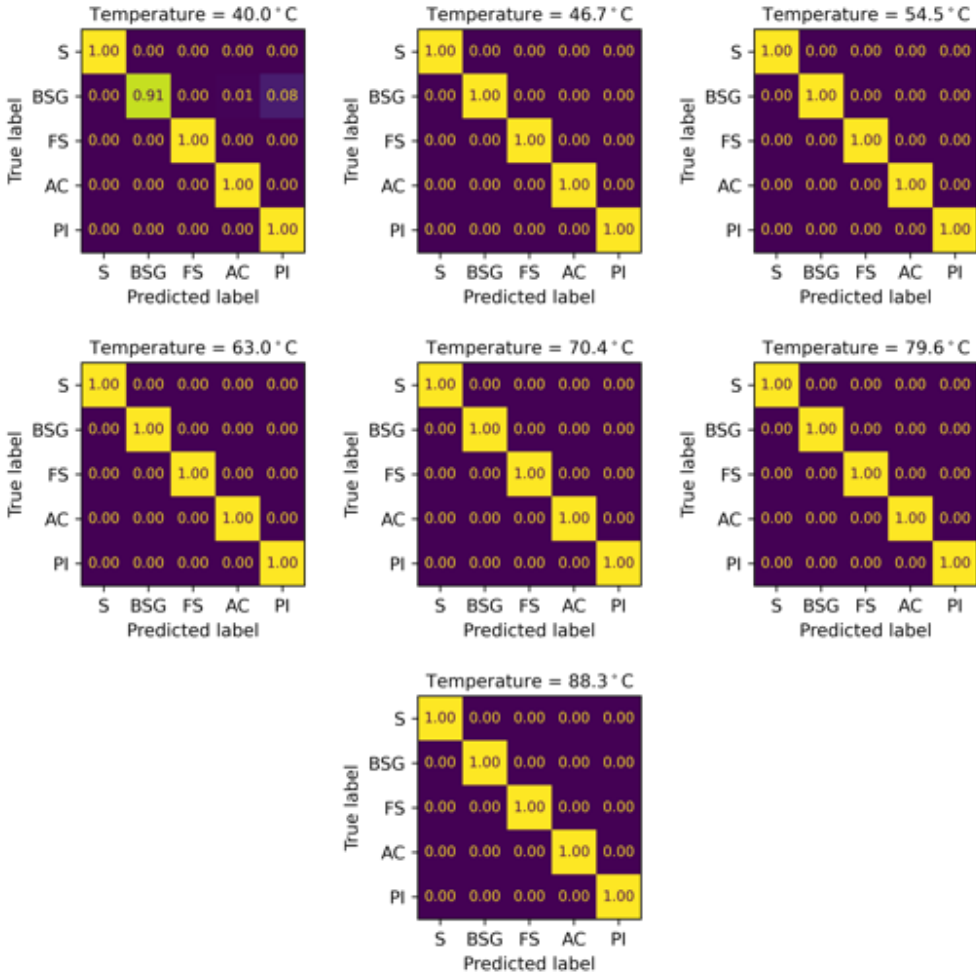
Figure A.10: Confusion matrices calculated from the MLR predictions shown in Figure A.9. The matrices show the results of the 7 intermediate temperatures in the dataset related to Chapter 7.

B

Python Scripts

B.1 Alignment application
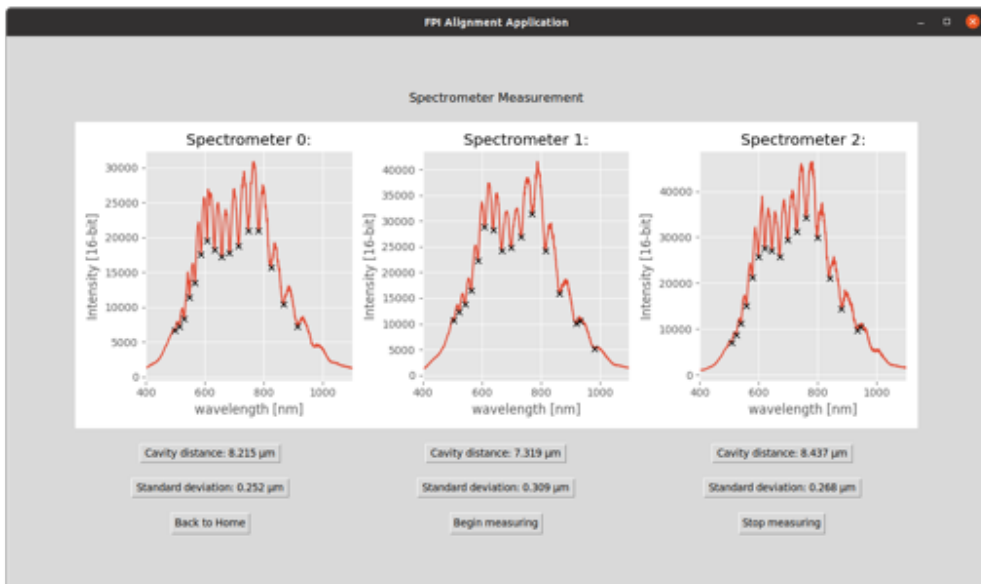
Figure B.1: A blown up view of the alignment application window used for the assembly of the FPI. The three graph windows show live measurements from the IBSEN spectrometers. In the version shown here the application measures the minima positions and calculate the absolute distance between the FPI mirrors based on these positions for each individual spectrometer.

B.1.1 FPI alignment app

This application builds on top of the main communication script FT4222.py provided by Ibsen Photonics. The FT4222 script was slightly modified to improve overall speed and spectrum acquisition time for the FPI alignment application.

```python
import matplotlib
matplotlib.use("TkAgg")
from matplotlib.backends.backend_tkagg import FigureCanvasTkAgg, NavigationToolbar2Tk
from matplotlib.figure import Figure
import matplotlib.animation as animation
from matplotlib import style
from controls.FT4222 import *
import threading
import time
import sys
from scipy.signal import find_peaks, argrelextrema
import numpy as np

import tkinter as tk
from tkinter import ttk

def check_number_of_devs(var):
    if var:
        tempvar = int(len(list_devices())/4)
        var.set("Number of spectrometers connected: %s" %tempvar)
        if tempvar == 3:
            return True


def thickness(l1,l2,n,alfa):
    return (l1*l2)/(2*n*(l2-l1)*np.cos(np.arcsin(np.sin(alfa)/n)))/1000


def animate(i):
    prominence_min = 1000
    prominence_max = None
    xlim_min = 400
    xlim_max = 1100
    peak_distance = 10
    peak_width = 5
    baseline_height = 2000
    refractive_index = 1
    minimaorder = 10
    minima = True
    maxima = False


    pullData = open("static/spec0Data.txt","r")
    dataList = pullData.read().split('\n')
    xList = []
    yList = []
```

```python
for eachLine in dataList:
    if len(eachLine) > 1:
        x, y = eachLine.split(',')
        xList.append(float(x))
        yList.append(int(y))

pullData.close()

meas = np.array(yList)[580:1380]
wvls = np.array(xList)[580:1380]

if maxima:
  peaks, _ = find_peaks(meas, distance=peak_distance, height=baseline_height,width=↵
      peak_width,prominence=[prominence_min,prominence_max])
if minima:
    peaks = argrelextrema(meas,np.less,order=minimaorder)[0]
    ## Remove outliers
    peaks = [peak for peak in peaks if meas[peak] > 5000]


thicknessarr = []
peak_wvls = wvls[peaks]
if len(peaks) > 1:
    for i in range(len(peak_wvls)-1):
        thicknessarr.append(thickness(peak_wvls[i],peak_wvls[i+1],refractive_index↵
            ,0.001))

    thicknessarr = np.array(thicknessarr)[(thicknessarr < np.median(thicknessarr) +↵
        0.500) & (thicknessarr > np.median(thicknessarr) - 0.500)]

    t=np.mean(thicknessarr)
    ts=np.std(thicknessarr)
    app.frames[MeasurePage].spec0_std.set('Standard deviation: '+str(round(ts,3)) +↵
        ' \mu m')
    app.frames[MeasurePage].spec0_dist.set('Cavity distance: '+str(round(t,3)) + ' ↵
        \mu m')

a1.clear()
a1.plot(xList, yList)
a1.plot(wvls[peaks], meas[peaks], "kx")
a1.set_title('Spectrometer 0: ')
a1.set_xlabel("wavelength [nm]")
a1.set_ylabel("Intensity [16-bit]")
a1.set_xlim((xlim_min,xlim_max))

pullData = open("static/spec1Data.txt","r")
dataList = pullData.read().split('\n')
xList = []
yList = []
for eachLine in dataList:
    if len(eachLine) > 1:
        x, y = eachLine.split(',')
        xList.append(float(x))
        yList.append(int(y))
```

```
    pullData.close()

    meas = np.array(yList)[580:1380]
    wvls = np.array(xList)[580:1380]

    if maxima:
      peaks, _ = find_peaks(meas, distance=peak_distance, height=baseline_height,width=←↩
          peak_width,prominence=[prominence_min,prominence_max])
    if minima:
        peaks = argrelextrema(meas,np.less,order=minimaorder)[0]
        peaks = [peak for peak in peaks if meas[peak] > 5000]

    thicknessarr = []
    peak_wvls = wvls[peaks]
    if len(peaks) > 1:
        for i in range(len(peak_wvls)-1):
          thicknessarr.append(thickness(peak_wvls[i],peak_wvls[i+1],refractive_index←↩
              ,0.001))

        thicknessarr = np.array(thicknessarr)[(thicknessarr < np.median(thicknessarr) +←↩
            0.500) & (thicknessarr > np.median(thicknessarr) - 0.500)]

        t=np.mean(thicknessarr)
        ts = np.std(thicknessarr)
        app.frames[MeasurePage].spec1_std.set('Standard deviation: '+str(round(ts,3)) +←↩
            ' \mu m')
        app.frames[MeasurePage].spec1_dist.set('Cavity distance: '+str(round(t,3)) + ' ←↩
            \mu m')

    a2.clear()
    a2.plot(xList, yList)
    a2.plot(wvls[peaks], meas[peaks], "kx")
    a2.set_title('Spectrometer 1: ')
    a2.set_xlabel("wavelength [nm]")
    a2.set_ylabel("Intensity [16-bit]")
    a2.set_xlim((xlim_min,xlim_max))

    pullData = open("static/spec2Data.txt","r")
    dataList = pullData.read().split('\n')
    xList = []
    yList = []
    for eachLine in dataList:
        if len(eachLine) > 1:
            x, y = eachLine.split(',')
            xList.append(float(x))
            yList.append(int(y))

    pullData.close()

    meas = np.array(yList)[580:1380]
    wvls = np.array(xList)[580:1380]

    if maxima:
      peaks, _ = find_peaks(meas, distance=peak_distance, height=baseline_height,width=←↩
          peak_width,prominence=[prominence_min,prominence_max])
```

```python
    if minima:
        peaks = argrelextrema(meas,np.less,order=minimaorder)[0]
        peaks = [peak for peak in peaks if meas[peak] > 5000]

    thicknessarr = []
    peak_wvls = wvls[peaks]
    if len(peaks) > 1:
        for i in range(len(peak_wvls)-1):
            thicknessarr.append(thickness(peak_wvls[i],peak_wvls[i+1],refractive_index↩
                ,0.001))

        thicknessarr = np.array(thicknessarr)[(thicknessarr < np.median(thicknessarr) +↩
            0.500) & (thicknessarr > np.median(thicknessarr) - 0.500)]

        t=np.mean(thicknessarr)
        ts=np.std(thicknessarr)


        app.frames[MeasurePage].spec2_std.set('Standard deviation: '+str(round(ts,3)) +↩
            ' \mu m')
        app.frames[MeasurePage].spec2_dist.set('Cavity distance: '+str(round(t,3)) + ' ↩
            \mu m')

    a3.clear()
    a3.plot(xList, yList)
    a3.plot(wvls[peaks], meas[peaks], "kx")
    a3.set_title('Spectrometer 2:')
    a3.set_xlabel("wavelength [nm]")
    a3.set_ylabel("Intensity [16-bit]")
    a3.set_xlim((xlim_min,xlim_max))


class SpecThread(threading.Thread):
  def __init__(self):
    self.running = True
    self.text_message = None
    self.button3 = None
    thread = threading.Thread(target=self.setDevicestring)
    thread.setDaemon(True)
    thread.start()

  def setDevicestring(self):
    while self.running:
        check = check_number_of_devs(self.text_message)
        if check:
            app.frames[MeasurePage].init_spec()
            self.button3.invoke()
        time.sleep(1)
    sys.exit()


class MeasureThread(threading.Thread):
  def __init__(self):
    self.running = True
    self.spec0 = None
```

```python
    self.spec1 = None
    self.spec2 = None
    thread = threading.Thread(target=self.thread_measuring)
    thread.setDaemon(True)
    thread.start()

  def thread_measuring(self):
    while self.running:
        if self.spec0 and self.spec1 and self.spec2:
            WriteSpectrum(self.spec0)
            WriteSpectrum(self.spec1)
            WriteSpectrum(self.spec2)
        time.sleep(0.1)
    sys.exit()
    self.running = False


class FPIapp(tk.Tk):

    def __init__(self, *args, **kwargs):

        tk.Tk.__init__(self, *args, **kwargs)

        tk.Tk.wm_title(self, "FPI Alignment Application")

        container = tk.Frame(self)
        container.pack(side="top", fill="both", expand = True)
        container.grid_rowconfigure(0, weight=1)
        container.grid_columnconfigure(0, weight=1)

        self.frames = {}

        for F in (StartPage, MeasurePage):

            frame = F(container, self)

            self.frames[F] = frame

            frame.grid(row=0, column=0, sticky="nsew")

        frame = self.frames[StartPage]
        frame.tkraise()

    def show_frame(self,child, cont):

        child.close()

        frame = self.frames[cont]
        frame.tkraise()

        frame.start()

    def close(self):
        return
```

```python
    def open(self):
        return


class StartPage(tk.Frame):

    def __init__(self, parent, controller):

        tk.Frame.__init__(self,parent)
        label = tk.Label(self, text="Start Page", font=LARGE_FONT)
        label.grid(row=1,column=1,columnspan=2,pady=10,padx=10,sticky='')


        self.button3 = ttk.Button(self, text="Graph Page",
                            command=lambda: controller.show_frame(self,MeasurePage))
        self.button3.grid(row=2,column=1,columnspan=2,ipadx=10,ipady=10,pady=10,padx←
            =10)


        # button = ttk.Button(self, text="Initiate devices",
        #                     command=lambda:    print('Hello World'))
        # button.grid(row=2,column=2,ipadx=10,ipady=10,pady=10,padx=10)


        var = tk.StringVar()
        label2 = tk.Message(self, textvariable=var, relief=tk.RAISED)
        var.set("Status:\nWaiting for spectrometers to be connected and initiated")
        label2.grid(row=3,column=1,columnspan=2,ipadx=10,ipady=10,pady=10,padx=10)


        self.var = tk.StringVar()
        label3 = tk.Message(self, textvariable=self.var, relief=tk.RAISED )
        label3.grid(row=4,column=1,columnspan=2,ipadx=10,ipady=10,pady=10,padx=10)


        self.rowconfigure(0, weight=1)
        self.rowconfigure(5, weight=1)
        self.columnconfigure(0, weight=1)
        self.columnconfigure(4, weight=1)


        self.t1 = SpecThread()
        self.t1.text_message = self.var
        self.t1.button3 = self.button3

    def close(self):
        self.t1.running = False

    def start(self):
        self.t1 = SpecThread()
        self.t1.text_message = self.var
        self.t1.button3 = self.button3


class MeasurePage(tk.Frame):
```

```python
def assign_calichars(self,obj):
    caliChars_391_352 = [4.81564E1,6.19383E-1,6.43391E-5,1.07503E-8,-1.87932E-11]
    caliChars_392_395 = [4.86887E1,6.24021E-1,4.98578E-5,2.36372E-8,-2.28991E-11]
    caliChars_393_374 = [5.14536E1,6.13356E-1,6.27419E-5,1.56729E-8,-2.10190E-11]


    if obj.serialNumber == 352:
        obj.caliChars = caliChars_391_352
        print("Loaded calibration parameters for spectrometer SN: 191391 (352)")
    elif obj.serialNumber == 395:
        obj.caliChars = caliChars_392_395
        print("Loaded calibration parameters for spectrometer SN: 191392 (395)")
    elif obj.serialNumber == 374:
        obj.caliChars = caliChars_393_374
        print("Loaded calibration parameters for spectrometer SN: 191393 (374)")
    else:
        print("Calibration parameters could not be assigned.")


def init_spec(self):
    self.spec0 = spectrometer('tempname1',0)
    self.spec1 = spectrometer('tempname2',1)
    self.spec2 = spectrometer('tempname3',2)

    for spec in [self.spec0,self.spec1,self.spec2]:
        if spec.serialNumber == 352:
            spec.name = 'spec0'
        elif spec.serialNumber == 395:
            spec.name = 'spec1'
        elif spec.serialNumber == 374:
            spec.name = 'spec2'
            print('spec2 was assigned')
        else:
            print("Spectrometer was not assigned to the correct position")

    self.assign_calichars(self.spec0)
    self.assign_calichars(self.spec1)
    self.assign_calichars(self.spec2)

    self.spec_init = True


def measure(self):
    if self.t1:
        # print(self.t1)
        if self.t1.running == False:
            print('Starting measureThread again')
            self.t1.__init__()
            self.t1.spec0 = self.spec0
            self.t1.spec1 = self.spec1
            self.t1.spec2 = self.spec2
        else:
            print('thread already running')
    else:
```

```python
        self.t1 = MeasureThread()
        self.t1.spec0 = self.spec0
        self.t1.spec1 = self.spec1
        self.t1.spec2 = self.spec2



    def __init__(self, parent, controller):

        self.t1 = None
        self.spec0 = None
        self.spec1 = None
        self.spec2 = None
        self.spec_init = None

        tk.Frame.__init__(self, parent)

        label = tk.Label(self, text="Spectrometer Measurement", font=LARGE_FONT)
        label.grid(row=1,column=1,columnspan=3,pady=10,padx=10)


        canvas = FigureCanvasTkAgg(f, self)
        canvas.draw()
        canvas.get_tk_widget().grid(row=2,column=1,columnspan=3,pady=10,padx=10)


        self.spec0_dist = tk.StringVar()
        Spec1_distance = tk.Message(self, textvariable=self.spec0_dist, relief=tk.↩
            RAISED, width=200)
        Spec1_distance.grid(row=3,column=1,pady=10,padx=50)

        self.spec1_dist = tk.StringVar()
        Spec2_distance = tk.Message(self, textvariable=self.spec1_dist, relief=tk.↩
            RAISED, width=200)
        Spec2_distance.grid(row=3,column=2,pady=10,padx=50)

        self.spec2_dist = tk.StringVar()
        Spec3_distance = tk.Message(self, textvariable=self.spec2_dist, relief=tk.↩
            RAISED, width=200)
        Spec3_distance.grid(row=3,column=3,pady=10,padx=50)


        self.spec0_std = tk.StringVar()
        Spec1_distance = tk.Message(self, textvariable=self.spec0_std, relief=tk.RAISED↩
            , width=200)
        Spec1_distance.grid(row=4,column=1,pady=10,padx=50)

        self.spec1_std = tk.StringVar()
        Spec2_distance = tk.Message(self, textvariable=self.spec1_std, relief=tk.RAISED↩
            , width=200)
        Spec2_distance.grid(row=4,column=2,pady=10,padx=50)

        self.spec2_std = tk.StringVar()
        Spec3_distance = tk.Message(self, textvariable=self.spec2_std, relief=tk.RAISED↩
            , width=200)
```

```
        Spec3_distance.grid(row=4,column=3,pady=10,padx=50)


        button0 = ttk.Button(self, text="Stop measuring", command=lambda: self.close())
        button0.grid(row=5,column=3,pady=10,padx=10 )

        button1 = ttk.Button(self, text="Back to Home", command=lambda: controller.↩
            show_frame(self,StartPage))
        button1.grid(row=5,column=1,pady=10,padx=10)

        button2 = ttk.Button(self, text="Begin measuring", command=lambda: self.measure↩
            ())
        button2.grid(row=5,column=2,pady=10,padx=10 )



        self.rowconfigure(0, weight=1)
        self.rowconfigure(6, weight=1)
        self.columnconfigure(0, weight=1)
        self.columnconfigure(4, weight=1)


    def close(self):
        self.t1.running = False
        print('Stopping measureThread')

    def start(self):
        # self.t1 = SpecThread()
        return

if __name__ == "__main__":

    LARGE_FONT= ("Verdana", 12)
    style.use("ggplot")

    f = Figure(figsize=(11,4), dpi=100,tight_layout=True)

    a1 = f.add_subplot(131)
    a2 = f.add_subplot(132)
    a3 = f.add_subplot(133)

    # an1 = AnimationThread(args=[a1])
    # an2 = AnimationThread(args=[a2])
    # an3 = AnimationThread(args=[a3])


    app = FPIapp()
    app.geometry("1280x720")
    ani = animation.FuncAnimation(f,animate,interval=500)
    app.mainloop()
```

C
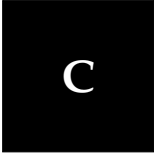
Articles

C.1   Acquisition and Analysis of Hyperspectral Thermal Images for Sample Segregation

Article

Acquisition and Analysis of Hyperspectral Thermal Images for Sample Segregation

Anders Løchte Jørgensen[1,2] ⓘ, Jakob Kjelstrup-Hansen[1],
Bjarke Jensen[2], Victor Petrunin[2], Sune Fuglsang Fink[2], and
Bjarke Jørgensen[2]

Abstract

This study presents the first results of a new type of hyperspectral imager in the long-wave thermal radiation range from 8.0 to 14.0 μm which is simpler than readily available Fourier transform infrared spectroscopy-based imagers. Conventional thermography images the thermal radiation from hot objects, but an accurate determination of temperature is hampered by the often unknown emissivities of different materials present in the same image. This paper describes the setup and development of a hyperspectral thermal camera based on a low-order scanning Fabry–Pérot interferometer acting as a bandpass filter. A three-dimensional hyperspectral data cube (two spatial and one spectral dimension) was measured by imaging a high-emissivity carbon nanotube-coated surface (Vantablack), black painted aluminum, borosilicate glass, Kapton tape, and bare aluminum. A principal component analysis (PCA) of the hyperspectral thermal image clearly segregates the individual samples. The most distinguishable sample from the PCA is the borosilicate Petri dish of which the Si–O–Si bond in borosilicate glass was the most noticeable. Additionally, it was found that the relatively large $1024 \times 768 \times 70$ data cube can be reduced to a much smaller cube of size $1024 \times 768 \times 5$ containing 92% of the variance in the original dataset. The possibility of discriminating between the samples by their spectroscopic signature was tested using a logistic regression classifier. The model was fitted to a chosen set of principal components obtained from a PCA of the original hyperspectral data cube. The model was used to predict all pixels in the original data cube resulting in estimates with very high true positive rate (TPR). The highest TPR was obtained for borosilicate glass with a value of 99% correctly predicted pixels. The remaining TPRs were 94% for black painted aluminum, 81% for bare aluminum, 79% for Kapton tape, and 70% for Vantablack. A standard thermographic image was acquired of the same objects where it was found that the samples were mutually indistinguishable in this image. This shows that the hyperspectral thermal image contains sample characteristics which are material related and therefore outperforms standard thermography in the amount of information contained in an image.

Introduction

Hyperspectral imaging was formally invented by Alexander Goetz as part of his work during the 1970s.[1] Recently, hyperspectral imaging has gained increased attention due to its promising industrial applicability, e.g., control and quality assurance within the food industry[2] and remote sensing in general.[3–5] This work focuses on hyperspectral imaging in the long-wave infrared (LWIR) region of the electromagnetic spectrum. The LWIR is typically considered the 'thermal' range of the optical spectrum, typically defined

as 8.0–14.0 μm, since the majority of the emission from objects at room temperature is within this range. This is utilized in thermography where the thermal radiation is captured and imaged. Thermography and thermal imaging

[1]NanoSYD, Mads Clausen Institute, University of Southern Denmark, Sønderborg, Denmark
[2]Research and Development, Newtec Engineering A/S, Odense, Denmark

Corresponding author:
Anders Løchte Jørgensen, SDU, Alsion 2, Sønderborg, Denmark.
Email: alj@newtec.dk

in general have been very beneficial in surveillance and detection of warm objects, however, when it comes to remote sensing of surface temperatures, significant drawbacks arise due to the varied emissivities of different materials which heavily alters the net thermal radiation emitted. Without a well-calibrated camera, the temperature predictability of a thermal image is gone. In this case, thermography is reduced to being able to tell relative temperatures of the same object. This is a considerable drawback of passive thermography which can only be overcome by the development of new methods.[6] Some workarounds have led to a set of techniques where illumination of the imaged object has been used to detect subtle characteristics such as delamination and crack formations in surfaces. These methods include lock-in thermography[7] and flying spot thermography,[8] where the active illumination is either modulated or raster scanned, respectively.

A hyperspectral thermal camera can provide a resolution to the problems related to passive thermography without introducing active illumination. The combination of recent advances in micromachining and chip production has led to significant improvements in imaging chips for the thermal range. This has allowed us to design and build a relatively cheap thermal camera capable of doing low-resolution spectroscopy in the thermal range with high spatial resolution. Such spectral information can be used to estimate the emissivity of unknown materials and thereby determine the surface temperature, based on Planck's law of radiation, with higher accuracy than with conventional thermal cameras. An additional advantage of hyperspectral thermal imaging compared to standard thermal imaging is the possibility of identifying and classifying materials based on their spectral fingerprint. This opportunity benefits thermographers and companies making thermographic inspections of the insulation in houses since reflections and disadvantageous weather significantly complicate the analysis of these images. Currently the insulation quality of constructions can only be assessed relatively, meaning that faulty constructions can be found but the important information about where most heat is lost is not available. Hyperspectral thermal cameras also have applications within defense and strategy,[9] where detection of thermal radiance from camouflaged targets is beneficial.[10,11] Other industries which might benefit from a low-cost hyperspectral thermal camera include production companies that generate environmentally damaging gases as by-products, since many of these have strong absorption bands in the thermal range.[12] Here, surveillance of the production facility could detect leaks and gas plumes.[13,14] Fourier transform (FT)-based thermal-range imagers have proven useful in medicine within quality assurance[15] and pathogen detection.[16] A different type of hyperspectral thermal cameras has been used to examine the mineral constitution of stretches of land.[17] These studies, carried out by NASA, rely on quantum well infrared photodetectors coupled with

a thermal spectrometer. The entire setup is mounted on airplanes in order to examine land and the pixel resolution is therefore in the square meter range (HyTES). Another recent project by NASA uses a hyperspectral imager based on a spectrometer in a satellite designed for remote sensing of vegetation (HyspIRI).[5]

The relevance and applicability of a hyperspectral thermal camera is significant; however, existing commercial solutions are scarce. These include the Telops Hypercam LW,[18] which is a FT spectrograph functioning in the 7.7–11.8 μm range, and the Specim LWIR HS or OWL[19] with uncooled and cooled detectors, respectively, are both push-broom cameras. The work reported in this paper focuses on the development of a relatively cheap, handheld camera ready to bring to the field, which differentiates our camera from previous research and commercial solutions.

In this study, a hyperspectral thermal camera based on a scanning Fabry–Pérot interferometer (FPI) has been developed and characterized by imaging samples of different materials. The images acquired have been analyzed and standard statistical classification algorithms have been applied to distinguish individual samples of different materials within a single image based on the spectrum observed in the individual pixels. A design of this type has been proposed earlier[20] and previous devices include an FPI-based hyperspectral camera taking images in the visible range,[21] however, to our knowledge, this is the first time an FPI-based hyperspectral imager covering the LWIR wavelengths has been demonstrated.

Materials and Methods

Hyperspectral Thermal Camera

The design is based on a plane-scanning FPI and the Lynred Pico 1024 Gen2 sensor, which is a state-of-the-art bolometer chip with 1024×768 pixel resolution. The chip has a constant sensitivity in the thermal range from 8 to 14 μm with gradual descents to zero outside this range. The bolometer chip was mounted in a QTechnology QT5022 camera, and an Ophir 35 mm f/1 objective consisting of two germanium lenses was used to focus the thermal radiation onto the focal plane array (FPA). An image grabbing event requires 33 ms, which gives a framerate of ∼30 Hz with an integration time of the analog pixel output of 42 μs.

An FPI was placed in the afocal region of the radiation in front of the objective to function as a filter for the incident thermal radiation. A sketch of the setup can be seen in Fig. 1a.

The FPI was constructed from two semi-reflecting mirrors produced in-house. These mirrors were Ø 5.08 cm (2 in.) and 5 mm thick ZnSe substrates with a Ø 40 mm thermally reflective coating on one side. The thermally reflective coating transmits ∼15% of the radiation in the 8.0–14.0 μm range. During assembly in a steel flange, the
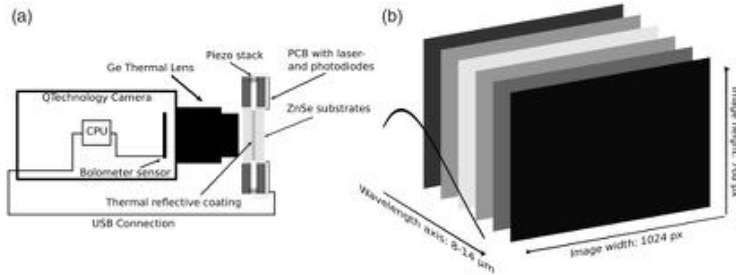
Figure 1. (a) Illustration of the hyperspectral thermal camera based on a QTechnology QT5022 camera body and the Lynred Gen2 Pico1024 bolometer chip. The FPI is placed in front of the thermal lens and consists of two ZnSe substrates with a reflective coating on top. The FPI filter is scanned by three piezo stacks, which all are connected to a microcontrolled custom PCB. The distance between the parallel mirrors is monitored by a photodiode measuring the optical interference from a laser diode and the reflected light inside the cavity of the uncoated region of the ZnSe substrates. A representation of the three-dimensional image stack is shown in (b). The image width and height correspond to the pixel value of the sensor, and the depth gives the spectral axis. Ideally, the Planck curve would be distributed along the spectral axis.

mirrors were positioned mutually parallel with a separation distance of 4 µm. This constitutes a bandpass filter with a peak transmission of ~55% and a full width at half-maximum (FWHM) of less than 440 nm. The total attenuation of the FPI was measured to 95% by numerically integrating the through FPI transmission in the 8.0–14.0 µm range measured using standard Fourier transform infrared (FT-IR) spectroscopy. With this mirror separation distance, the FPI functions in the first-order configuration for the LWIR. Three piezoelectric actuators, mounted on the rim of the steel flange holding the mirrors, were used to align the mirrors and to vary the mirror separation distance in order to scan the bandpass wavelength. The FWHM of the transmission profile of the FPI changes throughout the wavelength range from ~440 nm at a center wavelength of 8.4 µm (first-order transmission) to ~290 nm at the same center wavelength of 8.4 µm (second-order transmission). While the FPI was scanned, images were grabbed by the thermal camera. Thus, the hyperspectral camera functions as a plane-scanning camera and the hyperspectral data cube is created sequentially one frame at a time as represented in Fig. 1b. The images are grabbed while the three piezo legs are scanned, however, the time constant of grabbing an image is considerably lower than scanning the piezo, and therefore the mirror can be considered as stationary. The hyperspectral data cube therefore consists of single static images throughout the mirror separation range.

While the FPI is scanned, three laser beams (640 nm wavelength laser diodes) were incident on the edge of the ZnSe substrate cavity and the back-reflected light intensity was detected by photodiodes. The measured intensity was modulated by constructive and destructive interference of the light inside the cavity as the mirror separation distance was scanned. This allowed us to check the mirror spacing and ensure that the mirrors were parallel, which prevents unnecessary bandwidth broadening. The

interference response measured by the photodiodes was also used to calculate the wavelength of the imaged band on the FPA. FPI movement was calibrated using a 10.34 µm bandpass filter and a uniformly hot graybody. The exact physical separation between the mirrors was calculated by scanning the FPI and determining the two points with maximum intensity transmitted through the FPI with the bandpass filter in front. These two points correspond to the first- and second-order transmission of light with the bandpass filter wavelength. The correlation between these points and the interference fringes was used to calculate the wavelength of each individual band in the hyperspectral thermal image (HSTI).

Samples

The imaged object consisted of an aluminum block of 5 cm thickness and 16 cm height × 16 cm width onto which different samples were attached. The surface was covered with several strips of standard 25 µm thick Kapton tape in order to increase the emissivity. The aluminum block was heated to 103 °C by a constant current heat plate placed a short distance behind the block itself. After a waiting period of several hours, the temperature of the entire block stabilized to a precision of <0.1 °C checked by a digital thermometer measuring inside a hole drilled into the aluminum block. Heating the block ensures sufficient thermal radiance from the samples in each band of the HSTI. Additionally, the waiting period ensures that all samples remain at a constant temperature throughout image grabbing, even though the surface temperature of the individual samples might vary. Three samples were attached to the front side of the Kapton tape using silicone heat paste in order to get a high thermal conductance as well as good attachment. A 40 × 40 × 3 mm sample of Vantablack[22] is used as a black body reference. This sample was produced by Surrey
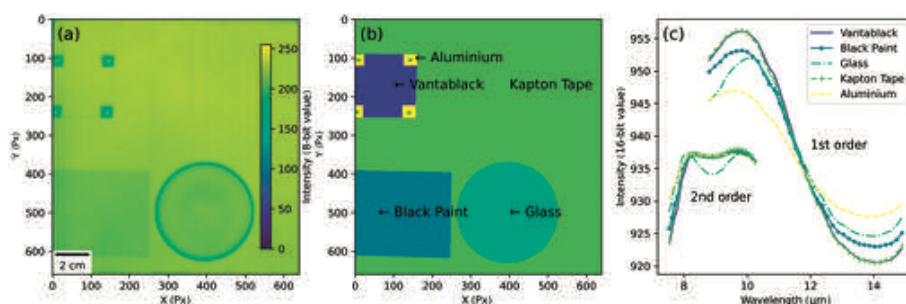
Figure 2. (a) A raw standard thermal image of the imaged scene. Since the Pico1024 sensor is used the image includes the net radiation in the range from 8.0 to 14.0 μm. (b) A masked image of the materials present in the image is shown. This mask is used as the 'true' scenario for validation of pixel predictions. The background consists of an aluminum plate covered by Kapton tape which increases the emissivity. The mean spectrum normalized to a sum of two[16] observed from each individual sample in the image is plotted in (c).

Nanosystems and consists of an aluminum plate onto which a covering layer of carbon nanotubes is grown. Each corner of the aluminum plate is free from carbon nanotubes and therefore consists of bare aluminum as can be seen in Fig. 2b. A $64 \times 54 \times 1$ mm aluminum plate painted with regular black paint and a Ø 60 mm Petri dish made from borosilicate glass were also attached to the Kapton tape as shown in Fig. 2. The aluminum block with the samples was placed at a distance of 45 cm from the front of the camera. The short distance to the heated aluminum block has a small effect on the temperature of the bolometer chip itself; when the scene is changed, a new equilibrium temperature is reached within seconds and therefore had no influence on the measurement.

Image Pre-Processing

The data were analyzed using Python 3.7 and the OpenCV and scikit-learn libraries for image processing, multivariate statistics, and statistical classification algorithms. The data contain 70 spectral bands within the wavelength interval covering the bolometer sensitivity as can be seen in Fig. 2c. The spectrum in each pixel was normalized to a sum of two[16] in order to eliminate the most extreme intensity variations caused by emissivity differences leaving mostly spectral differences. All images were handled and stored as 16-bit.

The FPI is continuously scanned from a physical separation of ∼4 μm to ∼7.5 μm, so the first-order transmission of the filter is shifted from 8 to 15 μm, which corresponds to the spectra indicated with first order in Fig. 2c. As the FPI mirrors are scanned beyond 7.5 μm, the first-order transmission moves out of the sensitivity range of the bolometer sensor, however, the second-order transmission starts moving into the sensitivity range. Further scanning of the mirrors up to ∼10 μm separation distance was then used to acquire the spectrum in the wavelength range from 7.5 up to 10 μm as indicated by second order in Fig. 2c.

Each image suffers from a fixed background noise pattern due to different offsets and radiance sensitivities of the individual pixels on the bolometer sensor, which arose during sensor manufacture. Therefore, a non-uniformity correction (NUC) or flat field correction is calculated for each pixel in order to eliminate these sensor artifacts. The calculation of this NUC is standard for uncooled bolometer arrays and functions as a one-time calibration where a linear fit is found for each pixel from images of a uniform graybody at a series of temperatures.[23,24] In our calibration, an aluminum block covered with Kapton tape functions as the graybody. The calibration was performed by letting the aluminum block fill the image plane whereafter 23 images were sequentially captured at temperatures ranging from 19.3 to 95.6 °C. These images are used to find the correction parameters for the responsivity and offset for each pixel. These correction parameters were subsequently used on all raw images from the hyperspectral data cube.

The specific HSTI analyzed in this study was originally 1024×768 pixels with 70 spectral bands. In order to simplify the analysis, the background located outside the aluminum block is cropped out of the image plane leaving a HSTI of 660×640 pixels with 70 spectral bands. Only cropped images are shown in all the figures in this paper.

Results and Discussion

A standard thermal image, shown in Fig. 2a, was taken alongside the HSTI in order to compare the two methods. Comparison of the thermal image presented in Fig. 2a and the sketch of where the samples are positioned in Fig. 2b shows that the contours of the different samples are relatively easily distinguished. The least noticeable difference lies between the Vantablack surface and the Kapton tape background. Table 1 presents the mean and standard deviation of the intensity values of all five samples. It can be observed that Vantablack and Kapton tape are

indistinguishable having essentially the same mean and standard deviations. Black paint and glass show the same behavior with almost equal mean intensities but slightly different standard deviation. However, both have intensities within a standard deviation of the other, making them indistinguishable by standard thermography. With our hyperspectral thermal imaging system, however, we are capable of distinguishing between the samples, which initially can be seen by observing Fig. 2c. From the figure it is immediately seen that the glass sample has a significant dip in second-order emission intensity around 9 μm, which is attributed to the Si–O–Si bond.[25] The remaining samples have more similar spectra and therefore statistical regression models were used to distinguish between these.

A principal component analysis (PCA)[26,27] of the hyperspectral data cube revealed the six principal components (PCs) with the highest variance, shown in Fig. 3. Figure 3g shows the relative variance explained by each of the six PCs. The first three components (Figs. 3a–3c) explain 91.4% of the total variance. Each successive component contains less than 0.3% of the total variance. The distribution of the variance in the remaining components is seen in Fig. 3(h). Based on the data in Figs. 3(g) and 3h, it can be concluded that even though the first three components contain the majority of the variance, it is not until around component 15 that the variance flattens out.

Components PC1 and PC3 clearly distinguish the borosilicate Petri dish from the rest of the image. It can be noted that the edge of the Petri dish has a different intensity from the rest of the dish. This is due to the fact that the edge walls of the Petri dish protrude from the surface of the heated aluminum block giving a noticeable temperature difference relative to the remaining part of the glass.

The clear radial gradient across the image in Fig. 3b suggests that this component contains information related to temperature variations across the aluminum block or otherwise lens aberrations. This leaves PC1 and PC3–PC6 with the information related to material characteristics. PC3 and PC5 contains a noticeable dark line between the Vantablack and the black paint marked by red bounding boxes. This is a region on the heated aluminum block where the Kapton tape is overlapping and thus two layers are present. This region is not visible on the pure thermal image shown in Fig. 2a, which again underlines the fact that additional information is stored in the hyperspectral data cube.

The ability to distinguish the samples from the hyperspectral images was tested using the scikit-learn Logistic Regression model. The logistic regression model is a linear classifier, which assumes that the object can be classified based on a linear combination of its features, which in this case are the LWIR bands. The probability that a set of features belongs to a certain class is calculated based on a logistic sigmoid function, and the model is fitted by minimizing the cost function. The model was given five classes, which corresponds to one class per material present in the image. Initially, the full hyperspectral data cube was used as input features to fit a prediction model. The fitted model was given a balanced weight of the classes, which ensures

Table I. Mean grayscale intensities and standard deviations, σ, for each individual sample based on the thermal image presented in Fig. 2.

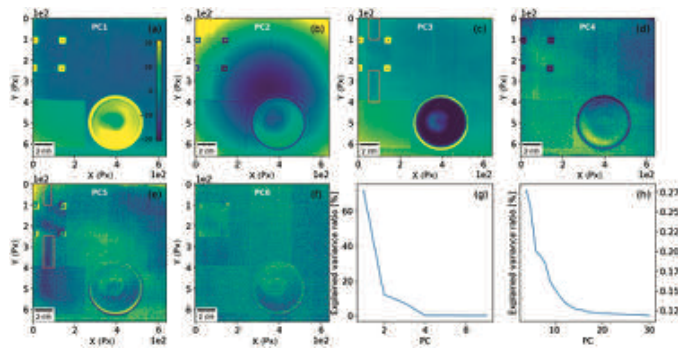| Sample material	Mean intensity	σ
Vantablack	227.3	5.5
Kapton tape	227.7	5.6
Black paint	210.4	2.5
Borosilicate glass	208.2	9.6
Aluminum	186.2	13.7

Figure 3. Six reconstructed images from the six first PCs following a PCA of the hyperspectral image stack shown in Fig. 2. Additionally, insets (g) and (h) show the relative explained ratio for the PCs following the PCA. The relative variance for the initial seven PCs is shown in (g) and (h) shows the relative variance for the last 26 PCs.
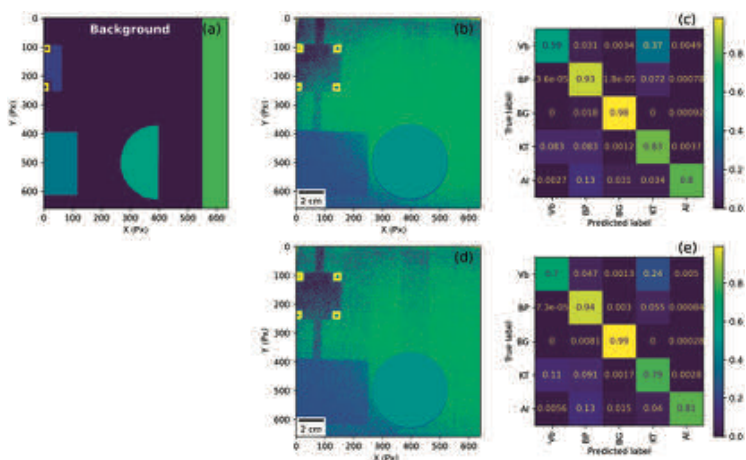
Figure 4. (a) The mask used to fit the logistic regression model. The dark blue region marked 'Background' is unused and therefore left out of the fit. (b) The results following a prediction of the samples using the fitted model and the full hyperspectral image stack. (c) The confusion matrix of the predictions vs. the true pixel values determined by image (b) in Fig. 2. (d) The results following a prediction of the samples using 69 PCs. (e) The confusion matrix of these predictions vs. the true pixel values determined by image (b) in Fig. 2. For both confusion matrices, the abbreviations Vb, BP, BG, KT, and Al have been used for Vantablack, black paint, borosilicate glass, Kapton tape, and aluminum, respectively.

that the cost function is equally biased for all classes. Additionally, the LIBLINEAR[28] solver was used to find the global minimum of the cost function. A slightly less accurate model can be fitted where the first five PCs are used as input features, which increases the speed of the process. This again underlines the promising applicability of the technique since accuracy might be sacrificed for speed in a handheld camera.

Since computation time was no issue in this case, the results obtained from the full hyperspectral data cube are presented. The model was fitted to a selected region of the hyperspectral image shown in Fig. 4a. Hereafter the full hyperspectral data cube was fed to the model to predict and find the samples present in the image. The results from this prediction are shown in Fig. 4b and the performance of the model is summarized in the confusion matrix shown in Fig. 4c.

The confusion matrix presented in Fig. 4c has been normalized for each row, and thus the main diagonal shows the true positive rate (TPR) for each sample, which is the ratio of true positives to the sum of true positives and false negatives. During this analysis, focus is put on the TPR since this makes the most sense for our application. The highest TPR is obtained for borosilicate glass with a value of 98%. This is followed by black painted aluminum with a TPR of 92%, Kapton tape with 83%, bare aluminum with 75%, and Vantablack with 59%. It is important to note the fact that five classes are defined. Therefore, a completely random guess would on average result in a 20% TPR of each class no matter its relative occupation of the image.

Within the area covered by Kapton tape (Fig. 2b), the prediction of Kapton tape in Fig. 4b shows a slight gradient from the corners to the center region of the image, with the most correctly predicted pixels concentrated in the center. Similarly, part of the Vantablack sample is mistakenly predicted to be Kapton tape where most errors appear near the center of the image. This pattern is very similar to the one observed in PC2 shown in Fig. 3b, which was ascribed to non-material-specific characteristics. Therefore, in an attempt to improve the prediction, another model was fitted using 69 out of 70 available PCs with PC2 as the only one excluded. The performance of this model is shown in Figs. 4d and 4e showing the predicted pixels and the summarizing confusion matrix, respectively. As can be seen in the confusion matrix in Fig. 4e, this model performs slightly better than the previous one having all samples predicted with a TPR of at least 70%. More importantly, the gradient observed in Fig. 4b is much less pronounced underlining the fact that true material characteristics are present in the spectra. Furthermore, it should be noted that the overlapping Kapton tape 'line' is much more apparent in Fig. 4d than 4b meaning that variations of the same sample can be distinguished from an image.

The most surprising result is the capability of distinguishing between Vantablack and Kapton tape which, as seen in Fig. 2c, have very similar spectra. Figures 5a and 5b show the second- and first-order mean spectra of each individual sample, respectively. The raw mean spectra have been ratioed against the Kapton tape spectrum, which exhibits the highest intensity across the entire measurement range.
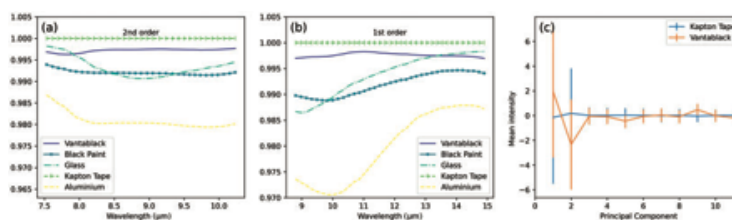
Figure 5. (a) The second-order spectrum of each sample ratioed against the mean Kapton tape spectrum. (b) The first-order spectrum of each sample ratioed against the Kapton tape spectrum. (c) The mean value of the PCs for Kapton tape and Vantablack plotted for components 1–11. The standard deviation is used as error bars.

It is immediately noticed that small variations are measured between the two samples. These variations probably originate from the Kapton tape, since the Vantablack sample is expected to perform essentially as a blackbody source of radiation. Another important feature is the fact that the differences can be measured in each individual pixel. A visualization of this is shown in Fig. 5c where the mean PC value of components 1–11 is plotted. The standard deviation of each component is plotted as error bars for the related sample. As can be seen, the components 1, 2, 5, and 9 show variations, which indicate minor differences between the two spectra.

A reproducibility and validity test has been made on three sequentially recorded HSTIs, which show that the measured spectra are reproducible and that a fitted model can be used to predict the samples reasonably well across several images. The results from this test are shown in the online Supplemental Material.

Conclusion

This work presents a new hyperspectral thermal imaging system capable of grabbing hyperspectral images in the long-wave thermal range of 8.0–14.0 μm. The camera relies on a high-resolution 1024×768 microbolometer FPA and a scanning FPI which filters the incident radiation.

The study presents a hyperspectral image, which is the first of its kind in this thermal radiation range. The results prove the applicability of a Fabry–Pérot-based hyperspectral camera, which makes hyperspectral long-wave cameras less complex than the currently available FT-IR-based solutions.

Images of five samples of different materials were analyzed in order to investigate for the possibility of discriminating between them. A standard thermographic image was unable to distinguish between the different samples, while all samples were distinguished with a TPR of 70% or more in the HSTI.

Future improvements include optimization of the classification model, where a natural further step would be to use a convolutional neural network that utilizes both spatial and spectral features of the HSTI. This has recently been used on standard hyperspectral datasets with promising

prospects.[29] Additionally, future improvements include the introduction of antireflective-coated mirrors to reduce the total attenuation in the FPI, and multiple image summing to improve the signal to noise in images at room temperature.

Declaration of Conflicting Interests

The author(s) declared no potential conflicts of interest with respect to the research, authorship, and/or publication of this article.

ORCID iD

Anders Løchte Jørgensen ⓘ https://orcid.org/0000-0001-9741-2025

Supplemental material

All supplemental material mentioned in the text is available in the online version of the journal.

References

1. J.S. MacDonald, S.L. Ustin, M.E. Schaepman. "The Contributions of Dr. Alexander F.H. Goetz to Imaging Spectrometry". Remote Sens. Environ. 2009. 113: S2–S4.
2. J. Qin. "Hyperspectral Imaging Instruments". In: D.-W. Sun, editor. Hyperspectral Imaging for Food Quality Analysis and Control. London: Academic Press, 2016, Chap. 5, pp.129–172.
3. J.A. Hackwell, D.W. Warren, R.P. Bongiovi, et al. "LWIR/MWIR Imaging Hyperspectral Sensor for Airborne and Ground-Based Remote Sensing". Int. Symp. Opt. Sci. 1996. 2819(1): 102–107.
4. W.R. Johnson, S.J. Hook, P. Mouroulis, et al. "HyTES: Thermal Imaging Spectrometer Development". IEEE Aerosp. Conf. Proc. 2011. 91109(818): 1–8.
5. C.M. Lee, M.L. Cable, S.J. Hook, et al. "An Introduction to the NASA Hyperspectral Infrared Imager (HyspIRI) Mission and Preparatory Activities". Remote Sens. Environ. 2015. 167: 6–19.
6. C. Meola, G.M. Carlomagno. "Recent Advances in the Use of Infrared Thermography". Meas. Sci. Technol. 2004. 15(9): R27.

7. D. Wu, G. Busse. "Lock-In Thermography for Nondestructive Evaluation of Materials". Revue Gen. Thermique. 1998. 37(8): 693–703.

8. Y.Q. Wang, P.K. Kuo, L.D. Favro, et al. "A Novel 'Flying-Spot' Infrared Camera for Imaging Very Fast Thermal-Wave Phenomena". In: J.C. Murphy, J.W.M. Spicer, L.C. Aamodt, et al, editors. Photoacoustic and Photothermal Phenomena II. Springer Series in Optical Sciences. Berlin/Heidelberg: Springer, 1990, pp.24–26.

9. Y. Montembeault, P. Lagueux, V. Farley, et al. "Hyper-Cam: Hyperspectral IR Imaging Applications in Defence Innovative Research". In: Second Workshop on Hyperspectral Image and Signal Processing: Evolution in Remote Sensing. Reykjavik, Iceland: June 14–16, 2010. Pp. 7–10.

10. Michael T. Eismann, Jack N. Cederquist, and Craig R. Schwartz "Infrared multispectral target/background field measurements", Proc. SPIE 2235, Signal and Data Processing of Small Targets 1994, (6 July 1994); https://doi.org/10.1117/12.179108.

11. Michael T. Eismann, John H. Seldin, Craig R. Schwartz, James R. Maxwell, Kenneth K. Ellis, Jack N. Cederquist, Alan D. Stocker, Ara Oshagan, Ray O. Johnson, William A. Shaffer. Marc R. Surette, Martin J. McHugh, Alan P. Schaum and Larry B. Stotts}, "Target detection in desert backgrounds: infrared hyperspectral measurements and analysis". Proc. SPIE 2561, Signal and Data Processing of Small Targets 1995, (1 September 1995); doi: 10.1117/12.217672}.

12. G. Socrates. Infrared and Raman Characteristic Group Frequencies. Chichester, UK: John Wiley and Sons, 2001.

13. C.C. Funk, J. Theiler, D.A. Roberts, et al. "Clustering to Improve Matched Filter Detection of Weak Gas Plumes in Hyperspectral Thermal Imagery". IEEE Trans. Geosci. Remote Sens. 2001. 39(7): 1410–1420.

14. G.C. Hulley, R.M. Duren, F.M. Hopkins, et al. "High Spatial Resolution Imaging of Methane and Other Trace Gases with the Airborne Hyperspectral Thermal Emission Spectrometer (Hytes)". Atmo. Meas. Tech. 2016. 9(5): 2393–2408.

15. Y. Roggo, A. Edmond, P. Chalus, et al. "Infrared Hyperspectral Imaging for Qualitative Analysis of Pharmaceutical Solid Forms". Anal. Chim. Acta. 2005. 535: 79–87.

16. P. Lasch, M. Stämmler, M. Zhang, et al. "FT-IR Hyperspectral Imaging and Artificial Neural Network Analysis for Identification of Pathogenic Bacteria". Anal. Chem. 2018. 90(15): 8896–8904.

17. S.J. Hook, W.R. Johnson, M.J. Abrams. "NASA's Hyperspectral Thermal Emission Spectrometer (HyTES)". In: C. Kuenzer, S. Dech, editors. Thermal Infrared Remote Sensing. Dordrecht: Springer, 2013, Chap. 5, pp.93–115.

18. Telops. "Hyperspectral IR Cameras". 2020. https://www.telops.com/products/hyperspectral-cameras [accessed Oct 19 2020].

19. Specim Spectral Imaging. "LWIR HS and OWL". 2020. https://www.specim.fi/spectral-cameras/.

20. W.J. Marinelli, C.M. Gittins, A.H. Gelb, et al. "Tunable Fabry–Perot Etalon-Based Long-Wavelength Infrared Imaging Spectroradiometer". Appl. Opt. 1999. 38(12): 2630–2639.

21. J.J. Makela, J.W. Meriwether, Y. Huang, et al. "Simulation and Analysis of a Multi-Order Imaging Fabry–Perot Interferometer for the Study of Thermospheric Winds and Temperatures". Appl. Opt. 2011. 50(22): 4403–4416.

22. A. Adams, F. Nicol, S. McHugh, et al. "Vantablack Properties in Commercial Thermal Infrared Imaging Systems". In: K.A. Krapels, G.C. Holst, editors. Infrared Imaging Systems: Design, Analysis, Modeling, and Testing XXX. 2019, p.28. doi:10.1117/12.2518768.

23. R.W. Helfrich. "Programmable Compensation Technique for Staring Arrays". In: D.F. Barbe, editor. Proc. SPIE 0178, Smart Sensors. 1979. Pp. 110–123. doi:10.1117/12.957271.

24. O. Riou, S. Berrebi, P. Bremond. "Nonuniformity Correction and Thermal Drift Compensation of Thermal Infrared Camera". Proc. SPIE 5405, Thermosense XXVI. 2004. 5405(1): 294.

25. L.J. Bellamy. The Infra-Red Spectra of Complex Molecules. Dordrecht: Springer, 1975.

26. K. Pearson. "LIII. On Lines and Planes of Closest Fit to Systems of Points in Space". London Edinburgh Dublin Philos. Mag. J. Sci. 1901. 2(11): 559–572.

27. S. Wold, K. Esbensen, P. Geladi. "Principal Component Analysis". Chemom. Intell. Lab. Syst. 1987. 2(1–3): 37–52.

28. R.-E. Fan, K.-W. Chang, C.-J. Hsieh, et al. "LIBLINEAR: A Library for Large Linear Classification, v.2.41". 2020. https://www.csie.ntu.edu.tw/~cjlin/liblinear/ [accessed Oct 19 2020].

29. Y. Liu, S. Zhou, W. Han, et al. "Convolutional Neural Network for Hyperspectral Data Analysis and Effective Wavelengths Selection". Anal. Chim. Acta. 2019. 1086: 46–54.

C.2 Surface Temperature Determination of Glass Types using Long Range Thermal Emission Spectroscopy by a Fabry-Pérot Interferometer

Surface temperature determination using long range thermal emission spectroscopy based on a first order scanning Fabry-Pérot interferometer

ANDERS LØCHTE JØRGENSEN,[1,2,*] MADS NIBE LARSEN,[1] VICTOR PETRUNIN[1], JAKOB KJELSTRUP-HANSEN[2], AND BJARKE JØRGENSEN[1]

[1] *Newtec Engineering A/S, 5230 Odense, Denmark*

[2] *NanoSYD, Mads Clausen Institute, University of Southern Denmark, 6400 Sønderborg, Denmark*

*alj@newtec.dk

1. Abstract

Determination of the surface temperature of different materials based on thermographic imaging is a difficult task as the thermal emission spectrum is both temperature and emissivity dependent. Without prior knowledge of the emissivity of the object under investigation, it makes up a temperature-emissivity underdetermined system. This work demonstrates the possibility of recognizing specific materials from hyperspectral thermal images (HSTI) in the wavelength range from 8-14 μm. The hyperspectral images were acquired using a microbolometer sensor array in combination with a scanning 1st order Fabry-Pérot interferometer acting as a bandpass filter. A logistic regression model was used to successfully differentiate between polyimide tape, sapphire, borosilicate glass, fused silica, and alumina ceramic at temperatures as low as 34 °C. Each material was recognized with true positive rates above 94 % calculated from individual ¨pixel spectra. The surface temperature of the samples was subsequently predicted using pre-fitted partial least squares (PLS) models, which predicted all surface temperature values with a common root mean square error (RMSE) of 1.10 °C and thereby outperforming conventional thermography. This approach paves the way for a practical solution to the underdetermined temperature-emissivity system.

2. Introduction

Hyperspectral imaging is an emerging field within industry and has a variety of applications. Recently, hyperspectral imaging within the visible spectrum has been used widely within the food industry for analysis and quality assurance of meat, fruit and vegetables including pathogen detection.[1–3] Similarly, the near infrared (NIR) region has been used for sorting fruit and vegetables[4,5] where specifically the detection of aflatoxin is highly valuable.[6,7] Another area with huge societal benefit is the development of robust sorting of plastic polymers, where NIR hyperspectral imaging has been shown to play a key role.[8,9] While the wide application of hyperspectral *thermal* imaging within industry still is underway, several other applications have been shown. These include SO_2 plume detection and monitoring from active volcanos,[10] mineral identification,[11–13] detection of explosive residues[14] and landscape scanning.[13,15,16] Common for these studies is the use of the Telops Hyper-Cam LW,[17] which is based on Fourier transform spectroscopy and a Michelson interferometer. The imaging system has a high resolution of 0.25 cm-1 and utilizes a cooled Mercury Cadmium Telluride (MCT) detector sensitive in the range from 7.7-11.8 µm. Additionally, thermal emission spectroscopy has been applied in space throughout several missions. These include the HyTES and HyspIRI, which both are satellite spectrometers orbiting and performing landscape scanning of the Earth.[18,19] Additionally, custom-made thermal emission spectrometers were equipped on the Mars Exploration Rovers, "Spirit" and "Opportunity", to detect minerals and rock types on Mars.[20–22]

In this study a hyperspectral thermal camera based on a Fabry Pérot interferometer (FPI) is used to record HSTI data of a selection of materials known to have vibrational absorption bands in the thermal range. A full temperature series is presented covering from room temperature to 100 ºC. The images are analysed and statistical models are used to show that specific material spectra are recognizable across a wide temperature span. Following material recognition, a material specific partial least squares (PLS) regression model is used to predict the surface temperature with a RMSE of 1.53 °C. This methodology shows that it is possible to measure the surface temperature accurately of materials with different emissivities within the same image frame. Effectively, this gives a solution to the underdetermined emissivity problem, which previously has been attempted to solve by iterative algorithms, where some claim to reach temperature predictions within two standard deviations of ±1.5 °C.[23–25]

3. Method

The hyperspectral thermal imaging system used in this study is based on a QTechnology QT5022 camera fitted with a Lynred Pico 1024 Gen2 1024×768 pixel bolometer sensor, which has a spectral range between 8 μm and 14 μm. This region is labelled the long wave infrared region (LWIR) and is often used for imaging due to its low atmospheric absorption on Earth.[26] An Ophir 35 mm, $f/1$ germanium objective lens is used to focus the light onto the sensor and a scanning FPI is placed in front of the lens acting as a variable band-pass filter (Fig. 1.). All optical surfaces between the front mirror of the FPI and the sensor itself are coated with high-efficiency broadband anti-reflective coatings. By varying the distance between the mirrors, the center wavelength of the filter is shifted. This is used to capture a hyperspectral thermal image by recording images at regular intervals while sweeping the cavity length – one image for every ≈ 80 nm of mirror displacement.
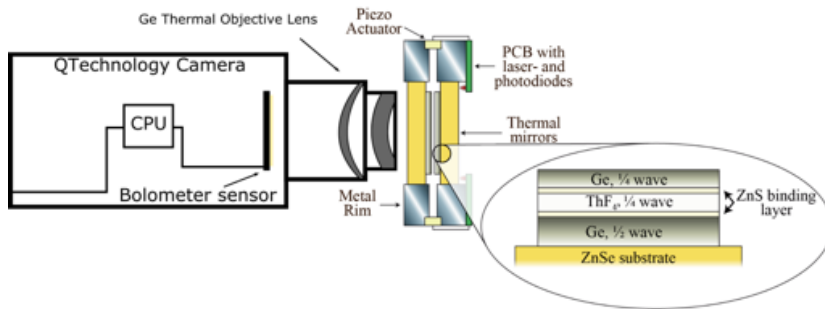

Fig. 1. *Schematic of the FPI configuration in front of the thermal camera (not to scale). Both thermal mirrors consist of a stack of Ge and ThF₄ on a ZnSe substrate, with optical thicknesses as shown in the zoom-in. The mirrors are mounted in a metal flange and the mirror distance is controlled by piezo actuators. Laser- and photodiodes mounted on a PCB around the perimeter of the mirrors keep track of the mirror separation during an imaging acquisition event.*

The FPI mirrors are made from a stack of germanium (Ge) and thorium tetrafluoride (ThF₄) with zinc sulfide (ZnS) acting as a binding layer. The stack is deposited on a 5 mm thick, Ø 50.8 mm (2 inch) substrate of zinc selenide (ZnSe) as depicted in Fig. 1. and the mirror has an average reflectivity of 84% in the range from 8 μm to 14 μm. During operation, the mirror separation is scanned in the range from ≈ 3.2 μm to ≈ 12.9 μm. This range covers the first three orders of the FPI at a wavelength of 8 μm which can be seen in Fig. S3. in the supplemental document. The full width at half maximum (FWHM) has been measured at 16 different mirror separation

distances using a Shimadzu 8400s FTIR spectrometer. The average FWHM of the first order is $\lambda_{FWHM}^{(1)} = 480 \pm 83$ nm, FWHM of the second order $\lambda_{FWHM}^{(2)} = 280 \pm 41$ nm, and FWHM of the third order is $\lambda_{FWHM}^{(1)} = 154 \pm 17$ nm. The indicated uncertainties correspond to the measured standard deviations.

The mirrors are mounted in a steel flange and three piezoelectric actuators are used to control the mirror separation. The mirror coating itself covers Ø 43 mm of the substrate leaving room for the light of three 655 nm laser diodes, equally spaced around the brim on the outside of the mirror, to individually interfere in the cavities formed by the uncoated substrate edges. While scanning, the intensity of the specular reflected light is modulated due to the constructive and destructive interference inside the cavities. The interferogram is detected by three photodiodes and is also used to ensure that the mirrors remain parallel while scanning.

The spectrum found in each pixel represents the intensity of the transmitted light as a function of the mirror separation. To calibrate the mirror separation axis, a HSTI of three different band pass filters is recorded, where the filters have the following specifications: 8226/461 nm 96%, 10224/356 nm 77% and a 11322/498 nm 92% filter. The three numbers describing each filter indicate the center wavelength, the FWHM, and the maximum transmission, respectively. From the HSTI, a small selection of each filter is made, and the average spectrum plotted for each selected region. The filters have been used for calibrating the spectral axis, which is elaborated in the supplementary information along with transfer matrix method calculations of the FPI.[27]

The samples imaged for material identification consist of an aluminum block (160×160×40 mm) covered in polyimide tape in order to obtain a high emissivity background. Taped to the block is a piece of sapphire (Ø 30 mm), a piece of borosilicate glass (1.5×3 inch), a piece of fused silica (Ø 50 mm), as well as a piece of Al_2O_3 ceramic of 95 % purity (30×400 mm) (Fig. 2c.). The aluminum block is placed against a heating element, which is used to control the temperature of the entire setup. A digital thermometer is placed in a hole drilled into the aluminum block to monitor the temperature. Images are then recorded at 20 different temperatures ranging from 27.1 ºC to 97.0 ºC. These 20 HSTIs are split into two different datasets where one is used for the training set and the other is used as an evaluation set. The training set was acquired at the following aluminum block temperatures: 27.1 ºC, 32.0 ºC, 36.5 ºC, 43.3 ºC, 49.9 ºC, 59.0 ºC, 67.2 ºC, 74.8 ºC, 83.7 ºC, and 92.3 ºC. The evaluation HSTIs are recorded at aluminum block temperatures of 30.2 ºC, 34.0 ºC, 40.0 ºC, 46.7 ºC, 54.5 ºC, 63.0 ºC, 70.4 ºC, 79.6 ºC, 88.3 ºC, and 97.0 ºC. An HSTI frame of the scene is shown in Fig. 2a. recorded at a mirror separation distance of 7.9 μm and a sample temperature of 97.0 ºC.
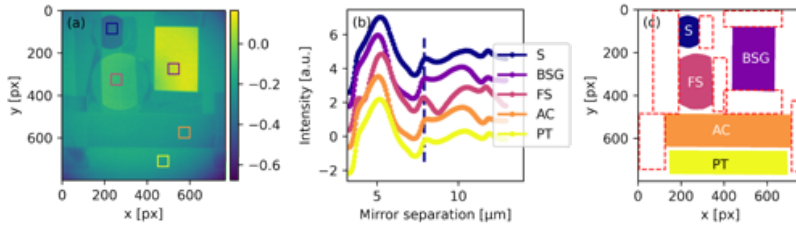
Fig. 2. *(a) Image of the samples mounted on an aluminum block using polyimide tape. The image is recorded at a sample temperature of 97.0 °C with a mirror separation of 7.9 μm. An area of each sample material is indicated by the colored squares and their average spectra are plotted in (b). The spectra have been offset on the y-axis for visualization purposes and the legend abbreviations are the following; S: sapphire, BSG: Borosilicate Glass, FS: Fused Silica, AC: Alumina Ceramic, and PT: Polyimide Tape. (c) The material mask which is used to fit the logistic regression model for material recognition. The dashed red boxes mark areas where double layers of polyimide tape have been used to tape the samples to the block. These regions are excluded from the material recognition data analysis.*

4.   Results

The overall goal of these experiments was to predict the surface temperature of materials of unknown and different emissivity within the same thermal image frame. Our approach is to first recognize the imaged material on the individual pixel level using the material specific thermal emission spectrum. Following a correct material recognition prediction, the PLS regression model belonging to the observed material is then used to predict the surface temperature from HSTI data sets recorded at other temperatures.

The thermographic images are arranged in a cube with two spatial axes representing each pixel in an image while the third axis is spectral, containing each image recorded while scanning the mirrors. All images are standardized in order to reduce the contributions from temperature variations of the samples. This is done by centering the spectral axis, which results in a mean of 0 as well as scaling, which makes the standard deviation of each pixel spectrum unity. If s represents the raw spectrum stored in a single pixel, the standardized spectrum, s', is thus calculated as

s' = (s – s) / σ

where $\bar{s}$ is the raw spectrum mean and σ is its standard deviation. This means that all intensity variations of the spectra are removed, and our recognition model will therefore solely find material characteristics. It should be noted that slight differences in the Planck curve will affect standardized spectra, however, these contributions are relatively small compared to the material spectral features and therefore have negligible influence on the performance of the model.

Fig. 2b. shows the mean spectra of the 50x50 px wide bounding boxes shown in Fig. 2a.. These bounding boxes have carefully been placed such that each box only include a single material, and thus Fig. 2b. shows the mean spectrum of each material. The legend abbreviations match the sample materials (S: sapphire, BSG: Borosilicate Glass, FS: Fused Silica, AC: Alumina Ceramic, and PT: Polyimide Tape). The dashed line in Fig. 2b. mark the mirror separation position of 7.9 μm and thereby show the selected band, which is shown in Fig. 2a. While the full-size image measures 1024×768 pixel, the image is cropped to a size of 800x768 to remove irrelevant features and reduce processing time. All images recorded during these experiments contain 140 spectral bands within the mirror separation range between 3.2 μm and 12.9 μm.

Recognizing the different materials in the image is done using the multinomial logistic regression (MLR) function implemented in scikit-learn.[28]

The training data set is used to fit a MLR model for each material across the temperatures imaged in this data set. The resulting fitted model is then used as a prediction model, which calculates the probability of a spectrum belonging to a particular material class from a linear combination of each of its spectral bands.[29] The class with the highest probability determines the material assigned to a given spectrum. The algorithm used in the optimization problem is the Newton Conjugate Gradient and the class weight is balanced to ensure equal bias for all classes regardless of their abundance. To fit and validate the model, a mask defining the location of all material classes is constructed based on one of the images from the data series which is shown in Fig. 2c..
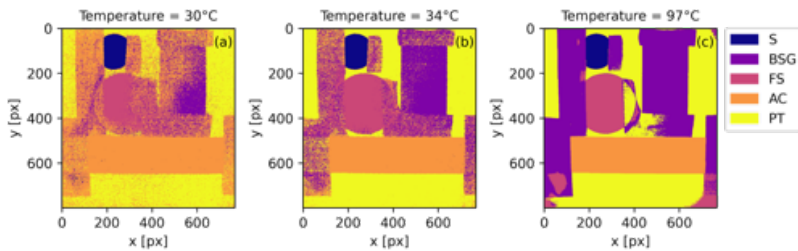

Fig. 3. *Predicted classes for HSTIs acquired at temperatures of 30.2 ℃ (A), 34.0 ℃ (B) and*

97.0 ℃ (C) in the evaluation set using the logistic regression classification model. The color-coded materials follow that of Fig. 2c and the abbreviations S, BSG, FS, AC, and PT belong to the five materials: sapphire, borosilicate glass, fused silica, alumina ceramic and polyimide tape, respectively.

The fitted MLR model is validated on the evaluation data set and the results at three different temperatures are presented in Fig. 3. with corresponding confusion matrices in Fig. 4. The images shown in Fig. 3. are reconstructions with color codes matching the predicted material by the MLR model. The x-axes of the confusion matrices shown in Fig. 4. represent the predictions made by the MLR model and these are compared to the true classification indicated along the y-axis. Each row is normalized to a sum of 1, meaning that the diagonal represents the true positive rate (TPR), which is the ratio between the true positives and the sum of both true positives and false negatives. Figs. 3. and 4. both show that the MLR model predicts the correct material in most pixels without error. The accuracy increases with increasing temperature, which is caused by the increase of emitted light and thereby the signal measured by the camera. Figs. 3a. and 4a. indicate that a temperature of 30 °C is slightly too low for the MLR model to perform well, which is primarily seen in the borosilicate glass region. However, increasing the temperature to 34 °C causes the model to perform near perfect. As seen in Fig. 3a.-3c. the regions marked by dashed red lines in Fig. 2c. are at low temperature classified as Alumina Ceramic and then at increased temperatures classified as borosilicate glass. These regions are double layers of polyimide tape, which is not part of the MLR model and thereby explain the misclassification. A single layer of polyimide tape transmits thermal radiation at distinct wavelengths in the LWIR range and therefore the material directly under the polyimide tape alters the spectrum measured in our HSTI. This have been verified during these experiments by FTIR measurements. The region marked PT in Fig. 2c. is therefore used alone for evaluating the polyimide tape predictions of the MLR model and the white region in Fig. 2c. is ignored during analysis.
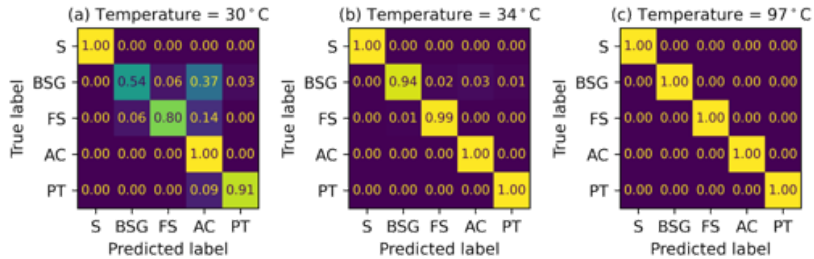
Fig. 4. *Normalized confusion matrices describing the relationship between predicted sample type and the truth described by the material mask in Fig. 2c at temperatures of of 30.2 °C (A), 34.0 °C (B) and 97.0 °C (C). S, BSG, FS, AC, and PT are abbreviations for the five materials: sapphire, borosilicate glass, fused silica, alumina ceramic and polyimide tape. Each row is normalized to a sum of 1, describing the percentage of each predicted label to the true class label.*

In order to predict the surface temperature of the imaged samples, a PLS regression is performed. The PLS model is fitted using the training set and the performance of the model is found using the evaluation HSTIs. The evaluation HSTIs are not standardized before fitting the PLS model, since the relative intensity between each image band functions as the primary predictor. The PLS model is typically used in data sets where many predictors are mutually correlated. This model is therefore a reasonable choice in our application, since our data structure contains 140 variables of which many correlates. This is due to the fact that the FWHM of the transmitted light through the FPI at a given wavelength is larger than the separation between two subsequent image frames in the HSTI and therefore, a significant overlap between images is present and two subsequent images are therefore mutually correlated.

Following a successful fit of the PLS model to the testing set, the model is applied to predict the surface temperature of the evaluation set. The results are presented in Fig. 5. along with the root mean square error (RMSE), which summarizes the accuracy of the temperature predictions. The graphs in Fig. 5. show the sample number, which in this case are individual pixels plotted versus the temperature of that pixel. All data values are plotted for each material and the sample numbers have been sorted by ascending temperature. The solid orange line indicates the true temperature and the solid green line indicate the predicted temperature based on the PLS model. Since our samples have differing thicknesses and thermal conductivities, it is highly likely that the sample surface temperatures are different from the temperature measured of the aluminum block. Therefore, our system was calibrated using a temperature model for the polyimide tape

where the temperature was measured by the thermometer inside the aluminum block which was assumed to match the temperature on the surface. This model was used on the polyimide tape taped directly to the sample surfaces to find the temperature of the polyimide tape in these areas. These values can then be used as an estimate of the sample surface temperature since both sample surface and polyimide tape are in direct contact. The temperature model was based on a single image frame from the HSTI in the training and evaluation data set, and was selected at a mirror separation corresponding to ~12 µm light where polyimide tape has a transmission of 0 %. The results of the PLS predictions are shown in Fig. 5. and the RMSE of the predictions have been summarized and included in the title of each subfigure. It is seen that all materials are predicted within an acceptable RMSE of less than 1.5 °C.
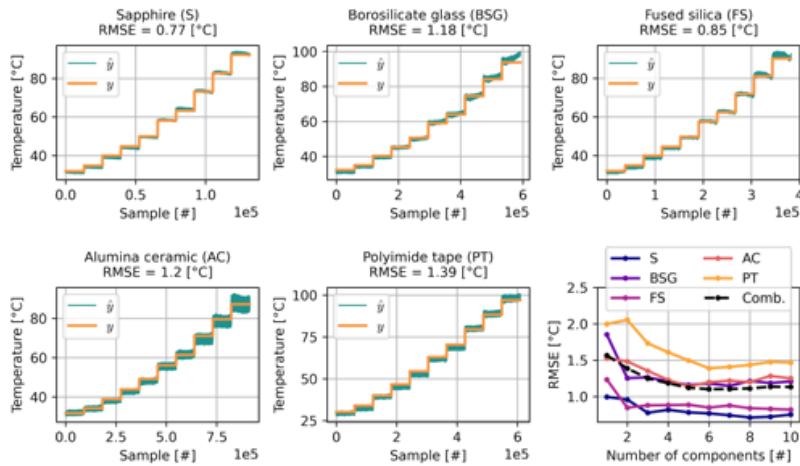

Fig. 5. *Surface temperature predictions based on PLS models fitted on all the HSTIs in the training set. The PLS models have been fitted to the spectra of each individual material marked by the mask in Fig. 2. (c). Each individual figure shows the pixelwise surface temperature predictions of every material present in the image. The predictions have been sorted in order to match a stepwise increase in temperature. The solid orange line marked y indicates the measured temperature by the thermometer, which is considered the true temperature, while the solid green line marked ŷ indicates the predicted temperatures. The root mean squared error (RMSE) of the entire set is indicated in every plot title and lastly the PLS number of components are plotted versus the RMSE of the evaluation set in the bottom right-hand figure.*

5. Discussion

At the lowest temperature of 30 °C, the material predictions are not ideal, with the Sapphire and alumina ceramic recognized with TPRs of 100 %, the fused silica TPR of 81 % and the borosilicate glass TPR of 54 % as seen in Fig. 4a. Both silica types are falsely predicted as being alumina ceramic. While the predictions are not perfect the model performs significantly better than a random guess which would result in a TPR of 20 % since a total of five classes is present. The poor model performance can mainly be ascribed to low spectral signal to noise ratio (SNR) at 30 °C. Additionally, it has previously been shown that the exact mirror separation of the HSTI bands varies slightly between different data sets.[30] The small deviations in mirror separation between image grabbing points will effectively include extra noise in the data series, which again has a huge influence at low SNR. This effect, combined with slightly concave mirrors, due to thin film stresses, has a strong impact on the performance of the model at low SNR. At 34 °C, all materials are correctly identified with the lowest TPR being 94 % for borosilicate glass (Fig. 3b. and Fig. 4b.). From a substrate temperature of 34 °C and above, the lowest TPR is 94 % and at 47 °C and above, all TPR is 100 % which can be seen in Fig. S6 and S7 in the supplemental document.

At 97 °C the corners of the thermal image shown in Fig. 3c. prediction mistakes on polyimide tape can be observed as red pixels indicating fused silica. Since these regions do not overlap with the area marked PT in Fig. 2c., the prediction mistakes do not show up in the presented confusion matrices in Fig. 4.. These prediction mistakes arise from a vignetting effect in the camera caused by the angle of incidence of the light entering the FPI. The effect is elaborated in the supplemental documentation section 3 and can be corrected by collimating the thermal light before entering the FPI.[31] It is expected that collimating the light prior to entering the FPI would improve our data, however, designing the Germanium lenses and lens system is beyond the scope of this work.

The accuracy of standard thermal imaging predictions has been made in order to compare to the PLS predictions and to show the importance of the emissivity settings. Eight conventional thermal images were grabbed of the experimental setup and the polyimide tape-region was used for a linear fit of the intensity versus temperature of the aluminum block. The surface temperature for the remaining samples were then corrected in a similar manner as described earlier. A summary of the data set is presented in section 4 in the supplemental document. Here, a table summarizes the prediction error of the surface temperature using conventional thermography. At a PT temperature of 73.2 ºC the sapphire would at an equivalent emitted intensity have a temperature of 88.2 ºC resulting in an error of 15 ºC. Equivalent errors are

found for alumina ceramic, fused silica and borosilicate with values of 1.9 ºC, 9.4 ºC, and 6.0 ºC respectively. Thus, comparing to the RMSE of the predictions shown in Fig. 5. the PLS models outperforms conventional thermography significantly. Additionally, the RMSE is well within the accuracy of the temperature emissivity separation algorithms which previously has been presented in the literature to have a two standard deviation of ±1.5 ºC.[25]

These findings show that it is possible to recognize the material specific features in the thermal emission spectra using a Fabry Pérot-based hyperspectral thermal imager at temperatures near room temperature. These material specific spectra can the subsequently be used to predict the surface temperature of the sample under investigation. The performance of such a prediction has been shown to beat conventional thermography, given that the emissivity of the sample is unknown.

6. Conclusion

In summary, hyperspectral thermal images have been recorded of samples of polyimide tape, sapphire, borosilicate glass, fused silica, and alumina ceramic. 20 HSTIs have been recorded at different temperatures ranging from 27.1 °C to 97.0 °C. Half of the data set has been used to fit a logistic regression model to recognize the material characteristic spectra of the different samples. This model was used to predict the materials present on the other half of the HSTIs resulting in TPR values above 94 % for all samples at temperatures of 34 °C and above. This shows that the emission spectra of materials are measurable by a Fabry-Pérot-based hyperspectral camera and that the spectra contain significant information at temperatures as low as 34 °C. The hyperspectral imaging system was used to predict the surface temperature of the samples present in the experimental setup based on sample specific PLS models. The models predicted the surface temperature with a common RMSE of 1.10 °C.

While the room temperature measurements showed weak predictions, we propose several improvements in order to achieve FPI-based hyperspectral images at room temperature. These include stress compensated FPI thermal mirrors in order to reduce spectral broadening due to mirror curvature and improved control software for the mirror scanning in order to get absolute mirror separations during the imaging sequence. This would allow us to align the spectral axis in the post-acquisition phase, and thereby eliminate the need for calibration. A significant improvement includes the mentioned option of collimating the thermal light before entering the FPI cavity, which again would reduce wavelength shifting and thereby increase the homogeneity of the measured thermal emission spectra across the entire sensor array.

Lastly, the addition of overlapping RGB images would make it possible to conduct even more advanced data analysis, which would allow for classification of materials of equal thermal

spectra but differing color. Additionally, the boundaries of materials can be found using edge detection from the RGB camera, which could reduce the misclassification, by binning spectra within the same boundaries.

7. Acknowledgements

8. Disclosures

The authors declare that there are no conflicts of interest related to this article.

9. Supplemental Document

See Supplement 1 for supporting content

10. References

1. G. Elmasry and D. Sun, *Meat Quality Assessment Using a Hyperspectral Imaging System* (2010).
2. D. Lorente, N. Aleixos, J. Gómez-Sanchis, S. Cubero, O. L. García-Navarrete, and J. Blasco, "Recent Advances and Applications of Hyperspectral Imaging for Fruit and Vegetable Quality Assessment," Food Bioprocess Technol. **5**(4), 1121–1142 (2012).
3. E. Bonah, X. Huang, J. H. Aheto, and R. Osae, "Application of Hyperspectral Imaging as a Nondestructive Technique for Foodborne Pathogen Detection and Characterization," Foodborne Pathog. Dis. **16**(10), 712–722 (2019).
4. K. B. Walsh, M. Golic, and C. V. Greensill, "Sorting of fruit using near infrared spectroscopy: Application to a range of fruit and vegetables for soluble solids and dry matter content," J. Near Infrared Spectrosc. **12**(3), 141–148 (2004).
5. P. Tatzer, M. Wolf, and T. Panner, "Industrial application for inline material sorting using hyperspectral imaging in the NIR range," Real-Time Imaging **11**(2), 99–107 (2005).
6. A. P. Wacoo, D. Wendiro, P. C. Vuzi, and J. F. Hawumba, "Methods for Detection of Aflatoxins in Agricultural Food Crops," J. Appl. Chem. **2014**, 1–15 (2014).
7. T. C. Pearson, D. T. Wicklow, E. B. Maghirang, F. Xie, and F. E. Dowell, "Detecting Aflatoxin In Single Corn Kernels By Transmittance And Reflectance Spectroscopy," Trans. ASAE **44**(5), 1247–1254 (2001).
8. A. Vázquez-Guardado, M. Money, N. McKinney, and D. Chanda, "Multi-spectral infrared spectroscopy for robust plastic identification," Appl. Opt. **54**(24), 7396 (2015).
9. D. Caballero, M. Bevilacqua, and J. M. Amigo, "Application of hyperspectral imaging and chemometrics for classifying plastics with brominated flame retardants," J. Spectr. Imaging **8**, 1–16 (2019).
10. A. Gabrieli, R. Wright, J. N. Porter, P. G. Lucey, and C. Honnibal, "Applications of quantitative thermal infrared hyperspectral imaging (8–14 μm): measuring volcanic SO2 mass flux and determining plume transport velocity using a single sensor," Bull. Volcanol. **81**(8), (2019).
11. T. L. Myers, T. J. Johnson, N. B. Gallagher, B. E. Bernacki, T. N. Beiswenger, J. E. Szecsody, R. G.

Tonkyn, A. M. Bradley, Y.-F. Su, and T. O. Danby, "Hyperspectral imaging of minerals in the longwave infrared: the use of laboratory directional-hemispherical reference measurements for field exploration data," J. Appl. Remote Sens. **13**(03), 1 (2019).

12.   B. Yousefi, S. Sojasi, C. Ibarra Castanedo, G. Beaudoin, F. Huot, X. P. V. Maldague, M. Chamberland, and E. Lalonde, "Mineral identification in hyperspectral imaging using Sparse-PCA," Thermosense Therm. Infrared Appl. XXXVIII **9861**(418), 986118 (2016).

13.   S. Boubanga-Tombet, A. Huot, I. Vitins, S. Heuberger, C. Veuve, A. Eisele, R. Hewson, E. Guyot, F. Marcotte, and M. Chamberland, "Thermal infrared hyperspectral imaging for mineralogy mapping of a mine face," Remote Sens. **10**(10), 1–15 (2018).

14.   T. A. Blake, J. F. Kelly, N. B. Gallagher, P. L. Gassman, and T. J. Johnson, "Passive standoff detection of RDX residues on metal surfaces via infrared hyperspectral imaging," Anal. Bioanal. Chem. **395**(2), 337–348 (2009).

15.   M. Schlerf, G. Rock, P. Lagueux, F. Ronellenfitsch, M. Gerhards, L. Hoffmann, and T. Udelhoven, "A hyperspectral thermal infrared imaging instrument for natural resources applications," Remote Sens. **4**(12), 3995–4009 (2012).

16.   P. J. Riggan and J. W. Hoffman, "Field applications of a multi-spectral, thermal imaging radiometer," IEEE Aerosp. Appl. Conf. Proc. **3**, 443–449 (1999).

17.   "Telops Hyper-Cam LW," https://www.telops.com/products/hyperspectral-cameras.

18.   S. J. Hook, W. R. Johnson, and M. J. Abrams, "NASA's Hyperspectral Thermal Emission Spectrometer (HyTES)," in *Thermal Infrared Remote Sensing, Sensors, Methods, Applications* (2013), pp. 93–115.

19.   M. J. Abrams and S. J. Hook, "NASA's Hyperspectral Infrared Imager (HyspIRI)," in *Thermal Infrared Remote Sensing, Sensors, Methods, Applications* (2013), pp. 117–130.

20.   S. Silverman, R. Peralta, P. Christensen, and G. Mehall, "Miniature thermal emission spectrometer for the Mars Exploration Rover," Acta Astronaut. **59**(8–11), 990–999 (2006).

21.   P. R. Christensen, M. B. Wyatt, T. D. Glotch, A. D. Rogers, S. Anwar, R. E. Arvidson, J. L. Bandfield, D. L. Blaney, C. Budney, W. M. Calvin, A. Fallacaro, R. L. Fergason, N. Gorelick, T. G. Graff, V. E. Hamilton, A. G. Hayes, J. R. Johnson, A. T. Knudson, H. Y. McSween, G. L. Mehall, L. K. Mehall, J. E. Moersch, R. V. Morris, M. D. Smith, S. W. Squyres, S. W. Ruff, and M. J. Wolff, "Mineralogy at Meridiani Planum from the Mini-TES experiment on the opportunity rover," Science (80-.). **306**(5702), 1733–1739 (2004).

22.   P. R. Christensen, S. W. Ruff, R. L. Fergason, A. T. Knudson, S. Anwar, R. E. Arvidson, J. L. Bandfield, D. L. Blaney, C. Budney, W. M. Calvin, T. D. Glotch, M. P. Golombek, N. Gorelick, T. G. Graff, V. E. Hamilton, A. Hayes, J. R. Johnson, H. Y. McSween, G. L. Mehall, L. K. Mehall, J. E. Moersch, R. V. Morris, A. D. Rogers, M. D. Smith, S. W. Squyres, M. J. Wolff, and M. B. Wyatt, "Initial results from the Mini-TES experiment in Gusev crater from the Spirit rover," Science (80-.). **305**(5685), 837–842 (2004).

23.   H. Haixia, Z. Bing, L. Bo, Z. Wenjuan, and L. Ru, "Temperature and emissivity separation from ASTER data based on the urban land cover classification," 2009 Jt. Urban Remote Sens. Event (2009).

24.   H. Shao, C. Liu, C. Li, J. Wang, and F. Xie, "Temperature and emissivity inversion accuracy of spectral parameter changes and noise of hyperspectral thermal infrared imaging spectrometers," Sensors (Switzerland) **20**(7), (2020).

25.   A. Gillespie, S. Rokugawa, T. Matsunaga, J. Steven Cothern, S. Hook, and A. B. Kahle, "A temperature and emissivity separation algorithm for advanced spaceborne thermal emission and reflection radiometer (ASTER) images," IEEE Trans. Geosci. Remote Sens. **36**(4), 1113–1126 (1998).

26.   S. Lord, "Gemini," https://www.gemini.edu/observing/telescopes-and-sites/sites#Transmission.

27.   S. J. Byrnes, "Multilayer optical calculations," 1–20 (2016).

28.   F. Pedregosa, G. Varoquaux, A. Gramfort, V. Michel, B. Thirion, O. Grisel, M. Blondel, A. Müller, J. Nothman, G. Louppe, P. Prettenhofer, R. Weiss, V. Dubourg, J. Vanderplas, A. Passos, D. Cournapeau, M. Brucher, M. Perrot, and É. Duchesnay, "Scikit-learn: Machine Learning in Python," J. Mach. Learn. Res. **127**(9), 2825–2830 (2012).

29.   J. M. Hilbe, *Logistic Regression Models* (Chapman and Hall/CRC, 2009).

30.   A. L. Jørgensen, J. Kjelstrup-Hansen, B. Jensen, V. Petrunin, S. F. Fink, and B. Jørgensen, "Acquisition and Analysis of Hyperspectral Thermal Images for Sample Segregation," Appl. Spectrosc. **75**(3), 317–324 (2021).

31.   W. J. Marinelli, C. M. Gittins, A. H. Gelb, and B. D. Green, "Tunable Fabry-Perot etalon-based long-wavelength infrared imaging spectroradiometer," Appl. Opt. **38**(12), 2630–2639 (1999).